

UNIVERSITÄT ULM

DOCTORAL THESIS

**Elastic and inelastic collisions in an
atom-ion experiment**

*Dissertation to obtain the degree Dr. rer. nat. of the Faculty of
Natural Sciences of the University of Ulm*

submitted by

Amir MAHDIAN

from
Shahreza

Supervisor: Prof. Johannes Hecker Denschlag

2022

Dean of Natural Sciences: Prof. Dr. Thorsten Bernhardt

Supervisor: Prof. Dr. Johannes Hecker Denschlag

Second reviewer: Prof. Dr. Alexander Kubanek

Date of oral examination: 26.09.2022

The work described in this dissertation was carried out at the

Universität Ulm

Institute of Quantum Matter

Albert-Einstein-Allee 45

89081 Ulm.

Declaration of Authorship

I hereby declare that I have done the work independently and have not used any other sources and resources than those indicated, have identified the passages taken over in words or content as references and have complied with the statutes of the University of Ulm for the Protection of Good Scientific Practice as currently published.

I agree that the dissertation may also be used for the purpose of verifying compliance with generally accepted scientific standards, in particular by using electronic data processing programs.

UNIVERSITÄT ULM

Abstract

Faculty of Natural Sciences
Department of Physics

Dr. rer. nat.

Elastic and inelastic collisions in an atom-ion experiment

by Amir MAHDIAN

In our hybrid atom-ion experiment, we study the interaction of single ions immersed in an ultracold cloud of Rb atoms. In this thesis, two main studies are presented. The first part involves the collisional cooling of the Rb^+ ion via ultracold atoms, while the second part involves quantum chemistry and the reactive collisions of a Ba^+ ion.

I describe and experimentally demonstrate swap cooling, a novel cooling mechanism in a homo-nuclear atom ion system, which can be by orders of magnitude faster than sympathetic cooling. Swap cooling exploits resonant charge exchange, to bring about a cold ion in a single glancing collision. Experimental techniques are laid out for direct observation of this cooling process in a Rb-Rb^+ system, detailing how to prepare a single ion in a well-defined kinetic energy state, let it interact with the atoms for a deterministic time interval, and measure how quickly its energy drops. The findings are theoretically explained and numerically confirmed using Monte Carlo calculations. Moreover, using numerical simulations swap cooling is investigated for multiple species, namely alkali and alkaline-earth metals, and its universal behaviour is examined.

The inelastic and reactive collisions of a laser-cooled Ba^+ ion when interacting with ultracold Rb atoms is investigated. Experimental analyses and theoretical discussions are provided to better understand collision dynamics. I will discuss and experimentally investigate how the combined spin-state of colliding particles affects the cross section of reactive processes and how preparing the reactants in specific quantum states can suppress certain reaction channels. It is shown experimentally that chemical reactions in our system can be almost completely shut off using the hyperfine level of Rb atoms.

Acknowledgements

I would like to take this opportunity to express my gratitude towards all who have supported me during these years while working on my PhD project. I will mention the names of a few people to whom I owe a debt of thanks, but by no means is the following list complete. I am a blessed individual, always surrounded by compassionate and supportive people who have helped me throughout my life and during my time as a PhD candidate.

First and foremost, I would like to thank the head of the institute, Johannes Hecker Denschlag, who made it possible for me to work in his group and who was always available for discussions.

I would like to extend my gratitude to my colleagues in the lab. It is hard to overestimate how much I have learned from Artjom Krüchow due to his deep technical knowledge, his exceptional ability for explaining complex matters, and his very friendly demeanour. I am sincerely grateful for all he has taught me which certainly goes beyond specialised details on how to operate the lab. Likewise, I'd like to thank Amir Mohammadi for his support over the years, his willingness to help and the fruitful discussions we had. The same goes for Joschka Wolf. Here, I also acknowledge Shinsuke Haze who currently runs the experiment and is always ready to support others.

I thank Thomas Paintner and Daniel Hoffmann for keeping the doors of LiLaLab open and for never hesitating to help me. Many thanks also go to Markus Deiss and Björn Drews from the Rubidium experiment who have always been friendly and ready to answer my questions.

Furthermore, I would like to thank Holger Schieferdecker, Moritz Bieber, Wladimir Schoch, and Wolfgang Limmer. They have always been kind and helpful whenever I have required assistance with a scientific or technical problem.

Olivier Dulieu has welcomed me in his group in Orsay for one month. I have learned a lot from him and Humberto da Silva Jr and had a good time interacting with their friendly group. I would like to express my gratitude to each and every one of them. I also got the opportunity to spend a few months in Basel with Stefan Willitsch's group, where I had a wonderful and fruitful time that deserves my appreciation.

Martina Schweizer and Astrid Sproll, the institute's previous and current secretaries, deserve special thanks for their kindness and assistance in a variety of ways, as well as for handling a lot of my time-consuming paperwork.

I would also like to thank a friend of mine, Amir Sabzalipour, for being supportive whenever the going got rough. Last but not least, my deepest gratitude and appreciation belongs to my family, particularly my parents, for their unwavering support and for always being a source of hope and encouragement.

Contents

Abstract	v
Acknowledgements	vii
1 Introduction	1
1.1 History	1
1.2 Outline of the thesis	4
1.3 Atom-ion experiment in Ulm	5
2 Theoretical background	9
2.1 Atom-ion interaction	9
2.2 Classical two-body scattering	10
2.2.1 Classical cross section	12
2.3 Elastic cross section	13
2.3.1 Decomposition into partial waves	14
2.4 Semi-classical interpretation	15
2.4.1 Elastic atom-ion collisions	16
2.5 Inelastic collisions	17
2.5.1 Radiative processes	20
2.6 Capture models	21
2.7 Resonant charge exchange	23
3 Direct observation of swap cooling in atom-ion collisions	29
3.1 Abstract	30
3.2 Introduction	30
3.3 Resonant charge exchange collisions	31
3.4 Experiments and results	33
3.5 Conclusion	37
3.6 Methods	37
3.6.1 Preparation of the ultracold Rb clouds.	37
3.6.2 Ion trap configuration.	38
3.6.3 Preparation of single ions at mK-temperatures.	38
3.6.4 Setting the initial kinetic energy of the ion.	38
3.6.5 Determining whether ions have been cooled down to $50 \text{ K} \times k_B$ or below.	39
3.6.6 Detection of ions.	39

3.6.7	Theoretical model for swap cooling.	40
3.6.8	Description of the simulation.	41
4	Numerical study on the universality of swap cooling	45
4.1	Introduction	45
4.2	Swap cooling cross section	46
4.3	Comparative performance of swap cooling	48
4.4	Swap cooling for alkali and alkaline earth metals	51
4.5	Concluding remarks	56
5	Controlled reaction of a Ba⁺ ion interacting with Rb atoms	57
5.1	Introduction	57
5.2	Theoretical considerations	58
5.3	Experiments and results	59
5.3.1	Reaction products	65
5.4	Concluding remarks	69
6	Summary and outlook	71
6.1	Outlook	72
6.1.1	Shape resonance	72
6.1.2	Photon-induced reactive collisions	73
A	Life and death of a cold BaRb⁺ molecule inside an ultracold cloud of Rb atoms	75
A.1	Abstract	76
A.2	Introduction	76
A.3	Experimental setup and production of molecular ion	77
A.4	Experimental Investigation of the evolution of the molecular ion	79
A.5	Insights from calculations	81
A.6	Evolution of the molecular ion	83
A.7	Radiative relaxation	84
A.8	Photodissociation of electronic ground state molecules	85
A.9	Conclusions and outlook	87
A.10	Density evolution of atom cloud	88
A.11	Mass filtering	88
A.12	Detection of the ion	89
A.12.1	Fluorescence detection of a single Ba ⁺ ion	89
A.12.2	Detection of the ion via atom loss and discrimination of ion species	90
A.13	Calculation of cross sections	91
A.13.1	Cross sections from QCT calculations	91
A.13.2	Spin-flip cross section	94
A.13.3	Radiative relaxation and photodissociation cross sections	96

A.14 Monte Carlo Simulations	104
A.14.1 Restricted model	106
A.14.2 Full model	107
B MATLAB code	113
Bibliography	127

List of Abbreviations

BEC	Bose-Einstein Condensation
COM	Centre Of Mass
FCF	Frank-Condon Factor
MC	Monte Carlo
MOT	Magneto-Optical Trap
nRCT	nonRadiative Charge Transfer
PEC	Potential Energy Curve
QCT	Quasi-Classical Trajectory
RA	Radiative Association
RCEx	Resonant Charge Exchange
RCT	Radiative Charge Transfer
TBR	Three-Body-Recombination
TOF	Time Of Flight

Chapter 1

Introduction

1.1 History

At the end of the 19th century, physics had matured to a level that it was generally accepted that all the important laws of physics had been discovered and that, henceforward, research would be mainly concerned with applying the already established laws to the detailed explanations of the experiment [Mic94]. Classical mechanics was proven to be able to explain complex problems regarding macroscopic systems, and the conservation laws for energy and momentum (and mass) were widely accepted. Thermodynamics and the kinetic theory of gases were well established, and Maxwell equations made it possible to understand optics in terms of electromagnetic waves. However, around 1900 serious doubts arose about the completeness of the classical theories. Some theoretical formulations led to paradoxes when pushed to the limit to explain certain physical phenomena, such as the energy distribution in blackbody radiation and the photoelectric effect. These shortcomings were never to be resolved within the framework of classical physics, and new ideas were required. At the beginning of the 20th century, a significant revolution shook the world of physics, ushering in a new era, generally referred to as modern physics. A fundamental part of modern physics is quantum mechanics, which was developed in the mid-1920s by Niels Bohr, Erwin Schrödinger, Werner Heisenberg, Max Born and others. By 1930, David Hilbert, Paul Dirac, and John von Neumann had further unified and formalized quantum mechanics, focusing more on measurement, the statistical nature of our knowledge of reality, and philosophical speculation on the 'observer'. Many new disciplines have emerged since then, including quantum chemistry, quantum electronics, quantum optics, and quantum information science.

The work on quantum coherence theory by R. J. Glauber [Gla63b; Gla63a], a Nobel laureate in 2005, and the development of the laser theory by H. Haken, M. O. Scully, and W. E. Lamb, a Nobel laureate in 1955, gave rise to theoretical quantum optics in the 1960s. Following that, the topic has become a well-established area of physics due to the high level of quantum engineering, i.e. the preparation, manipulation, control, and detection of quantum systems developed and realized by atomic physics and quantum optics. The development of wholly new areas of atomic physics and quantum optics, such as atom optics [Mey01], as well as new frontiers in precision

metrology and quantum engineering, has resulted from laser cooling and mechanical manipulations of particles with light [MS03]. The Nobel Foundation recognized these advancements in 1997, awarding the prize to S. Chu [Chu98], C. Cohen-Tannoudji [CT98], and W. D. Phillips [Phi98] "for the development of methods to cool and trap atoms with laser light." In 1995, laser cooling along with evaporative cooling enabled the experimental realization of a new phase of matter, the Bose-Einstein condensed (BEC) phase [And+95; Bra+95; Dav+95]. BEC was predicted by Einstein in the 1920s based on certain original ideas by Bose, and its experimental confirmation in 1995 marked the start of a new era in the so-called AMO community, which includes atomic, molecular, optical, and quantum optical physics. A few years later, in 1999, atomic degenerate Fermi gases were realized [DJ99; Sch+01; Tru+01], clearing the path for Fermi superfluidity to be observed. Ultracold atomic and molecular systems are now at the forefront of modern quantum physics and are regarded as the most controllable systems for studying many-body physics. These systems are expected to have a wide range of applications in quantum information and quantum metrology, as well as the potential to serve as quantum simulators.

After successful demonstration of cold ion trapping in 1980 using a quadrupole trap [Neu+80], H.G. Dehmelt and W. Paul shared half of the Nobel Prize in Physics in 1989 "for the development of the ion trap technique", which arguably set one of the most significant benchmarks in the study of single-particle quantum systems¹. Cirac and Zoller proposed in 1995 [CZ95] that a quantum computer can be implemented based on a string of cold ions confined in a linear trap, where the electronic states of the ions represent the quantum bits of information. Cold trapped ions were then experimentally investigated to realize such scalable quantum gates using a bottom-up approach [SK+03; Hom+09]. Being one of the leading contenders in the experimental realization of quantum computers, the field of trapped ions has seen remarkable technological growth in the last two decades. As quantum coherence in confined ions has been made to be highly resistive to the external noise, many research groups are working on more complex protocols and building up quantum networks based on trapped ions [DM10; Bru+19]. Another fascinating new field is quantum simulation with trapped ions, which is based on Richard Feynman's original idea of simulating Hamiltonians with a well-controlled quantum system [Fey82]. The first results showed that phonon-mediated ion-ion interactions can be used to build multiple spin models in which the spin states correspond to the ion's internal states [MW01; PC04]. Experimental works in using trapped ions as a test-bed for quantum simulations have since been undergoing rapid development [Fri+08; Kim+10; Bar+11; BR12]. Researchers have been able to apply quantum simulation with trapped ions to a wide range of new phenomena. Experimental demonstration of a digital quantum simulation of a lattice gauge theory on a few-qubit trapped-ion quantum computer [Mar+16], observation of a discrete time crystal [Zha+17a], generating many-body

¹N. F. Ramsey received the other half of the prize that year "for the invention of the separated oscillatory fields method and its use in the hydrogen maser and other atomic clocks".

localization states in a quantum simulator with programmable random disorder [Smi+16], and studying non-equilibrium dynamics in the transverse-field Ising model with long-range interactions [Zha+17b] are but a few examples. Cold trapped ions have even been used to investigate statistical mechanics in quantum systems [Clo+16; Ney+17; EFG15] and to study thermodynamics to the limit of single atoms.

The technological advancement that pushed the two fields of ultracold gases and trapped ions forward has inspired scientists at the beginning of the 21st century to combine these two well-established and controllable systems and study their interaction. Various theoretical investigations into atom-ion interactions moved the focus towards the ultracold regime at the turn of the third millennium, with an eye on the near-term potential applications. Studies of charge transfer and total elastic cross sections in ultracold atom-ion collisions [CD00] were followed by the investigation of charge mobilities in an ultracold gas [C00] and near resonant charge exchange [BZD08]. The promise of having a different inter-particle interaction than what has been used by then, with neutrals or ions only, fuelled the new research field. Due to the polarization potential between an atom and an ion with an r^{-4} dependence at large distances [Lan05], it was proposed to use hybrid atom-ion systems as a testbed for studying strongly correlated many-body processes [CKL02; Goo+10; CTD11; MPS05], as a quantum gate [DIC10; ICZ07], or to emulate solid-state physics [Bis+13]. A quantum theory to study atom-ion scattering in the ultracold regime was also developed, predicting shape and Feshbach resonances at finite temperatures [CD00; Idz+09; Idz+11] and providing a universal bound spectrum for atom-ion systems [Gao10]. Moreover, sympathetic cooling of ions via collisions with ultracold atoms was theoretically investigated [Mak+03; Kry+11; Hud09].

As the theoretical studies into atom-ion collisions were building up, several experiments were being set up to explore the new field. In 2006, the first progress report on a hybrid atom-ion experiment was published [SML05]. Soon after, such systems were experimentally realized, and one of the first topics studied was cold elastic collisions between trapped ions and trapped atoms in the semiclassical regime [Gri+09; Zip+10a; SHD10; Haz+13]. Collisional cooling of atomic [Zip+11; Rav+12; Här+12; Siv+12] and molecular [Rel+13] ions immersed in a bath of ultracold neutral atoms was demonstrated. Hybrid atom-ion experiments have also entered the realm of quantum chemistry by studying inelastic and reactive collisions. Charge transfer [Gri+09; SHD10; Rel+11; Hal+11; HW12; Smi+14; Haz+15; Sik+18b], molecular formation [Hal+11; Rel+11; Sul+12; Här+13b; Hal+13b; Hal+13a; Sar+16; Moh+21], and spin-exchange [Rat+13; Für+18; Sik+18a] were studied in inelastic two-body collisions for several species.

Many novel phenomena were explored as the new research field progressed towards experimental maturity. To name a few, three-body-recombination in atom-atom-ion collisions [Här+12], non-equilibrium dynamics [Zip+11] and the micromotion induced power-law energy distribution of the ion [Mei+16], using ion-induced atom loss [Zip+10a] to detect the density profile of the atomic cloud [SHD10] or

minimize excess micromotion [SHD10; Zip+10b; Här+13a; Moh+19] were reported. Moreover, bifurcation of ion energies [Sch+16], interactions between trapped ions and ultracold Rydberg atoms [Ewa+19], buffer gas cooling of a trapped ion to the quantum regime [Fel+20], long-range versus short-range effects in cold molecular ion-neutral collisions [Dör+19], and swap cooling [Rav+12; DR18; MKD21] were investigated.

Furthermore, full control of two independent subsystems in hybrid atom-ion experiments allowed for controlled chemistry employing a variety of methods to manipulate reactive and chemical processes. The energy dependence of inelastic and reactive collisions was experimentally studied [Gri+09; Zip+10b; Hal+13a; Krü+16a; Ebe+16]. Tuning the reaction rates of trapped ions with ultracold neutral atoms by exerting control over both their quantum states was investigated. This comprises research into different electronic states of the reactants [Hal+11; HW12; Rat+12; Sul+12; Haz+15], as well as preparation in different spin states [Sik+18b; Sik+18a] and external field control [Sik+18a]. Moreover, Feshbach resonances between a single ion and ultracold atoms were observed, allowing to tune the rate of both three-body reactions and two-body sympathetic cooling [Wec+21].

[HHD14; SK14; Wil15] provide an overview of the burgeoning field of hybrid atom-ion experiments. A more recent and comprehensive review of the theoretical and experimental progress in research on cold hybrid ion-atom systems is given in [Tom+19].

1.2 Outline of the thesis

The structure of this thesis is as follows:

In the remaining part of this chapter, I will give a brief overview of the hybrid atom-ion experiment in Ulm, using which I have been able to perform the measurements presented in the current thesis.

The purpose of **chapter 2** is to provide a short overview of the fundamental theoretical concepts and formulas that are pertinent to the study of atom-ion interactions. The focus here is on atom-ion collisions and various elastic and inelastic processes that can in principle occur, rather than established cooling and trapping techniques for each given system.

In **chapter 3**, I present direct experimental evidence for "swap cooling," a novel and swift cooling process in which a hot ion can lose nearly all of its kinetic energy in a single collision with an ultracold atom. Swap cooling can be by orders of magnitude more efficient than conventional buffer gas cooling. In a nutshell, the hot ion and the ultracold atom swap their identities in a collision where merely an electron is exchanged.

Chapter 4 further elaborates on swap cooling using numerical simulations. To show the universality of the process, the calculations are extended to include several species. Moreover, geometrical configurations of the trapping potentials and the

energy ranges that were not empirically accessible in our experiment are numerically investigated.

Chapter 5 involves controlled chemistry in atom ion collisions using the initial quantum states of the reactants. I look at the reaction rate of a cold Ba^+ ion in an ultracold cloud of Rb atoms. The experimental results reveal that by preparing the Rb atoms in different hyperfine states, the reactive process can be virtually completely controlled. I also provide theoretical justifications for the obtained results.

Chapter 6 provides a short summary of the thesis and suggests an outline for future investigations.

1.3 Atom-ion experiment in Ulm

Our Ulm experiment is one of the few hybrid atom-ion traps which allows studying the interaction between degenerate atomic samples and single ionic species. As the apparatus has been in operation since 2009, detailed descriptions of the machine and its working concept are available elsewhere [Sch+12; Sch12; Här13]. Therefore, I only review the main characteristics of the set-up and the vacuum system.

The vacuum system comprises three connected chambers named MOT, BEC, and science chamber after their respective functions (see Fig. 1.1). The chambers are separated so that the optical access to the science chamber is maximized, and the mutual electromagnetic disturbance between the atom and the ion system is suppressed. The sequence of preparing ultracold atoms starts with few seconds of loading ^{87}Rb atoms into a magneto-optical trap (MOT) from the background vapour at a pressure of about $P_{\text{MOT}} \approx 10^{-9}$ mbar. This process is followed by optical molasses, which further cools down the atoms. Depending on the polarization of one of the laser beams, atoms are then pumped into one of the $|F = 1, m_F = -1\rangle_{\text{Rb}}$ or $|F = 2, m_F = 2\rangle_{\text{Rb}}$ states. The atoms in one of the said magnetically trappable spin states are subsequently transported to the BEC chamber by means of magnetic transport, resulting in a purely spin-polarized ensemble of atoms. The pressure in the BEC chamber is almost two orders of magnitude lower than the MOT chamber, allowing for the evaporative cooling down to the Bose-Einstein condensation (BEC). In the BEC chamber, the atom cloud is held in a combined magnetic and optical dipole trap. After an initial evaporative cooling in the magnetic quadrupole trap, atoms are cold enough to be only confined by the optical dipole trap. This process ensures high atom number stability when set up appropriately [Krü17]. If required, we can continue with the evaporative cooling in the optical trap to reach the sub μK regime and attain BEC. In the next step, the ultracold atom cloud is loaded into a one-dimensional optical lattice consisting of two counter-propagating laser beams. By changing the frequency of one of the laser beams, the atoms will be vertically transported from the BEC chamber to the science chamber. A crossed optical dipole trap is employed to confine the atoms in the science chamber at a final position chosen to be the centre of the Paul trap, which allows atom-ion experiments to be

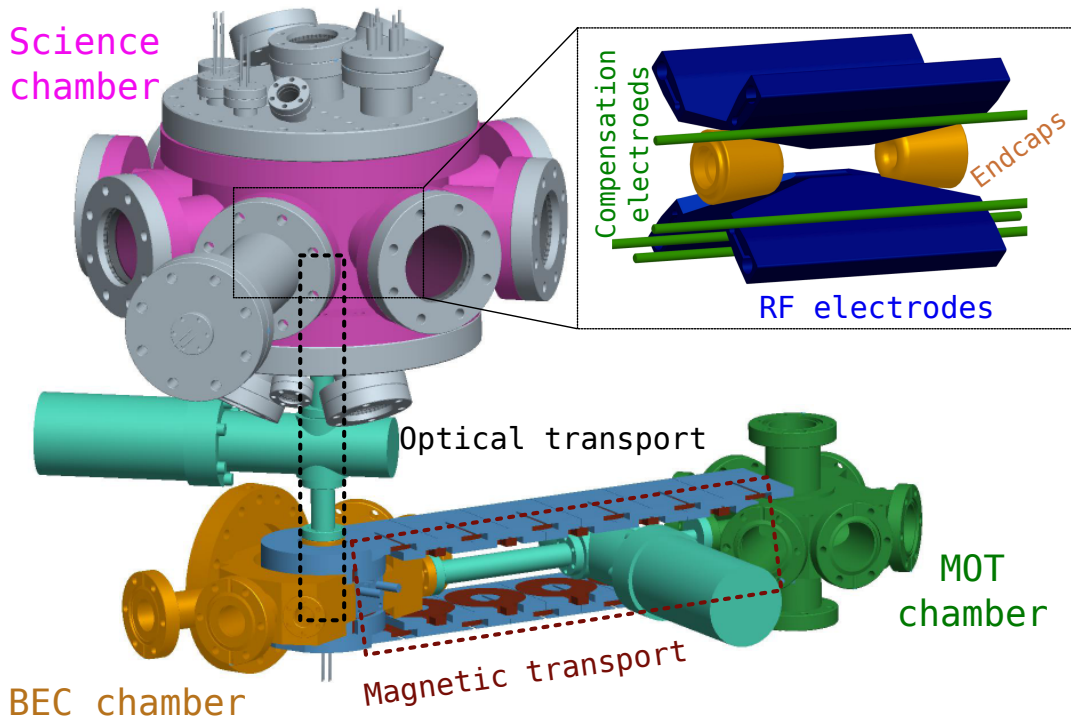


FIGURE 1.1: Schematic drawing of the atom-ion experiment in Ulm. Shown are the three vacuum chambers, each labelled according to its role: MOT, BEC, and Science chamber. Magnetic transport is used to bring the Rubidium atom cloud from the MOT to the BEC chamber, from which it can be optically transported to the Science chamber. The upper right image depicts a zoomed in picture of the linear Paul trap in the science chamber, used to trap ions.

performed. Time of flight (TOF) absorption imaging is used to determine the number and temperature of the atomic cloud.

Now, I continue with a brief representation of the ion system. The ions are trapped in a linear Paul trap, shown schematically in the top-right of figure 1.1. Our Paul trap consists of four blades known as RF-electrodes, which confine the ion radially by producing an oscillating quadrupole electric field. The net result of the oscillating electromagnetic field will be a (near) harmonic trapping potential in the radial direction [Ber+98]. Two end-cap electrodes with static potentials are used for axial confinement of the ion. Additionally, four compensation electrodes can apply DC electric fields in the radial direction of the Paul trap to centre the ion at the minimum of the RF trapping potential. This way, the undesired excess micromotion can be suppressed [Ber+98], ensuring cold and controlled collision energies. Alternatively, an intentional DC field can be applied to shift the ion radially as a means to control the collision energy [Krü+16a]. We typically work with single $^{138}\text{Ba}^+$ or $^{87}\text{Rb}^+$ ions. Ba^+ ions are produced by two-photon ionization of the neutral Barium atoms. They are then laser-cooled down to the Doppler-cooling limit. Rb^+ ions are produced indirectly from neutral Rb atoms [Här+13b]. Moreover, we can create Rb_2^+ and BaRb^+ molecular ions [Moh+21]. In a typical atom-ion experiment, before loading the atom cloud, the ion is axially shifted from the centre of the Paul trap

to prevent unwanted atom-ion interactions. The measurement starts with overlapping the two trapping potentials and immersing the ion into the ultracold atoms.

Chapter 2

Theoretical background

2.1 Atom-ion interaction

The rich physics and chemistry in hybrid atom-ion systems, some of which was listed in chapter 1, rely essentially on the nature of the interaction of charged particles with ultracold neutral atoms. The interaction potential between colliding particles depends on the characteristics of the species. The long-range part of the interaction potential $V(r)$, where r is the inter-particle distance, can be formulated as [DO18]

$$V(r) = \sum_{n=1}^{\infty} -\frac{C_n}{r^n} \quad (2.1)$$

where C_n are long-range coefficients which can be derived from the multipole expansion of the interspecies interaction operator. It is apparent from equation 2.1 that the potential originating from successively higher n falls off increasingly rapidly with distance, indicating that terms with smaller n progressively dominate the potential at long-range. In most cases, it suffices to truncate equation 2.1 to only include the dominant term. Ions mainly interact with the strong and long-range Coulomb potential, which has an r^{-1} dependency. The interaction of polarizable neutral atoms in the electronic ground state is determined by induced dipole moments, resulting in an r^{-6} (mostly) attractive van der Waals potential. In atom-ion collisions, the effect of the ion's electric field $\varepsilon(r) = e/(4\pi\epsilon_0 r^2)$ on the polarizable atom dominates the interaction potential. Here, e is the elementary charge, ϵ_0 the vacuum permittivity and r the separation between atom and ion. The electric charge induces a dipole moment $p(r) = \alpha\varepsilon(r)$ in an atom with polarizability α . The induced dipole feels an attractive force towards the ion due to the inhomogeneity of the field. The polarization potential thus characterizes the atom-ion interaction,

$$V_{pol}(r) = -\frac{1}{2}p(r)\varepsilon(r) = -\frac{e^2}{(4\pi\epsilon_0)^2} \frac{\alpha}{2r^4} = -\frac{C_4}{r^4} \quad (2.2)$$

with¹ $C_4 = \frac{e^2}{(4\pi\epsilon_0)^2} (\alpha/2)$.

¹In atomic units $C_4 = \alpha/2$. It should also be noted that in some literature, see e.g. [CD00], the polarization potential is defined as $V_{pol}(r) = -\frac{C_4}{2r^4}$ which leads to a C_4 that differs in a factor of two with what is given here.

The internal spin state of the particles turns out to be relevant if they get close enough for their spins to interact. Therefore, spin orientations become inconsequential for interacting ions but notable when neutral atoms collide, owing to the distinct range characteristics of the two potentials. The atom-ion polarization potential is a middle ground that allows for both long-range interactions and the internal spin state of the particles to be of significance. This topic will be explored in further depth in chapter 5.

2.2 Classical two-body scattering

The collision of two (structureless) particles that interact via a spherically symmetric potential $V(r)$ is discussed in this section. The collision is elastic, meaning the total kinetic energy of the particles before and after the collision is conserved, as there are no internal degrees of freedom that could exchange energy with the translational degrees of freedom. The following is mainly adopted from [HH08].

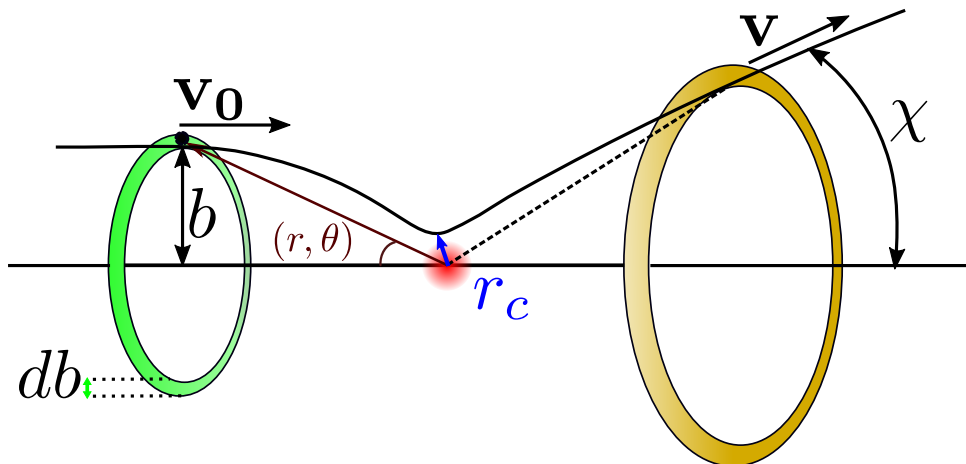


FIGURE 2.1: Schematic drawing of classical two-body scattering in the centre of mass reference frame. A particle with reduced mass μ and initial relative velocity \mathbf{v}_0 is scattered from a fixed centre, shown by a red circle. Polar coordinates (r, θ) , can be used to describe the motion. The impact parameter is defined as the perpendicular distance between the path of the projectile and the centre of scattering. The distance of the closest approach is shown by r_c . The deflection angle χ is the deviation from the incident straight-line path due to scattering.

The dynamics of the two-body collision can be divided into centre-of-mass motion and relative motion with the reduced mass of the two particles $\mu = m_A m_B / (m_A + m_B)$. As depicted in figure 2.1, the collision can be thought of as the scattering of a particle with the reduced mass μ and the initial relative velocity \mathbf{v}_0 from a fixed centre (shown by a red circle in Fig. 2.1). The deflection angle of the trajectory χ is the deviation from the incident straight-line path due to attracting and repulsive forces. The deflection angle describes the outcome of the elastic collision and is the main quantity to be determined. Since the collision is elastic, the kinetic energy in

the relative motion is conserved. Moreover, the interaction's spherical symmetry implies that the angular momentum of the relative motion is conserved. As a result, the collision will take place in the plane defined by the initial values of the radius and momentum vectors. This means that the relative motion may be described using only two coordinates which here are chosen to be the polar coordinates in the plane (r, θ) . The total energy associated with the relative motion, also known as the collision energy, can be written as $E_{col} = (1/2)\mu v^2 + \frac{L^2}{2\mu r^2} + V(r)$ in which $v = dr/dt$ and $L = \mu r^2 d\theta/dt$. The collision energy $E_{col} = (1/2)\mu v_0^2$ and the magnitude of the angular momentum $L = \mu r v_0 \sin \theta$ are constants of motion, where v_0 is the relative speed prior to the collision and θ is the angle between \mathbf{r} and \mathbf{v}_0 . An impact parameter can be defined as $b = r \sin \theta$, and therefore, $L = \mu v_0 b = b\sqrt{2\mu E_{col}}$.

It is useful to define an effective potential as

$$V_{eff}(r) \equiv V(r) + \frac{L^2}{2\mu r^2} = V(r) + \frac{E_{col} b^2}{r^2}. \quad (2.3)$$

Figure 2.2 shows the long-range part of the effective potential for an arbitrary (attractive) potential $V(r)$ for three different values of L , $l_0 = 0 < l_1 < l_2$. If $E_{col} = V_{eff}(r)$ has a real-valued positive solution for r , then there will be a distance of the closest approach r_c for the total energy E_{col} for which $dr/dt = 0$. Evidently, such a solution, i.e., a turning point, will always exist for a potential with a repulsive part. For non-zero impact parameters, turning points may also exist in the attractive part of the potential, where $V(r) < 0$. Due to the centrifugal energy, a barrier can appear in the effective potential when $b > 0$. In figure 2.2 the maximum of the effective potential for two different angular momenta, corresponding to two different impact parameters, happen at $r = r_0(L)$. The collision energy is higher than the centrifugal barrier for the effective potential corresponding to $L = l_1$. Therefore, the particles can have a close encounter and experience the short-range part of the potential (not shown in the graph). For $L = l_2$, on the other hand, the intersection between E_{col} and the potential barrier determines the distance of the closest approach, $r_c(l_2)$, which is the classical turning point of the collision.

In order to obtain an expression for the deflection angle, one notes that $\theta(t) = \int_{-\infty}^t \frac{L}{\mu r^2} dt$. Since $\theta(t \rightarrow -\infty) = 0$, and given that $dr/dt = 0$ at $E_{col} = V_{eff}(r)$, it is straightforward to show

$$\theta(r) = -b \int_{\infty}^r \frac{1}{\tilde{r}^2 \sqrt{1 - b^2/\tilde{r}^2 - V(\tilde{r})/E_{col}}} d\tilde{r}$$

As said above, for potentials with a repulsive part, a distance of the closest approach $r = r_c$ will exist with the corresponding angle $\theta = \theta_c$. It can be shown [HH08] that the trajectory is symmetric around a line at $\theta = \theta_c$. Since a non-deflected trajectory

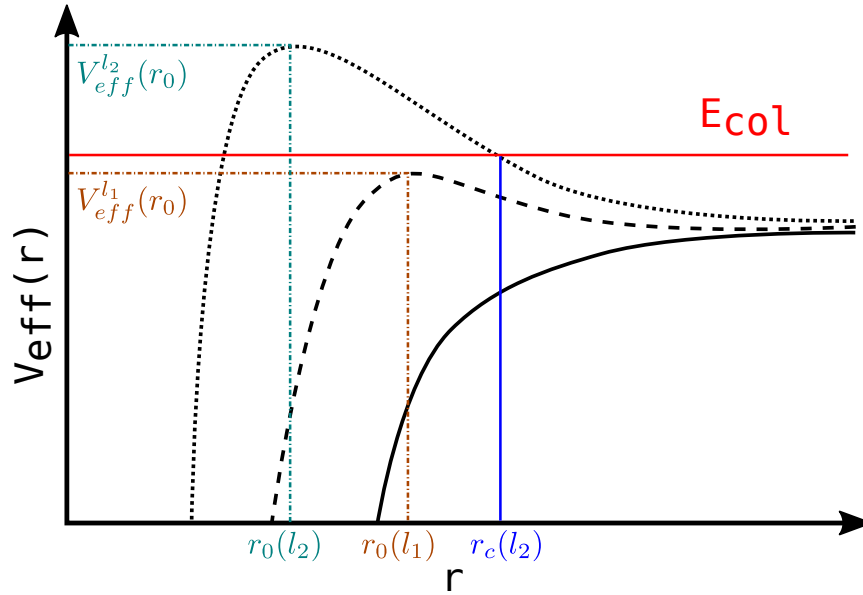


FIGURE 2.2: Long-range part of a classical effective potential according to equation 2.3 for an arbitrary attractive potential $V(r)$ for three different values of $L, l_0 = 0 < l_1 < l_2$. The maximum of the effective potential happens at $r_0(L)$. The intersection of E_{col} and the $V_{eff}^L(r)$ gives the distance of the closest approach, shown by r_c . If the collision energy is higher than the maximum of the centrifugal barrier, as is the case for l_0 and l_1 , the particles will have a close encounter, experiencing the short-range part of the potential (not shown here).

corresponds to $\theta = \pi$ the deflection angle is defined as

$$\chi(E_{col}, b) = \pi - 2\theta_c = \pi - 2b \int_{r_c}^{\infty} \frac{1}{r^2 \sqrt{1 - b^2/r^2 - V(r)/E_{col}}} dr \quad (2.4)$$

Therefore, the deflection angle depends on the impact parameter and the collision energy E_{col} .

2.2.1 Classical cross section

Before defining the classical collision cross section, one needs to clarify what a "collision" means. Classically, a collision is said to take place whenever two particles exert a force on one another in the framework of Newton's mechanics [Lev05]. A chemical reaction could occur as a result of the collision, or the two particles could just be deviated off their uninterrupted straight-line trajectory, or anything in between. Whatever the outcome, a collision is considered to have occurred when a force due to the potential acted. This force does not have to be repulsive, and in fact, the long-range part of the force is generally weakly attractive. Now, the cross-section can be defined as the area that the relative motion of the particles must cross in a plane perpendicular to the initial velocity, in order for a collision to occur.

As shown in figure 2.1, the impact parameter is defined in a perpendicular plane to the initial velocity \mathbf{v}_0 . Consider a circular target region in that plane, the centre

of which is at $b = 0$. A collision with an impact parameter in the range b to $b + db$ must pass through a ring with a radius of b and a width of db to cross the target. Such a ring has an area of $2\pi b db$. Therefore, the differential collision cross section reads $d\sigma = 2\pi b db$. The total collision cross section is then the integral over all the values of b that lead to a collision

$$\sigma = 2\pi \int P(b) b db$$

where $P(b)$ is the opacity function, which determines the probability that a particular trajectory will lead to the process in question.

2.3 Elastic cross section

Here, I give an overview of the quantum theory of elastic collisions, which is the most basic type of collisional process. In the context of this thesis, elastic collisions are of relevance for the sympathetic cooling of ions by ultracold atoms. The collision of two structureless particles via a spherically symmetric potential $V(r)$, which tends asymptotically to zero more rapidly than $1/r$, is considered. It is convenient to use the centre of mass (COM) coordinate systems in which the Schrödinger equation of the relative particle reads

$$\left[-\frac{\hbar^2}{2\mu}\Delta + V(r)\right]\psi(r) = E_{col}\psi(r)$$

where μ is the reduced mass, and the collision energy $E_{col} = 1/2\mu v^2$. In particular, if $V(r)$ approaches zero asymptotically faster than $1/r$, this equation possesses an eigensolution of energy E_{col} with asymptotic behaviour [MT61]

$$\exp(i\mathbf{k}\cdot\mathbf{r}) + f(\Omega)\frac{\exp(ikr)}{r} \quad (2.5)$$

in which $\mathbf{k} = \mu\mathbf{v}/\hbar$ is the wave vector of the relative particle. The term $\exp(i\mathbf{k}\cdot\mathbf{r})$ can be interpreted as a beam of monoenergetic particles with momentum $\hbar\mathbf{k}$ and density 1 that represents the incident beam. The expression $f(\Omega)\frac{\exp(ikr)}{r}$ refers to a radial beam of particles emitted from the scattering centre, representing the scattered particles. According to this interpretation [MT61], the number of particles emitted per unit time into the solid angle $d\Omega$ in the direction Ω is equal to the flux of scattered particles through a spherical surface element with a very large radius that subtends the solid angle $(\Omega, \Omega + d\Omega)$, namely $(\hbar k/\mu)f(\Omega)^2 d\Omega$. The scattering cross section is obtained upon dividing by the incident flux $J = \hbar k/\mu$

$$\sigma(\Omega) = |f(\Omega)|^2. \quad (2.6)$$

$f(\Omega)$ is called the scattering amplitude.

2.3.1 Decomposition into partial waves

In order to calculate the cross section, the asymptotic form of the stationary scattering wave ψ is needed, which can be obtained by solving the Schrödinger equation in spherical coordinates. Since the axis of the rotational symmetry of the problem is the direction of the incident wave vector \mathbf{k} , we take it as the polar axis. Then, the wave function ψ and the scattering amplitude f are independent of ϕ . Expanding in terms of the complete set of Legendre Polynomials reads

$$\psi(r, \theta) = \sum_l \frac{y_l(r)}{r} P_l(\cos \theta) \quad (2.7)$$

$$f(\theta) = \sum_l f_l P_l(\cos \theta) \quad (2.8)$$

where y_l is a regular solution of the radial equation

$$\left[\frac{d^2}{dr^2} + \left(k^2 - \frac{l(l+1)}{r^2} - \frac{2\mu V(r)}{\hbar^2} \right) \right] y_l = 0, \quad (2.9)$$

and its asymptotic form reads [MT61]

$$y_l \underset{r \rightarrow \infty}{\sim} a_l \sin \left(kr - \frac{1}{2} l \pi + \delta_l \right). \quad (2.10)$$

Here, δ_l is the phase shift, and the normalization constant a_l is adjusted so that $\psi(r, \theta)$ has the required asymptotic behaviour. One can also write the asymptotic form of the wave function ψ (see eq. 2.5) in terms of a series of Legendre polynomials:

$$e^{i\mathbf{k} \cdot \mathbf{r}} + f(\theta) \frac{e^{ikr}}{r} = \sum_l \left((2l+1) i^l j_l(kr) + f_l \frac{e^{ikr}}{r} \right) P_l(\cos \theta).$$

Here, $j_l(kr)$ is the regular spherical Bessel function. Taking the asymptotic form of $j_l(kr)$ into account [AS68], one can rewrite this expression by separating the incoming and outgoing waves

$$r\psi(r, \theta) \sim \sum_l \left[(-)^{l+1} \frac{2l+1}{2ik} e^{-ikr} + \left(\frac{2l+1}{2ik} + f_l \right) e^{ikr} \right] P_l(\cos \theta).$$

The term in brackets in the right-hand side must be equal to the asymptotic form of y_l . This condition uniquely identifies a_l and allow for writing f_l as a function of the phase shift.

$$a_l = i^l \frac{2l+1}{k} e^{i\delta_l},$$

$$f_l = \frac{2l+1}{k} e^{i\delta_l} \sin \delta_l.$$

Upon substituting this expression in eq. 2.8, $f(\theta)$ is obtained as a function of the phase shift δ_l

$$f(\theta) = 1/k \sum_{l=0}^{\infty} (2l+1) e^{i\delta_l} \sin \delta_l P_l(\cos \theta) \quad (2.11)$$

In order to obtain an intuitive interpretation of the phase shift, one can compare the asymptotic form of y_l with the corresponding expression of the function $(2l+1)i^l j_l(kr)$. The former is the component of angular momentum l of the stationary state of the scattering, while the latter represents the component of the same angular momentum of the plane wave $\exp(i\mathbf{k}\cdot\mathbf{r})$. We have

$$\frac{y_l}{r} \sim \frac{(2l+1)}{2ikr} \left[(-)^{l+1} e^{-ikr} + e^{2i\delta_l} e^{ikr} \right],$$

$$(2l+1)i^l j_l(kr) \sim \frac{2l+1}{2ikr} \left[(-)^{l+1} e^{-ikr} + e^{ikr} \right].$$

They are both superposition of the same intensity, incoming and outgoing waves. The incoming wave for both functions is exactly the same. The phase factor $\exp(2i\delta_l)$ distinguishes the outgoing wave of the stationary state of scattering from that of the plane wave, meaning that the effect of the scattering potential is shifting the phase of each outgoing partial wave.

The differential cross section is obtained from the square modulus of $f(\theta)$, which is then integrated over the angles (θ, ϕ) to provide the total cross section σ_{tot} . Keeping in mind the orthogonality of the Legendre polynomials, one obtains

$$\sigma_{tot} = \frac{4\pi}{k^2} \sum_{l=0}^{\infty} (2l+1) \sin^2 \delta_l \quad (2.12)$$

in which each term

$$\sigma_l = \frac{4\pi}{k^2} (2l+1) \sin^2 \delta_l \quad (2.13)$$

represents the contribution of the corresponding angular momentum l to the scattering cross section. Evidently, the inequality $\sigma_l \leq \frac{4\pi}{k^2} (2l+1)$ holds.

2.4 Semi-classical interpretation

As in section 2.3 the collision of a classical particle with mass m in a central force field is considered. The following is mainly adopted from [MT61]. The incident particle's energy is set to $E = p_0^2/2m$, where p_0 is the magnitude of the initial momentum. Each trajectory may be identified by its impact parameter b , which is defined as the distance between the centre of force C and the straight line holding the initial momentum \mathbf{p}_0 . The angular momentum L is a constant of motion in such a collision, and is directly proportional to b , i.e. $L = bp$.

If the force field has a finite range r_0 , meaning that $V(r) = 0$ for $r > r_0$, then whether the incident particle is deflected or not is determined by whether $b < r_0$ or $b > r_0$. Only a sufficiently small angular momentum leads to a deflection.

A quantum collision differs from a classical collision in that it is fundamentally a wave phenomenon. However, if beyond a certain distance r_0 , the scattering potential $V(r)$ is negligible (but not necessarily zero) the effect is similar to the scattering of a beam of classical particles by a potential of finite range r_0 . Therefore, in general, if $l/k \geq r_0$, the contribution of the l th partial wave σ_l is negligible. On the other hand, σ_l may assume all values between zero and its maximum $\frac{4\pi}{k^2}(2l+1)$, if $l/k < r_0$.

In classical scattering, those particles whose impact parameter vary from l/k to $(l+1)/k$, and thus whose angular momentum range from $l\hbar$ to $(l+1)\hbar$, make up the portion of the beam that corresponds to the l th partial wave. Keeping the formulation of the classical cross section in mind, the contribution σ_l vanishes if $l/k > r_0$, assumes $\frac{\pi}{k^2}(2l+1)$ if $(l+1)/k < r_0$, and takes on some intermediate value if r_0 lies between l/k and $(l+1)/k$.

The following semi-quantitative argument underpins the preceding rule for quantum-mechanical scattering. The incident wave can be thought of as a superposition of spherical waves of given angular momenta. The radial portion of the term corresponding to the partial wave of angular momentum l is proportional to $j_l(kr)$, resulting in a relative probability density of $r^2 j_l^2(kr)$ in the spherical shell $(r, r+dr)$. As long as $r < \sqrt{l(l+1)}/k$ this density is very low, and it oscillates between 0 and ≈ 1 when $r > \sqrt{l(l+1)}/k$. If $r_0 < l/k$, the wave essentially does not enter the region of strong potential; thus, there is minimal possibility that the presence of the potential will have a significant impact on the wave.

2.4.1 Elastic atom-ion collisions

The quantum mechanical elastic cross section is already presented in equation 2.12 with the phase shift δ_l resulting from the scattering potential for a given partial wave l and wavenumber k . In principle, this formula can be applied to scattering in any field $V(r)$ that vanishes at infinity. The use of this formula requires simply a study of the features of phase shift δ_l [LLM91]. For atom-ion interactions at low temperature ($1\text{mK} \lesssim T \lesssim 1\text{K}$), however, numerous partial waves contribute to the scattering observables. As a result, a semi-classical approach to describing the elastic cross section for hybrid atom-ion systems may be viable.

Within the semi-classical scattering framework, and for a sufficiently large value of l , the phase shift can be shown to be [LLM91]

$$\delta_l \simeq -\frac{\mu}{\hbar^2} \int_{r_c}^{\infty} \frac{V(r)dr}{\sqrt{k^2 - (l+1/2)^2/r^2}} \quad (2.14)$$

where the Langer correction, i.e. $l(l+1) \rightarrow (l+1/2)^2$, is assumed. The lower limit of the integral r_c represents the outer classical turning point (see Fig. 2.2), and its order

of magnitude is $r_c \sim l/k$. If $l \gg 1$, equation 2.14 can be solved using the atom-ion long-range interaction of² $V(r) = -C_4/2r^4$ which yields [CD00]

$$\delta_l \sim \frac{\pi\mu C_4 k^2}{8\hbar^2 l^3}. \quad (2.15)$$

Substituting eq. 2.15 into eq. 2.12 gives an analytical expression of the elastic cross section for neutral-ion collisions with a polarization interaction. However, this stage requires some consideration [R20]. It should be mentioned that the semi-classical opacity agrees quite well with its quantal counterpart for large values of l down to a certain value, $l = L$, where some discrepancies arise. As l decreases below L , the semi-classical and quantal opacities as a function of l reveal rapid oscillatory behaviour. Therefore, for $l < L$, $\sin^2 \delta_l$ may be approximated by its averaged value of $1/2$, which is generally referred to as the random phase approximation. Therefore, the cross section may be given as

$$\sigma_{el}(E_{col}) = \frac{4\pi}{k^2} \sum_l (2l+1) \sin^2(\delta_l(k)) \simeq \frac{2\pi}{k^2} L^2 + \frac{4\pi}{k^2} \int_L^\infty 2l \sin^2(\delta_l(k)) dl, \quad (2.16)$$

and assuming that for $l > L$ the phase shifts are small so that $\sin \delta_l \approx \delta_l$, we have

$$\sigma_{el}(E_{col}) \approx \frac{2\pi}{k^2} L^2 (1 + \delta_L^2(k)). \quad (2.17)$$

The value of L depends on the system under consideration and the collision energy. However, it turns out that a reasonable choice for L is such that $\delta_L(k) = \pi/4$ (or $\sin^2 \delta_l = 1/2$) [CD00]. Then, the semi-classical cross section reads

$$\sigma_{el}(E_{col}) = \pi \left(\frac{\mu C_4^2}{\hbar^2} \right)^{1/3} \left(1 + \frac{\pi^2}{16} \right) E_{col}^{-1/3}. \quad (2.18)$$

This expression shows that the elastic cross section for atom-ion collisions has a weaker energy dependency than the Langevin model ($\propto E_{col}^{-1/2}$, as will be seen in section 2.6). The said semi-classical approach is often sufficient to represent elastic collisions for collision energies in the region of ($1\text{mK} \lesssim E_{col} \lesssim 1\text{K}$), which is commonly accessed in atom-ion experiments. In ref. [Hud09], the Eikonal approximation is used to outline an alternate derivation of the elastic ion-neutral scattering cross section. In many cases, one can also use the Langevin rate to approximate the elastic atom-ion collision rate [Zip+11; CSH14; RW15] (see section 2.6).

2.5 Inelastic collisions

Collisions that induce a change in the internal quantum state of at least one of the colliding partners are termed inelastic collisions. They play a significant role in

²Please note that the interaction potential is presented here following the given reference, which differs from what is defined in section 2.1 in a factor of two.

many circumstances, ranging from buffer-gas cooling of internal degrees of freedom [Rel+13; Han+14; WLF19] to energy transfer in astrochemical environments : see e.g. [Ham+07; GC+14]. Furthermore, the time scales of the available inelastic channels establish a natural time restriction on the systems in which elastic collisions are of interest. Apart from the evident example of sympathetic cooling via elastic collisions, many-body proposals for atom-ion systems, such as the mesoscopic molecular ion [CKL02] or polaron formation [CTD11], exemplify this. Since only the long-range interaction is considered in such proposals, it is very unlikely that the generated many-body state will be the absolute ground state of the combined system. Any transition to a lower-lying state due to an inelastic collision would release energy, posing a threat to the many-body system's sustainability.

Spin flips, or hyperfine transitions in general, are well-known examples of inelastic collisions in ultracold atoms. Spin exchange can occur during a collision if the colliding particles are not in the spin stretched states. The energy difference between the associated states will be released, resulting in a heating or loss mechanism. Spin exchange and spin relaxation can also happen in cold atom-ion collisions and has been experimentally investigated [Rat+13; Für+18; Sik+18a; Sik+18b].

In cold ion-neutral systems, a plethora of inelastic and reactive processes have been anticipated and observed [SHD10; Zip+10b; Här+12; HHD14; Sul+12; Rel+11; Rel+13; Rat+12; Rav+12; Hal+13a; Hal+11; Hal+13b; HW12; Jr+15; Tom+19]. Only two chemical reactions, however, are conceivable in atomic ion-neutral collisions: charge transfer ($A^+ + B \rightarrow A + B^+$) and association ($A^+ + B \rightarrow AB^+$). Charge transfer can either happen due to nonradiative or radiative couplings of potential energy curves (PECs). Association requires a third particle, be it an extra atom ($A^+ + B + M \rightarrow AB^+ + M$) or a photon (e.g. $A^+ + B \rightarrow AB^+ + h\nu$) to ensure energy and momentum conservation. Atom-atom-ion three-body recombination is reported to be the dominant reactive channel in our experiment [Här+12; Krü+16b], which exploits high-density ($\sim 10^{18}m^{-3}$) atomic clouds confined in an optical dipole trap. However, many atom-ion experiments use a magneto-optical trap (MOT) with atomic densities of $\sim 10^{15}m^{-3}$ in which associative collisions are assumed to be radiative [Tom+19].

Resonant charge exchange (RCEX) in homonuclear atom-ion collisions ($A^+ + A \rightarrow A + A^+$) is a prominent example of nonradiative charge transfer. RCEX is expected to happen at a rate several orders of magnitude larger than charge transfer in most heteronuclear systems, as the entrance and scattering channels are the same in the resonant case. It has been measured in an $Yb - Yb^+$ system in the ultracold regime, with a rate constant explained by the Langevin capture probability [Gri+09]. Due to its importance in the current thesis, a more detailed account of the theory of resonant charge exchange (RCEX) will be presented separately in section 2.7.

Nonradiative charge transfer (nRCT) for a more general case of heteronuclear atom-ion collisions is schematically represented in figure 2.3 by the transition $A^+ + B \rightarrow A + B^+$. nRCT is an inelastic process in which the charge hops from one atom

into the other via an avoided crossing between the relevant electronic states. A closer look at the potential energy curves is presented in the following to acquire a better understanding of this process.

The two adiabatic potential energy curves (APECs) labelled V_1^a and V_2^a in figure 2.3 divide the involved energy space into four regions [Yan+20]. If the nonadiabatic electronic couplings between the two APECs are insignificant, regions *I* and *III* will be the bound and continuum regions of potential V_1^a , respectively. And region *IV* will contain both the continuum states of potential V_1^a and the bound states of potential V_2^a independent of one another. Quasi-bound states can be formed in region *II* due to the potential barrier. These temporary quasi-bound states would decay into continuums by tunnelling and are known as shape resonances.

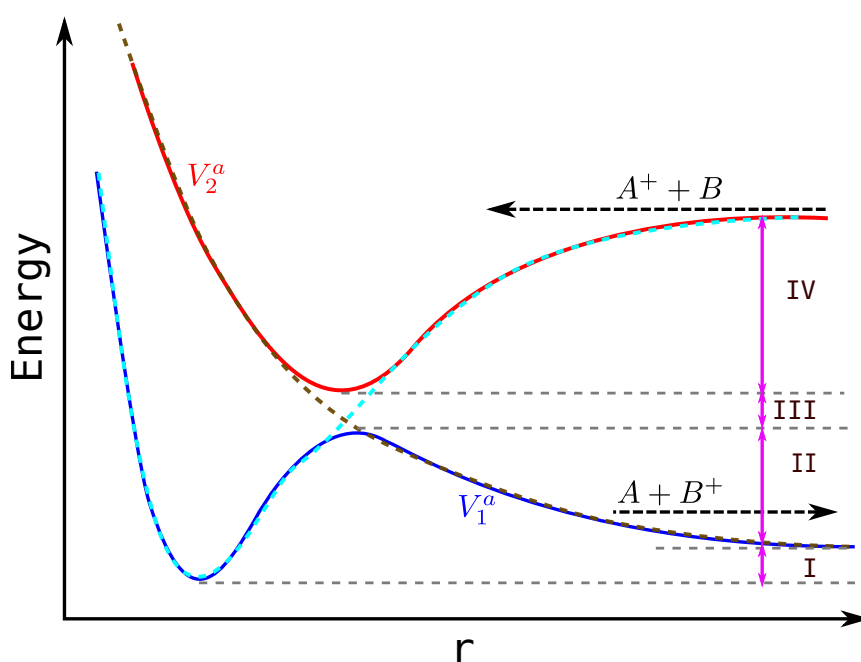


FIGURE 2.3: Schematic representation of nRCT (see the text). Two adiabatic potential energy curves are shown with solid lines, with nonadiabatic couplings represented by dashed lines. The system enters the upper (red) adiabatic curve as $A^+ + B$. Due to the nonadiabatic couplings between the entrance curve and the lower lying adiabatic curve which corresponds to the charge transfer asymptote $A + B^+$, the charge can hop from one atom into another at the avoided crossing between the curves. Four different regions are depicted the explanation of which can be found in the text.

In the case of a system with sizable nonadiabatic electronic couplings, region *I* remains the bound state region, primarily related to potential V_1^a , and the quasi-bound states in region *II* are modified by the electronic couplings. However, in region *IV*, the bound states of potential V_2^a can no longer be sustained due to electronic couplings, and they leak or decay into continuum states of potential V_1^a . These states are known as Feshbach resonances, or Fano resonances, and are interpreted as the result of interactions between bound and continuum channels.

In figure 2.3 the system enters as $A^+ + B$ on a curve that corresponds to the experiment's collision channel. This entry curve interacts with a charge transfer state with the asymptote $A + B^+$, which is assumed to have the same spin multiplicity and symmetry and hence undergoes an avoided crossing. The system may pass through this avoided crossing in an adiabatic (staying on the same adiabatic curve) or nonadiabatic, i.e., jumping over the avoided crossing and onto the other adiabatic curve, manner. In the latter case, a charge transfer has taken place. The probability of a nonadiabatic transition P_{na} can be approximated within the Landau-Zener model to give [Wit05]

$$P_{na} = \exp(-2\omega_{ad}\tau_d).$$

The parameter ω_{ad} is a characteristic frequency. For example, at the crossing point, it is the Rabi frequency with which the system oscillates between diabatic potentials (shown by dotted curves in Fig. 2.3). The parameter τ_d is a measure of the duration of the interaction.

2.5.1 Radiative processes

Radiative chemical reactions can have significant importance in cold and dilute environments like the interstellar medium or cold atom-ion experiments [Kim+93; ZD90; SLD98; DDY90; BH06]. In addition to photoexcitation and photoionization which are driven by the radiation field, collisional radiative processes such as radiative charge transfer (RCT) and radiative association (RA) may become relevant in atom-ion chemistry at ultracold temperatures.

When ions and neutrals collide, the collision complex may emit a photon to populate levels associated with lower-lying molecular potential surfaces. When the ion's electron affinity (related to the ionization energy of its neutral precursor) is greater than the ionization energy of the neutral collision partner, RCT and RA can occur, (see Fig. 2.4). In such cases, lower-lying electronic states of the collision system must always connect to charge-transfer asymptotes, i.e., asymptotes where the charge has been exchanged between the collision partners. In figure 2.4, if the emission populates a continuum, the scattering results in the dissociation of the collision complex along the charge transfer asymptote, a process referred to as radiative charge transfer (RCT). Radiative association (RA) is a related process in which the spontaneous emission of the initial scattering state leads to the formation of a molecular ion, i.e. $A^+ + B \rightarrow AB^+ + h\nu$, through decaying to one of the lower-lying bound levels.

Mathematical descriptions of the quantum mechanical cross sections for RCT and RA can be found in [ZD90; Hal+13a; Jr+15]. Here, suffice it to say that apart from transition selection rules, the efficiency of these radiative processes is determined by two main factors: the cube of the emitted photon's frequency and the specific Frank-Condon factors (FCFs). The latter refers to the degree of overlap between the wave functions corresponding to the states in the upper and lower curves, assuming

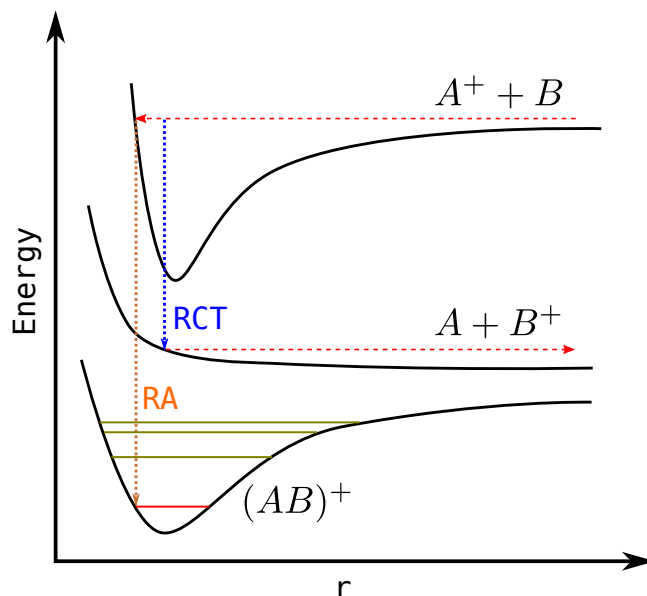


FIGURE 2.4: Schematic representation of radiative processes in atom-ion collisions. In radiative charge transfer (RCT), the collision complex populates a continuum in a lower-lying electronic state by emitting a photon. Radiative association (RA) is a process in which the spontaneous emission of the initial scattering state leads to the formation of a molecular ion in one of the rovibrational levels.

a vertical transition (i.e. instantaneous on the timescale of nuclear motion). The FCFs, and hence the relative efficiency of RCT and RA, highly depend on the specific shape of the potential energy curves and vary significantly from case to case.

2.6 Capture models

Although reactive collisions can theoretically be addressed using quantum scattering theory, the computation of involved integrals are often cumbersome, even for small systems. However, a number of simplified approximate treatments for ion-neutral collisions have been established that do not require complex numerical calculations and may be applied to large systems. Barrierless ion-neutral reactions are frequently modelled within the realm of capture theories. In capture models, the reaction rate is determined by the long-range tail of the interaction potential that leads to the capture of collision partners, while the short-range reaction probability is assumed to be unity [DO18]. This indicates, classically, that all trajectories that pass through the centrifugal potential barrier are inward-spiralling and lead to a reaction [GS58] (see Fig. 2.5).

Substituting the long-range interaction potential from equation 2.1 into equation 2.3, the effective potential of the collision for partial wave l will be

$$V_{eff}^l(r) = \frac{l^2}{2\mu r^2} - \frac{C_n}{r^n} \quad (2.19)$$

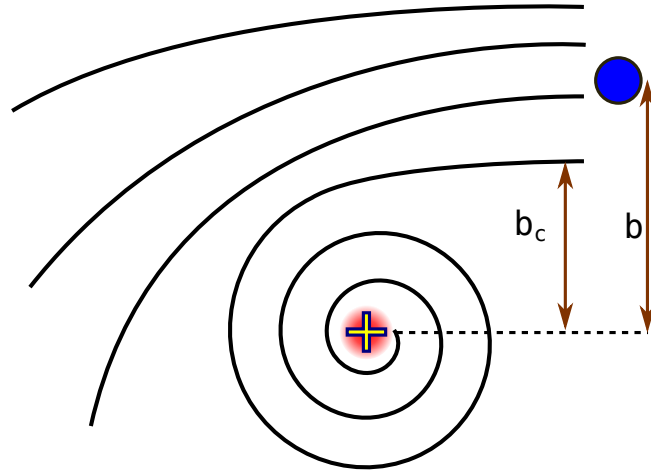


FIGURE 2.5: Schematic classical trajectories in atom-ion collisions. If the impact parameter is larger than a critical value b_c , collisions only lead to glancing collisions with a weak deflection of the colliding partners. The particles enter an inward-spiralling trajectory with impact parameters below b_c , resulting in a short-range collision.

The classical cross section using the capture model can be derived for $n > 2$ as follows [DO18]. First, we find the position of the maximum of the effective potential r_0 (see Fig. 2.2) by differentiating equation 2.19

$$r_0 = \left(\frac{n\mu}{l^2} C_n \right)^{\frac{1}{n-2}}. \quad (2.20)$$

The maximum of the effective potential occurs at the position r_0 and reads as

$$V_{eff}^l(r_0) = \left(\frac{l^2}{\mu} \right)^{\frac{n}{n-2}} \frac{n-2}{2n} (nC_n)^{-\frac{2}{n-2}}. \quad (2.21)$$

Only when the colliding particles can reach beyond r_0 can they cross the effective potential barrier and enter the region of chemical forces. Hence, the requirement for a reaction is that the particles can reach $r = r_0$ with at least some kinetic energy left to enter the "reaction zone". Concretely, if the collision energy E_{col} exceeds the maximum effective potential energy $V_{eff}(r_0)$ (see Fig. 2.2), the trajectory is inward-spiralling and can lead to a reaction. As a result, l has a maximum value that allows for the capture of the colliding particles:

$$l_{max} = (\mu n)^{1/2} C_n^{\frac{1}{n}} \left(\frac{2E_{col}}{n-2} \right)^{\frac{n-2}{2n}}, \quad (2.22)$$

which corresponds to a critical impact parameter

$$b_c = \frac{l_{max}}{\mu v}. \quad (2.23)$$

As is illustrated in figure 2.5, every collision with an impact parameter smaller than b_c will lead to an inward-spiralling trajectory and the capture of collision partners in

the short-range potential. Therefore, the classical capture cross section reads

$$\sigma(E_{col}) = \pi b_c^2 = \frac{\pi}{2} n \left(\frac{2}{n-2} \right)^{\frac{n-2}{n}} \left(\frac{C_n}{E_{col}} \right)^{\frac{2}{n}}. \quad (2.24)$$

For the case of an ion being captured by a structureless neutral particle, such as closed-shell atoms, and to a decent approximation, non-polar molecules, one has $n=4$. Therefore, the cross section reads

$$\sigma_{LNg}(E_{col}) = 2\pi \sqrt{C_4/E_{col}}, \quad (2.25)$$

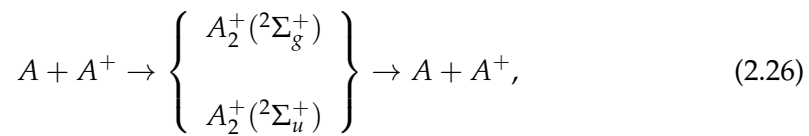
which is referred to as the Langevin cross section, after the pioneering work on ion-neutral collisions conducted by P. Langevin [Lan05]. The corresponding expression for the rate constant $v\sigma_{LNg}$ is a special case in which classical capture theory predicts a rate constant independent of the collision energy.

2.7 Resonant charge exchange

We now turn our attention to the charge transfer process in the special case of homonuclear atom ion collisions, the so-called resonant charge exchange (RCEX) process. What is presented in this section, is to a large extent taken from [C16].

In homonuclear systems $A + A^+$, the charge can be on either centre, resulting in an even or odd electronic wave function under the inversion symmetry (through the midpoint between the two nuclei), ie, a gerade (g) or ungerade (u) state. The multiplicity is determined by the system under consideration. Alkali metals and alkaline earth metals are most commonly used in ultracold atom-ion experiments due to the existence of simple cycling transitions for laser cooling. Therefore, I focus my attention on them in the following. The atom-ion complex will have a single active electron if A is an alkali metal element (Li, Na, K, Rb, Cs, or Fr). For alkaline earth metals (Be, Mg, Ca, Sr, Ba, or Ra), the complex has an active hole. In both cases, the total electronic spin is $S = 1/2$, resulting in doublet molecular potential curves $^2\Sigma_g^+$ and $^2\Sigma_u^+$.

When an ion A^+ collides with its neutral parent atom A , the particles approach each other along two possible potential curves corresponding to the electronic molecular states $^2\Sigma_g^+$ and $^2\Sigma_u^+$ (see e.g. Fig. 2.6 for Rubidium as an example). Elastic scattering, in which the charge remains on the same centre, is one of the two conceivable outcomes:



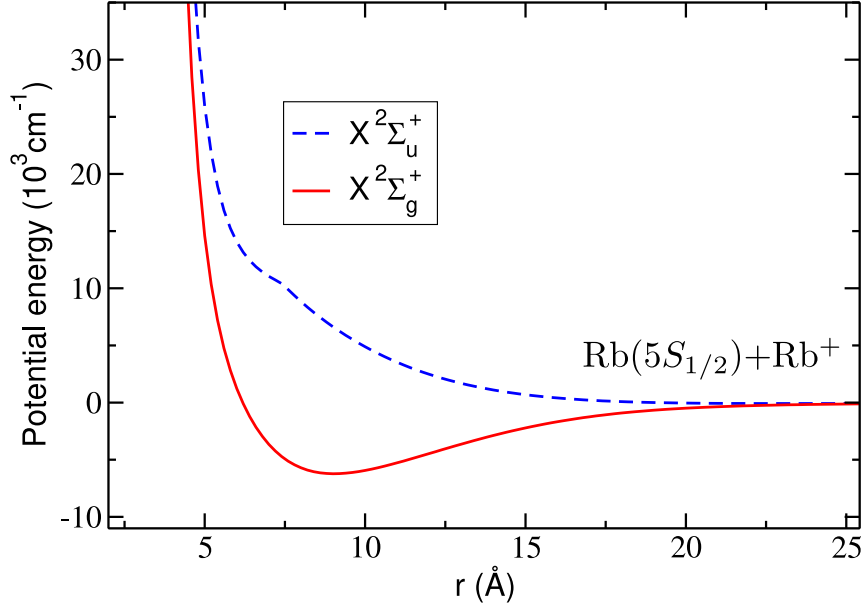
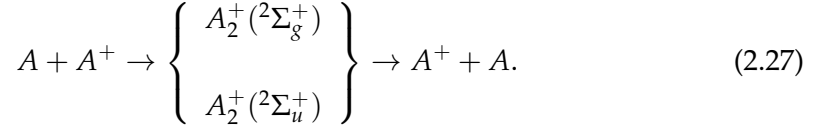


FIGURE 2.6: The two lowest potential energy curves for Rb_2^+ molecular ion. Data taken from [Jyo+16].

and a charge exchange where the charge transfers onto the other centre is the other possibility:



In the resonant scattering of an ion and its neutral parent atom of the same isotope the two nuclei are identical, but from now on I label them with A and B to keep them distinguishable. Preceding the collision when the internuclear distance r is large, the charge can be attached either to the nucleus A or B with the corresponding electronic wave functions $\Phi_{A/B}$, respectively. The total wave function of the system with proper inversion symmetry can be constructed with a linear combination of $\Phi_{A/B}$,

$$\Phi_{g/u} = \frac{1}{\sqrt{2}}(\Phi_A \pm \Phi_B), \quad (2.28)$$

where $\Phi_{g/u}$ are the even and odd electronic wave functions corresponding to g and u potentials. The asymptotic form of the scattering wave functions on either g or u potential curves (see equation 2.5) can be used to calculate the elastic and charge exchange cross sections,

$$\Psi_{g/u}(k, r) = \left(e^{i\mathbf{k}\cdot\mathbf{r}} + f_k^{g/u}(\theta) \frac{e^{ikr}}{r} \right) \Phi_{g/u}. \quad (2.29)$$

Here, $e^{i\mathbf{k}\cdot\mathbf{r}}$ is the unscattered plane wave, and $\frac{e^{ikr}}{r}$ is the outgoing scattered spherical wave with the scattering amplitude $f_k^{g/u}$.

If the charge is initially on a given nucleus, say A , the asymptotic wave function of the system after the scattering is

$$\Psi = \frac{1}{\sqrt{2}}(\Psi_g + \Psi_u) \sim \frac{1}{2} \left(e^{i\mathbf{k}\cdot\mathbf{r}} + (f^g + f^u) \frac{e^{ikr}}{r} \right) \Phi_A + \frac{1}{2}(f^g - f^u) \frac{e^{ikr}}{r} \Phi_B. \quad (2.30)$$

From this expression, the scattering amplitude for the elastic process where the charge remains on the nucleus A can be identified to be $f_{el} = \frac{1}{2}(f^g + f^u)$. The charge-exchange scattering amplitude $f_{RCEx} = \frac{1}{2}(f^g - f^u)$ is determined from what reads in front of Φ_B , i.e. when the charge is centred on the nucleus B after the collision. Accordingly, the differential cross sections I_{el} and I_{RCEx} for the elastic and charge exchange processes, respectively, will be:

$$\begin{cases} I_{el}(\theta) = \frac{1}{4} |f^g(\theta) + f^u(\theta)|^2 \\ I_{RCEx}(\theta) = \frac{1}{4} |f^g(\theta) - f^u(\theta)|^2 \end{cases}. \quad (2.31)$$

From equation 2.31, one can calculate the total differential cross section $I_{tot}(\theta) = I_{el}(\theta) + I_{RCEx}(\theta)$. Integrating over the solid angle Ω yields the cross sections for a given scattering energy, i.e. $\sigma = \int d\Omega I(\theta)$. As was outlined in section 2.3, the cross sections for total scattering may be obtained by following the standard procedure of expanding in partial waves l , and expressing f^u and f^g in terms of the phase shifts δ_l^g and δ_l^u [ZDC09]

$$\sigma_{tot} = \frac{2\pi}{k^2} \sum_{l=0}^{\infty} (2l+1) (\sin^2 \delta_l^u + \sin^2 \delta_l^g) = \frac{1}{2} (\sigma_{el}^g + \sigma_{el}^u), \quad (2.32)$$

where $\sigma_{el}^{g,u} \equiv \frac{4\pi}{k^2} \sum_{l=0}^{\infty} (2l+1) \sin^2 \delta_l^{g,u}$. Similarly, the charge exchange cross section will be

$$\sigma_{RCEx} = \frac{\pi}{k^2} \sum_{l=0}^{\infty} (2l+1) \sin^2(\delta_l^u - \delta_l^g). \quad (2.33)$$

Here, $k = \sqrt{2\mu E_{col}}/\hbar$ is the wave number and μ is the reduced mass. These two expressions can be used to calculate the elastic cross section: $\sigma_{el} = \sigma_{tot} - \sigma_{RCEx}$. The phase shifts $\delta_l^{g,u}(k)$ are determined by matching the regular solutions of the partial wave equation $y_{l,k}^{g,u}(r)$ (see eq. 2.9), with the asymptotic form, see equation 2.10.

Approximated values for the phase shifts, and cross sections accordingly, could be obtained in different scattering regimes depending on the collision energy E_{col} . The categorization of three distinct energy regimes is in order.

Only s-waves ($l=0$) contribute at ultracold temperatures, and phase shifts can be characterized by the effective range expansion [OSR61] which at low collision energies in first approximation are independent of k and result in simple forms of

cross sections [ZDC09]

$$\begin{aligned}
 \sigma_{tot} &= 4\pi(a_g^2 + a_u^2), \text{ with } \sigma_{tot}^{g,u} = 4\pi a_{g,u}^2, \\
 \sigma_{RCEx} &= \pi(a_g - a_u)^2, \\
 \sigma_{el} &= \sigma_{tot} - \sigma_{RCEx} = \pi(3a_g^2 + 2a_g a_u + 3a_u^2).
 \end{aligned} \tag{2.34}$$

Here, $a_{g,u}$ are the scattering lengths for the g and u states, respectively.

Due to the contribution of higher partial waves and the emergence of shape resonances, additional structure emerges as the energy increases. For a large enough l , the phase shifts are determined by the long-range interactions, as the centrifugal barrier ensures that the inner region of the potential contributes minimally to the scattering (see Fig. 2.2). Therefore, the semiclassical approximation (see eq. 2.14) can be employed. This is the energy regime that was already discussed in section 2.4.1, resulting in a simple expression for the semiclassical phase shift δ_l^{sc} (eq. 2.15) and the elastic cross section given in equation 2.18. Here, I just note that since the long-range tail of the potential is the same for both g and u potential curves, one obtains $\sigma_{el}^g = \sigma_{el}^u$, and according to equation 2.32, $\sigma_{tot} = \frac{1}{2}(\sigma_{el}^g + \sigma_{el}^u) = \sigma_{el}^{g,u}(E_{col})$.

For charge exchange, the scattering from the attractive r^{-4} potential of one of the two potential curves dominates the cross section at energies above the ultracold regime. The process is characterized by small values of angular momentum, and σ_{RCEx} may be approximated by the conventional Langevin formula $\sigma_{LNg} = \pi b_c^2$, where b_c is the maximum impact parameter still permitting the wave function to penetrate beyond the centrifugal barrier (see section 2.6). The initial state of the system is distributed evenly between the g and u states, i.e., half on each curve, resulting in $\sigma_{RCEx} = 1/2(\sigma_{LNg}^g + \sigma_{LNg}^u)$. However, as can be seen in Fig. 2.6 for Rubidium (as a representative case), one of the curves is significantly deeper than the other [C16]. Therefore, the shallow curve's centrifugal barrier grows much more rapidly as l increases, preventing the wave function from penetrating to a short separation and resulting in negligible charge exchange. Hence, charge exchange scattering is mainly determined by only one of the curves, and one can write

$$\sigma_{RCEx}(E_{col}) = \frac{1}{2}\sigma_{LNg} = \pi \sqrt{\frac{C_4}{E_{col}}}, \tag{2.35}$$

where $C_4 = \frac{e^2}{2(4\pi\epsilon_0)^2}\alpha$ (see eq. 2.2). The same conclusion can be reached using the definition of σ_{RCEx} with the following argument. Starting with equation 2.33, one can divide the sum into three different contributions as follows. $\sigma_{RCEx} = \frac{\pi}{k^2}(S_1 + S_2 + S_\infty)$, where $S_i = \sum_{l=l_i^{mit}}^{l_i^{final}} (2l+1) \sin^2(\delta_l^u - \delta_l^g)$. The first sum ranges from $l = 0$ to $l = l^*$, the second between $l^* + 1$ and l_{max} , and the third from $l_{max} + 1$ to ∞ . Here, l^* and l_{max} are the maximum l allowing penetration through the shallow and deep potential well, respectively. For $l > l_{max}$, the semiclassical formula 2.14 can be used to approximate the phase shifts of both curves, which quickly become equal to each

other by approaching δ_l^{sc} given by equation 2.15, resulting in a negligible contribution $S_\infty \approx 0$. In S_1 , both phase shifts vary significantly and independently with l , resulting in an average value of $\sin^2(\delta_l^u - \delta_l^g) \sim 1/2$, whereas in S_2 , only the phase shift corresponding to the shallow potential follows the semiclassical expression (eq. 2.15), yielding again $\sin^2(\delta_l^u - \delta_l^g) \sim 1/2$. Hence, one can approximate $(2l + 1) \sin^2(\delta_l^u - \delta_l^g) \approx l$ for both sums leading to $S_1 + S_2 = \sum_{l=0}^{l_{max}} (2l + 1) \sin^2(\delta_l^u - \delta_l^g) \approx \frac{1}{2} l_{max}^2$, and therefore recovering equation 2.35, $\sigma_{RCEx} \approx \pi l_{max}^2 / 2k^2 = \sigma_{LNg} / 2$.

At higher collision energies in the range of eV, the contribution of the long-range attractive force tends to cancel out and the cross section is governed by the exponential decay of the difference between the g and u potentials, which changes as [DB58]

$$\sigma_{RCEx}(E_{col}) = (a \ln E_{col} - b)^2. \quad (2.36)$$

In the above formula a and b are constants which depend on the species under consideration. For instance, if the collision energy is given in eV and σ_{RCEx} in atomic units, $a = 1.33$ and $b = 22.943$ for $\text{Na} + \text{Na}^+$ [CD00], and in case of $\text{Yb} + \text{Yb}^+$, $a = 1.88$ and $b = 32.44$ [ZDC09].

To summarize, three energy regimes regarding the resonant charge exchange were discussed: an s-wave regime at ultralow energies described by scattering lengths, a Langevin regime at medium energies which follows $E_{col}^{-1/2}$, and an "exchange" regime scaling as $(a \ln E_{col} - b)^2$.

Chapter 3

Direct observation of swap cooling in atom-ion collisions

The content of this chapter has been published in *New Journal of Physics*. The material is taken from:

Amir Mahdian, Artjom Krüchow, and Johannes Hecker Denschlag. "Direct observation of swap cooling in atom-ion collisions". In: *New Journal of Physics* 23.6 (June 2021). Publisher: IOP Publishing, p. 065008. ISSN: 1367-2630. DOI: [10.1088/1367-2630/ac0575](https://doi.org/10.1088/1367-2630/ac0575). URL: <https://doi.org/10.1088/1367-2630/ac0575> (visited on 08/19/2021)

The article is published under the license CC BY 4.0. See also license text: <https://creativecommons.org/licenses/by/4.0/>

Remarks: The authors acknowledge the publication in *New Journal of Physics*. The content can also be found on <https://arxiv.org/abs/2012.07759v3>. Please note that the format of the (journal) article was modified in order to fit the style and layout of the thesis. Hence, a consecutive numbering of figures and references for the whole thesis was applied as well.

3.1 Abstract

Collisions with cold particles can dissipate a hot particle's energy and therefore can be exploited as a cooling mechanism. Kinetics teaches us that cooling a particle down by several orders of magnitude typically takes many elastic collisions as each one only carries away a fraction of the collision energy. Recently, for a system comprising hot ions and cold atoms, a very fast cooling process has been suggested [Rav+12] where cooling over several orders of magnitude can occur in a single step. Namely, in a homo-nuclear atom-ion collision, an electron can resonantly hop from an ultracold atom onto the hot ion, converting the cold atom into a cold ion. Here, we demonstrate such swap cooling in a direct way as we experimentally observe how a single energetic ion loses energy in a cold atom cloud. In order to contrast swap cooling with sympathetic cooling, we perform the same measurements with a hetero-nuclear atom-ion system, for which swap cooling cannot take place, and indeed observe much different cooling dynamics. Ab initio numerical model calculations agree well with our measured data and corroborate our interpretations.

3.2 Introduction

Preparing cold ions is often a precondition for modern experiments in various scientific fields, ranging from ultracold chemistry [Wil+08] to quantum information processing [CZ95]. While laser cooling opened up research in the ultracold regime [Ket02], it is generally limited to the species with closed cycling transitions. Another method commonly used for cooling particles to subkelvin temperatures is collision-induced cooling, such as sympathetic cooling or buffer gas cooling [Wil+08; Mya+97; Tru+01; Wei+98; Siv+12; Dor+09]. Besides the translational degrees of freedom, collisions can also cool internal degrees of freedom of molecules [Han+14; Rel+13]. Sympathetic cooling of a highly energetic particle to orders of magnitude lower kinetic energies typically requires many collisions. Because on average, each collision can only take away a small fraction of the energy. Swap cooling, by contrast, can bring about a cold ion in a single collision [Rav+12]. In order to lay out the swap cooling process, we consider a homo-nuclear atom-ion system. As the hot ion passes by a cold neutral atom at close proximity, the electron can resonantly hop from the atom onto the ion, while the energy and momentum exchange between the particles is negligible, (see Fig. 1). Thus, the former neutral atom has been turned into a cold ion. First indirect experimental evidence for swap cooling was recently observed in terms of an increased lifetime of Cs^+ ions in an ion trap when sympathetically cooled with an ultracold cloud of Cs atoms instead of Rb atoms [Rav+12; DR18].

Here, we present direct experimental evidence for swap cooling for a single $^{87}\text{Rb}^+$ ion as it crosses an ultracold cloud of neutral rubidium atoms. Our scheme allows for a deterministic measurement of the cooling probability of the ion after a chosen interaction time. We can perform our experiments in a regime where

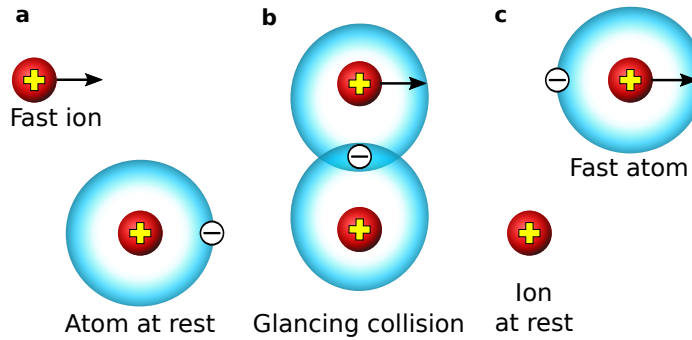


FIGURE 3.1: **Scheme for swap cooling process** **a**, A fast ion approaches a neutral parent atom at rest in a glancing collision. **b**, When the electron orbitals around the two nuclei overlap, a resonant charge exchange can take place. **c**, The new ion is now at rest to the extent that the transferred momentum during the collision is negligible.

sympathetic cooling via elastic collisions is negligible, and the obtained results are therefore attributed to swap cooling. Moreover, we investigate how swap cooling depends on the initial kinetic energy of the ion and find agreement with theoretical predictions. Furthermore, in order to highlight the difference between swap cooling and sympathetic cooling, we repeat the cooling experiments with a Ba^+ ion colliding with ultracold Rb atoms, a system for which swap cooling mechanism does not exist. As expected, we find that cooling a highly energetic Ba^+ ion, which can only take place via sympathetic cooling, is much slower than for Rb^+ . We carry out simulations for sympathetic and swap cooling and find good agreement with all our experimental data.

3.3 Resonant charge exchange collisions

In general, one can classify atom-ion collisions into two types: Langevin collisions and glancing collisions. A Langevin collision occurs when the impact parameter b is smaller than a critical value b_c which is a function of the collision energy E_{col} . In a classical picture, atom and ion fall onto each other in a spiralling motion and finally scatter from the inner-core repulsive potential with an isotropic angle distribution in the centre of mass frame. A glancing collision has $b > b_c$, the atom-ion distance remains on the order of b and generally only leads to small deflections. Resonant charge exchange (RCEX) can occur in both Langevin and glancing collisions. Figure 3.2a shows the probability for resonant charge exchange for a $\text{Rb}^+ - \text{Rb}$ collision with a collision energy of $1000 \text{ K} \times k_B$ in a semi-classical picture. The vertical red dashed line marks the critical impact parameter (b_c) for that particular collision energy E_{col} , defined in the centre of mass frame. For Langevin collisions, $b < b_c$, the electron has an equal chance to end up in each of the two identical (ionic) cores after the collision, which means that there is a 50 percent probability for charge transfer. For glancing collisions the asymptotic theory by Smirnov [Smi01] is used to calculate the RCEX probability (see Methods). For the given example of Rb, resonant charge

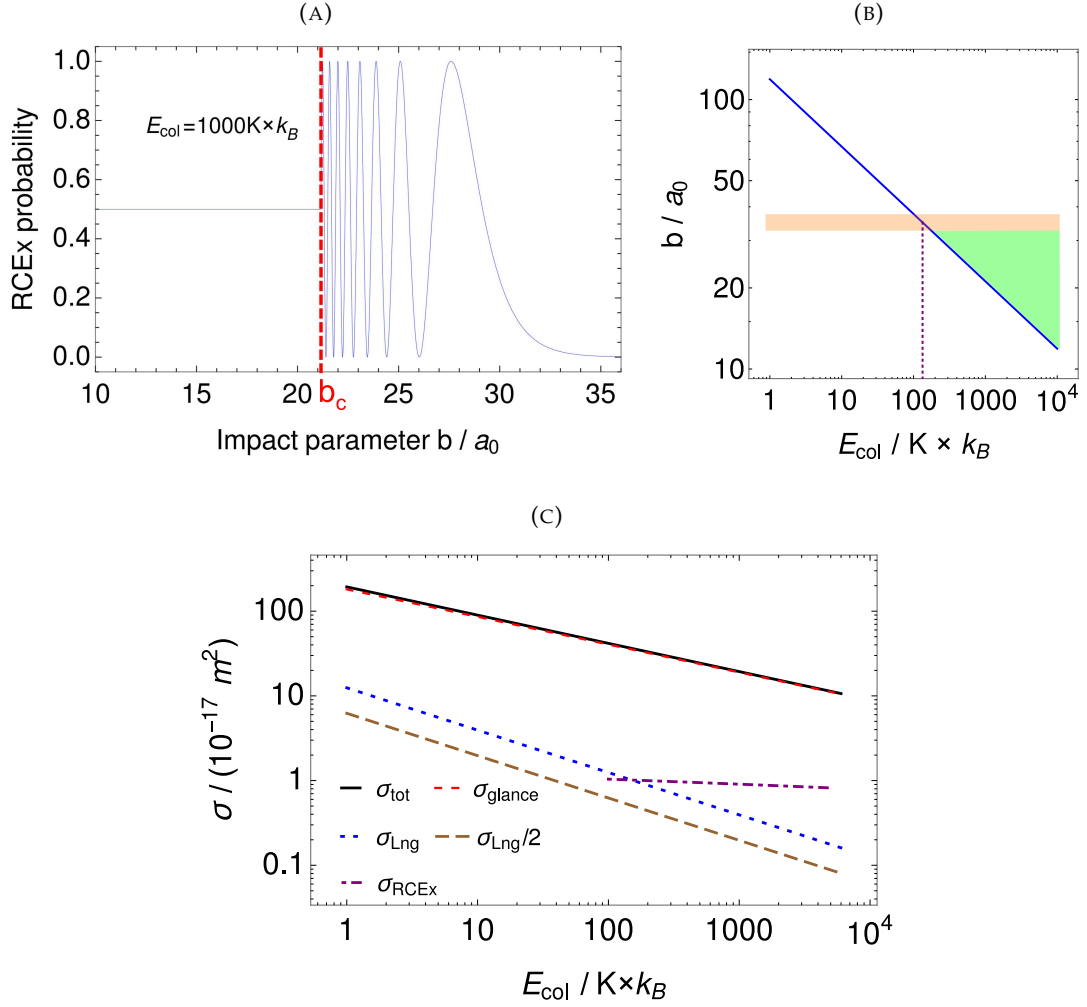


FIGURE 3.2: **Resonant charge exchange, glancing collisions and Langevin collisions.** **a**, The probability for RCEX in a Rb-Rb⁺ collision as a function of the impact parameter in a semi-classical picture. The vertical red dashed line marks the critical impact parameter (b_c) for the given collision energy $E_{col} = 1000 K \times k_B$. Swap cooling occurs when RCEX takes place for $b > b_c$. The oscillations are a result of the coherent, quantum-mechanical electron hopping between the two ionic cores while atom and ion pass each other, see also text. **b**, The solid blue line gives the critical impact parameter b_c as a function of E_{col} . The horizontal orange line marks the maximum impact parameter for which swap cooling is possible. Thus, for collision energies below $\approx 100 K \times k_B$, RCEX can only occur via a Langevin collision (corresponding to $b < b_c$). For $E_{col} > \approx 100 K \times k_B$ glancing collisions also contribute to the RCEX. The green area is where swap cooling can take place. **c**, Cross sections for resonant charge exchange σ_{RCEX} , for Langevin collisions σ_{LNg} , for glancing collisions σ_{glance} , as well as for the total cross section $\sigma_{tot} = \sigma_{LNg} + \sigma_{glance}$, as a function of collision energy E_{col} . The Langevin cross section is directly linked to the impact parameter b_c by $\sigma_{LNg} = \pi b_c^2$ (see also Methods). The RCEX cross section is plotted only within the range of validity of asymptotic theory (see text). For collision energies below about $100 K \times k_B$, σ_{RCEX} is essentially given by $\sigma_{LNg}/2$.

transfer can occur for impact parameters of up to about $35 a_0$ where a_0 is the Bohr radius, leading to swap cooling. The oscillations in Figure 3.2a can be understood as a result of the coherent, quantum-mechanical electron hopping between the two ionic cores while atom and ion fly by each other. This process is analogous to coherent Rabi-flopping in a two-level quantum system, where the coupling is switched on and off in a non-adiabatic fashion.

Figure 3.2b shows the critical impact parameter b_c as a function of the collision energy (blue line). The orange horizontal line shows the maximum impact parameter for which swap cooling is possible. In Figure 3.2a this maximum impact parameter is clearly located at around $b = 30a_0$. Collisions with b below this line but above b_c (blue line) can lead to swap cooling, see green area in Figure 3.2b. The parameter range that contributes to swap cooling clearly increases with E_{col} .

Figure 3.2c shows calculated cross sections for resonant charge exchange σ_{RCEx} , for Langevin collisions σ_{LNg} , for the total cross section σ_{tot} , as well as for glancing collisions $\sigma_{glance} = \sigma_{tot} - \sigma_{LNg}$. Mathematical expressions for these cross sections can be found in the Methods. The cross section for RCEx is calculated by means of Smirnov's asymptotic theory which becomes less accurate at lower collision energies [Smi01] and is, therefore, only shown for energies down to $100 \text{ K} \times k_B$. In fact, for lower collision energies, the critical impact parameter is $> 35a_0$, so that the charge transfer takes place only by Langevin collisions. Since in a Langevin collision the probability for RCEx is $1/2$, the charge exchange cross section goes over to $\sigma_{RCEx} = \sigma_{LNg}/2$ for energies $E_{col} \approx 100 \text{ K} \times k_B$ or below. We further note that since the scattering angle in a Langevin collision is distributed randomly, it is futile to distinguish between an elastic and a charge exchange process in Langevin collisions. Figure 3.2c shows that the cross section for glancing collisions σ_{glance} is much larger than the cross sections for Langevin collisions or for RCEx. Nevertheless, the only significant contribution of glancing collisions in collisional cooling is in the form of swap cooling as glancing collisions generally involve very small momentum and energy transfer. Summarizing the results of Fig. 3.2c, for collision energies in the range from several $\text{mK} \times k_B$ to about $100 \text{ K} \times k_B$ the cooling process is dominated by Langevin collisions. For larger energies, swap cooling increasingly dominates the cooling process.

3.4 Experiments and results

In order to investigate the cooling process, the following experimental procedure was implemented. In brief, we first accelerated a single ion in a Paul trap towards a cold atom cloud, imparting a well-defined kinetic energy to the ion. A sketch of the setup is shown in Fig. 3.3a). This was done by quickly changing the endcap voltages of the Paul trap. In a second step, after the ion had interacted with the atom cloud, we determined whether the ion's energy had cooled down below $50 \text{ K} \times k_B$. For this, we lowered the voltage of an endcap electrode of the Paul trap to an appropriate value,

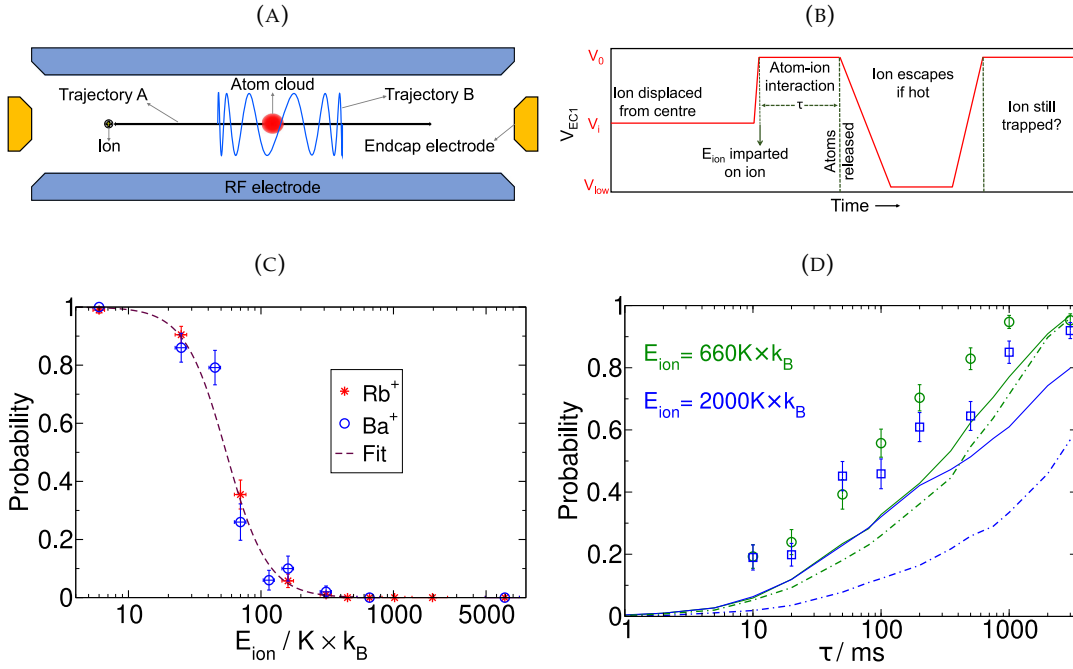


FIGURE 3.3: The ion's energy: detection scheme and evolution. **a**, Sketch of the experimental set-up showing Paul trap electrodes, the ion and the atom cloud. Two possible trajectories of the ion in the ion trap are displayed. The black, straight-line trajectory represents the initial ion motion along the longitudinal axis (z -axis) of the ion trap, after the ion's launch. It runs right through the cloud centre. The blue oscillating curve is an ion trajectory after a Langevin collision with a cold atom that imparted on the ion a sizable momentum in the transverse direction of the ion trap. As a consequence, the overlap of the new trajectory with the atom cloud is (on average) strongly reduced. This can significantly slow down further cooling of the ion. **b**, Time sequence of experiment. The red solid line is the voltage V_{EC1} on one of the two endcap electrodes. $V_{EC1} = V_i$ corresponds to the initial displacement of the ion. For $V_{EC1} = V_0$, the ion trap is centred on the atom cloud. After an interaction time τ , the atom cloud is released and V_{EC1} is lowered to V_{low} , so that a hot ion escapes. Afterwards, the voltage V_{EC1} is ramped up, and we probe whether the ion is still trapped. **c**, Probability for a Ba^+ or a Rb^+ ion with energy E_{ion} to remain trapped after the ion trap depth in axial direction has been slowly lowered to a fixed value (see text for details). The dashed line is a fit to the experimental results (see text). **d**, Probability for a Rb^+ ion to be cooled to an energy below $\approx 50 K \times k_B$ as a function of the interaction time τ . Plot symbols (circle, squares) are experimental data for initial ion energies ($660 K \times k_B$, $2000 K \times k_B$), respectively. Each data point is extracted from 120 experimental runs. Solid lines are full MC simulations. Dash-dotted lines are MC simulations without charge transfer.

and detected whether the ion was still trapped (The time sequence is shown in Fig. 3.3b).

In the following, we describe these two steps in more detail. For initially preparing the ion, we either loaded a single $^{138}\text{Ba}^+$ ion or a single $^{87}\text{Rb}^+$ ion into a linear Paul trap (see Methods) and displaced it from the trap centre by a variable, but well-defined, distance in the axial direction. We then loaded an ultracold cloud of ^{87}Rb atoms into a crossed optical dipole trap which was positioned at the centre of the Paul trap. The cloud size was smaller than the displacement of the ion, such that initially the ion could not interact with the atoms. After the initial displacement of the ion, it was accelerated towards the atoms by suddenly moving the centre of the trapping potential back to the middle of the atom cloud (see Fig. 3.2b and Methods). As a consequence, the ion was oscillating within the Paul trap along the axial direction, periodically crossing the cold atom cloud. The kinetic energy of the ion (E_{ion}) at the location of the atoms was initially precisely defined by the ion's initial displacement and by how fast the trap centre was moved back. E_{ion} could be tuned over several orders of magnitude, up to about $7000 \text{ K} \times k_B$. After a time τ during which the ion could collide with the atoms, we determined whether the ion had a energy (in axial direction) below $\approx 50 \text{ K} \times k_B$ and therefore learned whether it had been collisionally cooled below this threshold. For this, we removed the atoms and slowly lowered the depth of the ion's trapping potential in axial direction to a fixed value (see Methods for the details), such that the ion would only stay in the trap and could be detected if its energy had been cooled to below $\approx 50 \text{ K} \times k_B$. From many repetitions of the measurement we obtained the probability for cooling below this (somewhat soft [as explained below]) energy threshold within τ . In order to test and calibrate this method, we carried out reference measurements where we probed an ion with a known initial energy E_{ion} . For this, all experimental settings were the same, except that there was no atom cloud present. Figure 3.3c shows these measurements for both Ba^+ and Rb^+ . The dashed line is a phenomenological fit of the form $y = 1 / ((E_{ion}/a)^b + 1)$ to the experimental data, where $a = 54 \text{ K} \times k_B$ and $b = 2.76$. The fact that the curve is not a step function but has 80%-20% width of about $60 \text{ K} \times k_B$ is mainly due to the fact that the turn-down of the trap potential is not fully adiabatic and that it is not synchronized with the ions oscillatory motion. Nevertheless, Fig. 3.3c shows that once the ion has an axial energy lower than $50 \text{ K} \times k_B$, it will have a high probability to stay in the trap.

We now describe the cooling experiments. Figure 3.3d shows the probability to cool a highly energetic Rb^+ ion as a function of the interaction time τ . We show data of two different experiments, corresponding to an initial kinetic energy of the ion of $(660 \pm 65) \text{ K} \times k_B$ (green circles) and $(2000 \pm 300) \text{ K} \times k_B$ (blue squares). As expected, the cooling probability monotonically increases with τ . However, what might be surprising at first is that the cooling results for the two experiments are very similar, although their initial kinetic energies differ by almost a factor of three. This cannot be explained within standard sympathetic cooling - but is an indication of swap cooling

which can cool an ion in a single step. Another curiosity is that cooling seems to slow down as time τ increases. Already at $\tau = 10$ ms about 20% of the ions have been cooled down. At that cooling rate one might expect to reach a cooled fraction of nearly 100% by about 150ms. However, in the experiments we only get close to this limit after about 2 s. The main explanation for this behaviour is as follows: If in a collision (e.g. a Langevin collision) the ion obtains a sizable momentum kick in the radial direction, then there is a good chance that its new trajectory has a much smaller overlap with the atom cloud than before (see Fig. 3.3a). This drastically lowers the subsequent cooling rate. These scenarios are corroborated by Monte Carlo (MC) trajectory calculations for our experimental settings (solid and dash-dotted lines in Fig. 3.3d). Details of the model are given in the Methods. The solid lines in Fig. 3.3d are the full model, whereas the dash-dotted lines are a model without the RCEX process, i.e., without swap cooling. The model without swap cooling is inconsistent with the data as it clearly distinguishes between the two cases with different initial energies and predicts a much slower cooling rate, especially for the higher energy. The full model reproduces the overall behaviour of the measured data but seems to underestimate the cooling rate. This might be partially explained by systematic errors in the theory when applying it to our energy range. The theory by Smirnov [Smi01] is expected to be more accurate for keV collision energies and assumes the particle trajectories to be straight lines, which is probably not justified for our experiments.

In order to obtain more evidence for swap cooling, we determined the energy dependency of the cooling process. Furthermore, we compared cooling of a single $^{87}\text{Rb}^+$ ion with that of a single $^{138}\text{Ba}^+$ ion, for which RCEX, and therefore swap cooling, is absent. Figure 3.4 shows the probabilities for cooling each ion with an initial energy¹ E_{ion} to below $\approx 50 \text{ K} \times k_B$ within 200 ms. For low initial energies of up to $200 \text{ K} \times k_B$ both ions are essentially completely cooled down within the 200 ms interaction time. This is not surprising as the dynamics of the system is described by the Langevin collisions in this range of energy. By increasing the initial energy E_{ion} , the probability for cooling below the threshold decreases for both species, as expected. However, the cooling efficiency differs progressively for the two species as E_{ion} gets larger. For Ba^+ the cooling probability essentially drops to zero for $E_{ion} = 7000 \text{ K} \times k_B$. This is simply explained by the fact that swap cooling does not exist for Ba^+ and the time τ is too short for sympathetic cooling to reach the $\approx 50 \text{ K}$ temperature threshold. For Rb^+ , however, the probability to cool down the ion is still above 40%. The solid red line shows the cooling results for full MC calculation for Rb^+ . The red dotted line is the MC calculation for Rb^+ without RCEX but including sympathetic cooling via elastic collisions. The blue solid line shows the MC simulation results for sympathetic cooling of the Ba^+ ion. As expected, the last two are very similar apart from a small horizontal shift. The solid curves match the general trend of the experimental data quite well, which is consistent with our previous discussion.

¹For Rb^+ $E_{ion} = 2 \times E_{col}$. For Ba^+ , assuming the Rb atom is at rest, $E_{ion} = m_{\text{Ba}}/m_{\text{Red}} \times E_{col} = 2.59 E_{col}$ where $m_{\text{Red}} = \frac{m_{\text{Ba}} m_{\text{Rb}}}{m_{\text{Ba}} + m_{\text{Rb}}}$ is the reduced mass in the two-body collision.

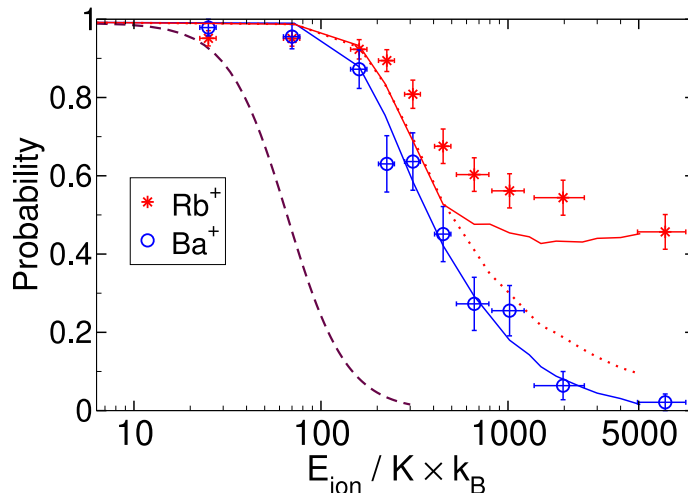


FIGURE 3.4: **Cooling of Rb^+ and Ba^+ ions.** Shown is the probability to cool an ion to below ≈ 50 K within $\tau = 200$ ms with ultracold cloud of Rb atoms. The probability is plotted as a function of the ion's initial kinetic energy E_{ion} . The dashed line is the reference curve from Fig 3.3c. The solid lines are full MC simulations. The dotted red line is MC simulation without RCEx for a Rb^+ ion.

3.5 Conclusion

The swap cooling process, demonstrated here for Rubidium, is based on a few very general principles and should therefore be a universal process in all homo-nuclear atom-ion collisions. Furthermore, it should even occur for molecules. Apart from the proof of principle, we expect the present work to be of practical value in applications, e.g. where ions with energies in the eV range need to be cooled down quickly. Swap cooling should play an important role in current cold atom-ion experiments, such as in [Här+12] where a chemical reaction process was driven by cold Rb^+ ions and emitted hot ones. Swap cooling is then an efficient means to keep the reaction process going. Moreover, it is essential to take into account the RCEx in investigating the mobility of a charged particle in parent neutral particles[CD00].

3.6 Methods

3.6.1 Preparation of the ultracold Rb clouds.

The atoms are confined in a far off-resonant crossed optical dipole trap at a wavelength of 1064.5 nm with a trap depth of $10 \mu\text{K} \times k_B$ and with trap frequencies of $\omega_{x,y,z} = 2\pi \times (24, 138, 145)$ Hz. Atom clouds are prepared differently for different purposes. Atom clouds that are used as coolant or as a means for ion detection typically consist of $N = 7 \times 10^4$ atoms. They are thermal ensembles with temperatures of about $T = 600$ nK. Their cloud shape is Gaussian with a standard deviation of $\sigma_{x,y,z} \approx (48, 8.8, 8.4)$ μm , and with a peak density of $n = 1.3 \times 10^{12} \text{ cm}^{-3}$. Atom clouds that are used for producing the Rb^+ ions (see section 'Preparation of single ions at mK-temperatures')

have a total atom number $N = 1.2 \times 10^6$ corresponding to peak densities higher than 10^{13} cm^{-3} . The initial temperature of these clouds is about $T = 510 \text{ nK}$.

3.6.2 Ion trap configuration.

We use a linear Paul trap [Sch+12] where radial confinement is achieved by driving the RF-electrodes with a radio-frequency of 4.21 MHz and axial confinement is obtained by applying static voltages of 7.6 V to the two endcap electrodes. The trap frequencies of a Ba^+ ion are $(\omega_{x,\text{Ba}}, \omega_{y,\text{Ba}}, \omega_{z,\text{Ba}}) = 2\pi \times (130, 131, 37.8) \text{ kHz}$, while for a Rb^+ ion they are $(\omega_{x,\text{Rb}}, \omega_{y,\text{Rb}}, \omega_{z,\text{Rb}}) = 2\pi \times (206, 208, 47.6) \text{ kHz}$. The depth of the Paul trap depends on the ion's mass but exceeds 1 eV for both ions.

3.6.3 Preparation of single ions at mK-temperatures.

We prepare a single mK-cold Rb^+ ion as follows. We produce an ultracold Rb cloud with a density of $n > 10^{13} \text{ cm}^{-3}$ in our dipole trap. Three-body recombination creates Rb_2 molecules within this cloud, a few of which are photo-ionized by our dipole trap laser in a resonant multi-photon ionization (REMPI) process [Här+13b]. In this way we produce Rb_2^+ molecular ions at an initial rate of about 0.5 s^{-1} . Subsequent inelastic collisions of these ionic molecules with cold Rb atoms, or photodissociation via the 1064 nm laser light produce Rb^+ ions. The Rb^+ ion will then have elastic collisions with Rb atoms which will decrease the density of the atoms by heating the cloud and kicking atoms out of the shallow trap. Therefore, the production rate of additional ions via three-body recombination quickly drops after the production of the first ion. As a consequence, with the proper settings of the experimental parameters we can prepare a single Rb^+ ion with more than 90 percent probability. In order to experimentally test whether we have created a single Rb^+ ion and to sympathetically cool it down to mK temperatures, we immerse the ion/ions for two seconds into a newly prepared Rb atom cloud with a comparatively low density of about 10^{12} cm^{-3} . We make use of ion-induced atom loss, in the same manner as explained in section 'Detection of ions', in order to determine the number of the ions in the trap. For our analysis, we only take into account experimental runs which initially had a single ion. If we need to prepare a single mK cold Ba^+ ion, instead of a Rb^+ ion, we use isotope-selective, resonant two-photon ionization of neutral Ba atoms passing through the centre of the Paul trap. Once produced, a Ba^+ ion is immediately trapped and laser cooled down to the Doppler cooling limit.

3.6.4 Setting the initial kinetic energy of the ion.

For setting the initial kinetic energy of the ion after it has been cooled to mK temperatures, the centre of the axial trapping potential of the Paul trap is adiabatically shifted by lowering the voltage of one of the endcap electrodes which leads to an adiabatic displacement of the ion. Afterwards, the voltage of the endcap is set to its original value using a well-defined voltage ramp. This imparts a well-defined kinetic energy

to the ion as it swings back to the trap centre where the atom cloud is located. The ion then undergoes essentially undamped harmonic oscillations in the trap along the axial direction until the first collision with a cold Rb atom which can change the ion momentum appreciably.

In order to calibrate the ion's energy, we measure the initial displacement of the ion as a function of the applied voltages to the endcap electrodes. The mean displacement of the ion can be measured with an accuracy on the order of 1 percent via fluorescence imaging of the Ba^+ ion. Since the minimum of the trapping potential is independent of the mass, the displacement is identical for Rb^+ . The imparted energy to the ion is determined by solving the equation of motion numerically, making use of the known axial trapping potential and including a 30 V/m stray electric field. As a typical example, linearly ramping the voltage on the endcap electrode from 0.6 V back to 7.6 V in 9.4 μs imparts an energy of $2000 \pm 300 \text{ K} \times k_B$ to the ion.

3.6.5 Determining whether ions have been cooled down to $50 \text{ K} \times k_B$ or below.

We use a scheme which is rather simple and empirical but gives a clear semi-quantitative measure of whether the ion energy has been cooled down in axial direction to $\approx 50 \text{ K} \times k_B$ or below by the atom cloud. Right after the atom-ion interaction, we lower the voltages on the electrodes of the Paul trap and hold them at that level for 200 ms. The ramp-down in the axial direction is done by adiabatically decreasing the voltage on one of the endcap electrodes (from 7.6 V to around 100 mV) within 150 ms. We note that this process also shifts the trap centre in the axial direction, which in general leads to some heating of the ion. In parallel, we lower the RF amplitude in the radial direction from 156 V to 50 V within 150 ms. These are the lowest (experimentally determined) voltages so that ions which are mK-cold before the ramp are still trapped with unit probability after the ramp. We measure the probability of losing the ion after the lowering process as a function of its initial kinetic energy in the axial direction. These calibration measurements are shown in Fig. 3.3c. Losses in the radial direction should be negligible because the radial confinement is still comparatively large. Moreover, our simulations for large initial energies $> 1000 \text{ K} \times k_B$ indicate that after the 200 ms interaction time of our measurements, the ion's kinetic energy for the axial motion is typically still much larger than the one for the radial motion. Therefore, in this energy range the measured energy in axial direction should be quite representative of the overall energy of the ion.

3.6.6 Detection of ions.

In order to detect how many ions are present in the Paul trap, we immerse them for two seconds into a newly prepared Rb atom cloud with a density of about 10^{12} cm^{-3} and with a well-defined atom number of $(7 \pm 0.2) \times 10^4$. Due to their micromotion the ions induce loss in the atomic cloud as a result of elastic collisions which kick

atoms out of the shallow dipole trap. We infer the ion number from a measurement of the atom loss [Här+12]. However, in order to specifically detect a single Ba⁺ ion we use a different method, where we perform intensive laser cooling by detuning the laser frequency 2.5 GHz to the red of the resonance and ramping it back in about 4s [Moh+21]. We have checked that this procedure cools down even the hottest Ba⁺ ions in our Paul trap with nearly 100 percent efficiency. Once the Ba⁺ ion is cooled down we collect its fluorescence signal on a EMCCD camera within 100 ms.

3.6.7 Theoretical model for swap cooling.

In the following we describe the semi-classical model for swap cooling in a homo-nuclear atom-ion collision. The long range atom-ion interaction is dominated by the attractive polarization potential[VW54] $V(r) = -C_4/(2r^4)$, where $C_4 = \alpha q^2/(4\pi\epsilon_0)^2$ is proportional to the static dipolar polarizability of the atom α , and q is the electron charge. $\alpha = 4\pi\epsilon_0 \times 47.4 \text{ \AA}^3$ for Rb [SN19]. For a given collision energy (E_{col}) in the centre of mass (COM) frame, a critical impact parameter $b_c = (2C_4/E_{col})^{1/4}$ can be defined. In a classical picture, a collision with impact parameter $b < b_c$ results in an inward spiralling trajectory, followed by a hard elastic or inelastic collision, and completed by an outward spiralling trajectory. The scattering angles for such a collision are uniformly distributed over the whole solid angle of 4π . This is called a Langevin collision, and its cross section is $\sigma_{Lng} = \pi b_c^2 = \pi\sqrt{2C_4/E_{col}}$. Collisions with impact parameters $b > b_c$ generally lead to small deflections and are therefore called glancing collisions. They are of interest for the swap cooling process. For glancing collisions, the atom-ion separation stays finite, and the two particles are scattered from each other with a deflection angle θ which is a function of the impact parameter b . For a $1/r^4$ potential the angle θ is given by [L01],

$$\theta = \pi - 2\tilde{b}\sqrt{2}\sqrt{\tilde{b}^2 - \sqrt{\tilde{b}^4 - 1}} \times \mathcal{K}(2\tilde{b}^4 - 2\tilde{b}^2\sqrt{\tilde{b}^4 - 1} - 1) \quad (3.1)$$

where $\tilde{b} = b/b_c$ is the normalized impact parameter and

$$\mathcal{K}(y) = \int_0^{\pi/2} \frac{1}{\sqrt{1 - y \sin^2 x}} dx$$

is the complete elliptic integral of the first kind. In the following we consider the collision of an incident Rb⁺ ion with a neutral Rb atom which is at rest in the lab frame. For an elastic collision the energy lost E_{loss} by the incident particle in the lab frame is equal to the energy E_{trans} transferred to the target particle which is initially at rest. These energies can be expressed as a function of the scattering angle θ in the COM frame (see e.g. [L01]),

$$E_{loss} = E_{trans} = E_{ion,i} \sin^2(\theta/2), \quad (3.2)$$

where $E_{ion,i}$ is the initial kinetic energy of incident ion. It is noteworthy that eq. (3.2) is merely a consequence of the conservation of momentum and energy. We now discuss the probability for resonant-charge-exchange in a collision. RCEX has been extensively studied theoretically [Smi03; JA89; Bra90] and has been experimentally investigated for collision energies ranging from eV to keV for different species, including Rubidium [PVD65]. Here we use the impact parameter dependent charge exchange probability $P_{RCEX}(b)$ obtained from the asymptotic theory presented by Smirnov [Smi01] which in atomic units reads,

$$P_{RCEX}(b) = \sin^2 \left(\frac{1}{v} \sqrt{\frac{\pi}{2\gamma}} A^2 \exp\left(-\frac{1}{\gamma}\right) b^{2/\gamma-1/2} \exp(-b\gamma) \right). \quad (3.3)$$

Here, v is the collision velocity (1 a.u. of velocity = $a_0 E_h / \hbar = 2.18769126364 \times 10^6$ m s⁻¹), $\gamma = \sqrt{-2I}$ where I is the atomic ionization potential, A is the asymptotic coefficient determined by comparing the asymptotic wave function with that obtained from numerical calculations, and b is the impact parameter in the collision. We adopt the numerical values of $\gamma = 0.554$ and $A = 0.48$ for Rubidium from reference [Smi01]. The total cross section σ_{RCEX} for resonant charge exchange is then,

$$\sigma_{RCEX} = \int_0^\infty 2\pi b db P_{RCEX}(b) \quad (3.4)$$

For swap cooling we are only interested in those charge transfer collisions that result in a cold enough ion. Therefore, we define the following swap cooling cross section,

$$\sigma_{swap}(b_{thr}) = \int_{b_{thr}}^\infty 2\pi b db P_{RCEX}(b). \quad (3.5)$$

This cross section depends on the threshold impact parameter $b_{thr} > b_c$. Every charge transfer collision with an impact parameter greater than b_{thr} produces a Rb⁺ ion with a kinetic energy less than a maximal final energy $C_{thr} = E_{ion,i} \sin^2(\theta(b_{thr})/2)$ which follows from eqs. (3.1) and (3.2). All these collisions are accounted for in the swap cooling cross section eq. (3.5). The calculated results for the swap cooling cross section are presented in figure 3.5 for different maximal final energies C_{thr} . We also show the total resonant-charge-exchange cross section from eq. (3.4) which is a slowly varying function of the collision energy. It is worth noticing that the swap cooling cross section is enhanced by increasing the collision energy. This effect is even more pronounced for lower maximal energies (C_{thr}) of the ion after the collision.

3.6.8 Description of the simulation.

We have performed Monte Carlo trajectory calculations for the motion of the ion in the ion trap and its collisions with the ultracold Rb atoms. These collisions include Langevin collisions, resonant charge exchange collisions and elastic collisions. The simulation takes into account the settings of the experiment, such as the ion trap

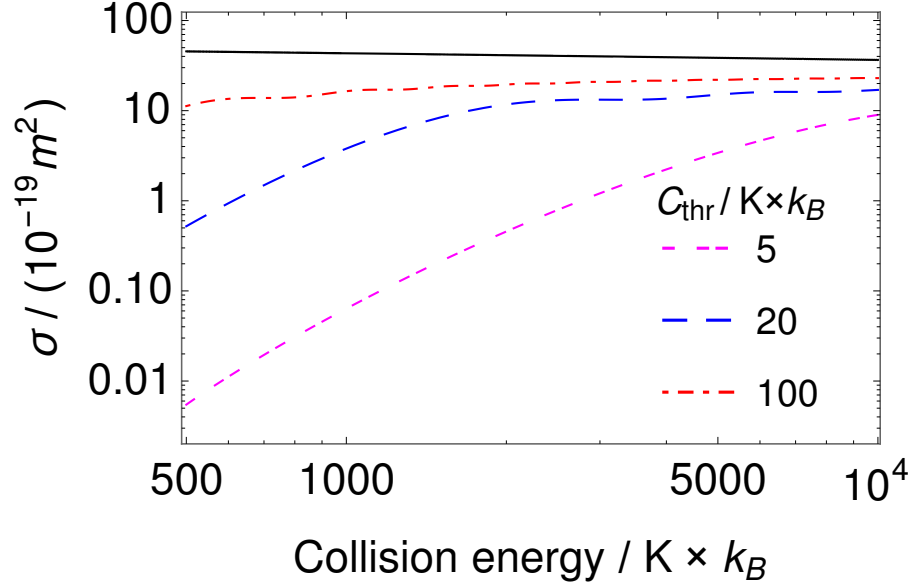


FIGURE 3.5: **The RCEX and swap cooling cross sections for a Rb-Rb⁺ collision.** The black curve is the calculated RCEX cross section using asymptotic theory [Smi01]. Three different swap cooling cross sections are also presented for different maximal energies (C_{thr}) of the ion after the collision.

frequencies, the density distribution of the atomic cloud, and the ion's initial position and energy. We use the semiclassical elastic scattering cross section of reference [CD00] as a total cross section σ_{tot} for both elastic and charge transfer processes,

$$\sigma_{tot}(E_{col}) = \pi \left(\frac{\mu C_4^2}{\hbar^2} \right)^{1/3} \left(1 + \frac{\pi^2}{16} \right) E_{col}^{-1/3}. \quad (3.6)$$

The finite value of σ_{tot} effectively limits the impact parameter to $b \leq b_m = \sqrt{\sigma_{tot}/\pi}$. This is not a problem, since trajectories with larger impact parameters experience negligible angles of deflection and negligible energy transfers anyway. The rate for a collision is given by

$$\Gamma = n_{atom} \sigma_{tot} v, \quad (3.7)$$

where n_{atom} is the density of the atom cloud at the position of the ion, and v is the ion's velocity in the lab frame. The ultracold atoms are considered to be at rest. We follow the method in reference [Zip+11] for efficient time advance. Once a collision occurs we generate the impact parameter b via² $b = b_m \sqrt{N_{Rand}}$ where N_{Rand} is a random number drawn from a uniform distribution in the interval $[0 \dots 1]$. The impact parameter determines whether the collision is of the Langevin type or a glancing collision. For a Langevin collision ($b < b_c$) the scattering angle θ in the centre of mass system is isotropically distributed. For the glancing collisions ($b_m > b > b_c$) which include both elastic and RCEX processes, the scattering angle θ is determined

²This formula corresponds to the inverse of the integrated probability distribution $P(b) = \int_0^b dP = \int_0^b 2\pi b' db' / \sigma_{tot} = (b/b_m)^2$

by eq. 3.1 and the transferred energy to the target particle (in the lab frame) is given by eq. 3.2. The probability for RCEX is calculated via eq. 3.3. The simulation runs until the total interaction time is reached. If the final energy of the ion in axial direction is smaller than a set threshold around $T_{low} = 50\text{K} \times k_B$, it will be counted as a cold ion which stays trapped in the Paul trap after the ramp down. In order to reproduce the finite energy resolution of the detection scheme (as shown in Fig. 3.3c) we generate a corresponding distribution of random numbers for the threshold in our simulation. In order to finally calculate the probability for the ion to stay trapped for a given T_{low} , we analyse typically 10000 MC runs and average over the trapping probability for all thresholds of the distribution.

During the Monte Carlo simulations, the atom cloud density distribution is assumed to be constant. This is reasonable since atomic losses due to background collisions, heating and atom-ion collisions during the interaction time are negligible.

Chapter 4

Numerical study on the universality of swap cooling

4.1 Introduction

In chapter 3 the experimental evidence for swap cooling, i.e. cooling a hot ion via resonant charge exchange (RCEX) in a homo-nuclear atom-ion system was presented for the representative case of a Rb^+ ion interacting with ultracold Rb atoms. In order to demonstrate swap cooling, the experiments were carried out in a regime where cooling by resonant charge exchange was overwhelmingly dominant over the conventional collisional cooling, i.e. sympathetic cooling via elastic collisions. As was pointed out, the swap cooling differentiates itself from sympathetic cooling in two main aspects. First is the fact that the former is a single collision process while the latter requires successive elastic collisions, each of which carries away some portion of the energy that is to be dissipated. Second, the swap cooling collision cross-section is a slowly varying function of the collision energy (see section 3.6.7 and the following section), as contrasted with strong $E_{col}^{-1/3}$ dependency of elastic collision cross-section (see eq. 2.12). These two major differences manifest themselves in the relative efficiency of each cooling mechanism depending on the experimental parameters which can be broadly categorized as the density distribution of the ions and atoms, interaction time, and collision energy.

In this chapter, I use numerical calculations to investigate the properties of the swap cooling process compared to sympathetic cooling in more detail. The relative performance of each cooling mechanism under various experimental conditions will be discussed. The Monte Carlo (MC) simulations are not limited to the exact characteristics of our experimental set-up and allow exploring a broader range of parameters. Moreover, following the theoretical procedure introduced in the previous chapter, I expand the scope of the study to other species, namely, alkali and alkaline earth metals. It is shown numerically that swap cooling happens for all the elements investigated, and it is indeed the dominant cooling channel for higher collision energies. Moreover, its characteristics seem to be universal and follow the same trend as Rubidium.

4.2 Swap cooling cross section

Before presenting the numerical simulations, I look at the cross section of different types of collisions relevant for this study, namely, RCEX, swap cooling, and the Langevin collision cross section. The mathematical formulas required for calculating these cross sections are given in chapter 3. Here, I only repeat the equation 3.5 used to calculate the swap cooling cross section:

$$\sigma_{swap}(b_{thr}) = \int_{b_{thr}}^{\infty} 2\pi b db P_{RCEX}(b),$$

where the probability of a resonant charge exchange collision P_{RCEX} in atomic units is given by (see section 3.6.7)

$$P_{RCEX}(b) = \sin^2 \left(\frac{1}{v} \sqrt{\frac{\pi}{2\gamma}} A^2 \exp\left(-\frac{1}{\gamma}\right) b^{2/\gamma-1/2} \exp(-b\gamma) \right).$$

Here, v is the collision velocity (1 a.u. of velocity = $a_0 E_h / \hbar = 2.18769126364 \times 10^6$ m s⁻¹), $\gamma = \sqrt{-2I}$ where I is the atomic ionization potential, A is the asymptotic coefficient determined by comparing the asymptotic wave function with that obtained from numerical calculations, and b is the impact parameter in the collision. Table 4.1 shows the numerical values for A and γ in addition to the static dipole polarizabilities α for alkali and alkaline earth metals. It can be seen from the above formula that

TABLE 4.1: Static scalar dipole polarizabilities, and asymptotic coefficients (see the text for definitions) for alkali and alkaline earth metals. Data for dipolar polarizabilities are taken from [SN19], while the asymptotic coefficients are adopted from [Smi01].

Element	α ($\frac{\text{\AA}^3}{4\pi\epsilon_0 \times a_0^3}$)	A (atomic units)	γ (atomic units)
Li	164.1125	0.82	0.630
Na	162.7	0.74	0.615
K	289.7	0.52	0.565
Rb	319.8	0.48	0.554
Cs	400.9	0.41	0.535
Be	37.74	1.6	0.828
Mg	71.2	1.3	0.750
Ca	160.8	0.95	0.670
Sr	197.2	0.86	0.647
Ba	272	0.78	0.619

the swap cooling cross section depends on a chosen threshold impact parameter, b_{thr} which in turn corresponds to a cooling threshold C_{thr} (see section 3.6.7). The latter is introduced to provide a quantitative definition of a "cold" ion. Namely, if the total

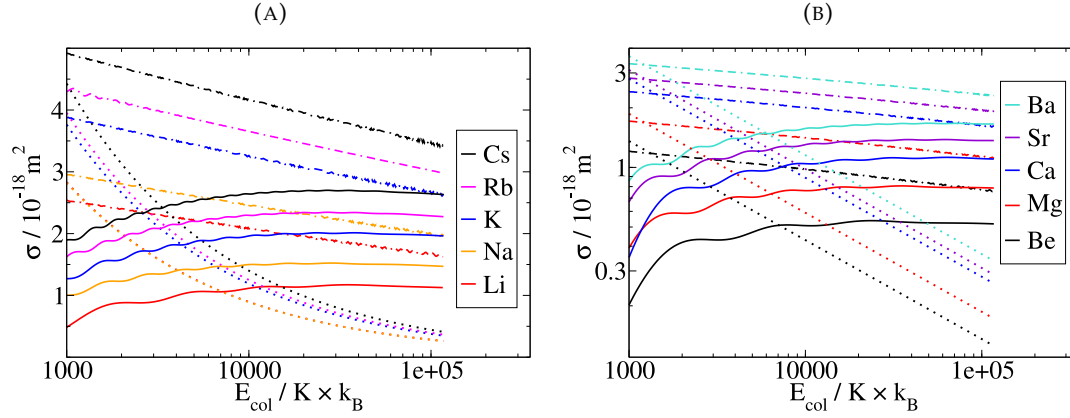


FIGURE 4.1: The cross section of different types of collision in homo-nuclear atom-ion systems for A) Alkali metals, and B) Alkaline earth metals. Solid lines show the cross section for swap cooling collisions for a cooling threshold of $C_{thr} = 100K \times k_B$ (see the text), while dash-dotted lines represent the total RCEX cross section. Dotted lines depict the cross section for the Langevin collisions. Different species are distinguished with different colours. Please note that the vertical axis in panel (A) uses linear scale, while in panel (B) is chosen to be logarithmic for better visibility. The Langevin cross section of Lithium and Sodium almost overlap because their polarizability is virtually the same (see Table 4.1).

kinetic energy of the ion after the collision is less than C_{thr} the ion is considered to be cooled down via a swap cooling collision.

Figure 4.1 shows different cross sections as a function of the collision energy (E_{col}) up to $E_{col} = 116000K \times k_B = 10\text{eV}$ for alkali and alkaline earth metals. The cooling threshold used for these calculations is set to be $C_{thr} = 100K \times k_B$. Please note that for two particles with the same mass, considered here, $E_{col} = 1/2E_{ion}$ where E_{ion} is the initial kinetic energy of the ion. Different species in figure 4.1 are shown with different colours. Swap cooling cross section is depicted with solid lines, while dash-dotted curves represent the RCEX collision cross section. Langevin cross sections are shown with dotted lines. As expected, different species behave similar to one another with regard to the calculated cross sections, and they follow the same trend. It is also notable that the numerical values for each type of collision cross section remain within the same order of magnitude upon changing the element for all alkali and alkaline earth metals.

It was laid out in chapter 3 that the cooling process in homo-nuclear atom-ion collisions is dominated by swap cooling and Langevin collisions. Fig. 4.1 clearly shows that increasing the collision energy favours swap cooling over Langevin collisions. It can be seen that the swap cooling cross section becomes larger than the Langevin cross section only after increasing the collision energy to several thousand $K \times k_B$. However, the signature characteristic of swap cooling, i.e., bringing about a cold ion in a single collision, makes it non-trivial to find the exact collision energy above which swap cooling starts to dominate the collisional cooling. Therefore,

numerical calculations simulating various experimental conditions are presented in the following section to provide a comparative study of the relative efficiency of each cooling process.

4.3 Comparative performance of swap cooling

The measurements that were presented in figure 3.4 were designed to demonstrate swap cooling. The interaction time in the experiment was, therefore, chosen to be 200 ms, which was too short for any significant contribution from sympathetic cooling for higher collision energies. The atom-ion interaction time in the MC simulations were accordingly fixed at the same value. The cooling probability was then determined by dividing the number of runs in which this interaction time is sufficient to cool the ion below the C_{thr} by the total number of runs. Here, the same MC simulation is used with a slightly different approach. Namely, the atom-ion interaction time is not fixed and in each run the simulation continues until the ion cools down to the ultracold temperatures. Concretely speaking, the cooling threshold is set to $C_{thr} = 10 \text{ mK} \times k_B$ (which differs from $C_{thr} \sim 50 \text{ K} \times k_B$ used in the previous chapter in accordance with the experiments). The first parameter of interest is then the average interaction time (T) needed to cool down the ion as a function of its initial kinetic energy for different experimental conditions. In the following, I first discuss how the spatial confinement and density distribution of atoms and ions affect T and the relative efficiency of each cooling mechanism. Simulations are performed for Rubidium as an exemplary case.

The solid blue line in figure 4.2 shows T for a typical setting of our experiment as a function of the initial kinetic energy of the ion in the units of $\text{K} \times k_B$. The initial conditions in the simulation are chosen to match the typical experimental parameters as in [MKD21]. The Rb^+ ion is confined in a linear Paul trap with trapping frequencies $(\omega_{x,\text{Rb}}, \omega_{y,\text{Rb}}, \omega_{z,\text{Rb}}) = 2\pi \times (206, 208, 47.6) \text{ kHz}$. In the simulations all the initial energy of the ion is allocated to the z component. The atom cloud has a Gaussian density distribution with a standard deviation of $\sigma_{x,y,z} \approx (48, 8.8, 8.4) \mu\text{m}$, and with a peak density of $n = 1.3 \times 10^{12} \text{ cm}^{-3}$. These conditions, i.e. local density distribution of the atom cloud and relatively low ionic trapping frequencies, lead to very small overlap between the ion trajectory and the atom cloud for higher initial kinetic energies of the ion. Therefore, enhancing E_{ion} will on average significantly increase the time needed to cool down the ion. For comparison, the same MC calculations are performed without swap cooling, which means no charge transfer occurs during the simulations. The average cooling time T when swap cooling does not take place is shown with red dashed line in figure 4.2 which progressively deviates from the corresponding full MC calculations (solid blue line) by increasing E_{ion} . For the highest calculated initial energy of $E_{ion} = 11600 \text{ K} \times k_B \approx 1 \text{ eV}$, mere sympathetic cooling takes about 9 times longer to cool the ion down as compared to the total collisional cooling that includes swap cooling.

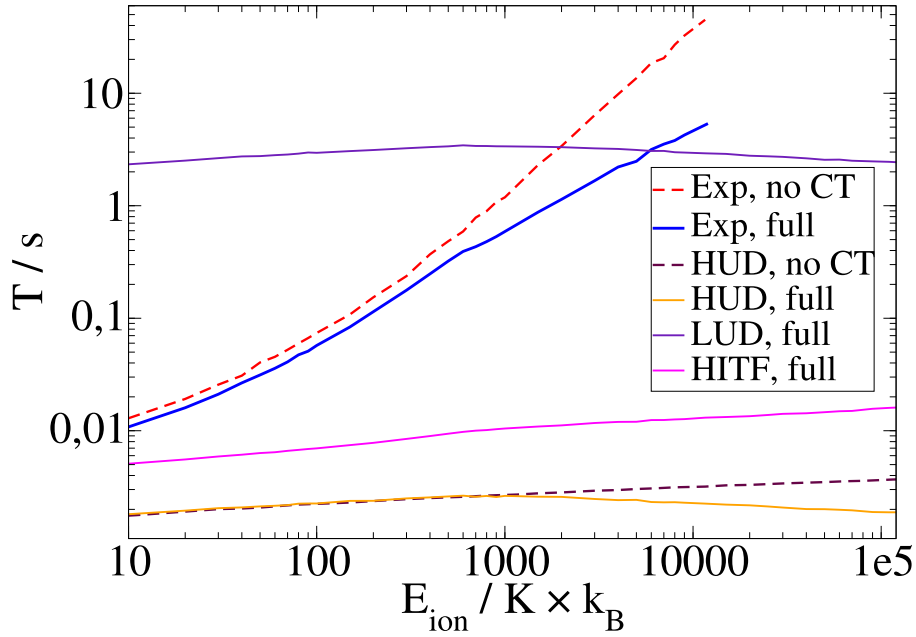


FIGURE 4.2: Average cooling time of a Rb^+ ion interacting with ultracold Rb atoms. The solid blue line simulates typical experimental conditions, in which the atoms are confined in an optical dipole trap with a Gaussian shape density distribution and the ion in a linear Paul trap with relatively low trapping frequencies (see the text). The dashed red line has the same configuration for the atom cloud and the ion but does not include swap cooling, i.e. no charge transfer (CT) happens during the simulation. Solid magenta line assumes the same atomic density distribution but almost 10 times higher ionic trapping potentials (see the text for exact numbers). The cooling time of a free ion interacting with ultracold atoms with uniform density distribution is shown with orange solid line for $n = 1.3 \times 10^{12} \text{cm}^{-3}$ (HUD) and with violet solid line for $n = 1 \times 10^9 \text{cm}^{-3}$ (LUD). The maroon dashed line also assumes the ion to be a free particle interacting with neutral atoms with a uniform density distribution of $n = 1.3 \times 10^{12} \text{cm}^{-3}$ but does not include swap cooling. All curves presented with solid lines use the full model that includes cooling via RCEX.

The main reason for slow cooling rates for the mentioned experimental conditions is the small overlap between ion trajectory and the atom cloud. I therefore performed simulations for high ionic trapping frequencies (HITF) but the same density distribution for atomic cloud which is shown by solid magenta line in figure 4.2. The chosen ionic trapping frequencies for these simulations are $(\omega_{x,\text{Rb}}, \omega_{y,\text{Rb}}, \omega_{z,\text{Rb}}) = 2\pi \times (2, 2, 1)$ MHz which result in much more localized ion trajectories, and therefore, better overlap with ultracold atoms. While these frequencies are much higher than what we typically have in our Paul trap, they are still in the range of accessible trapping frequencies which can be used in atom-ion experiments. It can be seen that this change makes the cooling more efficient and also less sensitive to the variations of E_{ion} . In the next step, the atom cloud is assumed to have a uniform density distribution of $n(x, y, z) = 1.3 \times 10^{12} \text{cm}^{-3}$, and the ion a free particle with initial energy E_{ion} . These conditions resemble buffer gas cooling. The corresponding MC calculations

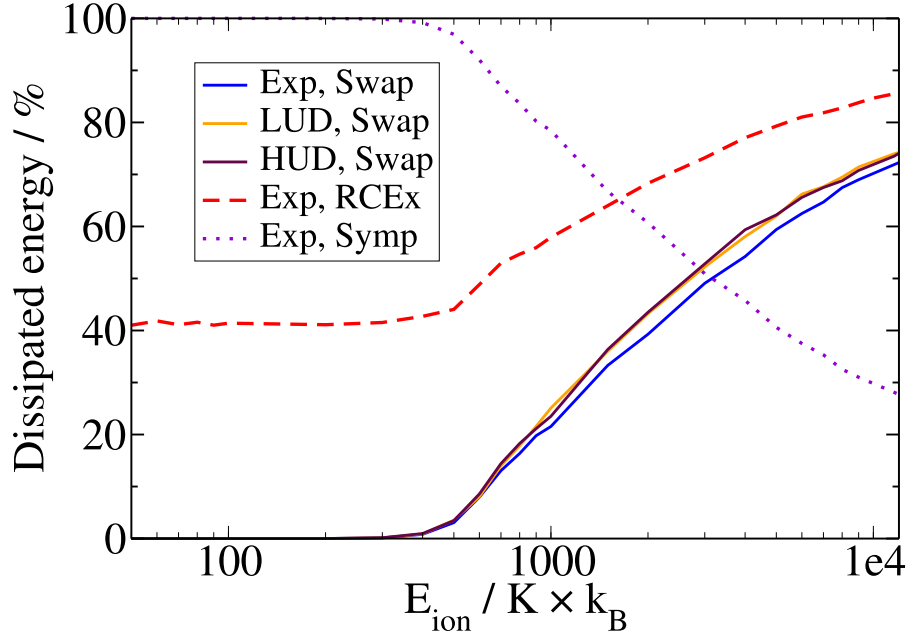


FIGURE 4.3: The x-axis shows the initial kinetic energy of the Rb^+ ion E_{ion} . The simulation runs until the ion is cooled below $10\text{mK} \times k_B$ due to collisions. The overall percentage of the total dissipated energy via different cooling processes is shown. The solid blue line depicts the proportion of the energy dissipated via swap cooling for typical experimental parameters. The dotted violet curve corresponds to the rest of the collisional cooling in the same simulation, i.e., sympathetic cooling. The dashed red curve represents all the energy dissipated via RCEX, which comprises swap cooling plus all Langevin collisions with a charge exchange. The solid maroon and orange curves represent the dissipation of a free Rb^+ ion's initial energy via swap cooling, assuming the atoms have a uniform distribution with the constant density of $n = 1.3 \times 10^{12}\text{cm}^{-3}$ and $n = 1 \times 10^9\text{cm}^{-3}$, respectively.

are labelled HUD (standing for high uniform density) in figure 4.2 and are shown by the solid orange line. The violet solid line in the same graph represents the same calculations for a lower uniform density (LUD) of $n(x, y, z) = 1 \times 10^9 \text{cm}^{-3}$. As expected, the orange and violet curves are the same apart from a constant prefactor corresponding to the ratio of the two atomic densities. More importantly, after a sufficiently high initial energy of about $E_{ion} = 1000\text{K} \times k_B$ the cooling happens at a faster rate by increasing E_{ion} . As we shall see in further details in the following, this happens as swap cooling becomes the dominating cooling channel in the collisional dynamics. For the sake of comparison, the maroon dashed line in figure 4.2 resulted from the MC simulations with the same parameters as for the orange curve, with the exception that RCEX is not included in the simulations. Clearly, the average cooling time in MC calculations without charge transfer (dashed maroon line) is an ever-increasing function of E_{ion} , contrary to the full model (solid orange line).

Figure 4.3 illustrates the relative performance of different cooling mechanisms, i.e. the percentage of initial energy of the ion which is dissipated via each process, as a function of E_{ion} . The curves labelled "Exp" present MC simulations that are

performed using typical experimental parameters in accordance with [MKD21], and with the aforementioned blue solid line in figure 4.2. Each time a charge transfer happens during the simulation, the code adds the energy difference of the ion before and after the collision to the swap cooling proportion only if the collision's impact parameter was higher than the critical impact parameter b_c . The red line in figure 4.3, on the other hand, shows the overall collisional cooling via RCEX. It accounts for a higher percentage of dissipated energy since, besides swap cooling, it also includes charge transfer events that happen via Langevin collisions. As mentioned in chapter 3, for lower collision energies, the dynamics of the system is mainly characterized by Langevin collisions, half of which lead to RCEX. The relative performance of swap cooling is also calculated for a free Rb^+ ion interacting with ultracold Rb atoms with a uniform density distribution. The maroon curve in figure 4.3 represents the higher uniform density (HUD) of $n(x, y, z) = 1.3 \times 10^{12} \text{ cm}^{-3}$, while the orange line shows the lower uniform density (LUD) of $n(x, y, z) = 1 \times 10^9 \text{ cm}^{-3}$. Although the average cooling time is directly proportional to the atomic density as can be seen in figure 4.2, the swap cooling proportion of the collisional cooling seems to be independent of the density as the LUD and HUD curves in figure 4.3 practically overlap. Moreover, regarding the percentage of cooling that is done via swap cooling, there is no significant difference between the local or uniform density distribution of the atomic cloud in spite of the sizable difference in the average cooling time. Therefore, since the comparative performance of different cooling processes is rather insensitive to the density distribution of the ultracold atoms, and taking into account the considerable difference in the computational cost, in what follows the MC calculations are performed for the case of a free ion interacting with ultracold atoms with a uniform density of $n(x, y, z) = 1.3 \times 10^{12} \text{ cm}^{-3}$.

4.4 Swap cooling for alkali and alkaline earth metals

So far in this chapter, the comparative role of swap cooling for different configurations of the atom and the ion systems is explored numerically. The next step is to investigate the swap cooling process in other species rather than Rubidium. Although switching to other species is experimentally challenging, expanding the numerical calculations is quite straightforward. The theoretical model for swap cooling and the details of the Monte Carlo simulations used to calculate collisional cooling are laid out in chapter 3 (see also Appendix B). Here, the same code is used for other species. The numerical values for the static dipolar polarizabilities of neutral atoms α which are required for calculating the collision rates are taken from [SN19]. The resonant charge exchange probability for glancing collisions is calculated using formula 3.3 in which numerical values for asymptotic parameters A and γ are adopted from [Smi01]. For Langevin collisions, the RCEX probability is 0.5. Table 4.1 shows the numerical values for α , A , and γ for alkali and alkaline earth metals used in the simulations.

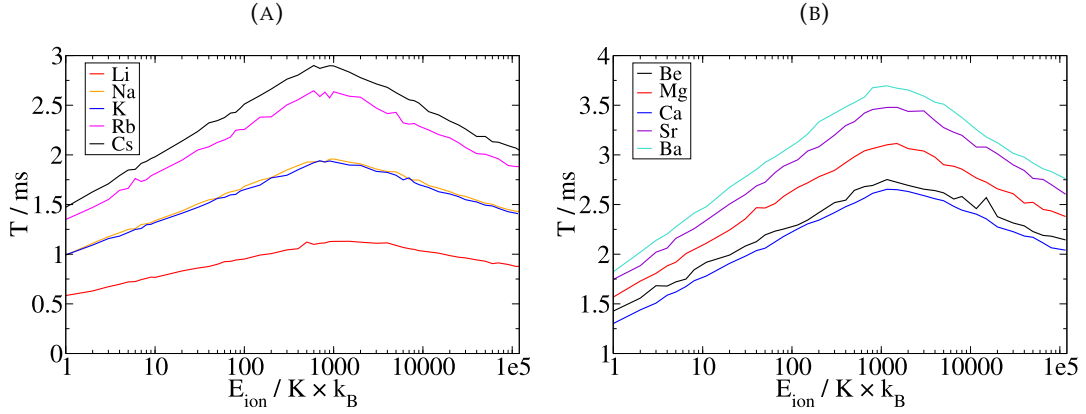


FIGURE 4.4: An energetic ion interacts with its parent neutral particle. Shown are MC calculations for the average time needed to cool down the ion as a function of its initial kinetic energy for A) Alkali metals, and B) Alkaline earth metals. The ion is assumed to be a free particle interacting with its parent neutral particles taken to be at rest with a uniform density distribution of $n(x, y, z) = 1.3 \times 10^{12} \text{ cm}^{-3}$.

Figure 4.4 presents MC calculations for a free energetic ion interacting with its parent neutral particles. The neutral atoms assumed to be at rest in the simulation with a uniform density distribution of $n(x, y, z) = 1.3 \times 10^{12} \text{ cm}^{-3}$. The average time T needed to cool down the ion below $10 \text{ mK} \times k_B$ is shown for different species. Each data point is averaged over 10000 repetitions. Panel A in figure 4.4 is dedicated to alkali metals, while panel B represents MC calculations for alkaline earth metals. The first thing that stands out from these two graphs is that for all the considered species, increasing the initial energy of the ion above a certain $E_{ion} \approx 1000 \text{ K} \times k_B$ does not increase the average cooling time. This energy dependency is, of course, in clear contrast with sympathetic cooling in which the average cooling time is expected to be directly proportional to the amount of the energy that needs to be dissipated, as shown for the case of Rubidium in figure 4.2 (the maroon dashed line). Increasing the initial energy makes the swap cooling the ever dominating cooling channel, which makes the overall cooling progressively more efficient. Another interesting feature is that for all the species and the entire range of E_{ion} considered here, the variation in the average cooling time remains within one order of magnitude.

In order to have a more quantitative understanding of the role that swap cooling plays in the overall collisional cooling of the ion, the percentage of the initial energy E_{ion} that is dissipated via swap cooling $E_{Diss,Swap}$, is directly calculated in the same manner already explained for the case of Rb^+ ion. Figure 4.5 shows the $E_{Diss,Swap}$ for both alkali metals (panel A) and alkaline earth metals (panel B).¹ Evidently, swap cooling plays a more prominent role by increasing E_{ion} , a fact which holds true quite universally regardless of the species under study. When the ion's initial energy

¹Sympathetic cooling will account for the rest of collisional cooling in Fig. 4.5 which is not shown for being trivial. Concretely, the percentage of E_{ion} that is dissipated via elastic collisions is $E_{Diss,Elastic} = 100 - E_{Diss,Swap}$.

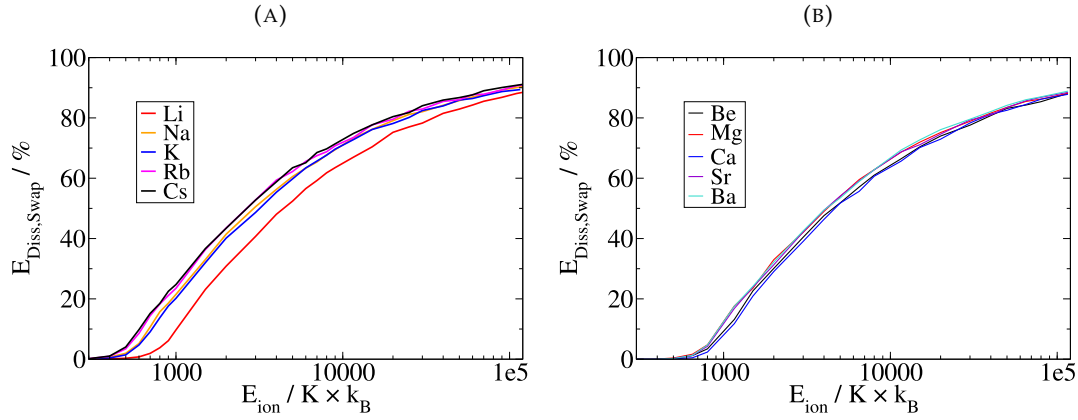


FIGURE 4.5: The percentage of the initial energy of the ion that is dissipated via the swap cooling process in homo-nuclear atom-ion collisions for A) Alkali metals, and B) Alkaline earth metals. The ion is assumed to be a free particle interacting with its parent neutral particles, taken to be at rest with a uniform density distribution of $n(x, y, z) = 1.3 \times 10^{12} \text{ cm}^{-3}$. It can be seen that the relative efficiency of the swap cooling process is virtually the same for all the studied elements.

reaches 10 eV, about 90 percent of the energy is lost by virtue of swap cooling. Moreover, it can be seen that all the species studied here, demonstrate similar behaviour with regard to the significance of swap cooling. It was also discussed in the previous section that the spatial configuration and density distribution of the atoms and ions contribute minimally to the relative efficiency of the swap cooling process. Therefore, it seems reasonable to conclude that the percentage of the energy that is dissipated via the swap cooling process in homonuclear atom-ion collisions is determined mainly by the initial kinetic energy of the ion. Another aspect that is worth noticing in figure 4.5 is that for E_{ion} up to several hundreds $K \times k_B$, swap cooling is practically negligible, and the cooling dynamics are described with sympathetic cooling. This is consistent with the aforementioned results of figure 4.4 in which, for very low initial energies of the ion, the average cooling time is an increasing function of E_{ion} . Further increase of the ion's initial energy results in the progressive dominance of swap cooling in collisional dynamics, which in turn leads to considerable modification of the average cooling time.

Perhaps the most striking feature of the swap cooling process is that it can bring about a cold ion in a single collision. Therefore, it is useful to look at the number of times that swap cooling happens during the atom-ion interaction. Figure 4.6 shows the said quantity for both alkali and alkaline earth metals. Of course, swap cooling can only happen in district occasions and the fractional number for swap cooling in the graph should be understood in the statistical sense. The MC simulation for each data point is repeated 10000 times and in each run the number of swap cooling collisions is counted which could be zero or an integer number. Shown is then the number of times that swap cooling happens averaged over the total number

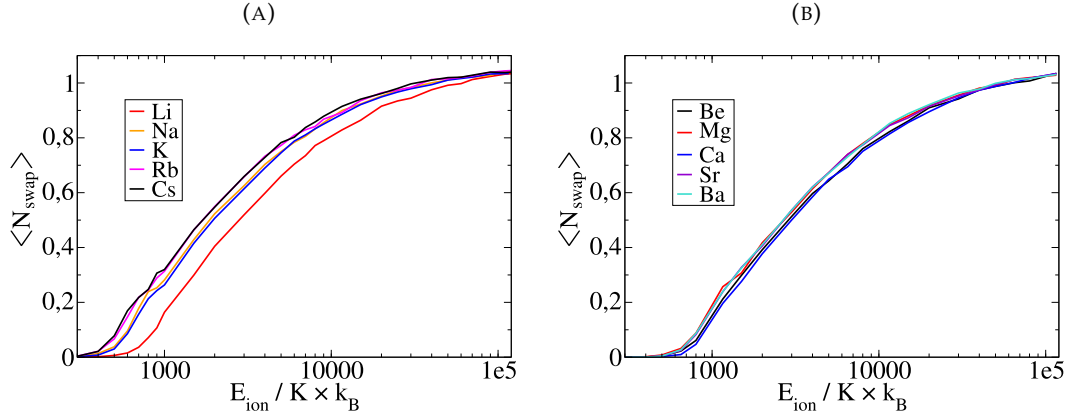


FIGURE 4.6: The statistical average of the number of times that a swap cooling collision happens. The atom-ion interaction time is as long as needed to cool down the ion below $10\text{mK} \times k_B$. A) Alkali metals, and B) Alkaline earth metals. The ion is assumed to be a free particle interacting with its parent neutral particles, taken to be at rest with a uniform density distribution of $n(x, y, z) = 1.3 \times 10^{12} \text{ cm}^{-3}$.

of repetitions. It is interesting to note that there is almost a one to one correspondence between figures 4.6 and 4.5 meaning that probability of having one swap cooling collision predicts the percentage of the energy that is dissipated via swap cooling in a statistical averaged sense. Another curiosity is that for very high initial energies in figure 4.6, the number of swap cooling collisions can slightly exceed 1 which is contrary to the expectation of having a cold ion after one swap cooling collision. This happens because in the MC simulation any resonant charge exchange collision with an impact parameter greater than b_c is counted as a swap cooling collision. If such a collision happens with an impact parameter close to b_c there is a chance that the ion is hot enough to undergo another swap cooling collision during the interaction time.

So far, I have focused on the swap cooling process and its role in the collisional cooling in homo-nuclear atom-ion collisions. A complete picture of collisional cooling, however, has to also take into account elastic collisions. The average number of elastic collisions² during the interaction time as a function of E_{ion} is provided in the top panels of figure 4.7 for the same species as before, while the bottom panels show the average number of Langevin collisions. Fig. 4.7 once again shows that there is an initial phase in which increasing the amount of energy that needs to be dissipated via collisions requires a higher number of elastic (Langevin) collisions, which is an intuitive outcome of the simulation. However, further increase of the initial energy after $E_{\text{ion}} \approx 1000 \text{ K} \times k_B$ will lead to fewer elastic (Langevin) collisions during the interaction time. This is inline with the previous explanations of collision dynamics in such systems. As mentioned before, the atom-ion interaction time is not fixed during the MC calculations and the simulation runs until the ion is colder than $10 \text{ mK} \times k_B$. As swap cooling prevails the collisional cooling by increasing E_{ion} , the interaction

²Here, elastic collisions are defined according to section 2.4.1, with the finite cross section given in equation 2.18.

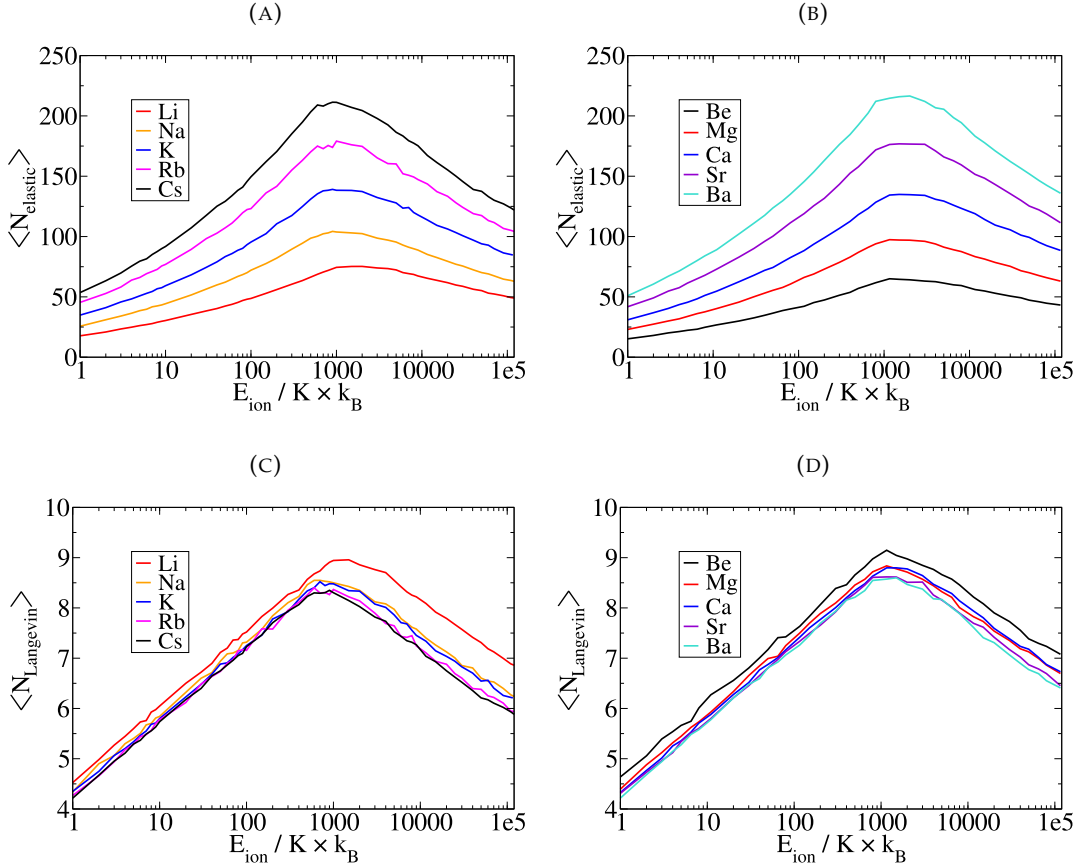


FIGURE 4.7: The statistical average of the number of times that an elastic collision happens during the atom-ion interaction time which is hold long enough to completely cool down the ion. A) Alkali metals, and B) Alkaline earth metals. The ion is assumed to be a free particle interacting with its parent neutral particles taken to be at rest with a uniform density distribution of $n(x, y, z) = 1.3 \times 10^{12} \text{ cm}^{-3}$. For energies above $E_{ion} \approx 1000 K \times k_B$ the number of collisions decreases by increasing E_{ion} which is an indication of the dominance of the swap cooling process (see the text).

time T and, consequently, the number of elastic (Langevin) collisions decreases. In other words, figure 4.7 can be best understood in tandem with figure 4.4.

As already discussed, $E_{Diss,Swap}$ does not strongly depend on the specific element under consideration. This in turn means that the performance of collisional cooling via elastic collisions in homo-nuclear atom ion systems should manifest the same universality regarding different species. However, there is a clear distinction between the number of elastic collisions of different species in figure 4.7. This is not surprising, as most of the elastic collisions are glancing collisions that contribute minimally to the collisional cooling. The number of Langevin collisions, on the other hand, show the same universality as swap cooling under changing the element. In Langevin collisions, the ion scatters with a uniformly distributed scattering angle in the centre of mass (COM) reference frame. According to the equation 3.2 the energy transfer from the ion to the cold atom with the same mass in the COM frame is equal to

$E_{trans} = E_{ion} \sin^2(\theta/2)$ in which E_{ion} is the initial kinetic energy of the ion. Since the average of the \sin^2 function is equal to $1/2$ the ion's energy after l Langevin collisions would be approximately $1/2^l$ of its initial energy. This indicates the importance of Langevin collisions in the cooling process.

4.5 Concluding remarks

After the experimental demonstration of swap cooling for a Rb^+ ion interacting with parent neutral Rb atoms in [MKD21], the numerical MC calculations are used to expand the scope of the study of swap cooling to other species. The obtained results denote that not only swap cooling can happen in other homo-nuclear atom-ion collisions, but also its properties are quite universal among different species.

While the overall collisional cooling of a highly energetic ion immersed in ultracold atoms strongly depends on the geometry of the problem, namely the density distribution of the atom cloud and the trapping frequency of the ion, the relative efficiency of swap cooling seems to be rather insensitive to such parameters and is almost solely determined by the initial energy of the ion.

As already shown in the case study of Rubidium, the swap cooling contribution to overall collisional cooling progressively grows by increasing the ion's initial energy. Virtually regardless of the specific element under consideration, swap cooling starts to take part in the cooling process for E_{ion} about several hundred $\text{K} \times k_B$. This estimation was justified in chapter 3 by looking at the energy dependency of the critical impact parameter. Moreover, swap cooling starts to play a more prominent role for initial energies above $E_{ion} = 1000 \text{ K} \times k_B$.

Due to swap cooling, the average cooling time of a hot ion immersed into an ultracold cloud of its parent neutral particles does not show a strong dependency on the E_{ion} and can even decrease for higher energies. This can be understood by taking into account that, contrary to all other relevant types of collision, the swap cooling cross section is an increasing function of E_{ion} (for the energy range studied here).

For alkali and alkaline earth metals studied here, the amount of energy dissipated via the swap cooling channel and the average number of swap cooling collisions seem to be rather insensitive to the specific elements being used.

While the glancing collisions' contribution in dissipating the ion's energy is mainly in terms of swap cooling, Langevin collisions play a considerable role in collisional cooling regardless of the occurrence of the resonant charge exchange.

Chapter 5

Controlled reaction of a Ba^+ ion interacting with Rb atoms

5.1 Introduction

A long-standing goal in chemical physics is to understand and eventually control how reactants become products. In a reactive process, having complete control over all quantum mechanical degrees of freedom, should that be possible, allows for the discovery of the relevant interaction processes and the steering of chemical reactions. However, in heteronuclear systems, the problem of studying collision dynamics is often perplexed due to numerous potential reaction channels. Therefore, to limit the manifold of collision pathways in our atom-ion experiment, we study the interactions of neutral atoms in their electronic ground state at ultracold temperatures with single ions. Moreover, in this chapter, I will discuss and experimentally investigate how the combined spin-state of colliding particles affects the cross section of reactive processes and how preparing the reactants in specific quantum states can suppress certain reaction channels. Therefore, in addition to obtaining a feasible way to control reactive collisions, it will also be possible to examine the accuracy of certain theoretical assumptions about the reactive processes in our system and study chemical reactions at the most elementary level.

It's also worth noting that at cold and ultracold temperatures, the energy scale involved in exoergic reactions could be immense. For example, if the reaction exoergicity is on the order of an electron volt ($\sim 10^4 \text{ K} \times k_B$) and the relative collision energy of the reactants is in the mK range, the products separate with an energy that is up to 9 – 10 orders of magnitude greater than their initial kinetic energy. The substantial difference in kinetic energy between products and reactants makes detecting reaction products and studying their quantum states problematic in the experiments designed for neutral particles. However, owing to the very deep trapping potentials of our RF ion trap, it is possible to detect the ionic products after reactive collisions and get an insight into the collision dynamics accordingly.

5.2 Theoretical considerations

We study the interaction of single laser-cooled $^{138}Ba^+$ ions with ultracold Rb atoms while both species are initially in their electronic ground states. Figure 5.1 shows the relevant potential energy curves for the system. Since the ionization energy of Ba is higher than that of Rb, the entrance channel in our experiments, which is marked by a dotted line at the zero level of potential energy in Fig. 5.1, is not the absolute ground state of the system. Moreover, depending on the initial quantum state of

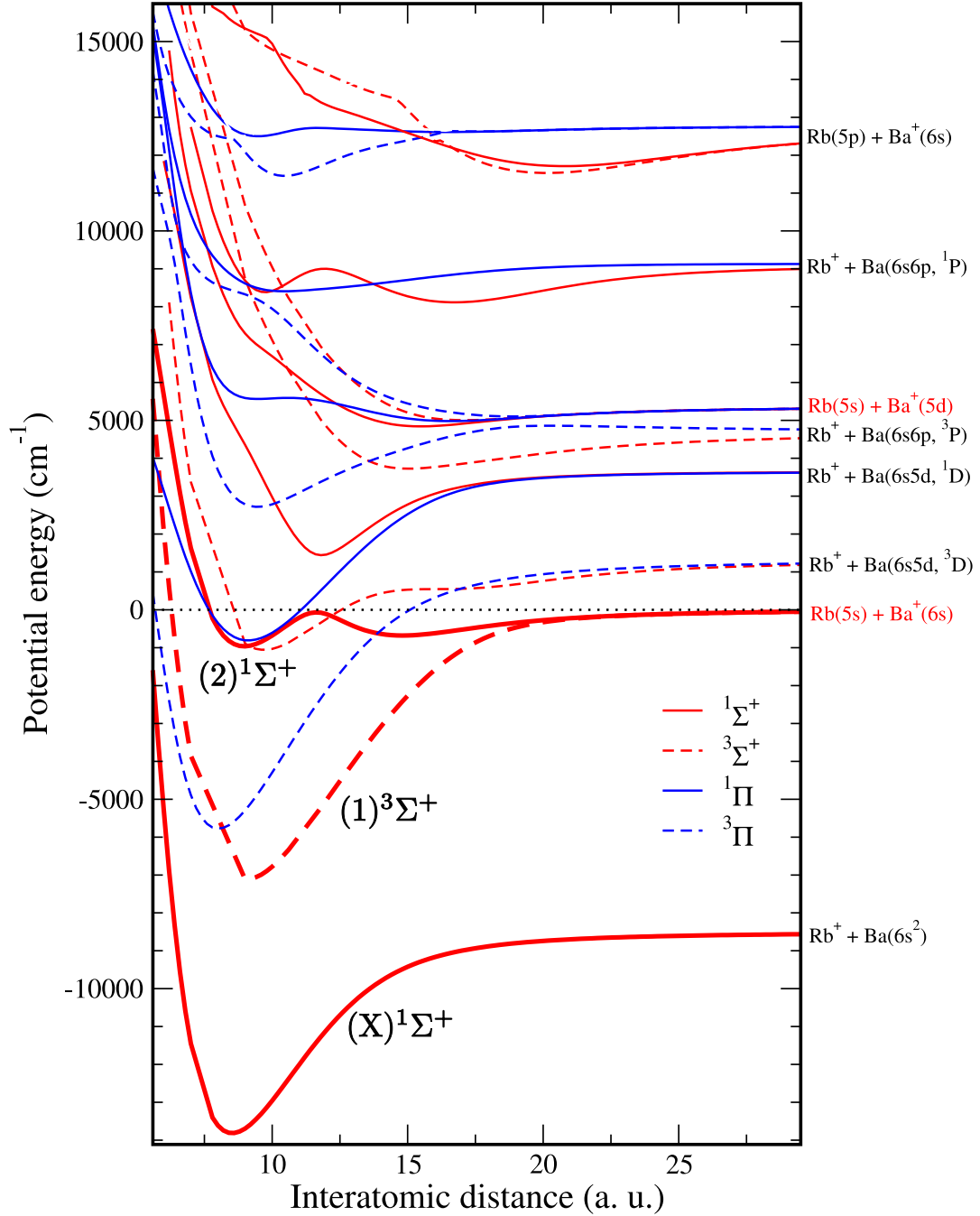


FIGURE 5.1: Potential energy curves for $BaRb^+$. Data taken from [Hal+13b]

the colliding partners, the scattering can take place via either of the singlet $(2)^1\Sigma^+$ or triplet $(1)^3\Sigma^+$ curves. Each of these channels will enable a variety of secondary inelastic and reactive processes, some of which are outlined below. As is shown in Figure 5.1 the $(2)^1\Sigma^+$ is not the electronic ground state which opens up the possibility of radiative charge transfer (RCT) and radiative association (RA) for the $(2)^1\Sigma^+$ entrance channel. In RCT, the collision complex emits a photon and decays to one of the continuum states of the electronic ground state $(X)^1\Sigma^+$ which asymptotically corresponds to the charge exchanged state. In RA, the collision complex relaxes to one of the molecular bound states of the $(X)^1\Sigma^+$ by emitting a photon (see also section 2.5.1). As long as the spin selection rules hold, RCT and RA are forbidden for the $(1)^3\Sigma^+$ entrance channel. Moreover, if a molecular ion is formed after a three-body-recombination in the $(2)^1\Sigma^+$ state, it can undergo radiative relaxation to the electronic ground state $(X)^1\Sigma^+$. Furthermore, the potential photoexcitation channel for the BaRb^+ complex via the 1064 nm laser light (which is used as the optical dipole trap for the Rb atoms) depends on the electronic state of the complex. Therefore, suppressing the singlet $(2)^1\Sigma^+$ entrance scattering channel would substantially limit the available decay channels and secondary processes, which could be used as a means to control the dynamics of the system. In the following section, I discuss the experimental realization of this goal.

5.3 Experiments and results

We have already investigated the reactive collisions between a $^{138}\text{Ba}^+$ ion prepared in an incoherent mix of its two spin ground states and an ultracold cloud of spin-polarized ^{87}Rb atoms, prepared in the hyperfine state $|F = 1, m_F = -1\rangle_{\text{Rb}}$ of the electronic ground state [Krü+16b; Moh+21]. It was shown in [Krü+16b] that the main decay channel in our experiments is three-body-recombination (TBR), and it was hypothesized that the outcome of such reactive process is the formation of a BaRb^+ molecular ion. Due to the (mentioned) initial quantum state of the reactants, a reactive collision allows for the formation of a BaRb^+ molecular ion in both the singlet $(2)^1\Sigma^+$ and triplet $(1)^3\Sigma^+$ states in those experiments.

In order to suppress scattering along the singlet $(2)^1\Sigma^+$ potential curve, I performed measurements by preparing the ultracold Rb atoms in the spin stretched $|F = 2, m_F = 2\rangle_{\text{Rb}}$ state. The Ba^+ ion can also be prepared in one of the Zeeman sublevels of $6s^2S_{1/2}$ state, either parallel $|^2S_{1/2}, m_j = 1/2\rangle_{\text{Ba}^+} = |\uparrow\rangle_{\text{Ba}^+}$ or antiparallel $|^2S_{1/2}, m_j = -1/2\rangle_{\text{Ba}^+} = |\downarrow\rangle_{\text{Ba}^+}$ to the magnetic field. This is done via optical pumping by using a σ^+ (σ^-)-polarized light along the direction of the magnetic field. As long as the total spin quantum number of the system is conserved, if the spin of the ion is aligned with the spin of the atoms prepared in the $|F = 2, m_F = 2\rangle_{\text{Rb}}$ state, i.e. for $|\uparrow\rangle_{\text{Ba}^+}$, only the triplet potential contributes to the collision dynamics. Preparing the ion in the $|\downarrow\rangle_{\text{Ba}^+}$ spin state will allow for spin exchange collisions, which will ultimately polarize the ion's spin parallel to the spins of the atomic bath.

Spin exchange collisions between an ion and ultracold atoms have been studied in similar atom-ion experiments, and the rate of such collisions is reported to scale with Langevin collision rate [Sik+18b; Für+18]. Since the objective of the current study is to investigate reactive processes by suppressing some of the available channels, the measurements presented in the following are performed with the spin of the ion initially prepared parallel to the polarized atoms to avoid spin-exchange collisions. I note, however, that in complementary measurements (presented later on in this chapter), I have not observed any significant difference in the reaction rates due to the initial spin state of the ion.

Asymptotically, the atom-ion interaction is dominantly determined by the attractive polarization potential of the form [VW54] $V(r) = -C_4/(2r^4)$, where $C_4 = \alpha q^2 / (4\pi\epsilon_0)^2$ is proportional to the static dipole polarizability of the atom α , and q is the electron charge. In the classical picture, the polarization potential characterizes the total two-body (three-body) collision rate, which is thus the same for Rb atoms in their ground state regardless of their total atomic angular momentum (F) quantum number. It is often assumed that in heteronuclear atom-ion systems, for any reactive process to take place, collisions with energies above the centrifugal barrier, i.e., Langevin collisions, are required (see section 2.6). The rate of Langevin collisions is energy-independent and is given by $\gamma_L = 2\pi\sqrt{C_4/\mu}n$, where μ is the reduced mass and n is the density of the neutral atomic cloud. In our experiments we have $\gamma_L/n = 2.19 \times 10^{-9} \text{cm}^3/\text{s}$, and we work with typical densities of $n = 10^{12} \text{cm}^{-3}$. The reactive collision in our experiments for Rb atoms prepared in the $|F = 1, m_F = -1\rangle_{Rb}$ state are measured [Krü+16b] to be dominated by three-body-recombination with a rate coefficient of $k_3 = 1.04 \times 10^{24} \text{cm}^6\text{s}^{-1}$.

In [Krü+16a], the quasi-classical trajectory (QCT) calculations have been used to explain the obtained reactive collision rates in our experiments for Rb atoms in the $|F = 1, m_F = -1\rangle_{Rb}$ state. The classical treatment was justified since the involved collision energies ($\sim \text{mK} \times k_B$ or above) are way beyond the threshold energy of $\sim 50 \text{nK} \times k_B$ for entering the s-wave regime of $Ba^+ - \text{Rb}$. The QCT calculations use the classical equation of motion and Monte Carlo sampling to determine the TBR rate as a function of collision energy. Any trajectory that leads to the formation of a dimer after TBR with negative binding energy is considered a recombination event [PRG15]. The short-range part of the interaction potential contributes minimally to the calculated TBR rate, and the long-range part is the same for both singlet and triplet potentials in the same entrance channel. Therefore, insofar as the QCT calculations can be trusted to describe our system, there should be no difference in the TBR rate for triplet and singlet potentials. I note, however, that these calculations cannot predict resonance features should they occur [Ber79].

To summarize all the above discussion, the expectation is to have the same decay rate of the Ba^+ ion when working with $|F = 2, m_F = 2\rangle_{Rb}$ atoms but with a different population distribution of the final products after the atom-ion interaction. To investigate this hypothesis, I performed two sets of measurements where all the

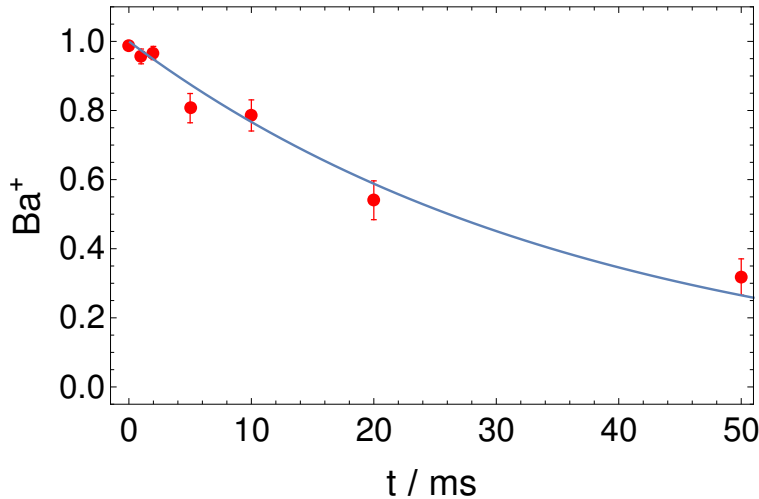


FIGURE 5.2: Detection probability of a spin polarized Ba^+ ion after the interaction with an ultracold cloud of Rb atoms in the $|F = 1, m_F = -1\rangle_{\text{Rb}}$ state with a peak density of $5 \times 10^{12} \text{ cm}^{-3}$. The solid line is an exponential fit to the data.

experimental parameters are the same except for the $|F, m_F\rangle_{\text{Rb}}$ quantum number of the Rb atoms. Figure 5.2 shows the probability of detecting a cold Ba^+ ion after a varied interaction time with an atomic cloud of ^{87}Rb atoms in the $|F = 1, m_F = -1\rangle_{\text{Rb}}$ electronic ground state. The cloud consists of $N=1.6 \times 10^5$ atoms with a peak density of $n = 5 \times 10^{12} \text{ cm}^{-3}$. The blue solid line is a simple exponential decay fit to the data. These measurements reproduce the previously reported decay rate in [Krü+16b] and match our expectations. We use fluorescence imaging of the ion to determine whether there is a cold (below $\sim 1\text{K} \times k_B$) Ba^+ in the Paul trap after the interaction. These ions are considered to have not been reacted since such processes in our system are typically highly exothermic and could also involve a charge transfer which leads to other ionic species rather than a Ba^+ ion. Numerical simulations using QCT predict that the initial reaction product after a three-body-recombination is a weakly bound BaRb^+ molecular ion [Krü+16a; Moh+21; PRG15]. I, therefore, note that if such molecules are dissociated before going through secondary inelastic or reactive collisions, we will not be able to distinguish them from an ion that has not undergone a reaction.

We now look at the decay probability of a spin polarized Ba^+ ion under the same experimental conditions except for the fact that Rb atoms are prepared in the $|F = 2, m_F = 2\rangle_{\text{Rb}}$ quantum state. Figure 5.3 shows the probability of detecting a cold Ba^+ ion after a variable interaction time in such a system. It can be seen that even increasing the interaction time by more than one order of magnitude is not sufficient for the ion to reach the same reaction probabilities as for the $|F = 1, m_F = -1\rangle_{\text{Rb}}$ measurements. The inset of Figure 5.3 shows a zoom of the shorter times corresponding to Figure 5.2 in order to allow for a direct comparison. After 50 ms the ion has more than 50% chance to react away when interacting with $|F = 1, m_F = -1\rangle_{\text{Rb}}$ atoms while the decay of the Ba^+ ion immersed in a cloud of ultracold Rb atoms in the $|F = 2, m_F = 2\rangle_{\text{Rb}}$ state is almost completely suppressed. Since these results are very

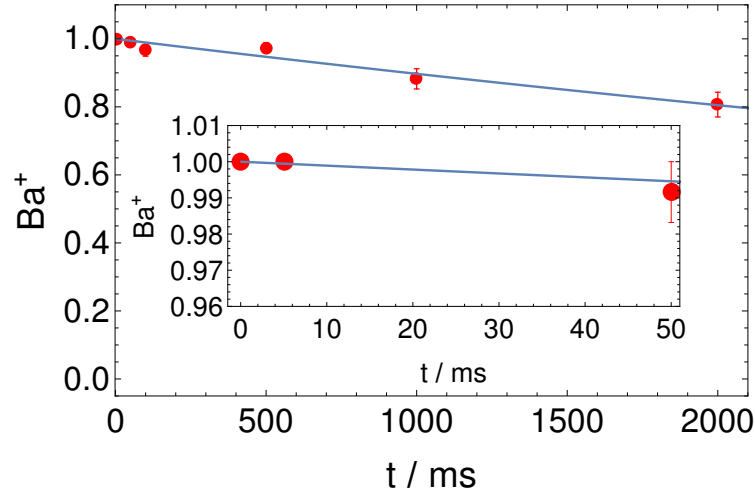


FIGURE 5.3: Probability of detecting a cold Ba^+ ion after the interaction with an ultracold cloud of Rb atoms in the $|F = 2, m_F = 2\rangle_{Rb}$ state with a peak density of $5 \times 10^{12} \text{ cm}^{-3}$. The solid line is an exponential fit to the data. The inset is a zoom of the data at shorter times corresponding to Fig. 5.2

intriguing, I have performed similar measurements for different configurations of the atom cloud, and they all confirm the very low decay rate of the Ba^+ ion while interacting with the Rb atoms in the $|F = 2, m_F = 2\rangle_{Rb}$ state. Figure 5.4, for instance, compares the reaction probability of the ion when immersed into a cloud of Rb atoms with a peak density of $n = 1.2 \times 10^{13} \text{ cm}^{-3}$ prepared in the two different quantum states.

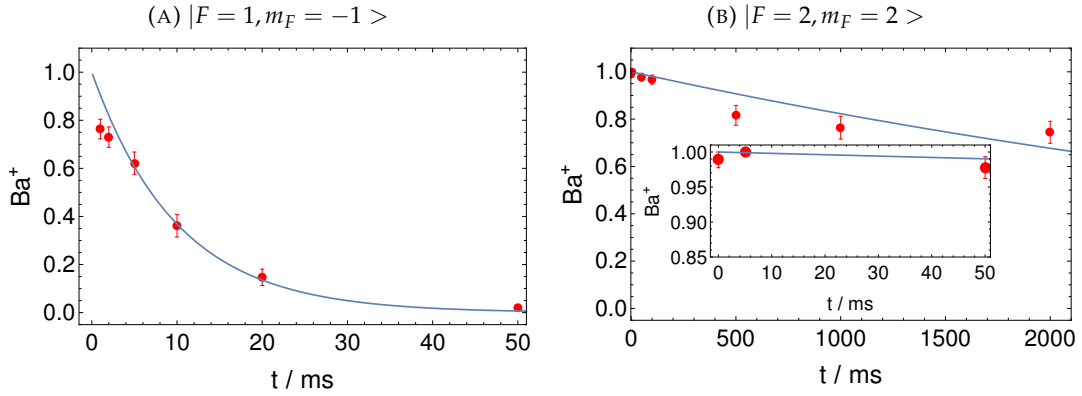


FIGURE 5.4: Probability of detecting a cold Ba^+ ion after the interaction with an ultracold cloud of Rb atoms with a peak density of $n = 1.2 \times 10^{13} \text{ cm}^{-3}$. A) The Rb atoms are prepared in the $|F = 1, m_F = -1\rangle_{Rb}$ state, and B) in the $|F = 2, m_F = 2\rangle_{Rb}$ state. The inset shows a zoom of shorter time scales corresponding to Fig 5.4a.

As previously stated, the distinct difference between the reaction rate of an ion via singlet or triplet channels was not anticipated in our measurements, and there are no other atom-ion experimental studies on this topic involving three-body reactive collisions. However, similar observations have been reported in two other atom-ion

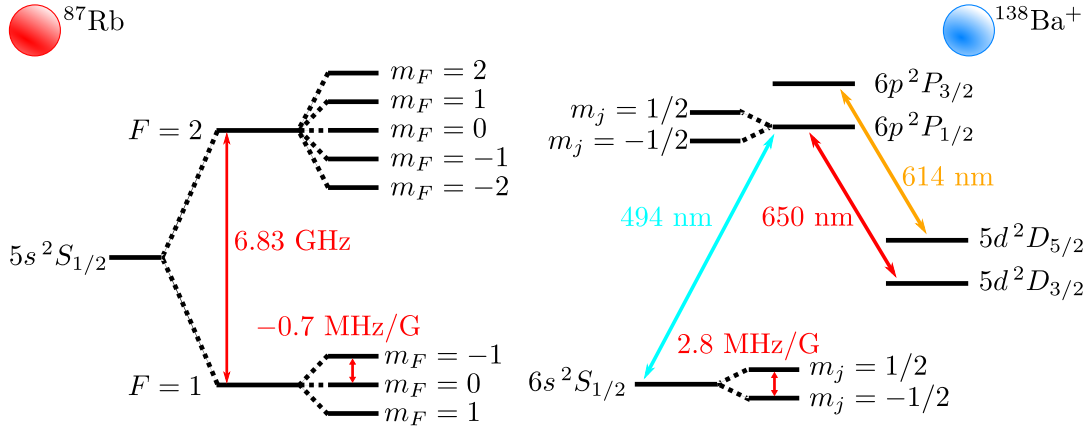


FIGURE 5.5: Energy level diagrams of $^{138}\text{Ba}^+$ ion [Cur04] and ^{87}Rb [Biz+99]. Shown are the hyperfine structure of the electronic ground state of Rb and the relevant electronic structure of the Ba^+ ion. The relevant Zeeman-splitting of both systems are also illustrated.

experiments in which reactive processes are dominantly two-body. In [Rat+12] the reaction rate of an Yb^+ ion prepared in its electronic ground state with Rb atoms in the $|F = 2, m_F = 2\rangle_{\text{Rb}}$ state was found to be 35 times smaller than reaction rate with atoms in the $|F = 1, m_F = 1\rangle_{\text{Rb}}$ state, and the observed suppression was broadly attributed to the difference in hyperfine interaction. In [Sik+18b] Rb-Sr $^+$ mixture was used to study chemical reactions. They observed charge-exchange reactions every $\sim 5 \times 10^4$ Langevin collisions when Rb was prepared in the $F = 1$ hyperfine level, and did not observe charge-exchange reactions when it was initialized in $F = 2$ level. The charge exchange reactions in [Sik+18b] are expected to happen radiatively. Therefore, the mentioned suppression of charge exchange is not surprising, as radiation can couple the charged-exchanged ground state to the singlet entrance channel and not to the triplet potential relevant for $F=2$ atoms. It was also suggested in [Sik+18b] that the suppression of charge exchange would be due to the increase in the steady-state temperature of the ion when Rb is initialized in $F=2$ and the hyperfine energy is occasionally released in a spin-relaxing collision. Since the latter point is also relevant for my experiments, I explore it in more details in the following.

The hyperfine level structure of the Rb atom in its electronic ground state is shown in figure 5.5. A collision-induced transition from the $F=2$ hyperfine level to the $F=1$ manifold will release the $E_a^H = h \times 6.83 \text{ GHz} \approx 326 \text{ mK} \times k_B$ energy gap, which will be distributed between the colliding partners. Let's denote the probability that a Langevin collision will lead to such a spin relaxation with the proportionality coefficient η , where $0 < \eta < 1$. Using energy and momentum conservation, it is straightforward to calculate the average kinetic energy intake by the ion per Langevin collision due to the hyperfine transition of the atom to be $\delta E_{\text{heat}} = \eta E_a^H \frac{m_a}{m_a + m_i}$. Here, m_a and m_i represent the mass of the atom and the ion, respectively. One can also show that for an ion with the kinetic energy E_{ion} prior to the collision, the average energy loss per Langevin collision is $\delta E_{\text{cool}} = \frac{-2m_a m_i}{(m_a + m_i)^2} E_{\text{ion}}$. Solving the resulting rate equation, one obtains the steady-state kinetic energy of the ion $\langle E_{\text{ion}} \rangle = \eta E_a^H \frac{m_a + m_i}{2m_i}$,

which corresponds to the average collision energy of $\langle E_{col} \rangle = \frac{m_a}{m_a+m_i} \langle E_{ion} \rangle$. In our case of a Ba^+ ion interacting with Rb atoms, we have $\langle E_{Ba^+} \rangle = \eta 265 \text{ mK} \times k_B$, and $\langle E_{col} \rangle = \eta 102 \text{ mK} \times k_B$.

The energy-dependency of reactive collisions in our experiments when Rb atoms are prepared in the $|F = 1, m_F = -1\rangle_{Rb}$ state has been independently studied [Krü+16a] using excess micromotion to tune the collision energy. It was found, empirically, that the three-body-recombination rate coefficient k_3 scales with the collision energy as $k_3 \sim E_{col}^{-0.46}$. To find an upper-limit for the suppression of reactive collisions due to additional heating via hyperfine energy release, one puts $\eta = 1$ which gives an upper limit for collision energy of $\sim 100 \text{ mK} \times k_B$. Using the said power law scaling, this collision energy, compared to the 1 mK collision energy typically used in our measurements with atoms in the $|F = 1, m_F = -1\rangle_{Rb}$ state, suppresses the reaction rate by a factor of 8. Although this effect is significant and has to be taken into account, it cannot fully explain the obtained suppression when working with the $|F = 2, m_F = 2\rangle_{Rb}$ atoms, since even increasing the interaction time by a factor of 10 is not nearly enough to get the same reaction rate as with $|F = 1, m_F = -1\rangle_{Rb}$. Moreover, it should be emphasized that spin relaxation can only happen via spin-nonconserving collisions, for example due to second-order spin-orbit interaction. Therefore, the estimated value for suppression due to an increase in collision energy via hyperfine transition using $\eta = 1$ should be considered a conservative upper limit.

Another consideration while explaining the observed low production rate of hot Ba^+ ions in my experiments with atoms in the $|F = 2, m_F = 2\rangle_{Rb}$ state is the following. It has been suggested that the electric field can dissociate very weakly bound molecular ions after their formation [Die+20]. If a three-body-recombination results in a weakly bound molecular ion which is dissociated via electric field before photo-dissociation, it will produce a relatively cold Ba^+ ion which will not be detected as a reacted ion by our scheme. I note, however, there is no reason to think that this phenomenon should happen at much larger rate for triplet molecules compared to singlet ones.

It is also possible that the initial reactive process in our atom-ion experiments when the atoms are prepared in the $|F = 1, m_F = -1\rangle_{Rb}$ state is due to the photoexcitation of a three-body complex into a bound or continuum excited state. Such an excited three-body complex can result in an excited molecular ion and a neutral atom, or a neutral molecule and an ion in the electronic excited or ground state. Of course, such possibilities are more involved to be considered theoretically, and numerical calculations for this problem might not be feasible at the current accessible computational powers.

Finally, it is certainly conceivable that the reaction dynamics of a spin polarized Ba^+ ion interacting with ultracold Rb atoms with $|F = 2, m_F = 2\rangle_{Rb}$ cannot be simply explained in a classical picture and will await quantum mechanical calculations. An exemplary quantum mechanical effect that could explain the sizable difference between the reaction rates via triplet or singlet potentials is Fano-Feshbach resonances.

Although the collision energies in our experiments are too high to discern Feshbach resonances, they can still influence overall reaction rates. The result of such resonances is the formation of meta-stable bound states, which could enhance the probability of photoexcitation of the collision complex via the available 1064 nm laser light. Feshbach resonances and the likelihood of photoexcitation of meta-stable states are both substantially influenced by the details of the short-range part of the potentials and thus can result in different reaction rates for triplet and singlet potentials. One way to test this hypothesis is to perform spectroscopy by using a laser beam that selectively couples the singlet (triplet) entrance channel to a repulsive excited state which is associated with the charge-exchanged asymptote (or the $5d^2D_{5/2}$ state of Ba^+ ion, see the next section). Finding resonance-enhanced transitions may allow for deterministic evaluation of the three-body recombination rates and probing of the meta-stable states before other secondary processes (see [Moh+21] for a discussion on such processes) have a chance to take place. I have performed measurements in which the ion was exposed to 614 nm and 650 nm laser light during the atom-ion interaction. My preliminary results showed that the exposure of the mentioned lasers does affect the reaction rates. However, complete spectroscopy with a dedicated laser wavelength was not possible at the time and remains to be investigated.

Before concluding this section and for the sake of completeness, the comparison between reaction probability of the Ba^+ ion when initially prepared parallel $|\uparrow\rangle_{\text{Ba}^+}$ or antiparallel $|\downarrow\rangle_{\text{Ba}^+}$ to the direction of the magnetic field is shown in figure 5.6. In both measurements, the atoms are prepared in the $|F = 2, m_F = 2\rangle_{\text{Rb}}$ state with a peak density of $n = 5 \times 10^{12} \text{ cm}^{-3}$. As it can be seen, the initial spin state of the ion does not have a sizable impact on the decay probability, which is inline with the aforementioned discussion. When the Ba^+ ion in the $|\downarrow\rangle_{\text{Ba}^+}$ state is immersed in the spin-polarized cloud of Rb atoms, two-body spin-exchange collisions can align the spin of the ion with that of the atoms. The timescale for such phenomena is determined by the Langevin collision rate, which for the said density of the atom cloud will be $\sim 10^4 \text{ s}^{-1}$. Since collision-induced spin polarization of the ion happens way faster than any reactive collisions, no difference in the decay rate of the ion due to its initial spin state is expected.

5.3.1 Reaction products

Analysing the ionic reaction products is a tool we can employ in our experiments to get insight into collision dynamics. After the atom-ion interaction and determining whether the Ba^+ ion has reacted, we perform an extensive laser cooling stage for 3 seconds to retrieve hot Ba^+ ions. This is done by red detuning the frequency of the 493 nm laser light used for laser cooling of the ion by 2.5 GHz and ramping it back to its original value. We have checked independently that this process can cool down any ground state hot Ba^+ ion in our Paul trap. Moreover, we can determine the percentage of the Ba^+ ions that as a result of the reactive processes end up in the metastable $5d^2D_{5/2}$ state after the interaction. The electronic level structure of the Ba^+

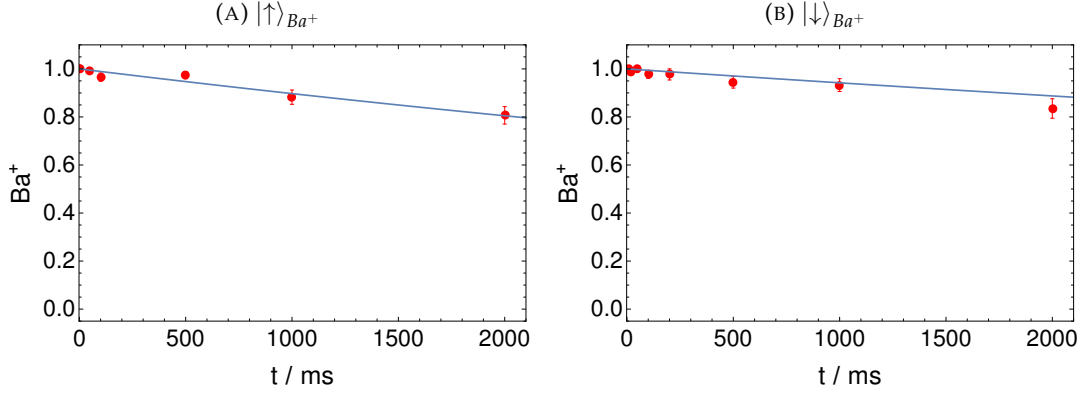


FIGURE 5.6: Probability of detecting a cold Ba^+ ion after the interaction with an ultracold cloud of Rb atoms in the $|F = 2, m_F = 2\rangle_{Rb}$ state with a peak density of $n = 5 \times 10^{12} \text{ cm}^{-3}$. A) The ion is initially prepared in the $|\uparrow\rangle_{Ba^+}$ state, and B) in the $|\downarrow\rangle_{Ba^+}$ state.

ion is shown in figure 5.5. The $5d^2D_{5/2}$ state has a lifetime of $\tau_{5D_{5/2}} = 31.2 \text{ s}$ [Auc+14], and is not used in our laser cooling cycle. Therefore, for all practical purposes, the fraction of the ions in the $5d^2D_{5/2}$ state can be deterministically measured by means of a depumping laser at 614 nm that couples this state to the $6P^2P_{3/2}$ state. It should be noted that the exit channel in which the Ba^+ ion is in the $5d$ electronic level cannot be accessed via collision only, as the collision energy is not enough to reach the excited level of Ba^+ . Thus, the existence of such ions is clear evidence of photoexcitation of the collision complex via 1064 nm laser light during the interaction. In a typical atom-ion experiment with Ba^+ ions, after determining whether the ion has gone through a reaction by fluorescence imaging, we continue our analysis by the said extensive laser cooling followed by another imaging. If the Ba^+ ion is retrieved after the cooling stage, I call them "hot Ba^+ " ions. In the next step, the 614 nm laser is also turned on while the extensive cooling is performed. If the Ba^+ ion is retrieved after this stage, it means that it has been in the $5d^2D_{5/2}$ state, and I denote such ions by "D-state Ba^+ ".

From those ions in Fig. 5.4a that have gone through a reactive process, the percentage of hot Ba^+ ions and the ones in the $5d^2D_{5/2}$ are depicted in Figure 5.7 for measurements with Rb atoms prepared in the $|F = 1, m_F = -1\rangle_{Rb}$ state. Such analysis for measurements with the $|F = 2, m_F = 2\rangle_{Rb}$ Rb atoms, though possible in principle, would not be reasonable due to very low reaction rates and the resulting high statistical uncertainty in reaction products.

It turns out that the percentage of the final reaction products in our experiments when working with the Rb atoms in the $|F = 1, m_F = -1\rangle_{Rb}$ state are rather insensitive to different experimental parameters, including atom numbers, the density of the atom cloud, interaction time, and even the collision energy, and the obtained results are similar (within the range of the uncertainty) to the ones shown here. I also note that our current laser cooling scheme for Ba^+ ion does not allow for the detection

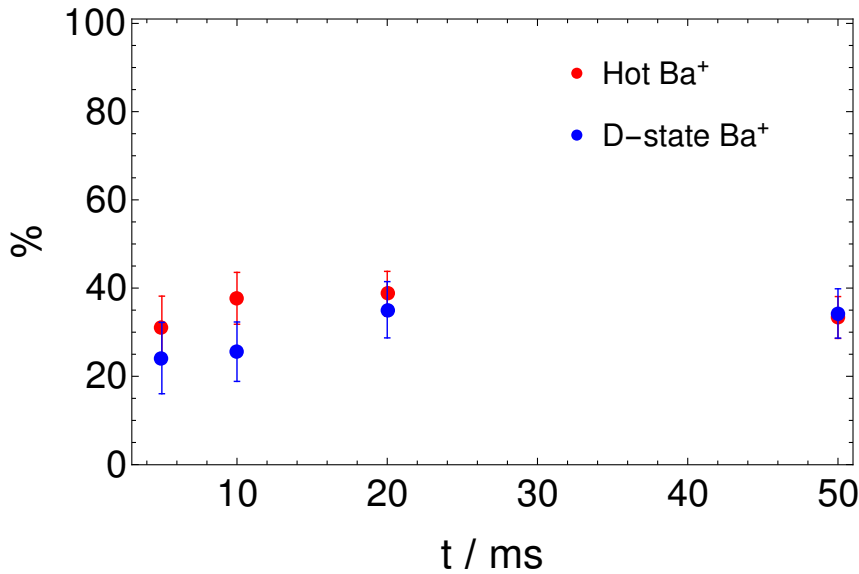


FIGURE 5.7: The percentage of hot and D-state Ba^+ ions with respect to reacted ions after the interaction with an ultracold cloud of Rb atoms with a peak density of $n = 1.2 \times 10^{13} \text{ cm}^{-3}$. The Rb atoms are prepared in the $|F = 1, m_F = -1\rangle_{\text{Rb}}$ state corresponding to Fig. 5.4a.

of the ions that end up in the $5d^2D_{3/2}$ state (see Fig. 5.5). However, by the same token that the Ba^+ in the $5d^2D_{5/2}$ is produced, the $5d^2D_{3/2}$ state can be accessed. In fact, since the percentage of the produced "hot Ba^+ " and "D-state Ba^+ " ions in our measurements are about the same (see Fig. 5.7) it is very well possible that all the retrieved Ba^+ ions in our measurements after reactive processes are populated in the $5d$ electronic level.

The suppressed reactivity of the Ba^+ ion when immersed in an ultracold cloud of Rb atoms in the $|F = 2, m_F = 2\rangle_{\text{Rb}}$ state can open up the possibility of controlled reactions with dedicated laser light, which can for example couple the collision complex in the triplet entrance channel to a repulsive excited state with the Ba^+ ion in the $5d$ state in the asymptotic limit.

In the remaining part of this section, I consider another reaction product, namely the BaRb^+ molecular ion. Using mass-selective parametric heating of the ion in the Paul trap, we can selectively remove different ionic species from the trap. After a certain interaction time, during which the ion might have experienced a reactive process, we remove all Ba^+ ions from the Paul trap by mass-filtering before shining any laser beam into the ion trap. We then perform the extensive laser cooling followed by fluorescence imaging. Since all the Ba^+ ions have been previously removed from the trap, any detected Ba^+ ion can only be produced via the photodissociation of BaRb^+ molecular ions by means of the cooling lasers. Figure 5.8 shows the results of such experiments when Rb atoms are prepared in the $|F = 2, m_F = 2\rangle_{\text{Rb}}$ state. The presented probabilities of detecting a Ba^+ ion in this plot should be interpreted in accordance with Figure 5.3 where the decay rate of the ion is depicted. For very short interaction times below 50 ms, shown in the inset of both graphs, the ion has virtually

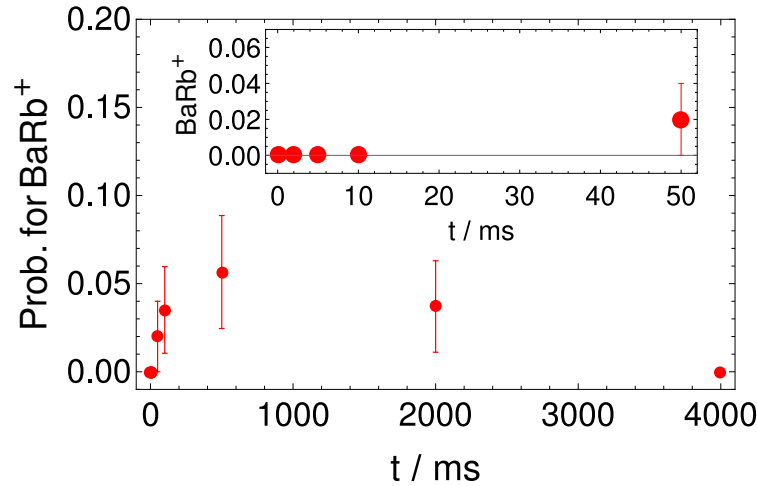


FIGURE 5.8: The probability of detecting a Ba^+ ion resulting from photodissociation of $BaRb^+$ molecular ions after removing all Ba^+ ions via mass filtering after the interaction. The atom cloud consists of ultracold Rb atoms in the $|F = 2, m_F = 2\rangle_{Rb}$ state with a peak density of $n = 5 \times 10^{12} \text{ cm}^{-3}$. The inset shows a zoom of shorter times.

no chance to react away and therefore there is no signal of Ba^+ ion coming from the photodissociation of the molecular ion. As time progresses, the reaction probability of the ion increases and so does the probability of having a $BaRb^+$ molecular ion after the interaction, up until about half a second. For longer times although the decay probability of the ion increases, the number of surviving $BaRb^+$ molecular ions after the interaction decreases. This is not surprising because 1064 nm laser light that is available during the interaction can photo-dissociate the molecular ions that are formed after a three-body-recombination. I note, however, that the photodissociation of the $BaRb^+$ can in principle produce a neutral Ba and a Rb^+ ion. Therefore, the signal used here for detecting the survived $BaRb^+$ molecular ions after the interaction provides a lower limit for the actual probability. Summarizing the results of figures 5.3 and 5.8, the spin-polarized Ba^+ ion is fairly inert when immersed in a cloud of spin-polarized Rb atoms in the $|F = 2, m_F = 2\rangle_{Rb}$ state, and the small fraction of the ions that react are very likely to produce $BaRb^+$ molecular ions which are stable for a relatively long time of about half a second.

For the sake of completeness, the same measurements concerning the detection of $BaRb^+$ molecular ions are performed for a Ba^+ ion interacting with Rb atoms in the $|F = 1, m_F = -1\rangle_{Rb}$ state, the results of which are shown in figure 5.9. Once again, it is important to keep in mind that the production rate of $BaRb^+$ molecular ions presented in Fig. 5.9 should be interpreted in accordance with the decay rate of Ba^+ ion depicted in Fig. 5.2. Concretely speaking, although the detection probability of the $BaRb^+$ molecular ions seems to be in the same order when the Rb atoms are prepared in different hyperfine levels, the percentage of survived molecules after the interaction with respect to the decay rate of the Ba^+ ion is much higher when the ion interacts with atoms in the F=2 level.

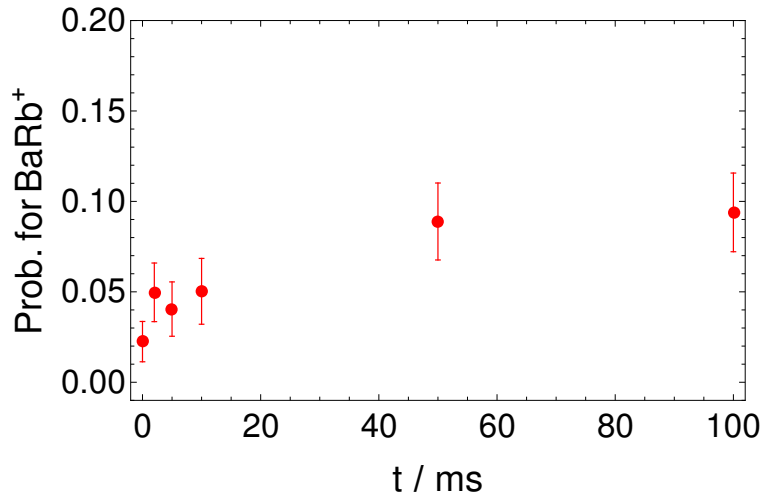


FIGURE 5.9: The probability of detecting a Ba^+ ion resulting from photodissociation of BaRb^+ molecular ions after removing all Ba^+ ions via mass filtering after the interaction. The atom cloud consists of ultracold Rb atoms in the $|F = 1, m_F = -1\rangle_{\text{Rb}}$ state with a peak density of $n = 5 \times 10^{12} \text{ cm}^{-3}$.

5.4 Concluding remarks

In this chapter, reactive collisions of a Ba^+ ion immersed in an ultracold cloud of Rb atoms were discussed. It was shown experimentally that the initial hyperfine state of the neutral atoms can be used to effectively turn the reactive processes on and off.

While the obtained results of the suppressed reactivity of the ion are not yet fully understood, they provide valuable insights into the theoretical understanding of collision dynamics and challenge our interpretation of the reactive processes in our system. I laid out feasible experimental proposals for further investigations.

Regardless of the underlying reasons behind the minute reaction rates, the empirical discovery of suppressed chemical reactions due to the hyperfine structure of the neutral atoms allows the atom-ion experiment to be used for other studies in which reactive collisions are not desired as they disrupt the system. Polaron type physics, where a charged impurity in an ultracold gas modifies the surrounding atom density [Goo+10; MPS05; CTD11], is an example of such a system.

Low baseline reactivity also permits steering chemical reactions in the desired direction using external control. As an example, laser light can be used for state-to-state chemistry or photoassociation. The latter is a two-body process. Therefore, finding resonant photoassociation transitions will allow comparative study of two-body and three-body reactive processes by re-examining the interaction of the Ba^+ ion with Rb atoms in the $|F = 1, m_F = -1\rangle_{\text{Rb}}$ state.

Chapter 6

Summary and outlook

The first line of research that was presented in this thesis is concerned with a novel collisional cooling mechanism that takes place in homo-nuclear atom-ion systems. This cooling process is called "swap cooling" as it entails the swapping of identities between a hot ion and an ultracold atom. It distinguishes itself from conventional sympathetic or buffer-gas cooling in that it is a single-collision phenomenon and becomes increasingly more efficient at higher collision energies. The concept of swap cooling was explained in Chapter 3, and the conditions for its observation were discussed theoretically, followed by presenting direct experimental evidence for its occurrence in a Rb-Rb⁺ system. Chapter 4 further elaborates on the study of swap cooling by extending the investigation into other species using numerical calculations. Monte Carlo simulations were presented, showing the universality of swap cooling among alkali and alkaline earth metals.

An extensive combined theoretical and experimental study of chemical reactions of a Ba⁺ ion immersed in an ultracold cloud of Rb atoms in the $|F = 1, m_F = -1\rangle_{Rb}$ state is presented in [Moh+21] (in which I am a co-author) to investigate the dynamics of the system during the interaction time. It provides a self-consistent interpretation predicated on the assumption that the initial reaction is a three-body-recombination (TBR), which results in a weakly bound molecular ion. The freshly formed molecule can, in turn, undergo secondary inelastic and reactive processes, including photo-excitations via 1064 nm laser light which is used as an optical dipole trap for Rb atoms. I pointed out in Chapter 5, however, that the same line of reasoning does not seem to be able to explain the experimental results when the atoms are initially prepared in the $|F = 2, m_F = 2\rangle_{Rb}$ state. The primary discrepancy was reported to be the extremely low reaction rates of the Ba⁺ ion when interacting with Rb atoms in the F=2 hyperfine level, which is not in agreement with the predicted TBR rate obtained from quasi-classical trajectory calculations. It was propounded that the semiclassical calculations based on the long-range interactions might not be sufficient to describe the collision dynamics in our system, and one may need to also take into account the short-range interactions and resonances. Taking into account the new insights derived from measurements with neutral atoms initially prepared in different hyperfine levels, I suggest in section 6.1.2 a blueprint for future experimental investigations.

6.1 Outlook

Throughout this thesis, I have mostly focused on presenting the experimental results and providing theoretical comments to help comprehend them. I have given lesser attention to the experimental methodologies and lab work for two main reasons. First, most of the employed experimental procedures have been described elsewhere. Second, paying too much attention to the specifics of measurement techniques will make it more difficult for the reader to follow the main storyline and the basic theory that underpins it. Here, I point out some of the empirical techniques used in this thesis and elaborate on how they can be used to design new measurements. In the following section, after a short introduction of an exotic phenomenon known as shape resonance, I propose a method for its experimental demonstration which is based on controlling the collision energy as was described in Chapter 3.

6.1.1 Shape resonance

The current collision energies in our system allow for many partial waves to contribute to the scattering process, and therefore collisions are often treated in a semi-classical way. However, there are certain quantum effects that, in principle, could be observed in atom-ion collisions in our setup. Shape resonances, which were briefly introduced in section 2.5, are an example of such a short-range quantum phenomenon. Even if many partial waves contribute to the collision, a particular partial wave in resonance with a quasi-bound state behind the centrifugal barrier can enhance the total cross section of inelastic and reactive collisions. Shape resonances have been theoretically investigated for various atom-ion mixtures, including Rb-Ba⁺, where calculations show a multitude of resonances at currently accessible collision energies [Hal+13b; Idz+09; Jr+15]. However, the occurrence of shape resonance in atom-ion systems is yet to be demonstrated.

Resolving shape resonances experimentally requires well-defined collision energies with narrow energy distributions. Calculations presented in [Jr+15] show that for a Rb-Ba⁺ system, even a Gaussian energy distribution as high as $2 \text{ mK} \times k_B$ half-width will still feature observable energy-dependent enhancements in reactive collision cross-sections. In [Krü+16a] an experimental technique based on tuning the excess micromotion is laid out to control the average collision energy in our system and study the energy-dependency of reactive collisions. However, this method cannot be used to observe shape resonances due to the high micromotion-induced energy distribution width. In chapter 3, I introduced another experimental technique to tune the collision energy. In brief, an initial kick prepares the ion in a well-defined initial kinetic energy state. The ion will then essentially undergo an undamped harmonic oscillation along the axial direction of the Paul trap. Since this motion is not driven and the ion remains in a region in which the excess micromotion is minimized, it is expected that the ion will have a narrow energy distribution (of about $1 \text{ mK} \times k_B$). One can further increase the precision in tuning the ion's energy by working at lower

trapping frequencies than what was used in Chapter 3. According to [Jr+15] a reasonable energy range for investigation would lie between $10 \text{ mK} \times k_B$ and several $100 \text{ mK} \times k_B$. In our system, these energies are easily accessible by setting the endcap voltages and choosing the appropriate profile for ramping the voltage (see section 3.6.4). So it is plausible that this technique could be used to achieve narrow enough collision energy distributions in the desired relative velocity range to observe shape resonances in our experiment.

In order to observe shape resonances, one can look at reactive collisions. Since in our experiment the reactive collisions are dominantly three-body processes, working with higher densities of the atomic cloud will favour reactive decays of the initial ion over two-body elastic collisions. The latter will redistribute the collision energy between colliding partners and is, therefore, an impediment to studying shape resonances. Working with a Rb BEC and short interaction times should provide the optimum conditions for resolving shape resonances.

6.1.2 Photon-induced reactive collisions

As mentioned above, it seems that the full understanding of the chemical processes in our atom-ion mixture awaits more experimental investigations. I suggested in Chapter 5 that dedicated laser light could be used to probe or control reaction dynamics, upon which I elaborate here. The main idea is to design measurements in which the population distribution of the reaction products of a Ba^+ ion interacting with a cloud of ultracold Rb atoms could be significantly altered by means of a control parameter. The same principle was used in [Moh+21] when the presence of 1064 nm laser light was manipulated to control the reaction pathways and, thereby, the final reaction products. However, since the 1064 nm laser is used as an optical dipole trap, this method limits full control over the experimental parameters such as interaction time and the density of the atomic cloud.

Assuming that the initial reaction product is a BaRb^+ molecular ion, laser light can be used to confirm its existence and probe its rovibrational levels. One can find a transition from a rovibrational level of the molecular ion to a repulsive excited state with a very strong Frank-Condon factor. If this excited state corresponds to a charge-transferred asymptote, it will effectively turn the Ba^+ ion into a Rb^+ ion after the interaction. Of course, a sizable change in the population distribution of the reaction products can only be obtained if a transition with a much higher cross section than that of the 1064 nm laser light is found. Since the photodissociation cross sections depend strongly on the initial spin multiplicity of the molecular ion, one can probe the singlet and triplet states by changing the frequency of the dissociation laser light. When the Rb atoms are prepared in the $|F = 1, m_F = -1\rangle_{\text{Rb}}$ state, the reaction rate is high, and both singlet and triplet molecules are formed. After finding a transition that indicates the production of triplet molecules, the same measurements will be performed with the atoms prepared in the $|F = 2, m_F = 2\rangle_{\text{Rb}}$ state to monitor the reaction rate and confirm whether any molecular ions were formed.

A more intricate approach when the atoms are initialized in the $|F = 1, m_F = -1\rangle_{Rb}$ state would be photoexcitation to a bound electronic excited state of the molecular ion that has a good overlap with the deeply-bound vibrational levels in the electronic ground state. Therefore, the net result of the reaction will be the formation of stable, deeply-bound molecular ions in the electronic ground state. Such molecules should be immune against secondary reactive collisions and will be detected via mass spectroscopy after the interaction. Since the derived transitions in this scenario are bound-bound, spectroscopy will reveal the population distribution of the rovibrational levels of the initially formed molecular ions. More importantly, this method can produce stable molecular ions in our system, which we have not yet been able to achieve.

Appendix A

Life and death of a cold BaRb^+ molecule inside an ultracold cloud of Rb atoms

This section is a publication where I am a co-author. The first author is Amir Mohammadi who has used this work as a main part of his PhD thesis (published by university of Ulm, 2020). The publication is inserted here because it is closely related to my own PhD topic.

The content of this chapter has been published in Phys. Rev. Research 3. The material is taken from:

Amir Mohammadi et al. "Life and death of a cold BaRb^+ molecule inside an ultracold cloud of Rb atoms". In: *Physical Review Research* 3.1 (Feb. 26, 2021). Publisher: American Physical Society, p. 013196. DOI: [10.1103/PhysRevResearch.3.013196](https://doi.org/10.1103/PhysRevResearch.3.013196). URL: <https://link.aps.org/doi/10.1103/PhysRevResearch.3.013196> (visited on 11/19/2021)

The article is published under the license CC BY 4.0. See also license text: <https://creativecommons.org/licenses/by/4.0/>

Remarks: The authors acknowledge the publication in Phys. Rev. Research 3. The content can also be found on [arXiv:2005.09338v1](https://arxiv.org/abs/2005.09338v1). Please note that the format of the (journal) article was modified in order to fit the style and layout of the thesis. Hence, a consecutive numbering of figures and references for the whole thesis was applied as well.

A.1 Abstract

We study the evolution of a single BaRb^+ molecule while it continuously collides with ultracold Rb atoms. The initially weakly-bound molecule can undergo a sequence of elastic, inelastic, reactive, and radiative processes. We investigate these processes by developing methods for discriminating between different ion species, electronic states, and kinetic ion energy ranges. By comparing the measurements to model calculations we obtain a consistent description of the typical trajectory of the ion through the manifold of available atomic and molecular states. As a further result, we determine rates for collisional and radiative relaxation as well as photodissociation, spin-flip collisions, and chemical reactions.

A.2 Introduction

In recent years, methods have been developed to produce ultracold molecules out of ultracold atoms, e.g. by photoassociation [Jon+06; HS06; Ulm+12], sweeping over a Feshbach resonance [KGJ06; Chi+10], radiative association in a two-body collision (e.g. [Hal+11; Jr+15]), or three-body recombination [MBV96; FRS96; Bur+97; SK+98; GGPR17]. Typically, the resulting cold molecules are internally highly-excited and very reactive. Therefore, several questions arise. What are the reaction and relaxation paths that the particles take while they are exposed to light fields and collisions? What are the dynamics?

Investigations on these topics can be conveniently performed in hybrid-atom-ion systems where trapped, cold molecular ions are immersed in a trapped gas of ultracold atoms [MW17; ZW17; HS15; MWW10; Ger08; Tom+19; HHD14]. Ion traps can be very deep so that an ion is still trapped even if large amounts of energy are released in an inelastic or reactive process. Furthermore, it is possible to selectively detect ionic products on the single particle level. Control over the locations of the traps allows for deterministically starting or stopping collisional dynamics between atoms and ion. In addition, low temperatures in the mK regime and below enable a high level of control for the preparation of the initial quantum state of the reactants and of the collision parameters such as the collision energy. A specific property of ion-neutral collisions is the long-range interaction between a charge and an induced dipole, which depends on the interatomic distance as $1/R^4$ [HHD14; Tom+19]. The combination of long-range interaction and low temperature corresponds to an interesting regime where reactions and inelastic processes can already take place at comparatively large inter-particle distances (see, e.g., [JM20]). This leads to large cross sections and promotes the formation of weakly-bound molecular states.

The young field of cold hybrid-atom-ion systems has shown tremendous progress studying inelastic collisions and reactions. This includes charge exchange between atoms and atomic ions [Gri+09; Sch12; Rav+12; Rat+12; Goo+15; Haz+15; Jog+17], and spin flips [Sik+18b; Für+18]. It was possible to observe collisionally induced

vibrational or rotational relaxation of a deeply-bound molecular ion [Rel+13; Hau+15], which is a collision at short internuclear distances. Furthermore, the formation of cold molecular ions from cold neutral and electrically charged atoms has been realized for several species (e.g., [Hal+11; Här+12; Hal+13b; Sul+12]), and reactive behaviour of molecular ions has been investigated [HW12; Dei+12; Pur+19; Pur+17].

Here we take a different approach, focussing less on a single, particular physical or chemical process. Instead we study the progression and interplay of the elastic, inelastic and reactive processes which take place. Concretely, we investigate, both experimentally and theoretically, the evolution of a cold, weakly-bound BaRb⁺ molecular ion as it continuously collides with ultracold Rb atoms. These collisions can be elastic, inelastic, or reactive. Our investigation includes the deterministic birth of the molecular ion inside the atom cloud, its typical life undergoing changes in the electronic and vibrational states, and its death as it reacts away. We find that the evolution of the BaRb⁺ ion directly after its formation is mainly dominated by vibrational relaxation collisions with Rb atoms at large internuclear distance. With increasing binding energy, radiative processes become progressively important until they are dominant. We observe Ba⁺, Rb₂⁺ and Rb⁺ ions as reaction products, resulting from a range of photo- or collisionally-induced processes which are discussed in detail. Interestingly, in the experiments of Ref. [Hal+13b] where the formation of BaRb⁺ molecules from cold Ba⁺ ions and Rb atoms was studied, also Rb⁺ and Rb₂⁺ as final products were detected. How these products came about, however, remained unclear. The results of our work, presented here, may be a key to also explain these findings.

This article is organized as follows. In Secs. A.3 to A.9, we study the elastic, inelastic and reactive processes of the BaRb⁺ ion for different phases of its evolution. A detailed discussion of experimental parameters and detection methods is provided in Secs. A.10 to A.12 of the Appendix. Finally, in Secs. A.13 and A.14 of the Appendix we give additional information on the theoretical models, calculations, and Monte-Carlo (MC) simulations.

A.3 Experimental setup and production of molecular ion

Our experiments are carried out in a hybrid atom-ion apparatus. The basic setup is described in detail in [Sch+12]. For the investigations presented here, we produce a single BaRb⁺ molecule which is trapped in a linear Paul trap with trap frequencies of $2\pi \times (80, 30)$ kHz in radial and axial direction, respectively. The BaRb⁺ ion is in contact with a cloud of 6×10^6 ultracold ⁸⁷Rb atoms with a temperature of $T = 750$ nK. The atoms are prepared in the electronic ground state $5S_{1/2}$ and are spin-polarized, having a total angular momentum $F = 1$ and $m_F = -1$. The atomic cloud is held in a far off-resonant crossed optical dipole trap (ODT) at 1064 nm with a trap depth of approximately $20 \mu\text{K} \times k_B$, where k_B is the Boltzmann constant. The density distribution of the cigar-shaped cloud can be described by a Gaussian with root mean

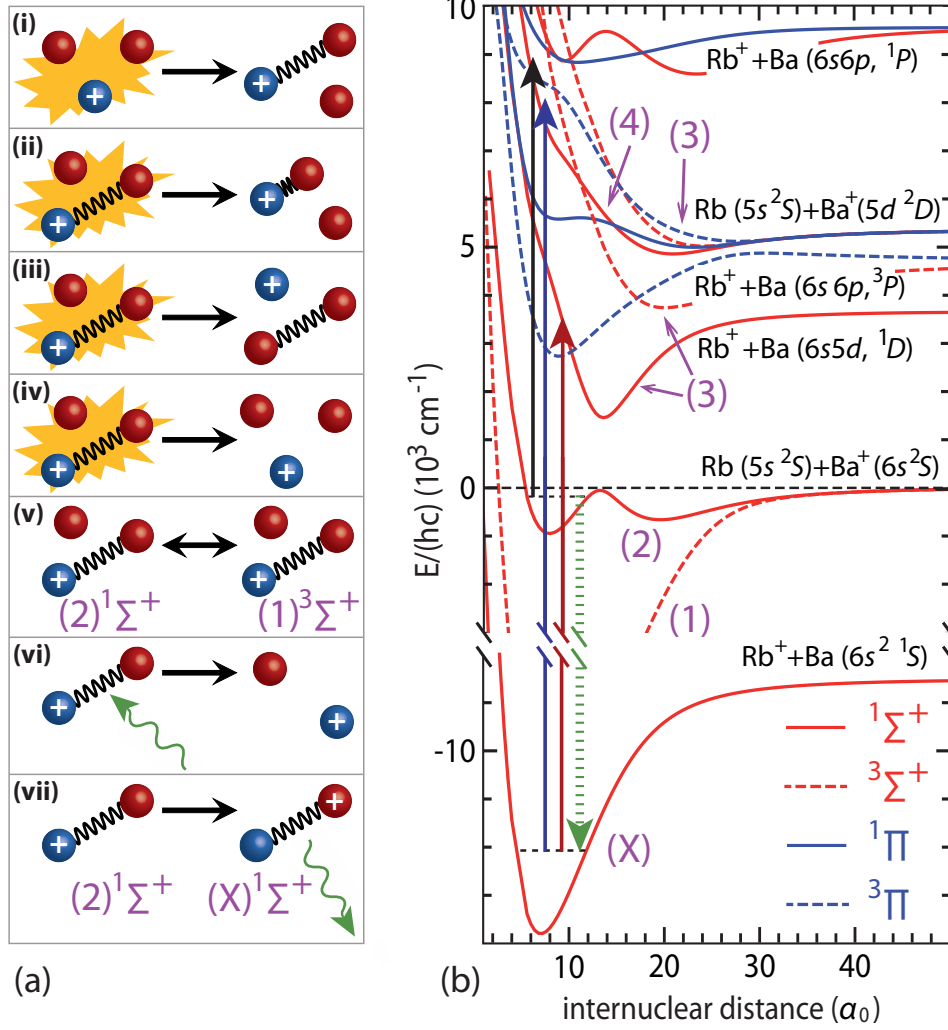


FIGURE A.1: (a) Illustration of various inelastic and reactive processes. (i) Formation of a BaRb^+ molecule via three-body recombination, (ii) collisional relaxation of a BaRb^+ , (iii) substitution reaction, (iv) collisional dissociation, (v) collisional spin exchange, (vi) photodissociation, and (vii) radiative relaxation. (b) PECs for BaRb^+ , taken from [Hal+13b]. The entrance channel $\text{Rb}(5s^2S) + \text{Ba}^+(6s^2S)$ marks zero energy. Solid black, blue, and red arrows show possible photodissociation transitions for 1064 nm, 493 nm, and 650 nm light, respectively. The dashed green arrow indicates radiative relaxation to the electronic ground state.

square widths of 9 and 60 μm in radial and axial direction, respectively (see Appendix A.10).

Initially, the cold BaRb^+ molecule is produced via three-body recombination $\text{Ba}^+ + \text{Rb} + \text{Rb} \rightarrow \text{BaRb}^+ + \text{Rb}$, typically at large internuclear distances [Krü+16b; Krü+16a], see (i) in Fig. A.1(a). For this, we prepare in the Paul trap a single, laser-cooled $^{138}\text{Ba}^+$ ion in the electronic ground state $6S_{1/2}$, and a dense Rb atom cloud in the ODT. At that time the two traps are separated by about 100 μm . Right before we start our experiments with the single Ba^+ ion we remove unwanted Rb^+ and Rb_2^+

ions, which can form spontaneously in our trapped atom cloud¹, with a mass-filter scheme, see Appendix A.11. After this purification step the 493 nm and 650 nm laser-cooling beams for the Ba⁺ ion are switched off and the Ba⁺ ion is moved into the atom cloud center. This is done within 100 μ s by abruptly changing the voltage on one of the endcap electrodes of the Paul trap by 1.5 V.

Once the Ba⁺ ion is in the atom cloud the Ba⁺ + Rb + Rb \rightarrow BaRb⁺ + Rb three-body recombination leads to the formation of BaRb⁺ molecules with a rate $\Gamma_{\text{tbr}} = k_3 n(t)^2$, where $k_3 = 1.04(4) \times 10^{-24} \text{ cm}^6 \text{ s}^{-1}$ is the three-body rate constant [Krü+16b], and $n(t)$ is the density of the atom cloud at a given time t at the ion trap center. For the central atomic density of $8.1 \times 10^{13} \text{ cm}^{-3}$ we obtain $\Gamma_{\text{tbr}} \approx 6.8 \times 10^3 \text{ s}^{-1}$. Three-body recombination is by orders of magnitude the leading reaction process of the Ba⁺ ion, and BaRb⁺ is the main product [Krü+16b; Krü+16a]. Initially, the BaRb⁺ molecule is weakly-bound below the atomic Rb($5s^2S$) + Ba⁺($6s^2S$) asymptote [see Fig. A.1(b)]. Its binding energy is expected to be $\sim 2\text{mK} \times k_B$ corresponding to the typical atom-ion collision energy in our Paul trap [Krü+16b; Krü+16a]. Furthermore, according to simple statistical arguments, we expect the BaRb⁺ molecular ion to be produced in the singlet state (2)¹ Σ^+ and triplet state (1)³ Σ^+ with a probability of 25% and 75%, respectively. For both of them the initial binding energy of $\sim 2\text{mK} \times k_B$ corresponds to a vibrational state $v = -5$ (see also Fig. A.5 of Appendix A.13.1). The negative vibrational quantum number v indicates that it is counted downwards from the atomic asymptote, starting with $v = -1$ for the most weakly-bound vibrational state. When v has a positive value, it is counted upwards from the most deeply-bound vibrational state $v = 0$.

A.4 Experimental Investigation of the evolution of the molecular ion

As will become clear later, we can learn a lot about the evolution of the BaRb⁺ molecule by monitoring the presence of the Ba⁺ ion and its state in the trap. Figure A.2(a) shows data for the measured probability P_{Ba^+} for detecting a Ba⁺ ion as a function of time for four different experiments. After immersing the cold Ba⁺ ion into the cloud for a variable time τ we quickly (within 20 μ s) pull out the remaining ion and take two fluorescence images (see Appendix A.12.1 for details). For the first image the imaging parameters are chosen such, that only a cold Ba⁺ ion with a temperature of about 100 mK or below can be detected. The filled blue circles in Fig. A.2(a) show these measurements for various immersion times τ . We essentially observe here the three-body recombination of Ba⁺ towards BaRb⁺. Next, we take a second fluorescence image which is preceded by a long laser cooling stage (for details

¹Rb₂⁺ ions can spontaneously be produced at a rate of about 5 s^{-1} in the dense Rb atom cloud due to three-body recombination of neutral Rb atoms and subsequent multi-photon ionization by the ODT light at 1064nm [Här+13b]. Subsequently, Rb⁺ ions can be created by decay of Rb₂⁺ ions into Rb⁺ ions in reactive collisions with neutral Rb atoms, or by photodissociation of Rb₂⁺ ions with 1064nm light [Jyo+16]

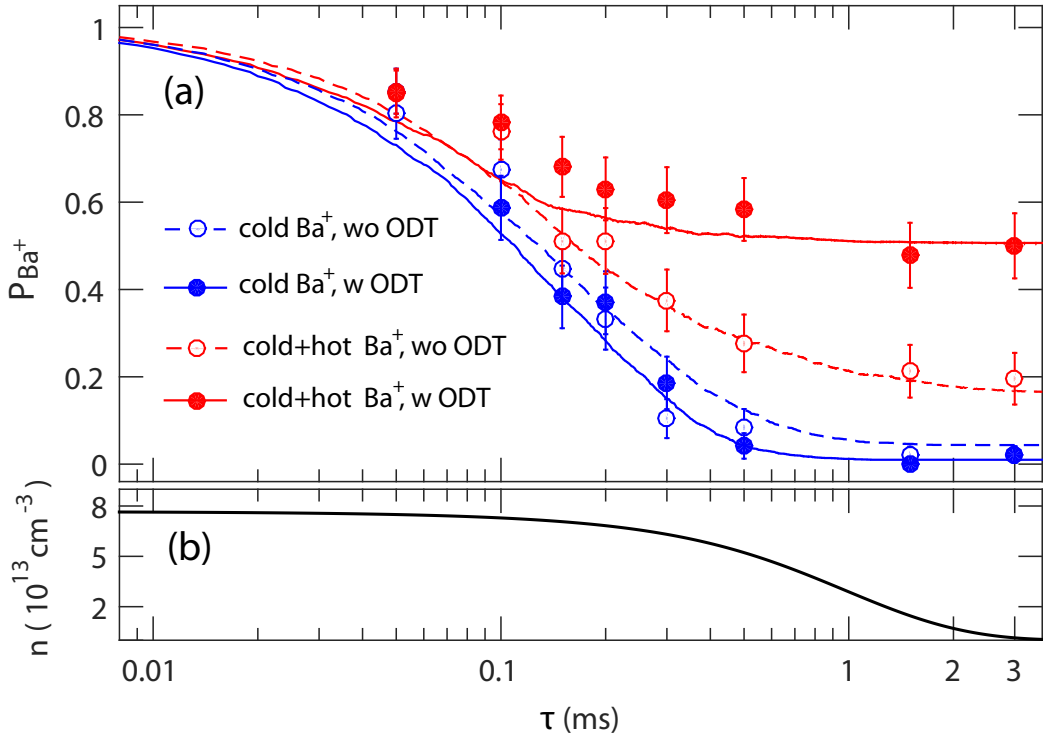


FIGURE A.2: (a) Probability P_{Ba^+} of detecting a Ba^+ ion as a function of time τ after immersion into a Rb atomic cloud. Circles are measured data. Each data point is the mean value of 50 repetitions of the experiment and the error bars represent the 1σ statistical uncertainty. Curves are the results of MC simulations (see Appendix A.14). (b) Time evolution of the atomic density n at the ion trap center after the ODT beams have been switched off at $\tau = -250 \mu\text{s}$.

see Appendix A.12.1). This retrieves almost 60% of the Ba^+ ions that had reacted away [filled red circles in Fig. A.2(a)]. We can explain this retrieval by the following scenario. There is a sizable probability for a freshly formed BaRb^+ molecular ion to break up via photodissociation. The break up produces a hot Ba^+ ion which is subsequently cooled down to below ≈ 100 mK by the long laser cooling stage so that it can be detected by fluorescence imaging (see Appendix A.12.1). Photodissociation can occur, e.g., by the ODT laser at 1064 nm. Figure A.1(b) shows indeed that 1064 nm photons can excite weakly-bound BaRb^+ ions below the $\text{Rb}(5s^2S) + \text{Ba}^+(6s^2S)$ asymptote to repulsive potential energy curves (PECs). The most relevant transitions to produce a hot Ba^+ ion are $(2)^1\Sigma^+ \rightarrow (4)^1\Sigma^+$ and $(1)^3\Sigma^+ \rightarrow (3)^3\Pi$. After the excitation, the Ba^+ ion and the Rb atom are accelerated away from each other, following the repulsive molecular potential. The Ba^+ ion will obtain a high kinetic energy of up to 0.2 eV. As a consequence, it will afterwards orbit most of the time outside the atom cloud, having a small probability for collisions with Rb atoms. Therefore, sympathetic cooling and three-body recombination are strongly suppressed and the hot Ba^+ ion remains hot until it is cooled down during the long laser cooling stage. We have direct evidence for this photodissociation process, since we detect a fraction of the Ba^+ ions in the electronically excited $5D_{5/2}$ state which corresponds to one of the asymptotic states

of the $(4)^1\Sigma^+$ and $(3)^3\Pi$ potentials [see Fig. A.1(b)]. Concretely, we find that about half of the retrieved hot Ba^+ ions populate the metastable $5D_{5/2}$ state with its natural lifetime of ~ 30 s. As the $\text{Rb}(5s) + \text{Ba}^+(5d D_{3/2,5/2})$ asymptotes are located more than 5000 cm^{-1} above the initially formed BaRb^+ molecular states, they only can be reached by photodissociation. We discriminate the population of the $\text{Ba}^+ 5D_{5/2}$ state from the population in the other Ba^+ states by using the fact, that a Ba^+ ion in state $5D_{5/2}$ can only be laser-cooled and detected after pumping it out of this metastable level with a 614 nm laser. Thus, when we switch off the 614 nm laser we lose the signal from the metastable $5D_{5/2} \text{Ba}^+$ ion.

To double check whether it is really the 1064 nm ODT laser which is responsible for photodissociation we carry out a second set of measurements, where the ODT is turned off 250 μs before the Ba^+ ion is immersed into the cold atom cloud. As a consequence the atomic cloud is now free falling and ballistically expanding. The calculated time evolution of the atomic density at the center of the ion trap is shown in Fig. A.2(b) (see also Appendix A.10). When we detect cold Ba^+ ions via fluorescence imaging [hollow blue circles in Fig. A.2(a)] there is essentially no change in signal as compared to the case with the ODT being on. This is expected since the atomic density is nearly constant on the time scale of the three-body recombination. However, the signal solely for the hot Ba^+ ion, which is obtained by subtracting the signal for cold Ba^+ from the signal for both cold+hot Ba^+ , is significantly smaller compared to when the ODT laser is on. Thus, this indeed shows that 1064 nm light photodissociates BaRb^+ molecules into hot Ba^+ ions and Rb atoms. Nevertheless, the signal for the hot Ba^+ ion is still on the order of 10% for sufficiently large times τ . Therefore, also light with a different wavelength than 1064 nm must contribute to the production of hot Ba^+ ions. As we will show in Sec. A.8 the remaining signal for hot Ba^+ can be explained due to photodissociation of ground state $(X)^1\Sigma^+$ molecules via the laser cooling light at 493 nm.

We note that photodissociation by 1064 nm light can also produce a hot Rb^+ ion, instead of a hot Ba^+ ion. This occurs in the transition $(1)^3\Sigma^+ \rightarrow (3)^3\Sigma^+$. So far, we have not experimentally studied this process in detail.

A.5 Insights from calculations

We now combine the information from our experimental data with insights from theoretical calculations. This sets strong constraints on possible scenarios for the evolution of the BaRb^+ molecule and essentially fixes all free parameters of our theoretical model. Our analysis mainly involves electronic and vibrational states, while rotational and hyperfine degrees of freedom are not taken into account to a large part.

For example, we have carried out calculations for photodissociation cross sections which are based on computed PECs and transition dipole moments for highly-excited electronic states [Hal+13b; Jr+15] (for details see Appendix A.13.3). In the calculations

we find that the photodissociation cross section for the $v = -5$ BaRb⁺ molecule with 1064 nm light is about two orders of magnitude too small to explain the hot Ba⁺ signal. However, the calculations also show that the photodissociation cross section increases approximately as $\propto E_b^{0.75}$ for both singlet $(2)^1\Sigma^+$ and triplet $(1)^3\Sigma^+$ BaRb⁺ molecules, where E_b is the binding energy (see Fig. A.8 of Appendix A.13.3). Apparently, shortly after production, while it is still immersed in the Rb cloud, the weakly-bound BaRb⁺ molecule must vibrationally relax by a number of vibrational levels before it is photodissociated. A theoretical treatment shows that the vibrational relaxation is due to inelastic atom-molecule collisions, for which we have derived cross sections in Appendix A.13.1 via quasi-classical trajectory (QCT) calculations. Furthermore, our calculations predict that while photodissociation of singlet $(2)^1\Sigma^+$ molecules via the 1064 nm laser indeed dominantly produces hot Ba⁺ ions, photodissociation of triplet $(1)^3\Sigma^+$ molecules mainly leads to hot Rb⁺ ions. Thus, in order to explain the measured substantial percentage of hot Ba⁺ ions, there has to be a mechanism which converts triplet molecules into singlet molecules. This spin-flip mechanism is provided by inelastic atom-molecule collisions, for which the cross section is estimated to be a fraction of the Langevin cross section (see Appendix A.13.2). Finally, our theoretical treatment reveals that radiative relaxation of the $(2)^1\Sigma^+$ molecules towards the electronic ground state $(X)^1\Sigma^+$ due to spontaneous emission [as illustrated by the green downward arrow in Fig. A.1(b)] needs to be taken into account. According to our calculations we obtain a broad population distribution of final vibrational levels in the ground state, ranging from about $v = 10$ to above $v = 200$, with a peak at $v = 55$, see Fig. A.12 in Appendix A.13.3. For a relaxation towards the $v = 55$ level a photon at a wavelength of about 850 nm is emitted. The relaxation rate is predicted to scale as $\propto E_b^{0.75}$, which is the same power law as for photodissociation, see Fig. A.11 in Appendix A.13.3. Hence, there is a constant competition between photodissociation and radiative relaxation for the singlet state $(2)^1\Sigma^+$. Once in the ground state the molecule is immune to photodissociation by 1064 nm light, because the photon energy is not sufficient. Photodissociation via laser cooling light, however, is possible.

We note that triplet $(1)^3\Sigma^+$ molecules cannot radiatively relax to $(X)^1\Sigma^+$ according to the selection rules for electric dipole transitions. Therefore, in the absence of any collisional or light-induced processes, these molecules remain within the triplet state $(1)^3\Sigma^+$.

Besides the already mentioned inelastic and reactive processes also collisional dissociation, substitution reactions and elastic collisions play a role for the evolution of the BaRb⁺ molecule. In order to theoretically model the evolution of the BaRb⁺ molecular ion in the atom cloud we carry out MC simulations and compare them to the measured data. In the simulations we take into account the most relevant processes shown in Fig. A.1(a), as well as additional ones. Details on the simulations, the various processes, and their respective cross sections can be found in the Appendices A.13 and A.14. The simulations produce the lines in Fig. A.2(a), showing reasonable

agreement with the experimental data. Additional results of the calculations can be found in Fig. A.17 in Appendix A.14.2.

A.6 Evolution of the molecular ion

In the following, we discuss the results of our analysis. Our theoretical investigations show that the evolution of the BaRb^+ molecule both for the singlet state $(2)^1\Sigma^+$ and the triplet state $(1)^3\Sigma^+$ will at first be dominated by vibrational relaxation collisions, which occur approximately with the Langevin rate $\Gamma_L = 164 \text{ ms}^{-1}$ for the peak atomic density of $8.1 \times 10^{13} \text{ cm}^{-3}$ in our cloud (see Appendix A.13.1). Typically, these collisions lead to vibrational relaxation in steps of one or two vibrational quanta, with an average of 1.4 vibrational quanta per Langevin collision (see Appendix A.14.1). Vibrational relaxation heats up the ion since binding energy is released in form of kinetic energy. This is counteracted by sympathetic cooling due to elastic collisions with Rb atoms, which occur at an average rate of about one elastic collision (with sizable momentum exchange) per vibrational relaxation step (see Appendix A.14.1). As a consequence the typical temperature of the BaRb^+ ion is below 15 mK during the initial, collision-dominated phase of the evolution. In general, when the collision energy is larger than the binding energy of the BaRb^+ molecule, the molecule can also dissociate into a (cold) Ba^+ ion and a Rb atom. For the initial vibrational level $v = -5$ with its binding energy of $2 \text{ mK} \times k_B$ this process occurs, however, only with a comparatively small rate of about $\Gamma_L/7$ (see Appendix A.13.1), and is negligible for deeper vibrational levels. Furthermore, our calculations reveal that for weakly-bound BaRb^+ ions in the states $(2)^1\Sigma^+$ and $(1)^3\Sigma^+$ the rate for the substitution reaction $\text{BaRb}^+ + \text{Rb} \rightarrow \text{Rb}_2 + \text{Ba}^+$ is negligible. This is a consequence of the fact that the interaction between the Rb atoms is much more short range than between a Rb atom and the Ba^+ ion, see also Appendix A.13.1. Concerning the spin-flip collisions we obtain good agreement with the experimental data when using a spin-flip rate of $\Gamma_L/42$ for flips from triplet to singlet (see Appendix A.13.2).

Our calculations predict that for the experiments with ODT, which is operated at an intensity of 18 kW cm^{-2} , the $(2)^1\Sigma^+$ molecules vibrationally relax typically to a level $v = -12$ ($E_b \approx 50 \text{ mK} \times k_B$) before either photodissociation or radiative relaxation to the ground state. By contrast, $(1)^3\Sigma^+$ molecules, which cannot radiatively relax to the ground state, typically reach a deeper vibrational level of $v = -21$ ($E_b \approx 460 \text{ mK} \times k_B$). The photodissociation rates are given by $\Gamma_{\text{PD}} = \sigma_{\text{PD}} I / (h\nu)$, where I , h , and ν are the laser intensity, the Planck constant, and the laser frequency, respectively, and σ_{PD} is the photodissociation cross section. Calculations for σ_{PD} are presented in Appendix A.13.3. For the experiments without ODT (and thus without corresponding photodissociation channel) $(2)^1\Sigma^+$ molecules are expected to relax typically to $v = -18$ ($E_b \approx 230 \text{ mK} \times k_B$) before radiative relaxation to the ground state takes place.

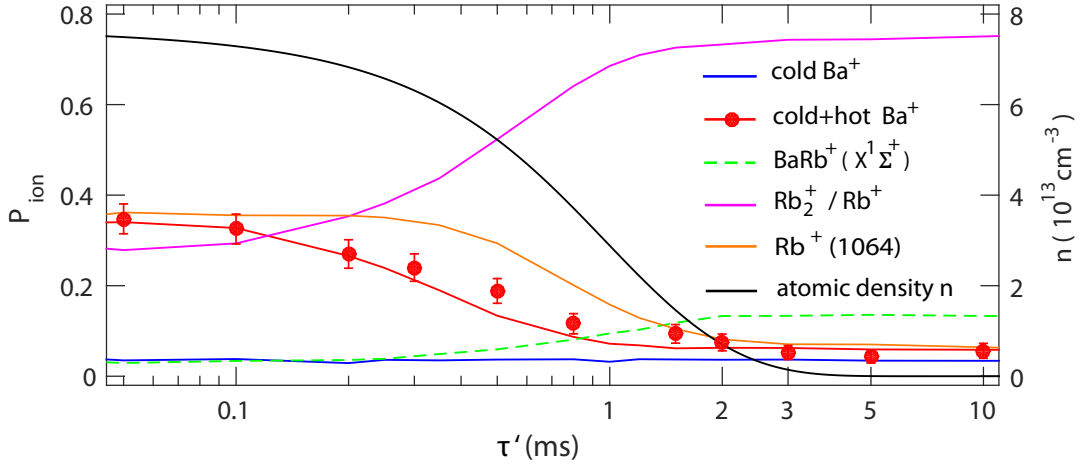


FIGURE A.3: Observation of radiative relaxation. The data points give the measured probability P_{Ba^+} of detecting a Ba⁺ ion after an extensive laser cooling stage as a function of the time τ' after which a 300 ms long 1064 nm light pulse is applied. For formation of a BaRb⁺ molecule, a cold Ba⁺ ion is immersed into the atom cloud at $\tau' = 0$. The solid black line represents the time evolution of the atomic density n at the ion trap center (see Appendix A.10). All other lines are results of MC calculations for the probabilities of finding the species as denoted in the legend.

A.7 Radiative relaxation

Since radiative relaxation to the ground state is predicted to be a central process in the evolution of the BaRb⁺ ion, we now test for it experimentally. The idea is to measure for how long BaRb⁺ molecules remain in the excited states $(2)^1\Sigma^+$ or $(1)^3\Sigma^+$ before they radiatively relax to the ground state $(X)^1\Sigma^+$. We probe the presence of a BaRb⁺ molecule in the states $(2)^1\Sigma^+$ or $(1)^3\Sigma^+$ by photodissociating it into a Ba⁺ ion and a Rb atom with the 1064 nm laser, and then detecting the hot Ba⁺ ion. BaRb⁺ molecules in the ground state $(X)^1\Sigma^+$ cannot be photodissociated by the 1064 nm laser because the photon energy is not sufficient. We start this experiment by moving a single and cold Ba⁺ ion into the atom cloud 250 μs after the 1064 nm ODT laser has been switched off. As before, a BaRb⁺ molecule will form on a time scale of $\Gamma_{\text{tbr}}^{-1} = 0.15$ ms. After the immersion of the Ba⁺ ion, we wait for a time τ' before we switch on again the 1064 nm laser² to photodissociate the molecule. Before applying the detection scheme for the released hot Ba⁺ ion, i.e. long laser cooling and subsequent fluorescence imaging, we remove any remaining BaRb⁺ molecule by mass-filtering (see Appendix A.11). The removal is done, because a remaining BaRb⁺ molecule can give rise to a spurious hot Ba⁺ signal as the laser cooling step can also photodissociate a BaRb⁺ molecule into a Ba⁺ ion and a Rb atom. This is discussed in detail later in Sec. A.8.

²We use the vertical ODT beam with an intensity of 1.8 kW cm^{-2} which is only about 10% of the intensity of the crossed ODT used for the experiments in Fig. 2. The light is switched on for 300 ms which is about three orders of magnitude longer than the typical photodissociation time scale.

The red data points in Fig. A.3 show the probability P_{Ba^+} to detect a Ba^+ ion (hot or cold) at the end of the given experimental sequence for various times τ' . As expected, the Ba^+ signal decreases as τ' increases because the BaRb^+ molecule has more time to relax to the $(X)^1\Sigma^+$ state. The decrease to about 1/3 of the initial value takes place within about $\tau' = 0.5$ ms, which represents an approximate time scale for the lifetime of the $(2)^1\Sigma^+$ and $(1)^3\Sigma^+$ BaRb^+ molecule, respectively, in the cloud of Rb atoms. For times longer than 2 ms an almost constant value of $P_{\text{Ba}^+} \approx 6\%$ is observed. This remaining population is composed of the following contributions: 4% are cold Ba^+ ions (blue solid line) that have not reacted at all³ or that have been released again as a result of collisional dissociation. 2% arise probably from BaRb^+ molecules that are stuck in the triplet state $(1)^3\Sigma^+$ after the collisional phase when all neutral atoms have left for $\tau' > 2$ ms, and are photodissociated from there by the 1064 nm light. The green dashed curve gives the probability for ending up with a BaRb^+ molecule in the electronic ground state. This probability nearly reaches $P_{\text{BaRb}^+} = 20\%$. In principle, this fraction would be about four times as large, if the substitution reaction $\text{BaRb}^+(X) + \text{Rb} \rightarrow \text{Ba} + \text{Rb}_2^+$, which depletes electronic ground state $\text{BaRb}^+(X)$ molecules, were absent⁴. The corresponding reaction rate is expected to be on the order of the Langevin rate (see Appendix A.13.1). We note that a Rb_2^+ molecular ion can also decay in the collision $\text{Rb}_2^+ + \text{Rb} \rightarrow \text{Rb}^+ + \text{Rb}_2$, if it is not too deeply bound⁵. In our simulations, however, we do not further pursue this process, and therefore give here the joint probability for finding a Rb_2^+ ion or its Rb^+ decay product (magenta line in Fig. A.3). The orange curve, in contrast, gives the probability for Rb^+ ions which are produced via photodissociation by the 1064 nm laser.

A.8 Photodissociation of electronic ground state molecules

Finally, we investigate photodissociation of the $(X)^1\Sigma^+$ state molecules. Once a BaRb^+ molecule has relaxed towards $(X)^1\Sigma^+$ it is stable with respect to 1064 nm light, however, photons from the cooling lasers for Ba^+ at the wavelengths of 650 nm or 493 nm can still photodissociate it, see blue and red arrows in Fig. A.1(b)⁶. Figure A.4 shows photodissociation as a function of exposure time Δt for light at 493 nm (a) and at 650 nm (b), respectively. The filled circles represent the fraction of experimental runs where we detect a BaRb^+ ion. We probe the presence of a BaRb^+ ion by measuring

³About a quarter of the cold Ba^+ signal stems from experiments where due to a technical glitch no initial Rb cloud was produced and therefore the Ba^+ ion could never collide with Rb atoms. These glitches occur in about 1% of all runs.

⁴The substitution reaction $\text{BaRb}^+ + \text{Rb} \rightarrow \text{BaRb} + \text{Rb}^+$ can be neglected, as discussed in ??

⁵The $X^1\Sigma_g^+$ electronic ground state of the Rb_2 molecule has a potential depth of about 4000 cm^{-1} [Str+10]. Furthermore, e.g. the vibrational level $v = 55$ of the $X^1\Sigma^+$ state of the BaRb^+ molecule has a binding energy of about 3800 cm^{-1} . When assuming that in the substitution reaction $\text{BaRb}^+ + \text{Rb} \rightarrow \text{Ba} + \text{Rb}_2^+$ a Rb_2^+ molecule can be produced with about the same binding energy as the former BaRb^+ molecule, then the substitution reaction $\text{Rb}_2^+ + \text{Rb} \rightarrow \text{Rb}^+ + \text{Rb}_2$ is energetically allowed.

⁶Photodissociation of a BaRb^+ molecule in the $(X)^1\Sigma^+$ state is also possible with a photon at 614 nm. We do not take into account this process here, because when working with the 614 nm laser only low powers of a few μW were used.

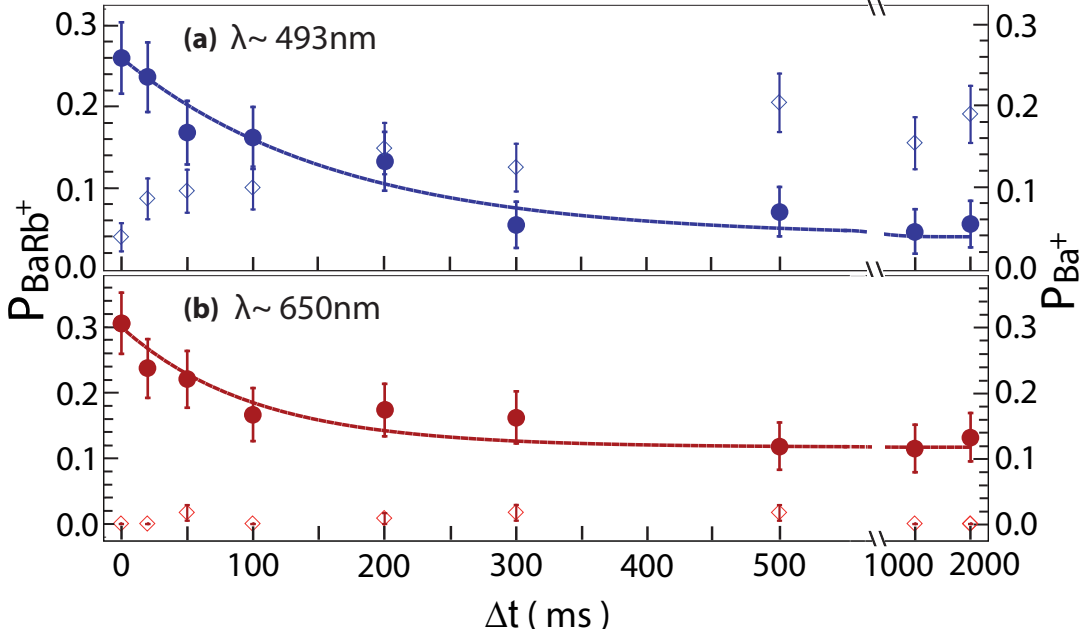


FIGURE A.4: Photodissociation of ground state BaRb⁺ molecules by 493 nm (a) and 650 nm (b) laser light as a function of exposure time Δt . Filled circles show the probability of detecting a BaRb⁺ molecule. Hollow diamonds give the probability of detecting a Ba⁺ ion. The solid lines are fits of an exponential decay plus offset.

whether a corresponding mass-filter removes the ion from the Paul trap, see Appendix A.11. The photodissociation laser is switched on $\tau = 10$ ms after immersing the Ba⁺ ion into the atom cloud without ODT. The observed decay of the BaRb⁺ fraction can be approximately described by an exponential plus offset, $P_0 \exp(-\Gamma \Delta t) + P_\infty$ (see solid lines in Fig. A.4). The offset P_∞ may stem from BaRb⁺ ions in certain vibrational levels of the states $(1)^3\Sigma^+$ or $(X)^1\Sigma^+$ which happen to have rather small photodissociation cross sections. As mentioned before, we expect the vibrational distributions in both states to be quite broad. In addition, the PECs indicate that the photodissociation cross sections for both the states $(1)^3\Sigma^+$ and $(2)^1\Sigma^+$ by 493 nm and 650 nm light might be extremely small, because of a missing Condon point at short range for the relevant transitions [Hal+11], see also Appendix A.13.3.

From the measured laser intensities of $I_{493} = (180 \pm 40)$ mW cm⁻² and $I_{650} = (260 \pm 50)$ mW cm⁻², we can determine effective, average photodissociation cross sections for the given $(X)^1\Sigma^+$ BaRb⁺ molecule population distribution over the vibrational states, using $\sigma = \Gamma h\nu / I$. We obtain $\sigma_{493} = (1.2 \pm 0.3) \times 10^{-17}$ cm² and $\sigma_{650} = (1.0 \pm 0.2) \times 10^{-17}$ cm².

We now test whether a Ba⁺ ion has been produced during photodissociation, see hollow diamonds in Fig. A.4. For the detection of the Ba⁺ ion the mass-filtering scheme is used to remove a possibly remaining BaRb⁺ ion, before long laser cooling and subsequent fluorescence imaging are carried out. For light at 650 nm we do not find any Ba⁺ signal. This can be explained with the help of Fig. A.1(b). The 650 nm laser couples the $(X)^1\Sigma^+$ state essentially only to the $(3)^1\Sigma^+$ state which, however,

dissociates into $\text{Rb}^+ + \text{Ba}$. In contrast, for light at 493 nm the production of Ba^+ ions is expected, and indeed the loss of BaRb^+ signal in Fig. A.4(a) directly correlates with an increase of Ba^+ signal. Furthermore, we observe that about half of the produced Ba^+ ions end up in the metastable state $5D_{5/2}$, since their signal is lost as soon as we switch off the 614 nm repump laser. Besides serving as a consistency check, this measurement also demonstrates that single ground state BaRb^+ molecules can be detected with high efficiency via fluorescence imaging.

From the experimentally determined cross sections we can estimate that when applying fluorescence imaging photodissociation of a $(X)^1\Sigma^+$ state molecule will on average result in a (hot) Ba^+ ion with a probability of about 70%, and in a Rb^+ ion with a probability of about 30%.

A.9 Conclusions and outlook

In conclusion, we have studied the evolution of a BaRb^+ molecule in a gas of ultracold Rb atoms. We find that due to the high predictive power of the theory for the collisional and radiative processes of the BaRb^+ molecule only a comparatively small amount of experimental input is necessary to qualitatively pin down the evolution of the molecular ion. In order to experimentally probe the current state of the ion we have developed novel methods which are based on the coordinated concatenation of mass spectrometry, controlled photodissociation, timing of atom-ion interaction, laser cooling, and fluorescence imaging. We find that while the molecular evolution is dominated by vibrational relaxation for the most weakly-bound levels, radiative processes become increasingly important for more deeply-bound levels. Furthermore, our work shows how differently the molecules behave depending on their electronic state. The holistic view of the molecular evolution presented here, opens up many new perspectives for future experiments, as it lays out how to prepare and manipulate specific molecular states and how to probe them. In the future, it will be interesting to extend the work presented here to resolve the vibrational and rotational states of the BaRb^+ ion. This will allow for investigating collisional and radiative processes and reaction paths so that our understanding can be tested on the quantum level. Some of the methods presented here are very general and can be directly adopted for studies of a broad range of other atomic and molecular species. These can be, e.g. of interest for research in astrochemistry where reaction chains in the cold interstellar medium are investigated [LGN12; SB08; PB07; Smi92].

Acknowledgments

This work was supported by the German Research Foundation (DFG, Deutsche Forschungsgemeinschaft) within SFB/TRR21 and by the FP7 Marie-Curie Initial

Training Network COMIQ (Grant ID 607491) of the European Commission. A. Mohammadi acknowledges support from DAAD. The Ulm team thanks Joschka Wolf for assistance in the lab.

A.10 Density evolution of atom cloud

Initially, the prepared ⁸⁷Rb atom cloud consists of about $N = 6 \times 10^6$ atoms⁷ and has a temperature of $T = 750$ nK. It is confined in a crossed ODT using laser light at 1064 nm. One ODT beam has a power of 1.6 W and a beam waist of 230 μm at the location of the atoms. The other one has a power of 2.1 W and a waist of 96 μm . Dipole trap frequencies are $(\omega_x, \omega_y, \omega_z) = 2\pi \times (145, 145, 22)$ Hz for the three directions of space $i \in \{x, y, z\}$. Here, the y -axis corresponds to the vertical axis, which is along the direction of the acceleration of gravity g . The initial widths $\sigma_{i,0}$ of the atomic cloud are $\sigma_{i,0} = \omega_i^{-1} \sqrt{k_B T / m_{\text{Rb}}}$, where m_{Rb} is the atomic mass of ⁸⁷Rb. We obtain $\sigma_{x,0} = \sigma_{y,0} = 9 \mu\text{m}$, and $\sigma_{z,0} = 60 \mu\text{m}$.

When switching off the ODT at a time $t = 0$, the evolution of the density $n(t)$ of the atomic cloud at the position of the ion can be expressed by

$$n(t) = \frac{N(2\pi)^{-3/2}}{\sigma_x(t)\sigma_y(t)\sigma_z(t)} \exp\left\{\left(-\frac{g^2 t^4}{8\sigma_y^2(t)}\right)\right\}, \quad (\text{A.1})$$

using the atom cloud widths $\sigma_i(t) = \sqrt{\sigma_{i,0}^2 + k_B T t^2 / m_{\text{Rb}}}$. In Fig. A.2(b) we show the density evolution of the atom cloud at the location of the ion trap centre. We note that the interaction time τ is given by $\tau = t - 250 \mu\text{s}$, since the atoms are released 250 μs before the ion is immersed into the atom cloud at $\tau = 0$. In Fig. A.3 we have essentially the same density evolution despite the fact that at τ' some laser light at 1064 nm is switched on. We have checked numerically that due to the low intensity of 1.8 kW cm⁻² used for these measurements the effect of the optical trapping potential is negligible.

A.11 Mass filtering

We can selectively remove an ion of a pre-chosen mass from the Paul trap by resonantly heating the ion out of the trap. For this we modulate the voltages on electrodes which are normally used for the compensation of radial stray electric fields at the ion trap center [Här+13a; Moh+19]. This modulation shifts the trap center periodically about the axial symmetry axis of the Paul trap. The frequency of the modulation is set to be the mass-dependent trap frequency of the chosen ion species. We typically modulate the trap for a duration of 3 s. We have performed test measurements for deterministically prepared Ba⁺, Rb⁺, and Rb₂⁺ ions. In these cases we observed an

⁷The measured atom number is $6.0 \pm 1.2 \times 10^6$. In our model simulations we use 6.2×10^6 because this optimizes the agreement with the experimental data.

efficiency of almost 100% for removing the ion by resonant modulation. We therefore also expect a similar efficiency for a BaRb^+ ion. A modulation with the resonance frequency for a particular ion species does not affect the trapping of an ion of a different species relevant for the present work.

A.12 Detection of the ion

In order to detect a single, trapped ion in the Paul trap we have two methods which we describe in the following.

A.12.1 Fluorescence detection of a single Ba^+ ion

In order to detect a Ba^+ ion we first separate the ion trap centre from the atom trap centre by a distance of $100\ \mu\text{m}$ which is much larger than the size of the atomic cloud in order to suppress unwanted collisions. This is done by applying appropriate dc voltages on the Paul trap endcap electrodes. Afterwards, the atoms are released from the ODT by switching it off. After 20 ms, when all atoms have left, we move the ion back to its former position, since this position corresponds to the centers of the cooling laser beams for the Ba^+ ion. Here, the lasers have beam waists ($1/e^2$ radii) of about $20\ \mu\text{m}$. The cooling laser beams consist of one beam at a wavelength of 493 nm for driving the $6S_{1/2}$ to $6P_{1/2}$ Doppler cooling transition, and one beam at a wavelength of 650 nm for repumping the Ba^+ ion from the metastable $5D_{3/2}$ state towards $6P_{1/2}$. During a laser-cooling time of 100 ms an electron multiplying CCD camera takes a first fluorescence image of the Ba^+ ion. This method allows for detection of a cold Ba^+ ion with a temperature of $T \approx 100\ \text{mK}$ or below, due to the short duration of the laser cooling. A hotter Ba^+ ion, e.g. resulting from photodissociation with a kinetic energy on the order of 0.2 eV, can be detected by taking a second image after long laser cooling. For this, the 493 nm laser beam frequency is red-detuned by 1 GHz and swept back towards resonance within three seconds. Afterwards, we take another fluorescence image, again for a duration of 100 ms. From the two images we can discriminate a hot ion from a cold one. For example, if a fluorescing Ba^+ ion is found in the second image but not in the first one, then this Ba^+ ion was hot at the time of the first image. Furthermore, we can detect whether a Ba^+ ion is in the metastable state $5D_{5/2}$. Such an ion will only appear in the fluorescence image, if we previously pump it out of the $5D_{5/2}$ state, e.g. with a 614 nm laser via the $6P_{3/2}$ level. Therefore, in order to probe for a $5D_{5/2}$ ion, we take two sets of fluorescence images. The first set is without the 614 nm repump laser and the second set is with the 614 nm repump laser. If we only obtain a fluorescence signal in the second set of the images, then the Ba^+ ion was in the metastable state $5D_{5/2}$.

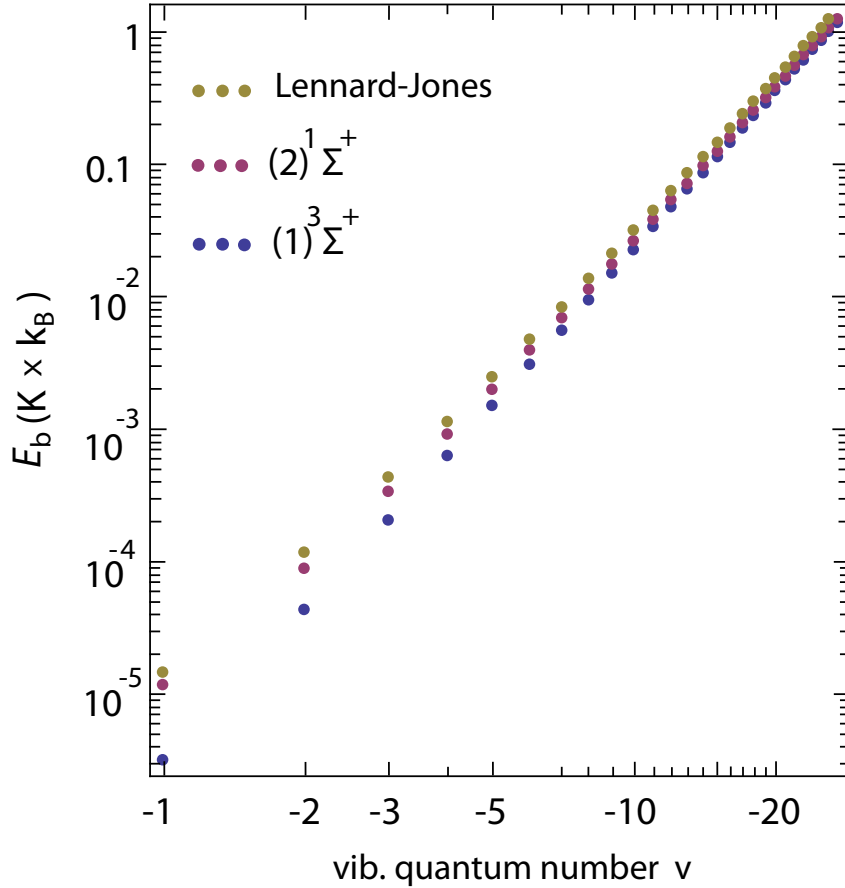


FIGURE A.5: Vibrational binding energies of a BaRb⁺ molecule for the electronic states $(1)^3\Sigma^+$ and $(2)^1\Sigma^+$. The rotation is in the ground state, i.e. $j = 0$. The brown data points result from the Lennard-Jones potential which is used for the QCT calculations. The purple and blue data points are the results from our calculated $(1)^3\Sigma^+$ and $(2)^1\Sigma^+$ PECs, as described in Appendix A.13.3.

A.12.2 Detection of the ion via atom loss and discrimination of ion species

In our setup only the Ba⁺ ion can be detected directly via fluorescence imaging. In order to detect a different ion species such as BaRb⁺, Rb⁺, Rb₂⁺ we use a scheme where the ion inflicts atom loss in a cold atom cloud [Här+13a; Här+13b]. For this, the ion is kept in the ion trap while a new cloud of neutral atoms is prepared. Then, the ion is immersed into this new atom cloud. Elastic collisions of the ion with the ultracold atoms lead to loss of atoms as they are kicked out of the ODT, which is much shallower than the ion trap. After a given interaction time the remaining number of atoms is measured via absorption imaging. If this number is significantly lower than for a reference measurement using a pure atom cloud an ion is present. Typically we already know from the preparation procedure (and, because all relevant ion species cannot escape from the deep Paul trap potential), that a single ion must be trapped in the Paul trap, but we would like to discriminate between the ion species BaRb⁺, Rb⁺, and Rb₂⁺. For this, we carry out mass-filtering in the Paul trap (see Appendix A.11), where we remove selectively the ion from the trap if it has a specific, pre-chosen mass.

Subsequently, we test whether the ion has been removed from the Paul trap with the ion detection scheme based on inflicted atom loss.

A.13 Calculation of cross sections

A.13.1 Cross sections from QCT calculations

Model

We use QCT calculations [PR19] to determine cross sections for elastic collisions, vibrational relaxation, collisional dissociation and substitution reactions in collisions of a BaRb⁺ ion with an ultracold Rb atom.

Since the three-body process occurs at large internuclear distances we assume that the three-body potential energy surface can be described by pair-wise additive ground-state potentials according to $V(\vec{R}_1, \vec{R}_2, \vec{R}_3) = V(\vec{R}_{12}) + V(\vec{R}_{13}) + V(\vec{R}_{23})$. Here, the Rb-Rb interaction is taken from [Str+10], while the Ba⁺-Rb and Ba-Rb⁺ interactions are modelled by means of the generalized Lennard-Jones potential $V(R) = -C_4[1 - (R_m/R)^4]/R^4$, where $C_4 = 160$ a.u., R is the internuclear distance, $R_m = 9.27 a_0$, and a_0 is the Bohr radius. We note in passing that $C_4 = \alpha_{\text{Rb}} e^2 / [2(4\pi\epsilon_0)^2]$ is proportional to the static dipolar polarizability $\alpha_{\text{Rb}} = 4\pi\epsilon_0 \times 4.739(8) \times 10^{-29} \text{m}^3$ of the Rb atom [Gre+15]. e is the elementary charge and ϵ_0 is the vacuum permittivity. The Lennard-Jones type potential describes the long-range interaction correctly and leads to a manageable computational time. We note that the C_4 coefficient for a Ba atom is 134 ± 10.8 a.u. [Sch+07]. Nevertheless, for saving computational time we simply use the same coefficient for the Ba atom as for the Rb atom in our model. This introduces small quantitative errors of about 5% but does not change the qualitative interpretation.

Using the QCT approach, we study the collisional behavior of BaRb⁺ molecules in the states $(2)^1\Sigma^+$, $(1)^3\Sigma^+$ as well as $(X)^1\Sigma^+$. We ignore any spin degrees of freedom, which means that the results are the same for both $(2)^1\Sigma^+$ and $(1)^3\Sigma^+$ BaRb⁺ molecules. Furthermore, we only consider collisions where BaRb⁺ molecules are initially nonrotating, i.e. $j = 0$. We have numerically checked that for other low j -states the results will not be significantly different at the level of our approximations. In order to determine cross sections and rates for a given electronic and vibrational state we sum over the corresponding rotational distribution of the final products.

In Fig. A.5, the energetically uppermost vibrational levels as derived from the Lennard-Jones potential are shown down to binding energies of about $1 \text{K} \times k_B$. For comparison, we also present the results from the PEC calculations for the $(2)^1\Sigma^+$ and $(1)^3\Sigma^+$ electronic states (see Appendix A.13.3).

We have carried out QCT calculations for the vibrational levels $v = (-1, -2, \dots, -16)$ and for a collisional energy range of $E_c = 1 - 100 \text{mK} \times k_B$. This range for E_c corresponds to a range of the kinetic energy of the BaRb⁺ ion of $E_c(1 - \mu/m_{\text{Rb}})^{-1} = 3.6 - 360 \text{mK} \times k_B$, when assuming zero kinetic energy for the atoms. Here, μ is the

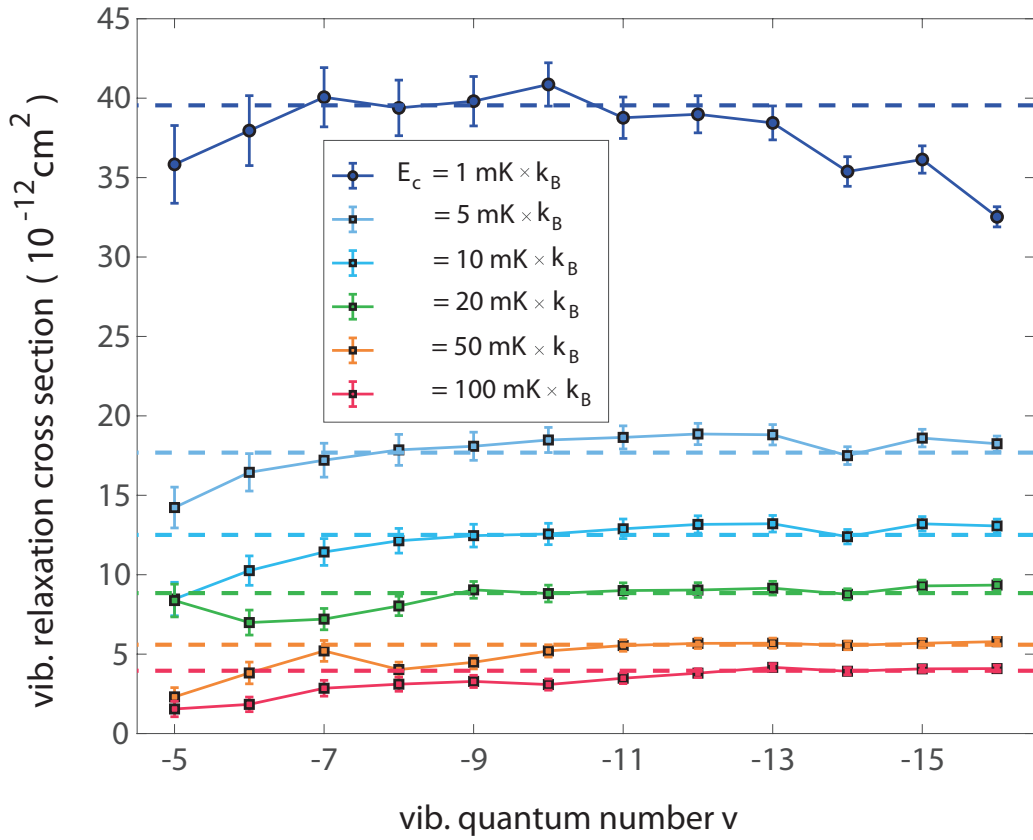


FIGURE A.6: Vibrational relaxation cross section as a function of the vibrational quantum number v , for various collision energies E_c . Shown are results of QCT calculations. The error bars represent 1σ standard deviation obtained by evaluating the numbers of trajectories leading to the same outcomes. The dashed lines are the Langevin cross sections.

reduced mass of the Rb-BaRb⁺ system. For a given set of v and E_c , we determine a suitable maximum impact parameter b_{\max} beyond which no reactions/inelastic processes occur anymore. b_{\max} is typically on the order of the Langevin radius $b_L = (4C_4/E_c)^{1/4}$. We run batches of 10^4 trajectories, effectively sampling the configuration space including different impact parameters $b < b_{\max}$ and molecular orientations. As a result we obtain a probability distribution for the different collisional processes. The cross section for a specific collision process κ can be calculated as $\sigma_\kappa = \pi b_{\max}^2 P_\kappa$, where P_κ is the probability for a trajectory undergoing this process.

Results

- Vibrational relaxation:* Figure A.6 shows the cross sections for vibrational relaxation for the states $(2)^1\Sigma^+$ and $(1)^3\Sigma^+$ for different collision energies. The calculations clearly reveal that in general the vibrational relaxation cross section is well approximated by the Langevin cross section $\sigma_L(E_c) = \pi\sqrt{4C_4/E_c}$. The corresponding Langevin rate $\Gamma_L(t) = \sigma_L v_{\text{ion}} n(t) = K_L n(t)$ is independent of the collision energy. Here, $v_{\text{ion}} = \sqrt{2E_c/\mu}$ is the velocity of the BaRb⁺ ion and $K_L = 2\pi\sqrt{2C_4/\mu} = 2.03 \times 10^{-9} \text{ cm}^3\text{s}^{-1}$ is the Langevin rate constant. We note that in our calculations vibrational relaxation typically leads to a change in the vibrational quantum number v by one or two units, i.e. $v' = v - 1, v - 2$. The average change is 1.4 units, as discussed later in Appendix A.14.1. Since these results are quite independent of the initial vibrational quantum number (see Fig. A.6), we adopt them for levels which are more deeply-bound than $v = -16$. Furthermore, we use them also for vibrational relaxation in the ground state $(X)^1\Sigma^+$. If the collision energy is large enough, in principle, also vibrational excitation could occur, but for our settings the calculations show that this is quite negligible.
- Substitution reaction BaRb⁺ + Rb → Rb₂ + Ba⁺:* For the weakly-bound levels of the $(2)^1\Sigma^+$ and $(1)^3\Sigma^+$ electronic states this reaction is in general so rare that it can be neglected. This can be explained as follows in a simple classical picture. The Ba⁺ ion and the Rb atom of the weakly-bound BaRb⁺ molecule are generally well separated. The colliding free Rb atom mainly interacts with the Ba⁺ ion via the long-range polarization potential while the interaction between the two Rb atoms is essentially negligible. Hence, the formation of the neutral Rb₂ molecule is unlikely. For the ground state $(X)^1\Sigma^+$ the reaction is energetically closed.
- Substitution reaction BaRb⁺ + Rb → BaRb + Rb⁺:* For the weakly-bound levels of the $(2)^1\Sigma^+$, $(1)^3\Sigma^+$ and $(X)^1\Sigma^+$ electronic states this reaction is rare because it entails the formation of a neutral molecule, following similar arguments as for the previously discussed reaction BaRb⁺ + Rb → Rb₂ + Ba⁺. In addition, for the weakly-bound levels of $(2)^1\Sigma^+$ and $(1)^3\Sigma^+$ the reaction would require a charge transfer between the Rb atom and the Ba⁺ ion, since for these electronic states

and long binding lengths the positive charge is almost completely located on the Ba atom within the BaRb⁺ molecule. For deeply-bound levels in the ground state $(X)^1\Sigma^+$ with $v \lesssim 90$ the reaction is energetically closed. This covers about 70% of the produced ground state molecules, as discussed in Appendix A.13.3. For these reasons we ignore this substitution reaction in our model.

- *Substitution reaction* $\text{BaRb}^+ + \text{Rb} \rightarrow \text{Rb}_2^+ + \text{Ba}$: For the weakly-bound levels of the states $(2)^1\Sigma^+$ and $(1)^3\Sigma^+$ this reaction involves a charge exchange and is therefore negligible. For the weakly-bound levels of the ground state $(X)^1\Sigma^+$, where the positive charge of the BaRb⁺ molecule is located on the Rb atom, the substitution reaction can have a sizable probability. From numerical QCT calculations for the most weakly-bound levels we can extrapolate roughly the scaling law $\sigma \approx a_0^2 E_b / (\text{mK} \times k_B)$ for the cross section. Thus, the cross section increases linearly with the binding energy. We expect this to be approximately valid up to a binding energy of about $1000 \text{ K} \times k_B$, where the expression should smoothly go over to the Langevin cross section.
- *Elastic collisions*: Due to the restriction $b < b_{\text{max}}$ we do in general not take into account all elastic collisions. In particular those with very little energy transfer are omitted since they are irrelevant for sympathetic cooling. To a first approximation, the elastic cross section for which sizable amounts of kinetic energy are transferred between the collision partners is the Langevin cross section. This is valid for all states, i.e. $(2)^1\Sigma^+$, $(1)^3\Sigma^+$, and $(X)^1\Sigma^+$.
- *Collisional dissociation*: A BaRb⁺ molecule can dissociate in a collision with a Rb atom, if the collision energy E_c is large enough. For a weakly-bound BaRb⁺ molecule in the state $(1)^3\Sigma^+$ or $(2)^1\Sigma^+$ this would lead to a release of a Ba⁺ ion and a Rb atom. In our experiments, however, the typical collision energy is too small. Therefore, this process is relevant only for the most weakly-bound BaRb⁺ molecules. In our simulation this only concerns the vibrational level $v = -5$ in the states $(2)^1\Sigma^+$ and $(1)^3\Sigma^+$. It has a binding energy of $\approx 2 \text{ mK} \times k_B$. For a collision energy of $E_c = 2 \text{ mK} \times k_B$, which is typical in the beginning of our experiments, the calculated dissociation cross section is then $4 \times 10^{-12} \text{ cm}^2$ [PR19]. This is about a factor of seven smaller than the Langevin cross section.

A.13.2 Spin-flip cross section

If the BaRb⁺ ion is in the triplet $(1)^3\Sigma^+$ (singlet $(2)^1\Sigma^+$) state it may undergo an electronic spin-flip towards the singlet $(2)^1\Sigma^+$ (triplet $(1)^3\Sigma^+$) state in a close-range collision with a Rb atom. Discussions of spin-flip processes for molecules can be found in the literature, see, e.g., [KD04; AB01; Kre08].

We estimate the spin-flip cross section in the following way. In the collision between a Rb atom and a BaRb⁺ molecular ion we only consider the interaction between the free Rb atom and the Ba⁺ ion which is loosely bound in the BaRb⁺

molecule. Spin-flips can occur when the two electron spins of the Ba^+ ion and the free Rb atom are opposite to each other, e.g. $m_s(\text{Ba}^+) = 1/2$ and $m_s(\text{Rb}) = -1/2$, such that after the collision the spins are $m_s(\text{Ba}^+) = -1/2$ and $m_s(\text{Rb}) = 1/2$. Here, m_s is the magnetic quantum number of the electron spin. Taken by itself, the state $m_s(\text{Ba}^+) = 1/2, m_s(\text{Rb}) = -1/2$ is a 50% / 50% superposition state of spin singlet and spin triplet. In the following we estimate the spin-flip cross section for such a superposition state. The actual spin-flip cross section for our experiment should be a fraction of this, because the statistical factors of the total spin-decomposition need to be taken into account. This requires an analysis, in how far a spin-flip of the bound Ba^+ ion leads to a flip of the total electron spin in the BaRb^+ molecule. Such an analysis is, however, beyond the scope of the present work.

The spin-exchange cross section for the 50% / 50% superposition state can be estimated using a partial-wave approach [DRB65; CD00] as

$$\sigma_{\text{sf}}(E_c) = \frac{\pi}{k^2} \sum_l (2l+1) \sin^2 \left(\delta_l^S(E_c) - \delta_l^T(E_c) \right), \quad (\text{A.2})$$

where $\delta_l^S(E_c)$ and $\delta_l^T(E_c)$ are the energy dependent phase-shifts of the partial wave l for the singlet and triplet atom-ion potential energy curves, respectively. Here, k is the wave number of the relative momentum in the center-of-mass frame. Next, we determine an angular momentum l_{max} such that for $l > l_{\text{max}}$ the phase-shift $\delta_l^S(E_c) \approx \delta_l^T(E_c)$. This is possible, because for large enough l the particles only probe the long-range tail of the ion-atom potential and this tail is essentially the same for singlet and triplet states. Therefore, only trajectories with $l \leq l_{\text{max}}$ contribute to the cross section. For $l \leq l_{\text{max}}$ we estimate the contribution of each partial wave term in Eq. (A.2) by using the random phase approximation for the phase-shifts, $\sin^2(\delta_l^S(E_c) - \delta_l^T(E_c)) = 1/2$ [CD00]. The partial wave l_{max} can be estimated [Rat13] using the critical impact parameter (Langevin radius) via $l_{\text{max}} = b_L k = (2C_4/E_c)^{1/4} k$, as for impact parameters $b > b_L$ the inelastic cross section vanishes in the classical regime. Carrying out the sum in Eq. (A.2) up to l_{max} we obtain

$$\sigma_{\text{sf}}(E_c) = \frac{\pi l_{\text{max}}^2}{2k^2} = \frac{\pi}{2} \left(\frac{2C_4}{E_c} \right)^{1/2} = \frac{\sigma_L(E_c)}{2}. \quad (\text{A.3})$$

The spin-flip rate is then simply proportional to the Langevin rate Γ_L . We stress again, that Eq. (A.3) is only an estimate. Therefore, for our simulations we allow for another constant fit parameter γ such that the spin-flip rate for a transition from the singlet state to the triplet state is given by

$$\Gamma_{\text{sf}} = \gamma \Gamma_L. \quad (\text{A.4})$$

For determining γ we use experimental data for which the ODT is off. When setting $\gamma = 1/14$ we obtain good agreement with our measurements.

Finally, we note that the spin-flip rate for a transition from a triplet state to a

TABLE A.1: List of the relevant electronic states, Λ , for the BaRb⁺ molecule that can be reached from the entrance channel upon absorption of a photon of 1064 nm wavelength. The entrance channel is spanned by the electronic states $(2)^1\Sigma^+$ and $(1)^3\Sigma^+$ which correlate in the asymptotic limit to Rb ($5s^2S$) + Ba⁺ ($6s^2S$). $E_{k,\max}$ is the atom-ion relative kinetic energy released after photodissociation when the initial molecule is weakly bound. σ_{\max} is the largest estimate for the state-to-state absorption cross section for a BaRb⁺ molecule with binding energy $E_b = 1 \text{ K} \times k_B$ (see also Appendix A.13.3).

Λ	Asymptotic limit	$E_{k,\max}$ (cm ⁻¹)	σ_{\max} (cm ²)
$(2)^3\Sigma^+$	Rb ⁺ + Ba ($6s5d^3D$)	≈ 8200	negligible
$(1)^3\Pi$			negligible
$(3)^1\Sigma^+$	Rb ⁺ + Ba ($6s5d^1D$)	≈ 5900	$\approx 10^{-25}$
$(1)^1\Pi$			$\approx 10^{-27}$
$(3)^3\Sigma^+$	Rb ⁺ + Ba ($6s6p^3P$)	≈ 4800	$\approx 9 \times 10^{-20}$
$(2)^3\Pi$			$\approx 4 \times 10^{-20}$
$(4)^1\Sigma^+$	Rb ($5s^2S$) + Ba ⁺ ($5d^2D$)	≈ 4000	$\approx 4 \times 10^{-19}$
$(2)^1\Pi$			$\approx 2 \times 10^{-27}$
$(4)^3\Sigma^+$			$\approx 4 \times 10^{-21}$
$(3)^3\Pi$			$\approx 2 \times 10^{-21}$

singlet state is not Γ_{sf} but $\Gamma_{sf}/3$. This is because a spin-flip process between the bound Ba⁺ ion and the free Rb atom does not necessarily change a triplet BaRb⁺ molecule into a singlet one. Collisions with an unpolarized sample of Rb will in general shuffle around the total spin S of the molecule equally between the four levels $S = 0, m_S = 0$ and $S = 1, m_S = -1, 0, 1$. Thus, on average only 1 in 3 spin-exchange collisions of a triplet BaRb⁺ molecule will produce a singlet BaRb⁺ molecule.

A.13.3 Radiative relaxation and photodissociation cross sections

In the following we calculate cross sections for radiative relaxation and photodissociation. For this, we first calculate PECs, wave functions and transition dipole moments. Table A.1 shows electronic states for relevant transitions. In the following discussion, the spin-orbit interaction will be neglected.

Potential energy curves

The PECs displayed in Fig. A.1(b), the permanent electric dipole moments (PEDMs), and the transition electric dipole moments (TEDMs) for the BaRb⁺ molecule are obtained by the methodology described, e.g., in [AD05; AD06; AGD11]. Briefly, the

calculations are carried out using the Configuration Interaction by Perturbation of a Multiconfiguration Wave Function Selected Iteratively (CIPSI) package [HMR73]. The electronic structure is modeled as an effective system with two valence electrons moving in the field of the Rb^+ and Ba^{2+} ions represented by effective core potentials (ECP), including relativistic scalar effects, taken from Refs. [DB74; DB75] for Rb^+ and Refs. [Fue+85; FR87] for Ba^{2+} . The ECPs are complemented with core polarization potentials (CPP) depending on the orbital angular momentum of the valence electron [MFM84; FMD92], and parametrized with the Rb^+ and Ba^{2+} static dipole polarizabilities and two sets of three cut-off radii [GAD10; AD12]. Only the remaining two valence electrons are used to calculate the Hartree-Fock and the excitation determinants, in atom-centered Gaussian basis sets, through the usual self-consistent field (SCF) methodology. The basis set used for the Rb atoms is from Refs. [AD05; AD06], and the one for Ba is from Refs. [AD12; Bou+10]. A full configuration interaction (FCI) is finally achieved to obtain all relevant PECs, PEDMs, and TEDMs. In Ref. [Jr+15] a comparison between these calculations for several systems, including BaRb^+ , and the ones available in the literature is given for the $(X)^1\Sigma^+$ and $(2)^1\Sigma^+$ electronic states.

Since for the states $(1)^3\Sigma^+$ and $(2)^1\Sigma^+$ we need to consider extremely weakly-bound vibrational levels, PECs have to be calculated up to large inter-particle distances. For this, we analytically extend the existing short-range PECs by matching them to the atom-ion long-range interaction behavior

$$\lim_{R \rightarrow \infty} V(\Lambda; R) = D_e - \frac{C_4}{R^4}, \quad (\text{A.5})$$

where D_e is the dissociation energy of the electronic state Λ . From fits of Eq. (A.5) to our *ab initio* PECs at around $25 a_0$, we obtain a C_4 value of about $C_4 = 171$ a.u., which is close to the known value $C_4 = 160$ a.u. for Rb atoms.

We note that the asymptotic energies ($R \rightarrow \infty$) for our PECs are in reasonable agreement with experimental values. There is virtually no error regarding those asymptotes for which each valence electron is localized on one atomic core [e.g., for the asymptotes $\text{Rb}(5s^2S) + \text{Ba}^+(6s^2S)$ and $\text{Rb}(5s^2S) + \text{Ba}^+(5d^2D)$]. However, if both valence electrons are localized on the Ba atom we obtain deviations from experimental values of -180 cm^{-1} for the $\text{Rb}^+ + \text{Ba}(6s^2^1S)$ asymptote, -120 cm^{-1} for the $\text{Rb}^+ + \text{Ba}(6s6p^3P)$ asymptote, and 420 cm^{-1} for the $\text{Rb}^+ + \text{Ba}(6s5d^1D)$ asymptote, respectively [AD12].

Calculation of wave functions

The diatomic eigenvalue problem is solved for each PEC $V(\Lambda; R)$ by means of the mapped Fourier grid Hamiltonian (MFGH) method [Kok+99], which diagonalizes a discrete variable representation (DVR) matrix of the Hamiltonian. We use a fairly large internuclear distance range, $R_{\text{max}} \approx 5000 a_0$, in order to even accommodate small binding energies E_b on the order of $E_b \approx 10 \mu\text{K} \times k_B$.

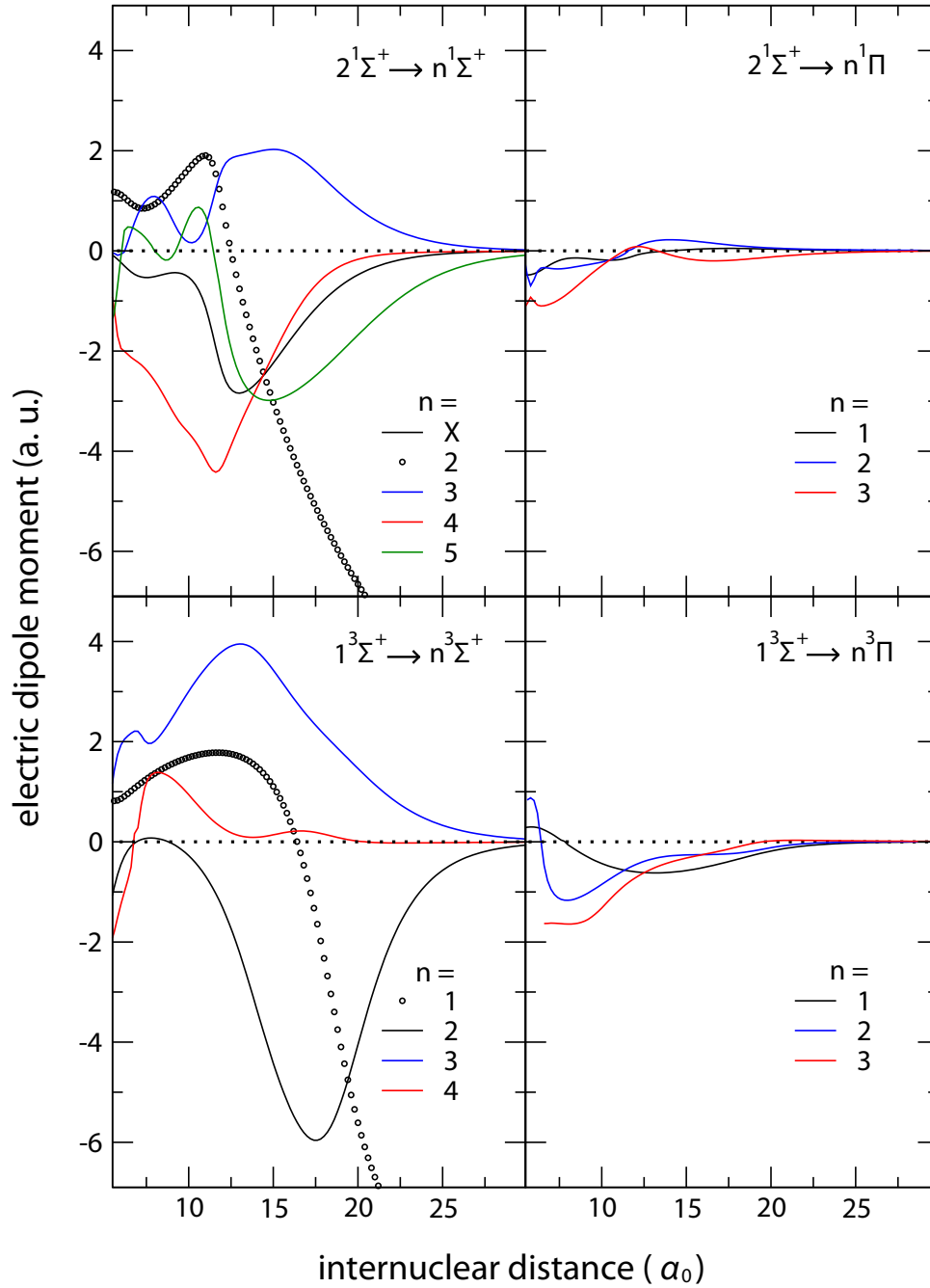


FIGURE A.7: PEDMs (circles) and TEDMs (solid lines) as functions of the internuclear distance of the BaRb⁺ molecule. Initial and final states are given in the plot. For Σ - Σ transitions the dipole moment along the internuclear axis is shown, whereas for Σ - Π transitions the dipole moment in transverse direction is shown.

The energy-normalized continuum wave functions $|\Lambda'j'; k\rangle$ are computed using a standard Numerov method [Joh78]. Here, j' is the rotational quantum number. Since the kinetic energies at long range for the exit channels correspond to several thousands of wave numbers the calculations are performed on a fairly dense and large grid (between 90,000 and 150,000 grid points) so that there are at least 20 points per wave function oscillation.

Transition electric dipole moments

The TEDMs $D_{\Lambda',\Lambda}(R)$ between relevant electronic states Λ and Λ' are shown in Fig. A.7 as functions of the internuclear distance R . The plots show that Σ - Σ transitions are generally stronger than Σ - Π transitions. Furthermore, the TEDMs vanish at large distances. Such a behavior is expected, since the $\text{Ba}^+ + \text{Rb}$ asymptote cannot be addressed from the $\text{Rb}^+ + \text{Ba}$ asymptote by optically exciting one of the atoms [see Fig. A.1(b)]. Therefore, for weakly-bound rovibrational states all outer turning points can be disregarded, i.e. radiative processes are driven at short range.

Photodissociation

In order to determine the photodissociation cross sections, we calculate the absorption cross sections $\sigma_{\Lambda'jk, \Lambda vj}(E')$ for the transitions between rovibrational levels (v, j) in the electronic state Λ towards the continuum of an electronic state Λ' [KVD89; BTG11]

$$\sigma_{\Lambda'jk, \Lambda vj}(E') = \frac{4\pi^2}{3c} \frac{E'}{2j+1} S(j', j) |\langle \Lambda'; k | D_{\Lambda',\Lambda}(R) | \Lambda v \rangle|^2. \quad (\text{A.6})$$

Here, $E' = h\nu - E_b$ is the final energy obtained for a given optical frequency ν and binding energy E_b . Furthermore, c is the speed of light, and j' represents the rotational quantum number of the final level. We note that the transition moment $\langle \Lambda'; k | D_{\Lambda',\Lambda}(R) | \Lambda v \rangle$ is essentially independent of j and j' for the low values of j relevant here. From QCT calculations we estimate a typical range of rotational quantum numbers of $j < 20$ for the BaRb^+ ion in our experiments. $S(j', j)$ denotes the Hönl-London factor [HW05]. In principle, transitions can be grouped into the three branches Q ($j' = j$, Σ - Π transitions only), R ($j' = j + 1$), and P ($j' = j - 1$). In our experiments we drive each of these transitions, if allowed by selection rules. Summing over the P, Q, R contributions one obtains a total cross section which is independent of j . Therefore it is sufficient to present in the following only total cross sections obtained for $j = 0$.

Figure A.8 shows the predictions for photodissociation cross sections for 1064 nm light as functions of the binding energy E_b of the initial rovibrational state. Here, the three dominant transitions are presented. We checked numerically that the

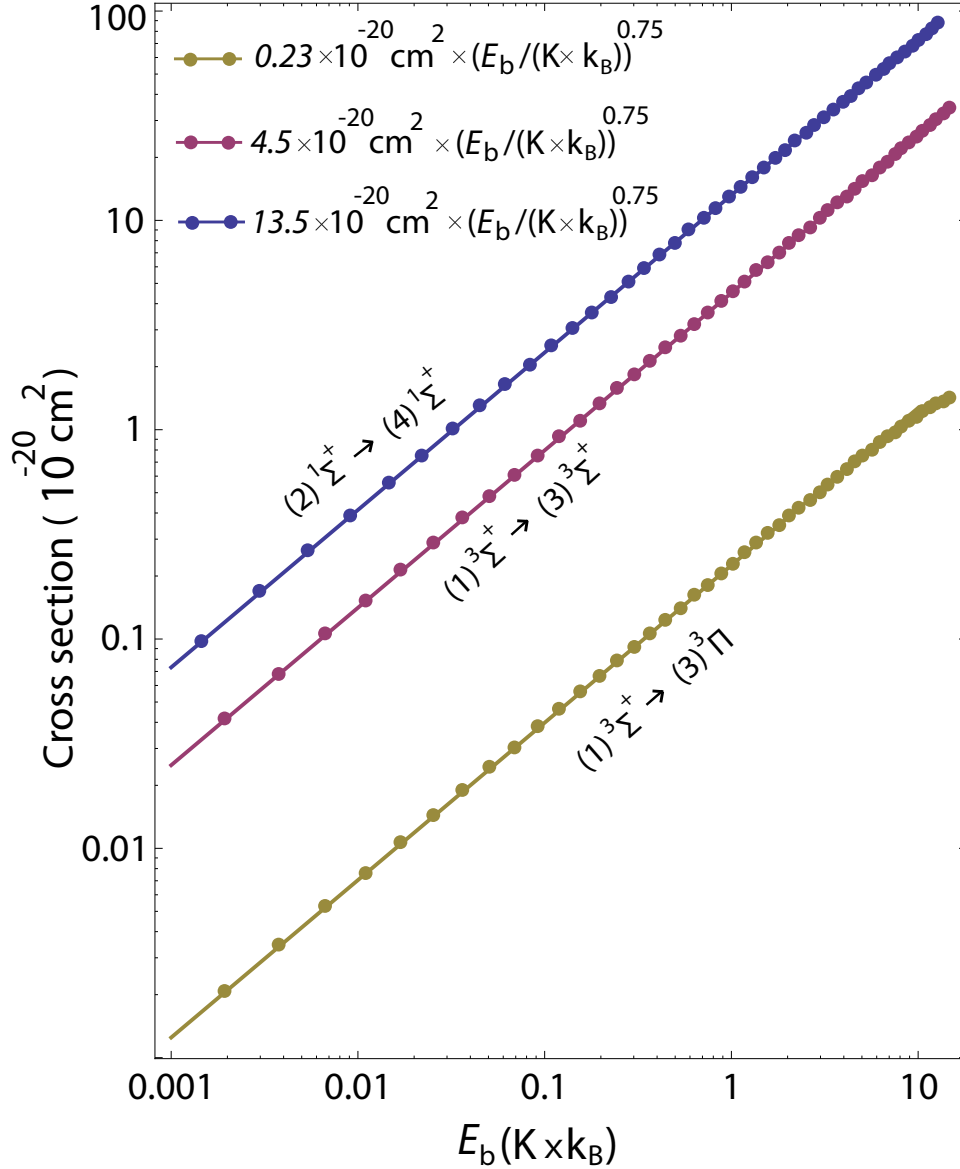


FIGURE A.8: Photodissociation cross sections as functions of the binding energy for an excited state BaRb^+ ion exposed to 1064 nm light. Shown are the results for the most relevant transitions in our experiments. Data points are calculations. Solid lines represent fits $\propto E_b^{0.75}$ to the data points (see legend).

cross sections follow a $E_b^{0.75}$ scaling law within the shown range of E_b ⁸. This can be explained by the increasing localization of the vibrational wave function with increasing binding energy E_b . Our calculations reveal that the transitions are mostly determined by the wave functions at the inner turning points of the PECs.

We note that because of an uncertainty in the calculation of the absolute energy position of the PECs of up to a few hundred $\text{cm}^{-1} \times (hc)$ there are corresponding

⁸Figure 8 indicates that for the transition $(1)^3\Sigma^+ \rightarrow (3)^3\Pi$ a deviation from the scaling law sets in at about $10 \text{ K} \times k_B$. For $(2)^1\Sigma^+ \rightarrow (4)^1\Sigma^+$ and $(1)^3\Sigma^+ \rightarrow (3)^3\Sigma^+$ such deviations set in at higher energies of $60 \text{ K} \times k_B$ and $600 \text{ K} \times k_B$, respectively (not shown in Fig. 8). For the $(2)^1\Sigma^+ \rightarrow (4)^1\Sigma^+$ transition, the deviation can partially be explained by distortions of the wave functions due to the double-well structure of the singlet entrance channel PEC [see Fig. 1(b)].

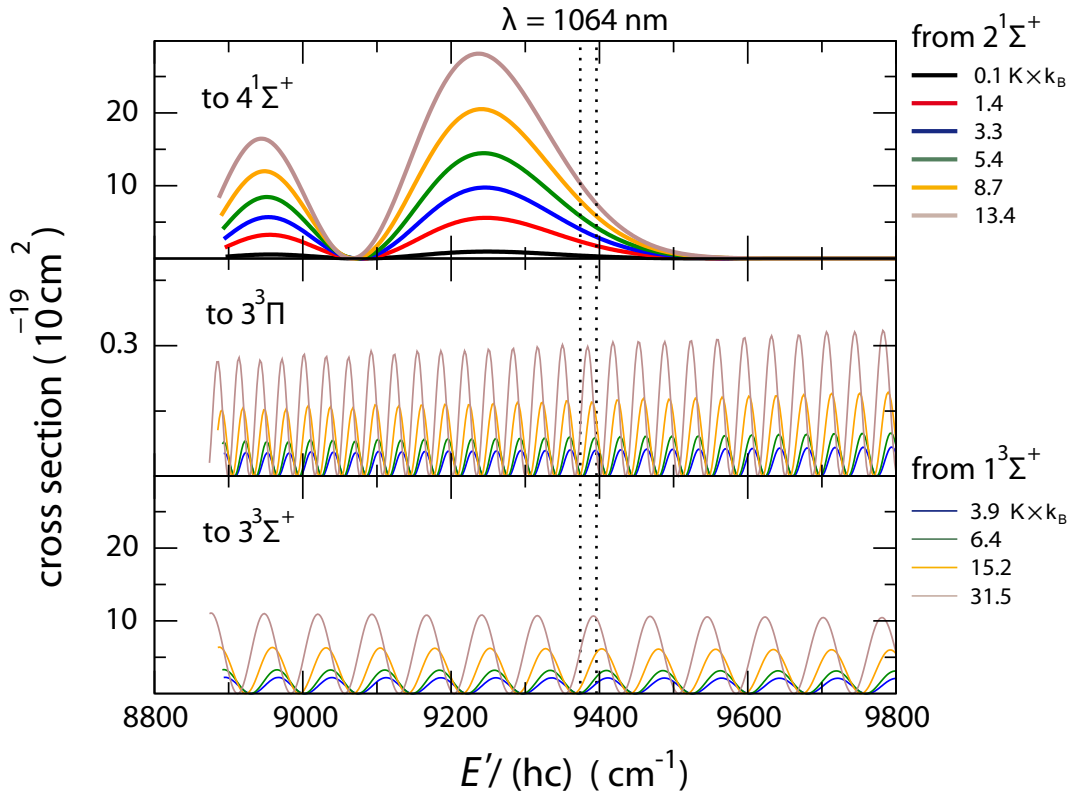


FIGURE A.9: Photodissociation cross sections as functions of the final energy $E' = h\nu - E_b$. Upper panel: $(2)^1\Sigma^+ \rightarrow (4)^1\Sigma^+$. Middle panel: $(1)^3\Sigma^+ \rightarrow (3)^3\Pi$. Lower panel: $(1)^3\Sigma^+ \rightarrow (3)^3\Sigma^+$. The color coding of the lines corresponds to the binding energy of the initial state as indicated on the right. The right (left) vertical dashed line marks the energy E' when a 1064 nm photon excites a molecule with $E_b = 0.1 \text{ K} \times k_B$ ($E_b = 31.5 \text{ K} \times k_B$).

uncertainties in the photodissociation cross sections. The possible range of cross sections is investigated in Fig. A.9. Here, $E'/(hc)$ is varied between 8800 and 9800 cm^{-1} , i.e. around typical values corresponding to final states addressed via light at 1064 nm and starting from initial states with rather small binding energies (see dashed vertical lines). These calculations are carried out for several binding energies.

The cross sections in Fig. A.9 exhibit oscillations. For a fixed binding energy, the energy interval $\Delta E'$ for a full oscillation between a minimum and a maximum is smaller than about $500 \text{ cm}^{-1} \times (hc)$ for all three presented transitions. This is about the uncertainty of the absolute energy positions of the PECs and therefore the true cross section can actually lie in the range between calculated minimum and maximum values.

The oscillations of the cross sections in Fig. A.9 are associated with the spatial oscillations of the initial rovibrational wave functions. For the sake of clarity, this is illustrated in detail in Fig. A.10. Wherever an anti-node of the initial wave function coincides with the anti-node of the scattering wave function at the inner turning point of the excited PEC, the cross section has a local maximum. This is known as the reflection principle (see, e.g., [Sch93]). The frequency separation of the local cross

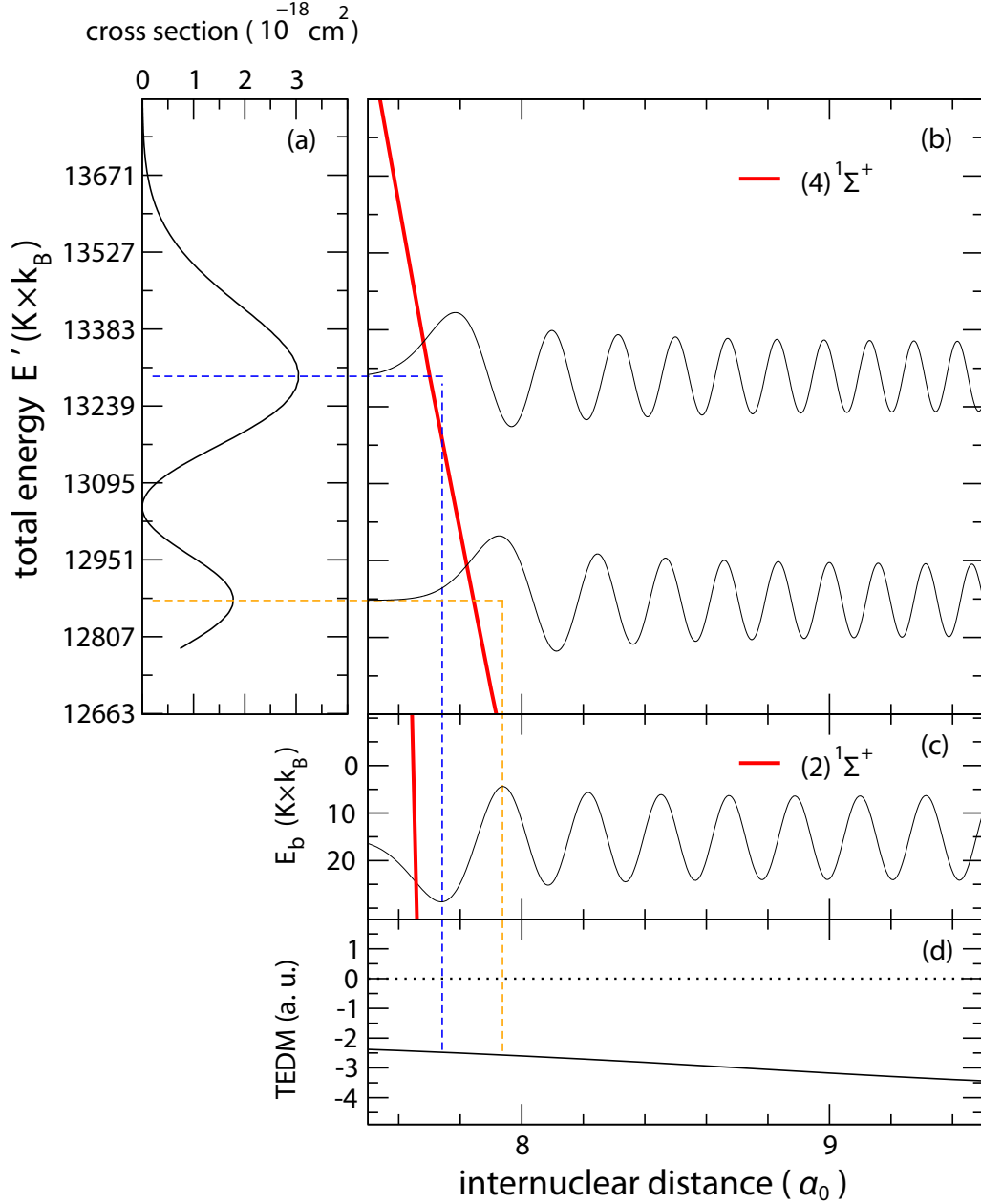


FIGURE A.10: (a) Photodissociation cross section as a function of final energy $E' = h\nu - E_b$ for the transition $(2)^1\Sigma^+ \rightarrow (4)^1\Sigma^+$. (b) The $(4)^1\Sigma^+$ PEC (red curve) and two energy-normalized continuum wave functions (black curves). (c) The $(2)^1\Sigma^+$ PEC (red curve) and the rovibrational wave function (black curve) for the binding energy of $E_b = 10.5 \text{ cm}^{-1}$. Blue and orange dashed lines help to illustrate that a good wave function overlap at the inner turning point of the excited PEC leads to a large cross section. (d) The respective TEDM as a function of the internuclear distance R .

section maxima clearly depends on the slope of the PEC and the wavelength of the initial wave function.

In order to describe the experimentally measured data (see Appendix A.14.2), we use photodissociation cross sections in our MC simulations of the form $\sigma_e \times (E_b / (\text{K} \times$

TABLE A.2: Cross sections σ_e for the three transitions that are taken into account in our MC simulation. The predicted maximal values are given beside the values resulting from fits to the experimental data in our MC simulation. In the last column the released ion for each transition is given.

Transition	max. σ_e (theor.) (10^{-20} cm 2)	σ_e (exp.) (10^{-20} cm 2)	rel. ion
$(2 \rightarrow 4)^1\Sigma^+$	40	540	Ba $^+$
$(1 \rightarrow 3)^3\Sigma^+$	9	7	Rb $^+$
$(1)^3\Sigma^+ \rightarrow (3)^3\Pi$	0.23	1.61	Ba $^+$

k_B)) $^{0.75}$. Thus, they exhibit the $E_b^{0.75}$ scaling, which our calculations predict. The pre-factor σ_e , however, is used as free parameter which is determined via fits to the data. In Table A.2 we compare the obtained values for σ_e to the theoretically predicted maximal values. We find that the experimental cross section for the transition $(2 \rightarrow 4)^1\Sigma^+$ (for the transition $(1)^3\Sigma^+ \rightarrow (3)^3\Pi$) is by a factor of 13.5 (by a factor of 7) larger than the predicted maximal value. At this point it is not clear how to explain these discrepancies. In contrast, for the transition $(1 \rightarrow 3)^3\Sigma^+$ we find consistency between theory and experiment.

Having discussed in detail the photodissociation by 1064 nm light, we now briefly comment on the photodissociation by 493 nm and 650 nm light. Calculated PECs for highly excited electronic states (not shown here) indicate that the photodissociation of weakly-bound molecules in the $(2)^1\Sigma^+$ and $(1)^3\Sigma^+$ states might be quite strongly suppressed because Condon points might not exist for the relevant transition. This agrees with the experiment, from which we do not have any evidence for this photodissociation process either. Concerning photodissociation of ground state $(X)^1\Sigma^+$ molecules via the laser cooling light, for which we do have experimental evidence (see Sec. A.8), a theoretical analysis has not been carried out yet.

The excited state $(2)^1\Sigma^+$ can decay radiatively to the ground state $(X)^1\Sigma^+$ by spontaneous emission of a photon. The corresponding radiative lifetime of the $(2)^1\Sigma^+$ molecule is shown in Fig. A.11 as a function of the binding energy E_b , as previously discussed in [Jr+15]. The relaxation can in principle lead to dissociation of the BaRb $^+$ molecule into a Rb $^+$ ion and a Ba atom. However, our calculations of the Franck-Condon factors show that it will dominantly produce a BaRb $^+$ molecule in the $(X)^1\Sigma^+$ state. Figure A.12 shows the predicted broad distribution of vibrational levels which are populated. During such a relaxation the kinetic energy of the BaRb $^+$ molecule essentially does not change, because the photon recoil is very small. The radiative relaxation rate is the inverse of the lifetime, i.e. $0.34 \times (E_b / (\text{mK} \times k_B))^{0.75} \text{ ms}^{-1}$ (see Fig. A.11). We use this relaxation rate in our MC simulations. The physics behind the scaling $\propto E_b^{0.75}$ is that for an increasing binding energy the wave function becomes more localized at short range where radiative relaxation dominantly occurs.

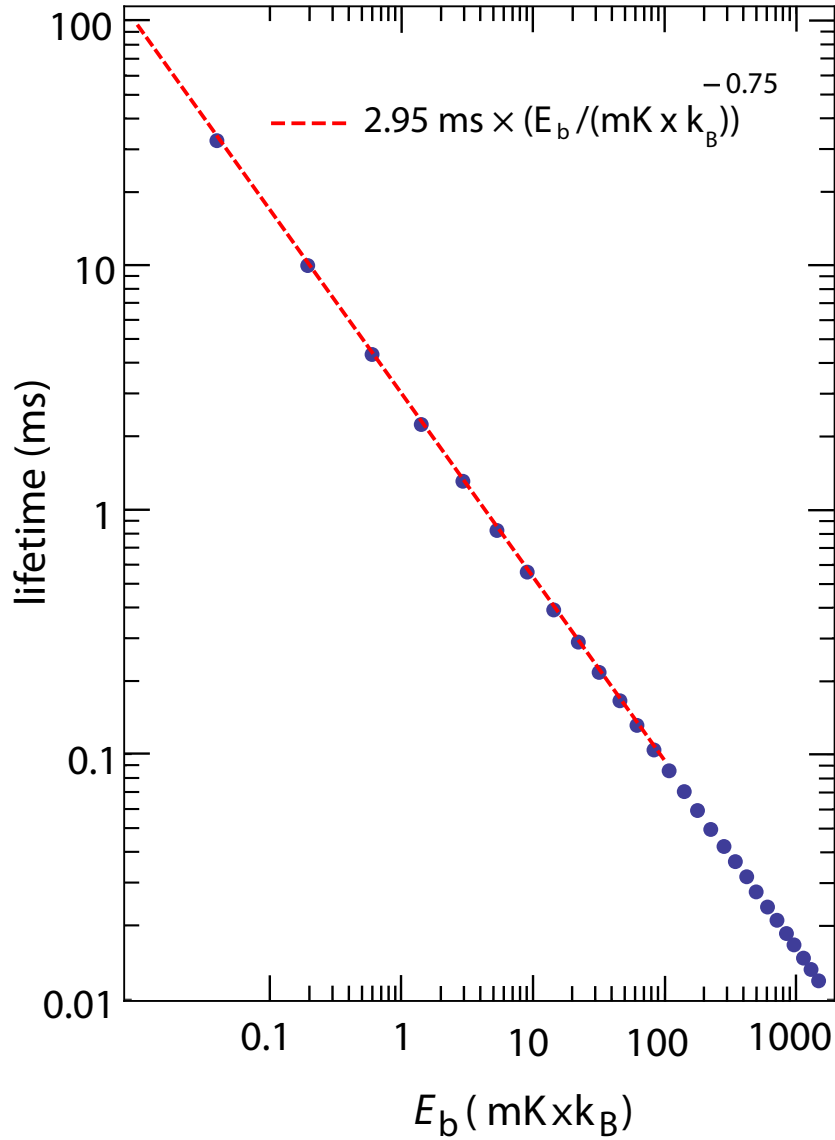


FIGURE A.11: Radiative lifetime (blue dots) for the highest rovibrational levels ($v, j = 0$) of the $(2)^1\Sigma^+$ electronic state, as a function of the binding energy E_b . The red dashed line is a fit $\propto E_b^{-0.75}$ to the data.

Radiative relaxation to the electronic ground state

For the sake of completeness, we note that radiative relaxation within a given PEC (such as $(2)^1\Sigma^+$ or $(1)^3\Sigma^+$) is negligible in our experiments. As already discussed in [Jr+15] these relaxation rates are on the order of seconds.

A.14 Monte Carlo Simulations

In this section we describe how we simulate the evolution of a BaRb⁺ molecule in a Rb atom cloud by means of MC trajectory calculations. For this, we make use of the cross sections we have determined in Appendix A.13. In order to reduce the

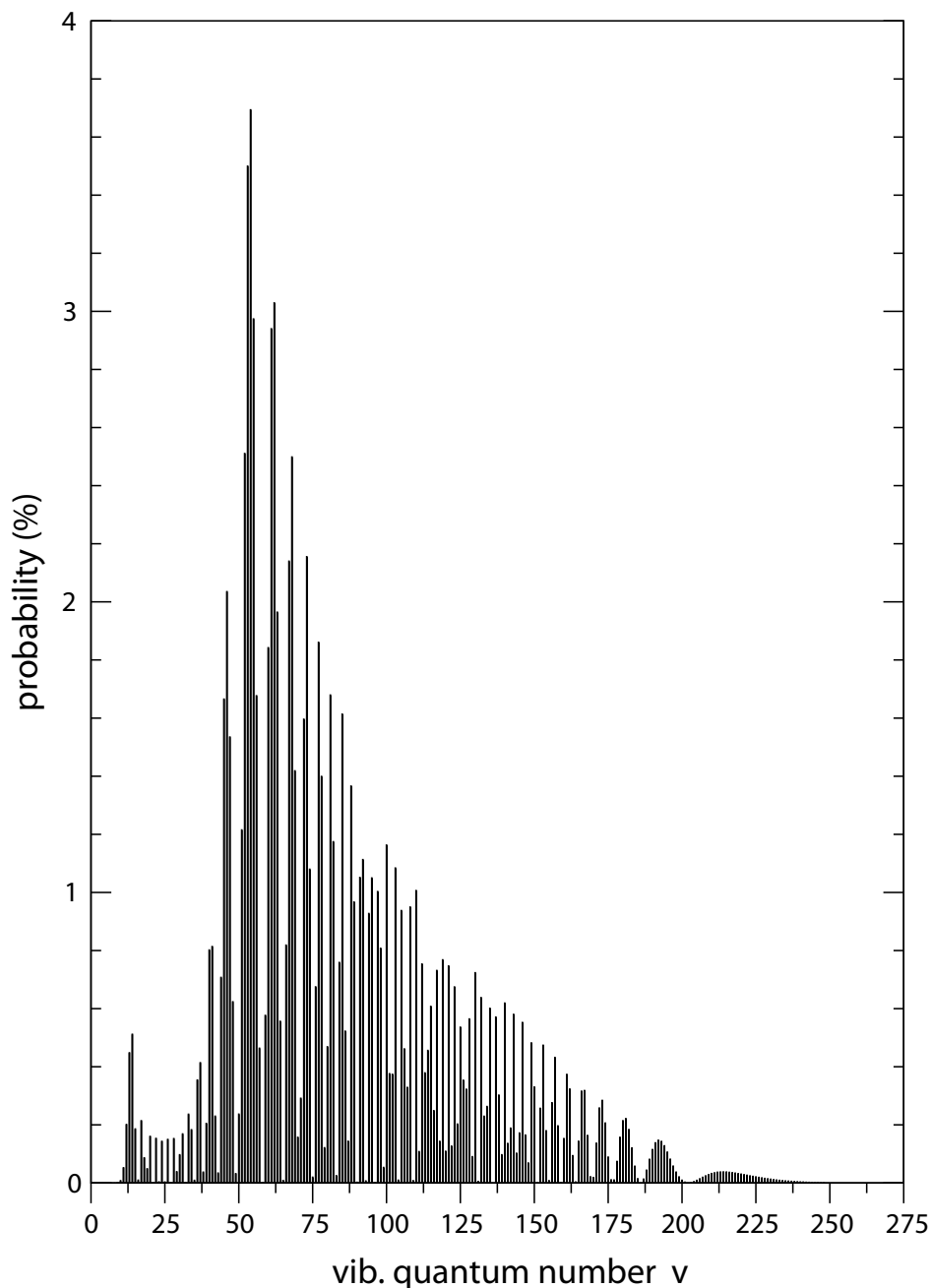


FIGURE A.12: Calculated population distribution for vibrational levels v of the electronic ground state $(X)^1\Sigma^+$ of the BaRb^+ molecule after radiative relaxation from a weakly-bound level in the $(2)^1\Sigma^+$ state with $j = 1$. Here, the same approach is used as described in [Jr+15].

complexity we carry out the calculations in two steps. In a first step we only consider a subset of collision processes. A main finding of these calculations is that the average kinetic energy of the BaRb^+ ion only slightly increases as it relaxes down to more deeply-bound vibrational states. We use this information in the second step of the MC calculations, where we now include all inelastic and reactive processes but for which we ignore elastic collisions and simply assume that the molecular ion has a constant kinetic energy.

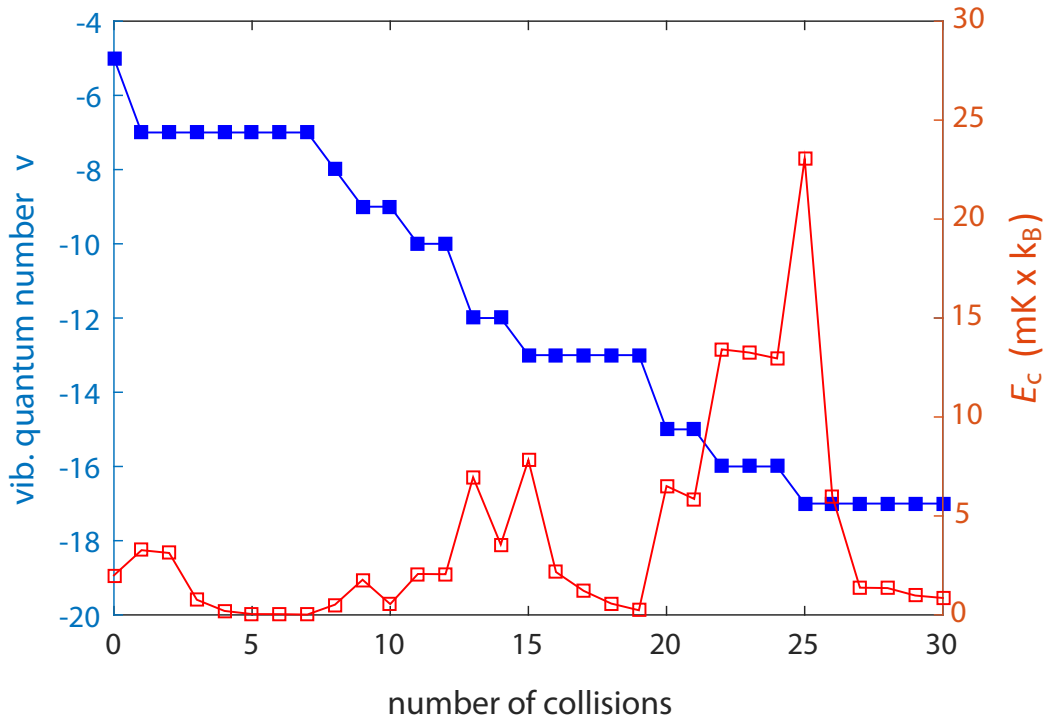


FIGURE A.13: Evolution of the vibrational quantum number of a BaRb^+ molecule in collisions with Rb atoms. We only consider the "relevant" collisions which have impact parameters $b < b_{max}$, as discussed in Appendix A.13.1. The y -axis on the left shows the vibrational quantum number v and the y -axis on the right shows the collision energy E_c . The data correspond to a single MC trajectory.

A.14.1 Restricted model

Here, we simulate trajectories of a spinless BaRb^+ molecule. During each trajectory the molecule can undergo multiple collisions within the gas of Rb atoms. We consider elastic collisions, vibrational relaxation collisions, and collisional dissociation.

The simulation starts with the molecular ion in the vibrational state $v = -5$ below the $\text{Ba}^+ + \text{Rb}$ asymptote. An example of the evolution of the vibrational state as a function of the collision number for a single trajectory is shown in Fig. A.13. The calculations reveal that vibrational relaxation typically takes place in steps of one or two vibrational quanta. The molecular kinetic energy increases after each vibrational relaxation step and decreases due to sympathetic cooling in elastic collisions. Precisely, how much energy is released in a vibrational relaxation step or carried away in an elastic collision depends on the scattering angle of the atom-molecule collision [LLM91]. In the simulations we choose random values for the scattering angle in the center-of-mass frame, which are uniformly distributed.

After analyzing 10^4 calculated trajectories we obtain the following results. Between two vibrational relaxation processes there is on average approximately one elastic collision (see Fig. A.14). Although, overall, the kinetic energy of the molecule increases as it relaxes to more deeply-bound states, within the range of interest the

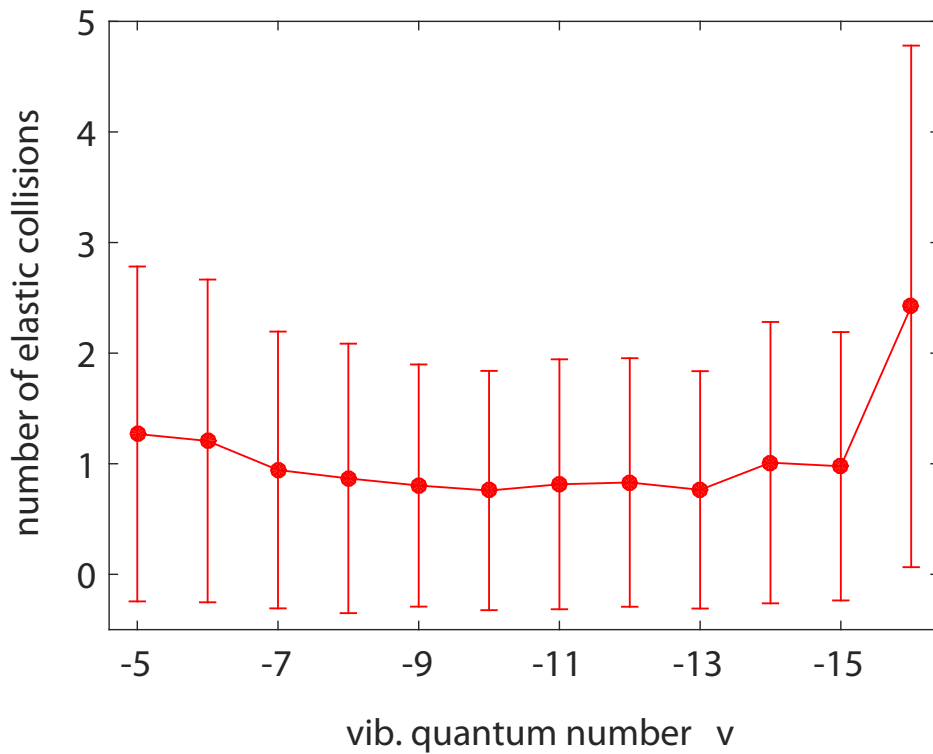


FIGURE A.14: Average number of elastic collisions of Rb atoms with a BaRb^+ ion in the vibrational state v before a relaxation (excitation) to another vibrational state occurs. Data points are from MC simulations. The error bars represent 1σ standard deviations.

molecular collision energies are typically only a few $\text{mK} \times k_B$ (see Fig. A.15). On average, the molecular ion requires 17.5 ± 4.2 collisions to relax from $v = -5$ down to $v = -17$ of which 9.0 ± 3.8 collisions are elastic. Figure A.16 shows the average vibrational quantum number v as a function of the number of vibrational relaxation collisions. We find that v decreases nearly linearly. On average about 1.4 vibrational quanta are lost per relaxation collision, independent of the initial vibrational quantum number. Since the vibrational relaxation cross section is well approximated by the Langevin cross section (see Fig. A.6) the vibrational quantum number will on average be lowered by one unit at a rate of $1.4 \times \Gamma_L$. We note that also in a recent theoretical investigation of vibrational quenching collisions of weakly-bound Rb_2^+ molecular ions with Rb atoms the changes in the vibrational quantum number are predicted to be small [JM20].

A.14.2 Full model

In the second set of MC trajectory calculations we take into account all the processes discussed in Appendix A.13. Furthermore, we also include the formation of the weakly-bound BaRb^+ molecule with vibrational quantum number $v = -5$ via three-body recombination. Adopting simple statistical arguments and considering that the

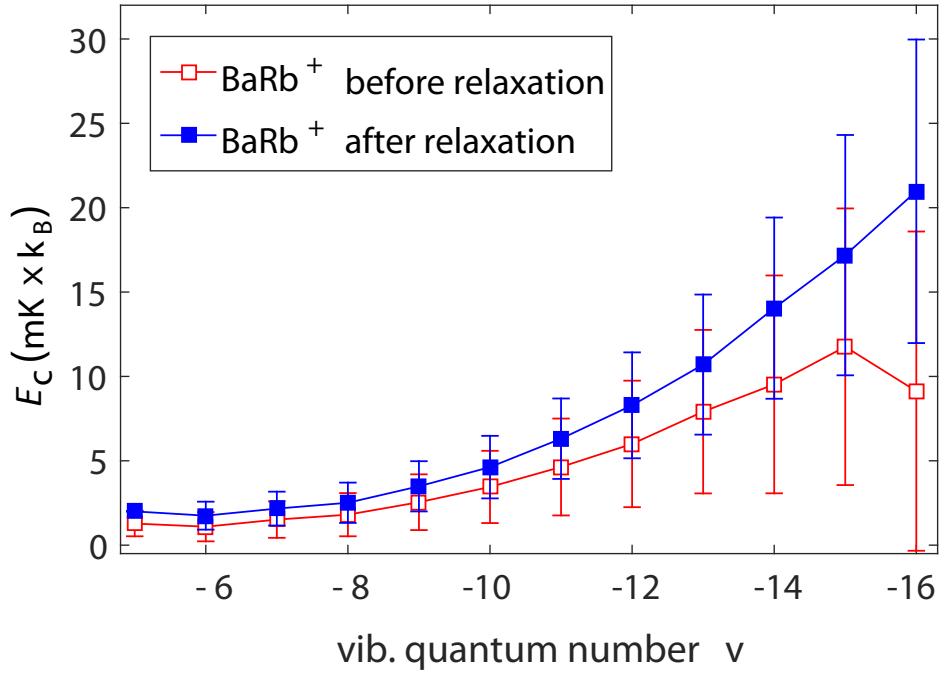


FIGURE A.15: Average collision energy of the BaRb⁺ ion right after (blue filled squares) and directly before (red open squares) vibrational relaxation as a function of the vibrational quantum number. Data points are results from the MC simulation. The error bars represent 1 σ standard deviations. Here, the difference between the curves describes the effect of cooling due to elastic collisions.

Ba⁺ ion is initially unpolarized, the probability for the freshly formed molecule to be in state (2)¹ Σ^+ ((1)³ Σ^+) is 1/4 (3/4), respectively.

Motivated by the results in Appendix A.14.1 we generally assume a collision energy E_c for the BaRb⁺ molecule of a few mK \times k_B . For the collisional dissociation regarding the $v = -5$ level we assume $E_c = 2$ mK \times k_B . Actually, for all other collisional processes the precise value for the collision energy is not relevant since their rates are proportional to the Langevin rate, which is independent of E_c . For the ground state (X)¹ Σ^+ , however, the assumption of low collision energy is in general not justified. This is because a vibrational relaxation from a deeply-bound vibrational level to the next one releases a large amount of energy. This puts the ion on an orbit through the Paul trap which is much larger than the size of the atom cloud. As a consequence the rate for further elastic, inelastic, or reactive collisions is significantly reduced. For example, when the BaRb⁺ molecule in state (X)¹ Σ^+ relaxes from $v = 55$ to $v = 54$ the motional energy of the BaRb⁺ molecule increases by about 16 K \times k_B . In order to get cooled back into the atom cloud, the energy has to be lowered to about 1 K \times k_B . On average, 44% of the energy is cooled away in a single elastic Langevin collision. Therefore, five elastic Langevin collisions are needed on average, to cool the BaRb⁺ ion back down into the Rb gas. When we take this cooling time to be 130 μ s long we find good agreement with the data.

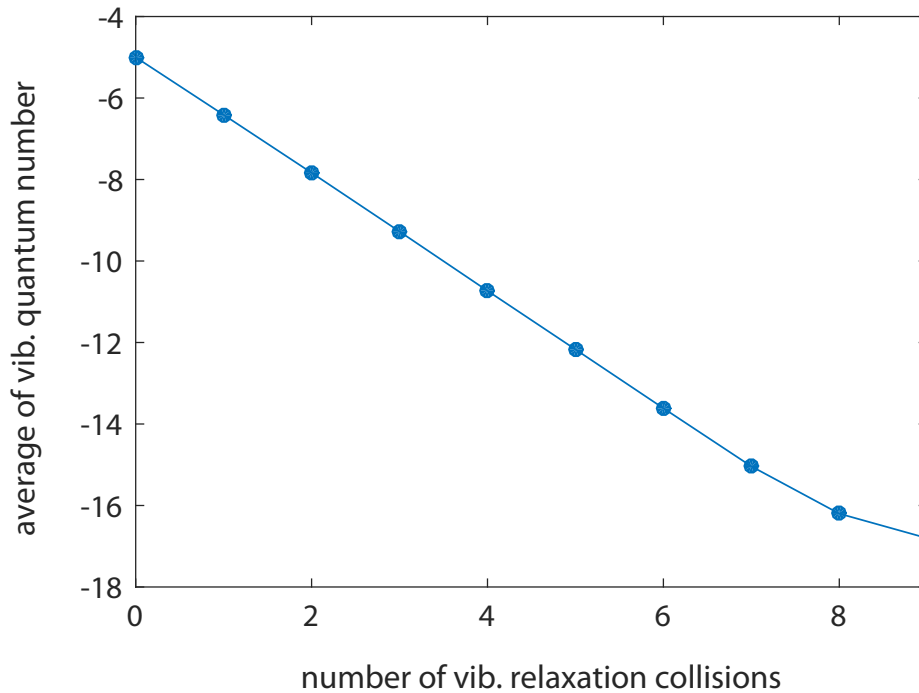


FIGURE A.16: Average vibrational quantum number for a BaRb^+ ion as a function of the number of vibrational relaxation collisions with Rb atoms. The data points represent the results of MC calculations.

Once a highly energetic Ba^+ , or a Rb^+ , or a Rb_2^+ ion is produced after photodissociation or a substitution reaction, no further reaction takes place in our simulation. However, if a cold Ba^+ ion is created it can again undergo a three-body recombination event with the respective rate and a new evolution starts. Time is typically incremented in steps of $\Delta t = 1 \mu\text{s}$. We typically carry out 2000 trajectories in a MC simulation for a given experimental procedure.

The results of the MC simulations are presented as lines in Figs. A.2(a), A.3, and A.17. In fact, Fig. A.17 is an extension of Fig. A.2(a), showing additional evolution traces for various ion states. The measurements and predictions are shown separately for the case with dipole trap (wODT) and the case without dipole trap (woODT) in Fig. A.17(a) and (b), respectively. The data points are the same as in Fig. A.2(a). The plots clearly show how initially the populations of the $(2)^1\Sigma^+$ and $(1)^3\Sigma^+$ states increase due to formation of the BaRb^+ ion via three-body recombination. At some point later these populations peak and decrease due to radiative relaxation to the ground state $(X)^1\Sigma^+$ and, in the presence of 1064 nm light, due to photodissociation. The calculations for the creation of either a hot Ba^+ or a Rb^+ ion via this photodissociation are given by the curves denoted by hot Ba^+ (1064) and Rb^+ (1064), respectively. Radiative relaxation leads at first to a growing population of the $(X)^1\Sigma^+$ ground state BaRb^+ molecule which, in secondary reactions, is converted into a Rb_2^+ or a Rb^+ ion. Here, we only consider the sum of the Rb_2^+ and Rb^+ populations, denoted $\text{Rb}_2^+ / \text{Rb}^+$. When the 1064 nm ODT is on, photodissociation is a dominant process for $(2)^1\Sigma^+$ and $(1)^3\Sigma^+$ molecules. Furthermore, the small fraction of molecules that relax to

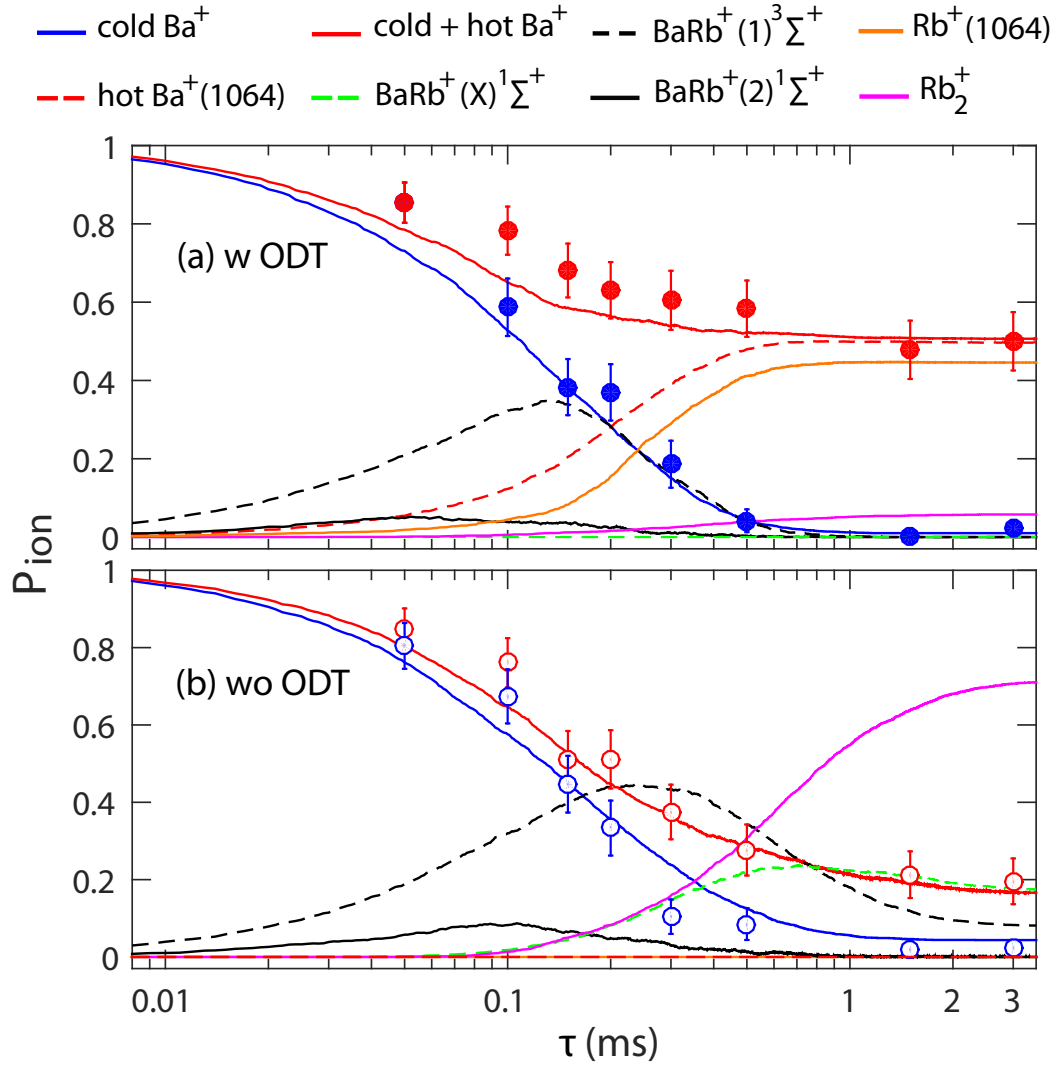


FIGURE A.17: Calculations (lines) for ion signals together with measured data (filled and open circles) of Fig. A.2(a). Shown are the probabilities for finding different ion states or species as given in the legend. In (a) the case with ODT is considered while in (b) the case without ODT is considered. "hot Ba^+ (PD)" and "Rb $^+$ (PD)" are populations due to photodissociation with 1064nm light. The population "Rb $_2^+$ / Rb $^+$ " is due to secondary collisional reactions of $\text{BaRb}^+ (X)^1\Sigma^+$ molecules with Rb atoms.

the ground state $(X)^1\Sigma^+$ are quickly removed in the trapped, dense atom cloud due to secondary reactions with Rb atoms. In contrast, when the ODT is off, almost the whole ion population is first converted into ground state BaRb^+ molecules, apart from a small fraction remaining in the state $(1)^3\Sigma^+$. A sizable fraction of the ground state molecules do not undergo secondary reactions and therefore persist, as the released Rb atom cloud quickly falls away. In order to describe the experimental signal for "cold+hot Ba^+ " we add the populations for "cold Ba^+ " and "hot $\text{Ba}^+(1064)$ " as well as 70% of the population of BaRb^+ molecules in the states $(X)^1\Sigma^+$ and $(2)^1\Sigma^+$. This last contribution is due to photodissociation of ground state molecules. The scenario

is the following. During the imaging all $(2)^1\Sigma^+$ singlet molecules will relax to the ground state $(X)^1\Sigma^+$. The cooling lasers will then dissociate these and the previously produced $(X)^1\Sigma^+$ ground state molecules. This photodissociation generates in 70% (30%) of the cases a hot Ba^+ (Rb^+) ion, as discussed in Sec. A.8.

Appendix B

MATLAB code

Here, I present the MATLAB script of the core function that I have used for numerical simulations of the swap cooling process, which were discussed in chapters 3 and 4.

```
function [InteractionTime,deltaESwap,NrofElasticCollisions,NrofLngCollisions,...
NrofSwapCollisions]=SwapSpecies(Kollisionen,InitialEnergy,CT)
% Here, CT can assume binary values of 0 and 1, corresponding to the absence
% and presence of charge transfer in the simulations, respectively.

rng('shuffle') %reset the RNG to a random state

%%% Fundamental constants -----
kB= 1.380649e-23; %J/K
hbar = 1.054 571 817e-34;
hplanck = hbar * 2 *pi;
e1 = 1.602 176 634 e-19; %C
eps0 = 8.854 187 8128 e-12; % F/m
a0 = 0.52917721067e-10; % m (= 1Bohr) from CODATA.
auofvelocity = 2.18769126277 * 10^6; %m/s
%v/auofvelocity gives the velocity in a.u.

%-----Constants-----
massconversion = 1.66054*10^-27;

%Data taken from CIAAW
mLi = 7.01600344*massconversion; %Kg
mNa =22.98976928*massconversion;
mK = 40.96182526*massconversion;
mRb = 86.90918053*massconversion;
mCs = 132.90545196*massconversion;
mYb = 173.93886755*massconversion;

mHe = 4.0026032545*massconversion;
mBe = 9.0121831*massconversion;
```

```
mMg = 23.98504170*massconversion;
mCa = 39.9625909*massconversion;
mSr = 87.90561226*massconversion;
mBa = 137.905247*massconversion;

%.....Polarizabilities.....

%Data taken from [SN19] https://doi.org/10.1080/00268976.2018.1535143
%alpha is published in atomic unit which times (a0^3*4*pi*eps0)
%will be in cubic Angstrom.

alphaLi = 164.1125*a0^3; ;
alphaNa = 162.7*a0^3;
alphaK = 289.7*a0^3;
alphaRb = 319.8*a0^3;
alphaCs = 400.9*a0^3;
alphaYb = 139*a0^3;

alphaHe = 1.38375*a0^3;
alphaBe = 37.74*a0^3;
alphaMg = 71.2*a0^3;
alphaCa = 160.8*a0^3;
alphaSr = 197.2*a0^3;
alphaBa = 272*a0^3;

%-----Charge transfer Constants-----

AsyCoALi = 0.82;
AsyCoANa = 0.74;
AsyCoAK = 0.52;
AsyCoARb = 0.48;
AsyCoACs = 0.41;
AsyCoAYb = 1;

AsyCoAHe = 2.9;
AsyCoABe = 1.6;
AsyCoAMg = 1.3;
AsyCoACa = 0.95;
AsyCoASr = 0.86;
AsyCoABa = 0.78;
%.....
GammaLi = 0.630;
```

```

GammaNa = 0.615;
GammaK = 0.565;
GammaRb = 0.554;
GammaCs = 0.535;

GammaYb = 0.678;

GammaHe = 1.344;
GammaBe = 0.828;
GammaMg = 0.750;
GammaCa = 0.670;
GammaSr = 0.647;
GammaBa = 0.619;

*****CHOOSE THE SPECIES THAT YOU WANT*****-----

asymptcoef = AsyCoARb;
GammaIon= GammaRb; %IonizationPot=GammaIon^2*13.6*el;

mAtom = mRb;
mIon=mRb;
mu = mIon*mAtom/(mIon+mAtom);

alpha = alphaRb; %m^-3
C4 = el^2*alpha/(4*pi*eps0);

sigmaelConstant=pi*(mu*C4^2/hbar^2)^(1/3)*(1+pi^2/16);
%sigma(E)=sigmaC*E^-1/3

% Generator of rotations
Jx = [ 0 0 0 ; 0 0 -1; 0 1 0 ];
Jy = [ 0 0 1 ; 0 0 0; -1 0 0 ];
Jz = [ 0 -1 0 ; 1 0 0; 0 0 0 ];

%%%%%%%%%%%%%% Characteristics of the atom system %%%%%%%%%%%%%%
Natoms = 77000;
Atomzahl = Natoms;
Tatom = 602e-9; % K
%Trapping frequencies of the optical dipole trap
omegaAtx = 2*pi* 24; % Hz Horizontal direction
omegaAty = 2*pi* 138; % Hz Vertical
omegaAtz = 2*pi* 145; % Hz Horizontal2

```

```

omegaAt = (omegaAtx*omegaAty* omegaAtz)^(1/3); %average trapping frequency

%%Cloud size after 15ms time of flight with imgx and imgy being the cloud's
%%imaged size in the ion coordinate system in m^3
Atingxsize = 119e-6;
Atingysize = 115e-6;
Atxsize = Atingxsize;
Atysize = Atingysize;

%%The following is the real space cloud size according to:
% size0^2=size^2/(1+omega^2*TOF^2)
%%which is of relevance for the collision process

Atxsize0 = sqrt(Atxsize^2/(1+omegaAtx^2*225e-6));%TOF=15 ms
Atysize0 = sqrt(Atysize^2/(1+omegaAty^2*225e-6));
Atzsize0 = (omegaAty/omegaAtz)*Atysize0;
Atsize0vec = [Atxsize0;Atysize0;Atzsize0];

%%Defining a 3D Gaussian density distribution for the atom cloud
%%the prefactor is such that the integration in the whole space results
%%in the total atom nubmer
MaxDensity = Atomzahl*(2*pi)^(-3/2)*(Atxsize0*Atysize0*Atzsize0)^-1;
%This is equivalent with the above defenition

% The atom trap has a 45 degree rotated coordinate system
% with respect to the ion trap.
% The y axis of the atom system is in the vertical direction.
RotierMatrix45y = expm( pi/4 *Jy );
RotierMatrix45z = expm( pi/4 *Jz );
RotierMatrix45invy = expm( -pi/4 *Jy );
RotierMatrix45invz = expm( -pi/4 *Jz );
%The second rotation is needed since the radial secular motion of the
%ion is along the diagonal direction of the trap
Atsize0vecIonbasis =RotierMatrix45invz* RotierMatrix45y * Atsize0vec;

%%%%%%%%%%%%%%%%%%%%%%%%%%%%%%%%%%%%%%%%%%%%%%%%%%%%%%%%%%%%%%%%%%%%%%%%%% Characteristics of the ion trap%%%%%%%%%%%%%%%%%%%%%%%%%%%%%%%%%%%%%%%%%%%%%%%%%%%%%%%%%%%%%%%%%%%%%%%%%%
OmegaT = 2*pi* 4.22e6 ; %Hz RF Frequency
cz = 0 ; % No rf pickup on the coils
beta = mAtom/(mAtom+mIon) ; % Mass ratio mn / (mi + mn)
omegazBa = 2*pi * 37.8e3; % Hz
omegaxBa = 2*pi * 130.1e3; % Hz

```

```

omegaxIon=2*pi*2e6;omegayIon=2*pi* 2.01e6;omegazIon=2*pi*1e6;%Hz
omegavecIon = [omegaxIon;omegayIon;omegazIon];

%%%%%%%%%%%%%%%%%%%%%%%%%%%%%%%%%%%%%%%%%%%%%%%%%%%%%%%%%%%%%%%%%%%%%%%%
%% Initial values, Energy in the Lab Frame
Eionvec = [0.01; 0.01; InitialEnergy]* kB;
phasevec = [0 ; 0; pi/2]; % x, y, z

%Eiontot= EmmMax+sum(Eionvec);
Eiontot = sum(Eionvec);
%% Maximum collisin rate
RateMax = MaxDensity* sigmaelConstant*(mu/mIon*Eiontot)^(-1/3)*...
(2*Eiontot/mIon)^(1/2);

dichteupdate= 0; %Assuming that the density of the atom cloud
                %does not change during the interaction

% Time generation
MaxKollisionen=Kollisionen;%1000;
t = 0;

tVEC = zeros(length(MaxKollisionen),1);
phaseVECx= tVEC;
phaseVECy= tVEC;
phaseVECz= tVEC;
EionVECx= tVEC;
EionVECy= tVEC;
EionVECz= tVEC;
EionVECz(1)=InitialEnergy*kB;

if (0)
    tVECCT = tVEC;
end

ij = 0;
RandomVECIndex=0;
RandomVECIndexCT=0;
Zeitschritte=0;
LngCollisions=0;
CTprobability=0;
CTcounter=0;

```

```

dissipatedEnergyinSwap=0;

RandomVECLength= MaxKollisionen;
%Generate random numbers upfront for faster access
LOGRandomVEC=log(rand(RandomVECLength,1));
RandomVEC=rand(RandomVECLength,1);
if (CT)
RandomVECCT=rand(RandomVECLength,1);
end

EioninkB=Eiontot./kB;
while (EioninkB>0.01)
%Stop the simulation if the ion is cooled down

RandomVECIndex=RandomVECIndex+1;
if RandomVECIndex >= RandomVECLength
% Random arrays are full, create new ones and restart counter
LOGRandomVEC=log(rand(RandomVECLength,1));
RandomVEC=rand(RandomVECLength,1);
RandomVECIndex = 1;
end

if ij >= MaxKollisionen
%Aborts as soon as all array entries are occupied
break
end

tinc = (- 1/ RateMax) * LOGRandomVEC(RandomVECIndex);
t = t+ tinc;

%% Calculations of the ion's coordinates
Rvecnormalized = sin(omegavecIon * t + phasevec);
Rsecvec = sqrt(2 * Eionvec / mIon) ./ omegavecIon .* Rvecnormalized;
vsecvec = sqrt(2 * Eionvec / mIon).*cos(omegavecIon * t + phasevec);

%%%%%%%%%%%%%%%%%%%%%%%%%%%%%%%%%%%%%%%%%%%%%%%%%%%%%%%%%%%%%%%%%%%%%%%%%
vionvec = vsecvec; %+ ummvec;
vsecvecsquare= vsecvec(1)^2 + vsecvec(2)^2 + vsecvec(3)^2;

```

```

vionvecsquare = vsecvecsquare;

RvecAtbasis = RotierMatrix45invy*RotierMatrix45z*...
[Rsecvec(1);Rsecvec(2);Rsecvec(3)];
%The first rotation around the ion's (and atom's) y axis puts the
%z axis along the axial direction of the Paul trap. The second
%rotation is needed since the radial secular motion of the ion
%is along the diagonal direction of the trap

AtDensityDisIonbasis=MaxDensity*exp(-RvecAtbasis(1)^2./(2.*Atxsize0^2))...
.*exp(-RvecAtbasis(2)^2./(2.*Atysize0^2)).*...
exp(-RvecAtbasis(3)^2./(2.*Atzsize0^2));

AtDensityDis = AtDensityDisIonbasis;

%%%%%%%%%%%%%%%%%%%%%%%%%%%%%%%%%%%%%%%%%%%%%%%%%%%%%%%%%%%%%%%%%%%%%%%% Collision %%%%%%%%%%
% Collision energy in the COM frame

Ecollision = 0.5* mu * vionvecsquare; %sum(vionvec.*vionvec) ;
%faster scalar product dot(vionvec,vionvec)

bc = (2*C4./Ecollision).^(1/4); % Langevin Radius
% calculate bmax
sigmaael = sigmaaelConstant*(Ecollision)^(-1/3);
bmax = sqrt( sigmaael / pi );
%% Check: Has a collision taken place?
dichteloc = AtDensityDis;

Rateloc = dichteloc * sigmaael* sqrt(vionvecsquare); %norm(vionvec);

    if RandomVEC(RandomVECIndex) < (Rateloc/RateMax)
% Then a collision has happened. Save all the relevant parameters.
    ij = ij + 1;

phaseVECx(ij)= phasevec(1);
phaseVECy(ij)= phasevec(2);
phaseVECz(ij)= phasevec(3);
EionVECx(ij) = Eionvec(1);
EionVECy(ij) = Eionvec(2);

```

```

EionVECz(ij) = Eionvec(3);

%% Sampling the impact parameter

b = sqrt(rand([1,1])) * bmax ;
% sqrt(rand([1,1]) produces a linear distribution of probability

%%%%%%%%%%%%%%%%%%%%%%%%%%%%%%%%%%%%%%%%%%%%%%%%%%%%%%%%%%%%%%%%%%%%%%%% Charge Transfer Calculations %%%%%%%%%%%%%%%%%%%%%%%%%%%%%%%%%%%%%%%%%%%%%%%%%%%%%%%%%%%%%%%%%%%%%%%%%

if b <= bc
    % Langevin Case
    % Scattering angles are distributed isotropically.
    LngCollisions = LngCollisions+1;
    phi = 2*pi* rand(1) ;
    theta = pi * rand(1) ;
    CTprobability = 0.5;
else
    if(1)
        phi = 2*pi* rand(1) ;
        btilde = b / bc;
        mmm = 2*btilde.^4 - 2*btilde.^2.*sqrt(btilde.^4-1)-1;
        Kell = ellipke(mmm);
        PHIstefan = sqrt(2)*btilde.*sqrt(btilde.^2-sqrt(btilde.^4-1)).*Kell;
        theta = -pi + 2*PHIstefan;
    end
    if (CT)
        zetaCT= (auofvelocity/sqrt(vsecvecsquare))*sqrt(pi/(2*GammaIon))...
            *(asymptcoef^2)*exp(-1/GammaIon)*(b/a0)^(2/GammaIon-1/2)...
            *exp(-b*GammaIon/a0);
        CTprobability = sin(zetaCT)^2;
    end
end

%% Calculation of the new ion velocity

if norm(vionvec) == 0
    vionvec = vionvec + 0.00001 ;
end
achsphi = vionvec / norm(vionvec) ;

```

```

achstheta = cross( achsphi, cross( [0; 0; 1], achsphi));
% Note: norm(achstheta) cannot be zero!
if norm(achstheta) == 0
    achstheta = [1; 0; 0 ];
end
achstheta = achstheta / norm(achstheta);

% Scalar product dot(achsphi, achstheta) should be zero!
rotmattheta = expm(theta * (achstheta(1)*Jx + achstheta(2)*Jy ...
+ achstheta(3)*Jz ));
rotmatphi = expm(phi * (achsphi(1)*Jx + achsphi(2)*Jy + achsphi(3)*Jz ));

% Rotation matrix R
rotationMat = rotmatphi * rotmattheta;
%%%%%%%%%%%%%%%%%%%%%%%%%%%%%%%%%%%%%%%%%%%%%%%%%%%%%%%%%%%%%%%%%%%%%%%% Charge Transfer %%%%%%%%%
if (CT)
RandomVECIndexCT=RandomVECIndexCT+1;

    if RandomVECCT(RandomVECIndexCT) < CTprobability
        %Then a charge transfer has happened

        %tVECCT(CTcounter) = t;
        vionvecf = beta*vionvec-beta * rotationMat * vionvec;
        %New ion velocity when a CT collision happens.
        vsecvecf = vionvecf;

        Eionvec = (vsecvecf.^2 + (omegavecIon .* Rsecvec).^2) * mIon / 2;
        if b>bc
            CTcounter = CTcounter+1;
            dissipatedEnergyinSwap=dissipatedEnergyinSwap+EioninkB...
            -sum(Eionvec)./kB;
            EioninkB=sum(Eionvec)./kB;
        end

    else
        %%%%%%%%%
        % New ion velocities
        vionvecf = (1- beta)*vionvec + beta * rotationMat * vionvec;

        vsecvecf = vionvecf;
        %For now the micromotion is ignored which is a justified assumption
        %taking into account the relevant energy scale and the size of the

```

```

%atom cloud

    Eionvec = (vsecvecf.^2 + (omegavecIon .* Rsecvec).^2) * mIon/2;
    EioninkB=sum(Eionvec)./kB;
    end

end

NoCT = 1-CT;
    if(NoCT)
        % New ion velocities
        vionvecf = (1- beta)*vionvec + beta * rotationMat * vionvec ;

        vsecvecf = vionvecf;

        Eionvec = (vsecvecf.^2 + (omegavecIon .* Rsecvec).^2) * mIon / 2;
        EioninkB=sum(Eionvec)./kB;
        end

%%%%%%%%%%%%%%%%%%%%%%%%%%%%%%%%%%%%%%%%%%%%%%%%%%%%%%%%%%%%%%%%%%%%%%%%
% Calculate new energies and phases

phasevec=mod(atan((omegavecIon.* Rsecvec)./ vsecvecf)-omegavecIon*t, pi);
% this current form returns the right phase for 0<phi<pi but subtracts a pi
% from the phase if pi<phi<2*pi. As long as the final energy distribution
% is concerned, this is fine due to the symmetry of the problem.

vionmax= sqrt(2*Eionvec/mIon);
%Once again the micromotion is not included
EkinMax = 0.5*mIon*sum(vionmax.*vionmax);

RateMax = MaxDensity* sigmaelConstant*(mu/mIon*EkinMax)^(-1/3)...
*(2*EkinMax/mIon)^(1/2);

    else % In this case there has been no collision
        end
%-----
end

EionVEC = [EionVECx; EionVECy; EionVECz]./kB';

```

```
totalEionVEC = EionVEC(1:3,1:end)';  
totalEion = totalEionVEC(:, 1) + totalEionVEC(:,2) + totalEionVEC(:,3);  
deltaESwap=dissipatedEnergyinSwap;  
NrofLngCollisions=LngCollisions;  
NrofSwapCollisions=CTcounter;  
InteractionTime=t;  
NrofElasticCollisions=ij;
```

```
clear phaseVECx phaseVECy phaseVECz EionVECx EionVECy EionVECz  
RsecVECx RsecVECy RsecVECz vsecVECx vsecVECy vsecVECz vmmVECx vmmVECy  
vmmVECz vionVECx vionVECy vionVECz  
%delete 1D arrays
```

```
%histoEionFull= [histoEionFull(:,1)/kB*1e3 histoEionFull(:,2)];  
%convert energy to mK  
%histoEionSec= [histoEionSec(:,1)/kB*1e3 histoEionSec(:,2)];  
%convert energy to mK
```

```
end
```


Physical Constants

Boltzmann constant	$k_B = 1.380\,649 \times 10^{-23} \text{ J K}^{-1}$ (exact)
Elementary Charge	$e = 1.602\,176\,634 \times 10^{-19} \text{ C}$ (exact)
Reduced Planck constant	$\hbar = 1.054\,571\,817 \dots \times 10^{-34} \text{ J s}$ (exact)
Speed of Light	$c = 2.997\,924\,58 \times 10^8 \text{ m s}^{-1}$ (exact)
Vacuum Permittivity	$\epsilon_0 = 8.854\,187\,812\,8(13) \times 10^{-12} \text{ F m}^{-1}$

Publications

Amir Mahdian, Artjom Krüchow, and Johannes Hecker Denschlag. “Direct observation of swap cooling in atom-ion collisions”. In: *New Journal of Physics* 23.6 (June 2021). Publisher: IOP Publishing, p. 065008. ISSN: 1367-2630. DOI: [10.1088/1367-2630/ac0575](https://doi.org/10.1088/1367-2630/ac0575). URL: <https://doi.org/10.1088/1367-2630/ac0575> (visited on 08/19/2021)

Amir Mohammadi et al. “Life and death of a cold BaRb^+ molecule inside an ultra-cold cloud of Rb atoms”. In: *Physical Review Research* 3.1 (Feb. 26, 2021). Publisher: American Physical Society, p. 013196. DOI: [10.1103/PhysRevResearch.3.013196](https://link.aps.org/doi/10.1103/PhysRevResearch.3.013196). URL: <https://link.aps.org/doi/10.1103/PhysRevResearch.3.013196> (visited on 11/19/2021)

Bibliography

- [AB01] Alexandr V. Avdeenkov and John L. Bohn. "Ultracold collisions of oxygen molecules". In: *Physical Review A* 64.5 (Oct. 2, 2001). Publisher: American Physical Society, p. 052703. DOI: [10.1103/PhysRevA.64.052703](https://doi.org/10.1103/PhysRevA.64.052703). URL: <https://link.aps.org/doi/10.1103/PhysRevA.64.052703> (visited on 11/17/2021).
- [AD05] M. Aymar and O. Dulieu. "Calculation of accurate permanent dipole moments of the lowest $1,3\Sigma^+$ states of heteronuclear alkali dimers using extended basis sets". In: *The Journal of Chemical Physics* 122.20 (May 22, 2005). Publisher: American Institute of Physics, p. 204302. ISSN: 0021-9606. DOI: [10.1063/1.1903944](https://doi.org/10.1063/1.1903944). URL: <https://aip.scitation.org/doi/10.1063/1.1903944> (visited on 11/17/2021).
- [AD06] M. Aymar and O. Dulieu. "Comment on "Calculation of accurate permanent dipole moments of the lowest $1,3\Sigma^+$ states of heteronuclear alkali dimers using extended basis sets" [J. Chem. Phys. 122, 204302 (2005)]". In: *The Journal of Chemical Physics* 125.4 (July 28, 2006). Publisher: American Institute of Physics, p. 047101. ISSN: 0021-9606. DOI: [10.1063/1.2222354](https://doi.org/10.1063/1.2222354). URL: <https://aip.scitation.org/doi/10.1063/1.2222354> (visited on 11/17/2021).
- [AD12] Mireille Aymar and Olivier Dulieu. "The electronic structure of the alkaline-earth-atom (Ca, Sr, Ba) hydride molecular ions". In: *Journal of Physics B: Atomic, Molecular and Optical Physics* 45.21 (Oct. 2012). Publisher: IOP Publishing, p. 215103. ISSN: 0953-4075. DOI: [10.1088/0953-4075/45/21/215103](https://doi.org/10.1088/0953-4075/45/21/215103). URL: <https://doi.org/10.1088/0953-4075/45/21/215103> (visited on 11/17/2021).
- [AGD11] M. Aymar, R. Guérout, and O. Dulieu. "Structure of the alkali-metal-atom + strontium molecular ions: Towards photoassociation and formation of cold molecular ions". In: *The Journal of Chemical Physics* 135.6 (Aug. 14, 2011). Publisher: American Institute of Physics, p. 064305. ISSN: 0021-9606. DOI: [10.1063/1.3611399](https://doi.org/10.1063/1.3611399). URL: <https://aip.scitation.org/doi/10.1063/1.3611399> (visited on 11/17/2021).
- [And+95] M. H. Anderson et al. "Observation of Bose-Einstein Condensation in a Dilute Atomic Vapor". In: *Science* 269.5221 (1995), pp. 198–201. ISSN: 0036-8075. DOI: [10.1126/science.269.5221.198](https://doi.org/10.1126/science.269.5221.198). eprint: <https://arxiv.org/abs/cond-mat/9503078>

- science.sciencemag.org/content/269/5221/198.full.pdf. URL: <https://science.sciencemag.org/content/269/5221/198>.
- [AS68] Milton Abramowitz and Irene A. Stegun. *Handbook of Mathematical Functions with Formulas, Graphs, and Mathematical Tables*. Google-Books-ID: ZboM5tOFWtsC. U.S. Government Printing Office, 1968. 1060 pp. ISBN: 978-0-16-000202-1.
- [Auc+14] Carolyn Auchter et al. "Measurement of the branching fractions and lifetime of the $5D_{5/2}$ level of Ba^+ ". In: *Physical Review A* 90.6 (Dec. 17, 2014). Publisher: American Physical Society, p. 060501. DOI: [10.1103/PhysRevA.90.060501](https://doi.org/10.1103/PhysRevA.90.060501). URL: <https://link.aps.org/doi/10.1103/PhysRevA.90.060501> (visited on 02/01/2022).
- [Bar+11] Julio T. Barreiro et al. "An open-system quantum simulator with trapped ions". In: *Nature* 470.7335 (Feb. 2011), pp. 486–491. ISSN: 1476-4687. DOI: [10.1038/nature09801](https://doi.org/10.1038/nature09801). URL: <https://www.nature.com/articles/nature09801> (visited on 08/04/2021).
- [Ber79] Richard Barry Bernstein, ed. *Atom - Molecule Collision Theory: A Guide for the Experimentalist*. International Studies in Economic Modelling. Springer US, 1979. ISBN: 978-0-306-40121-3. DOI: [10.1007/978-1-4613-2913-8](https://doi.org/10.1007/978-1-4613-2913-8). URL: <https://www.springer.com/gp/book/9780306401213> (visited on 02/09/2021).
- [Ber+98] D. J. Berkeland et al. "Minimization of ion micromotion in a Paul trap". In: *Journal of Applied Physics* 83.10 (May 15, 1998). Publisher: American Institute of Physics, pp. 5025–5033. ISSN: 0021-8979. DOI: [10.1063/1.367318](https://doi.org/10.1063/1.367318). URL: <https://aip.scitation.org/doi/10.1063/1.367318> (visited on 10/19/2021).
- [BH06] Ģirts Barinovs and Marc C. van Hemert. "CH⁺ Radiative Association". In: *The Astrophysical Journal* 636.2 (Jan. 2006). Publisher: American Astronomical Society, pp. 923–926. ISSN: 0004-637X. DOI: [10.1086/498080](https://doi.org/10.1086/498080). URL: <https://doi.org/10.1086/498080> (visited on 10/06/2021).
- [Bis+13] U. Bissbort et al. "Emulating Solid-State Physics with a Hybrid System of Ultracold Ions and Atoms". In: *Physical Review Letters* 111.8 (Aug. 20, 2013). Publisher: American Physical Society, p. 080501. DOI: [10.1103/PhysRevLett.111.080501](https://doi.org/10.1103/PhysRevLett.111.080501). URL: <https://link.aps.org/doi/10.1103/PhysRevLett.111.080501> (visited on 08/13/2021).
- [Biz+99] S. Bize et al. "High-accuracy measurement of the ^{87}Rb ground-state hyperfine splitting in an atomic fountain". In: *Europhysics Letters* 45.5 (Mar. 1, 1999). Publisher: IOP Publishing, p. 558. ISSN: 0295-5075. DOI: [10.1209/epl/i1999-00203-9](https://doi.org/10.1209/epl/i1999-00203-9). URL: <https://iopscience.iop.org/article/10.1209/epl/i1999-00203-9/meta> (visited on 01/19/2022).

- [Bou+10] Thomas Bouissou et al. "A comprehensive theoretical investigation of the electronic states of Ca_2 up to the $\text{Ca}(4s^2\ ^1\text{S})+\text{Ca}(4s5p\ ^1\text{P})$ dissociation limit". In: *The Journal of Chemical Physics* 133.16 (Oct. 28, 2010). Publisher: American Institute of Physics, p. 164317. ISSN: 0021-9606. DOI: [10.1063/1.3503655](https://doi.org/10.1063/1.3503655). URL: <https://aip.scitation.org/doi/10.1063/1.3503655> (visited on 11/17/2021).
- [BR12] R. Blatt and C. F. Roos. "Quantum simulations with trapped ions". In: *Nature Physics* 8.4 (Apr. 2012), pp. 277–284. ISSN: 1745-2481. DOI: [10.1038/nphys2252](https://doi.org/10.1038/nphys2252). URL: <https://www.nature.com/articles/nphys2252> (visited on 08/04/2021).
- [Bra90] B. H. Bransden. "Charge exchange in ion-atom collisions". In: *Contemporary Physics* 31.1 (Jan. 1, 1990). Publisher: Taylor & Francis. eprint: <https://doi.org/10.1080/00107519008221998>, pp. 19–33. ISSN: 0010-7514. DOI: [10.1080/00107519008221998](https://doi.org/10.1080/00107519008221998). URL: <https://doi.org/10.1080/00107519008221998> (visited on 10/26/2021).
- [Bra+95] C. C. Bradley et al. "Evidence of Bose-Einstein Condensation in an Atomic Gas with Attractive Interactions". In: *Phys. Rev. Lett.* 75 (9 1995), pp. 1687–1690. DOI: [10.1103/PhysRevLett.75.1687](https://doi.org/10.1103/PhysRevLett.75.1687). URL: <https://link.aps.org/doi/10.1103/PhysRevLett.75.1687>.
- [Bru+19] Colin D. Bruzewicz et al. "Trapped-ion quantum computing: Progress and challenges". In: *Applied Physics Reviews* 6.2 (2019), p. 021314. DOI: [10.1063/1.5088164](https://doi.org/10.1063/1.5088164). eprint: <https://doi.org/10.1063/1.5088164>. URL: <https://doi.org/10.1063/1.5088164>.
- [BTG11] S. Bovino, M. Tacconi, and F. A. Gianturco. "PHOTON-INDUCED EVOLUTIONARY RATES OF $\text{LiHe}^+(\ ^1\Sigma^+)$ IN EARLY UNIVERSE FROM ACCURATE QUANTUM COMPUTATIONS". In: 740.2 (Oct. 2011). Publisher: American Astronomical Society, p. 101. ISSN: 0004-637X. DOI: [10.1088/0004-637X/740/2/101](https://doi.org/10.1088/0004-637X/740/2/101). URL: <https://doi.org/10.1088/0004-637X/740/2/101> (visited on 11/17/2021).
- [Bur+97] E. A. Burt et al. "Coherence, Correlations, and Collisions: What One Learns about Bose-Einstein Condensates from Their Decay". In: *Physical Review Letters* 79.3 (July 21, 1997). Publisher: American Physical Society, pp. 337–340. DOI: [10.1103/PhysRevLett.79.337](https://doi.org/10.1103/PhysRevLett.79.337). URL: <https://link.aps.org/doi/10.1103/PhysRevLett.79.337> (visited on 11/10/2021).
- [BZD08] E. Bodo, P. Zhang, and A. Dalgarno. "Ultra-cold ion-atom collisions: near resonant charge exchange". In: *New Journal of Physics* 10.3 (Mar. 2008). Publisher: IOP Publishing, p. 033024. ISSN: 1367-2630. DOI: [10.1088/1367-2630/10/3/033024](https://doi.org/10.1088/1367-2630/10/3/033024). URL: <https://doi.org/10.1088/1367-2630/10/3/033024> (visited on 08/11/2021).

- [CÔ0] Robin Côté. “From Classical Mobility to Hopping Conductivity: Charge Hopping in an Ultracold Gas”. In: *Physical Review Letters* 85.25 (Dec. 18, 2000). Publisher: American Physical Society, pp. 5316–5319. DOI: [10.1103/PhysRevLett.85.5316](https://doi.org/10.1103/PhysRevLett.85.5316). URL: <https://link.aps.org/doi/10.1103/PhysRevLett.85.5316> (visited on 08/10/2021).
- [CÎ6] R. Côté. “Chapter Two - Ultracold Hybrid Atom-Ion Systems”. In: *Advances In Atomic, Molecular, and Optical Physics*. Ed. by Ennio Arimondo, Chun C. Lin, and Susanne F. Yelin. Vol. 65. Academic Press, Jan. 1, 2016, pp. 67–126. DOI: [10.1016/bs.aamop.2016.04.004](https://doi.org/10.1016/bs.aamop.2016.04.004). URL: <https://www.sciencedirect.com/science/article/pii/S1049250X16300088> (visited on 10/11/2021).
- [CD00] R. Côté and A. Dalgarno. “Ultracold atom-ion collisions”. In: *Physical Review A* 62.1 (June 14, 2000). Publisher: American Physical Society, p. 012709. DOI: [10.1103/PhysRevA.62.012709](https://doi.org/10.1103/PhysRevA.62.012709). URL: <https://link.aps.org/doi/10.1103/PhysRevA.62.012709> (visited on 08/10/2021).
- [Chi+10] Cheng Chin et al. “Feshbach resonances in ultracold gases”. In: *Reviews of Modern Physics* 82.2 (Apr. 29, 2010). Publisher: American Physical Society, pp. 1225–1286. DOI: [10.1103/RevModPhys.82.1225](https://doi.org/10.1103/RevModPhys.82.1225). URL: <https://link.aps.org/doi/10.1103/RevModPhys.82.1225> (visited on 11/10/2021).
- [Chu98] Steven Chu. “Nobel Lecture: The manipulation of neutral particles”. In: *Rev. Mod. Phys.* 70 (3 1998), pp. 685–706. DOI: [10.1103/RevModPhys.70.685](https://doi.org/10.1103/RevModPhys.70.685). URL: <https://link.aps.org/doi/10.1103/RevModPhys.70.685>.
- [CKL02] R. Côté, V. Kharchenko, and M. D. Lukin. “Mesoscopic Molecular Ions in Bose-Einstein Condensates”. In: *Physical Review Letters* 89.9 (Aug. 9, 2002). Publisher: American Physical Society, p. 093001. DOI: [10.1103/PhysRevLett.89.093001](https://doi.org/10.1103/PhysRevLett.89.093001). URL: <https://link.aps.org/doi/10.1103/PhysRevLett.89.093001> (visited on 08/11/2021).
- [Clo+16] Govinda Clos et al. “Time-Resolved Observation of Thermalization in an Isolated Quantum System”. In: *Physical Review Letters* 117.17 (Oct. 19, 2016). Publisher: American Physical Society, p. 170401. DOI: [10.1103/PhysRevLett.117.170401](https://doi.org/10.1103/PhysRevLett.117.170401). URL: <https://link.aps.org/doi/10.1103/PhysRevLett.117.170401> (visited on 08/05/2021).
- [CSH14] Kuang Chen, Scott T. Sullivan, and Eric R. Hudson. “Neutral Gas Sympathetic Cooling of an Ion in a Paul Trap”. In: *Physical Review Letters* 112.14 (Apr. 11, 2014). Publisher: American Physical Society, p. 143009. DOI: [10.1103/PhysRevLett.112.143009](https://doi.org/10.1103/PhysRevLett.112.143009). URL: <https://link.aps.org/doi/10.1103/PhysRevLett.112.143009> (visited on 09/22/2021).

- [CT98] Claude N. Cohen-Tannoudji. “Nobel Lecture: Manipulating atoms with photons”. In: *Rev. Mod. Phys.* 70 (3 1998), pp. 707–719. DOI: [10.1103/RevModPhys.70.707](https://doi.org/10.1103/RevModPhys.70.707). URL: <https://link.aps.org/doi/10.1103/RevModPhys.70.707>.
- [CTD11] W. Casteels, J. Tempere, and J. T. Devreese. “Polaronic Properties of an Ion in a Bose-Einstein Condensate in the Strong-Coupling Limit”. In: *Journal of Low Temperature Physics* 162.3 (Feb. 1, 2011), pp. 266–273. ISSN: 1573-7357. DOI: [10.1007/s10909-010-0286-0](https://doi.org/10.1007/s10909-010-0286-0). URL: <https://doi.org/10.1007/s10909-010-0286-0> (visited on 08/11/2021).
- [Cur04] J. J. Curry. “Compilation of Wavelengths, Energy Levels, and Transition Probabilities for Ba I and Ba II”. In: *Journal of Physical and Chemical Reference Data* 33.3 (Sept. 2004), pp. 725–746. ISSN: 0047-2689, 1529-7845. DOI: [10.1063/1.1643404](https://doi.org/10.1063/1.1643404). URL: <http://aip.scitation.org/doi/10.1063/1.1643404> (visited on 01/19/2022).
- [CZ95] J. I. Cirac and P. Zoller. “Quantum Computations with Cold Trapped Ions”. In: *Phys. Rev. Lett.* 74 (20 1995), pp. 4091–4094. DOI: [10.1103/PhysRevLett.74.4091](https://doi.org/10.1103/PhysRevLett.74.4091). URL: <https://link.aps.org/doi/10.1103/PhysRevLett.74.4091>.
- [Dav+95] K. B. Davis et al. “Bose-Einstein Condensation in a Gas of Sodium Atoms”. In: *Phys. Rev. Lett.* 75 (22 1995), pp. 3969–3973. DOI: [10.1103/PhysRevLett.75.3969](https://doi.org/10.1103/PhysRevLett.75.3969). URL: <https://link.aps.org/doi/10.1103/PhysRevLett.75.3969>.
- [DB58] Alexander Dalgarno and David Robert Bates. “The mobilities of ions in their parent gases”. In: *Philosophical Transactions of the Royal Society of London. Series A, Mathematical and Physical Sciences* (Apr. 17, 1958). Publisher: The Royal Society London. DOI: [10.1098/rsta.1958.0003](https://doi.org/10.1098/rsta.1958.0003). URL: <https://royalsocietypublishing.org/doi/abs/10.1098/rsta.1958.0003> (visited on 10/20/2021).
- [DB74] Ph. Durand and J. C. Barthelat. “New atomic pseudopotentials for electronic structure calculations of molecules and solids”. In: *Chemical Physics Letters* 27.2 (July 15, 1974), pp. 191–194. ISSN: 0009-2614. DOI: [10.1016/0009-2614\(74\)90201-2](https://doi.org/10.1016/0009-2614(74)90201-2). URL: <https://www.sciencedirect.com/science/article/pii/0009261474902012> (visited on 11/17/2021).
- [DB75] Philippe Durand and Jean-Claude Barthelat. “A theoretical method to determine atomic pseudopotentials for electronic structure calculations of molecules and solids”. In: *Theoretica chimica acta* 38.4 (Dec. 1, 1975), pp. 283–302. ISSN: 1432-2234. DOI: [10.1007/BF00963468](https://doi.org/10.1007/BF00963468). URL: <https://doi.org/10.1007/BF00963468> (visited on 11/17/2021).

- [DDY90] A. Dalgarno, M. L. Du, and J. H. You. “The Radiative Association of C and O and C⁺ and O”. In: *The Astrophysical Journal* 349 (Feb. 1, 1990). ADS Bibcode: 1990ApJ...349..675D, p. 675. ISSN: 0004-637X. DOI: [10.1086/168355](https://ui.adsabs.harvard.edu/abs/1990ApJ...349..675D). URL: <https://ui.adsabs.harvard.edu/abs/1990ApJ...349..675D> (visited on 10/06/2021).
- [Dei+12] J. Deiglmayr et al. “Reactive collisions of trapped anions with ultracold atoms”. In: *Physical Review A* 86.4 (Oct. 31, 2012). Publisher: American Physical Society, p. 043438. DOI: [10.1103/PhysRevA.86.043438](https://link.aps.org/doi/10.1103/PhysRevA.86.043438). URL: <https://link.aps.org/doi/10.1103/PhysRevA.86.043438> (visited on 11/12/2021).
- [DIC10] Hauke Doerk, Zbigniew Idziaszek, and Tommaso Calarco. “Atom-ion quantum gate”. In: *Physical Review A* 81.1 (Jan. 26, 2010). Publisher: American Physical Society, p. 012708. DOI: [10.1103/PhysRevA.81.012708](https://link.aps.org/doi/10.1103/PhysRevA.81.012708). URL: <https://link.aps.org/doi/10.1103/PhysRevA.81.012708> (visited on 08/11/2021).
- [Die+20] T. Dieterle et al. “Inelastic collision dynamics of a single cold ion immersed in a Bose-Einstein condensate”. In: *Physical Review A* 102.4 (Oct. 20, 2020), p. 041301. ISSN: 2469-9926, 2469-9934. DOI: [10.1103/PhysRevA.102.041301](https://link.aps.org/doi/10.1103/PhysRevA.102.041301). URL: <https://link.aps.org/doi/10.1103/PhysRevA.102.041301> (visited on 02/09/2021).
- [DJ99] B. DeMarco and D. S. Jin. “Onset of Fermi Degeneracy in a Trapped Atomic Gas”. In: *Science* 285.5434 (1999), pp. 1703–1706. ISSN: 0036-8075. DOI: [10.1126/science.285.5434.1703](https://science.sciencemag.org/content/285/5434/1703.full.pdf). eprint: <https://science.sciencemag.org/content/285/5434/1703.full.pdf>. URL: <https://science.sciencemag.org/content/285/5434/1703>.
- [DM10] L.-M. Duan and C. Monroe. “Colloquium: Quantum networks with trapped ions”. In: *Rev. Mod. Phys.* 82 (2 2010), pp. 1209–1224. DOI: [10.1103/RevModPhys.82.1209](https://link.aps.org/doi/10.1103/RevModPhys.82.1209). URL: <https://link.aps.org/doi/10.1103/RevModPhys.82.1209>.
- [DO18] Olivier Dulieu and Andreas Osterwalder, eds. *Cold Chemistry: Molecular Scattering and Reactivity Near Absolute Zero*. Theoretical and Computational Chemistry Series. The Royal Society of Chemistry, 2018. P001–670. ISBN: 978-1-78262-597-1. DOI: [10.1039/9781782626800](http://dx.doi.org/10.1039/9781782626800). URL: <http://dx.doi.org/10.1039/9781782626800>.
- [Dor+09] S. Charles Doret et al. “Buffer-Gas Cooled Bose-Einstein Condensate”. In: *Physical Review Letters* 103.10 (Sept. 3, 2009). Publisher: American Physical Society, p. 103005. DOI: [10.1103/PhysRevLett.103.103005](https://link.aps.org/doi/10.1103/PhysRevLett.103.103005). URL: <https://link.aps.org/doi/10.1103/PhysRevLett.103.103005> (visited on 10/25/2021).

- [Dör+19] Alexander D. Dörfler et al. “Long-range versus short-range effects in cold molecular ion-neutral collisions”. In: *Nature Communications* 10.1 (Nov. 28, 2019), p. 5429. ISSN: 2041-1723. DOI: [10.1038/s41467-019-13218-x](https://doi.org/10.1038/s41467-019-13218-x). URL: <https://www.nature.com/articles/s41467-019-13218-x> (visited on 08/20/2021).
- [DR18] Sourav Dutta and S. A. Rangwala. “Cooling of trapped ions by resonant charge exchange”. In: *Physical Review A* 97.4 (Apr. 6, 2018). Publisher: American Physical Society, p. 041401. DOI: [10.1103/PhysRevA.97.041401](https://doi.org/10.1103/PhysRevA.97.041401). URL: <https://link.aps.org/doi/10.1103/PhysRevA.97.041401> (visited on 08/19/2021).
- [DRB65] Alexander Dalgarno, M. R. H. Rudge, and David Robert Bates. “Spin-change cross-sections for collisions between alkali atoms”. In: *Proceedings of the Royal Society of London. Series A. Mathematical and Physical Sciences* 286.1407 (Aug. 3, 1965). Publisher: Royal Society, pp. 519–524. DOI: [10.1098/rspa.1965.0161](https://doi.org/10.1098/rspa.1965.0161). URL: <https://royalsocietypublishing.org/doi/10.1098/rspa.1965.0161> (visited on 11/17/2021).
- [Ebe+16] Pascal Eberle et al. “A Dynamic Ion-Atom Hybrid Trap for High Resolution Cold-Collision Studies”. In: *ChemPhysChem* 17.22 (2016), pp. 3769–3775. ISSN: 1439-7641. DOI: [10.1002/cphc.201600643](https://doi.org/10.1002/cphc.201600643). URL: <https://chemistry-europe.onlinelibrary.wiley.com/doi/abs/10.1002/cphc.201600643> (visited on 08/23/2021).
- [EFG15] J. Eisert, M. Friesdorf, and C. Gogolin. “Quantum many-body systems out of equilibrium”. In: *Nature Physics* 11.2 (Feb. 2015), pp. 124–130. ISSN: 1745-2481. DOI: [10.1038/nphys3215](https://doi.org/10.1038/nphys3215). URL: <https://www.nature.com/articles/nphys3215> (visited on 08/05/2021).
- [Ewa+19] N. V. Ewald et al. “Observation of Interactions between Trapped Ions and Ultracold Rydberg Atoms”. In: *Physical Review Letters* 122.25 (June 28, 2019). Publisher: American Physical Society, p. 253401. DOI: [10.1103/PhysRevLett.122.253401](https://doi.org/10.1103/PhysRevLett.122.253401). URL: <https://link.aps.org/doi/10.1103/PhysRevLett.122.253401> (visited on 08/20/2021).
- [Fel+20] T. Feldker et al. “Buffer gas cooling of a trapped ion to the quantum regime”. In: *Nature Physics* 16.4 (Apr. 2020), pp. 413–416. ISSN: 1745-2481. DOI: [10.1038/s41567-019-0772-5](https://doi.org/10.1038/s41567-019-0772-5). URL: <https://www.nature.com/articles/s41567-019-0772-5> (visited on 08/20/2021).
- [Fey82] Richard P. Feynman. “Simulating physics with computers”. In: *International Journal of Theoretical Physics* 21.6 (June 1, 1982), pp. 467–488. ISSN: 1572-9575. DOI: [10.1007/BF02650179](https://doi.org/10.1007/BF02650179). URL: <https://doi.org/10.1007/BF02650179> (visited on 08/04/2021).

- [FMD92] M. Foucrault, Ph. Millie, and J. P. Daudey. “Nonperturbative method for core-valence correlation in pseudopotential calculations: Application to the Rb_2 and Cs_2 molecules”. In: *The Journal of Chemical Physics* 96.2 (Jan. 15, 1992). Publisher: American Institute of Physics, pp. 1257–1264. ISSN: 0021-9606. DOI: [10.1063/1.462162](https://doi.org/10.1063/1.462162). URL: <https://aip.scitation.org/doi/10.1063/1.462162> (visited on 11/17/2021).
- [FR87] Patricio Fuentealba and Orfa Reyes. “Pseudopotential calculations on the ground state of the alkaline-earth monohydride ions”. In: *Molecular Physics* 62.6 (Dec. 20, 1987), pp. 1291–1296. ISSN: 0026-8976. DOI: [10.1080/00268978700102971](https://doi.org/10.1080/00268978700102971). URL: <https://doi.org/10.1080/00268978700102971> (visited on 11/17/2021).
- [Fri+08] A. Friedenauer et al. “Simulating a quantum magnet with trapped ions”. In: *Nature Physics* 4.10 (Oct. 2008), pp. 757–761. ISSN: 1745-2481. DOI: [10.1038/nphys1032](https://doi.org/10.1038/nphys1032). URL: <https://www.nature.com/articles/nphys1032> (visited on 08/04/2021).
- [FRS96] P. O. Fedichev, M. W. Reynolds, and G. V. Shlyapnikov. “Three-Body Recombination of Ultracold Atoms to a Weakly Bound s Level”. In: *Physical Review Letters* 77.14 (Sept. 30, 1996). Publisher: American Physical Society, pp. 2921–2924. DOI: [10.1103/PhysRevLett.77.2921](https://doi.org/10.1103/PhysRevLett.77.2921). URL: <https://link.aps.org/doi/10.1103/PhysRevLett.77.2921> (visited on 11/10/2021).
- [Fue+85] P. Fuentealba et al. “Pseudopotential calculations for alkaline-earth atoms”. In: *Journal of Physics B: Atomic and Molecular Physics* 18.7 (Apr. 1985). Publisher: IOP Publishing, pp. 1287–1296. ISSN: 0022-3700. DOI: [10.1088/0022-3700/18/7/010](https://doi.org/10.1088/0022-3700/18/7/010). URL: <https://doi.org/10.1088/0022-3700/18/7/010> (visited on 11/17/2021).
- [Für+18] H. Fürst et al. “Dynamics of a single ion-spin impurity in a spin-polarized atomic bath”. In: *Physical Review A* 98.1 (July 27, 2018). Publisher: American Physical Society, p. 012713. DOI: [10.1103/PhysRevA.98.012713](https://doi.org/10.1103/PhysRevA.98.012713). URL: <https://link.aps.org/doi/10.1103/PhysRevA.98.012713> (visited on 08/17/2021).
- [GAD10] R. Guérout, M. Aymar, and O. Dulieu. “Ground state of the polar alkali-metal-atom-strontium molecules: Potential energy curve and permanent dipole moment”. In: *Physical Review A* 82.4 (Oct. 15, 2010). Publisher: American Physical Society, p. 042508. DOI: [10.1103/PhysRevA.82.042508](https://doi.org/10.1103/PhysRevA.82.042508). URL: <https://link.aps.org/doi/10.1103/PhysRevA.82.042508> (visited on 11/17/2021).
- [Gao10] Bo Gao. “Universal Properties in Ultracold Ion-Atom Interactions”. In: *Physical Review Letters* 104.21 (May 25, 2010). Publisher: American Physical Society, p. 213201. DOI: [10.1103/PhysRevLett.104.213201](https://doi.org/10.1103/PhysRevLett.104.213201). URL:

- <https://link.aps.org/doi/10.1103/PhysRevLett.104.213201>
(visited on 08/13/2021).
- [GC+14] Susana Gómez-Carrasco et al. “OH⁺ IN ASTROPHYSICAL MEDIA: STATE-TO-STATE FORMATION RATES, EINSTEIN COEFFICIENTS AND INELASTIC COLLISION RATES WITH He”. In: *The Astrophysical Journal* 794.1 (Sept. 2014). Publisher: American Astronomical Society, p. 33. ISSN: 0004-637X. DOI: [10.1088/0004-637x/794/1/33](https://doi.org/10.1088/0004-637x/794/1/33). URL: <https://doi.org/10.1088/0004-637x/794/1/33> (visited on 09/23/2021).
- [Ger08] D. Gerlich. “The Study of Cold Collisions Using Ion Guides and Traps”. In: *Low Temperatures and Cold Molecules*. PUBLISHED BY IMPERIAL COLLEGE PRESS AND DISTRIBUTED BY WORLD SCIENTIFIC PUBLISHING CO., Sept. 1, 2008, pp. 121–174. ISBN: 978-1-84816-209-9. DOI: [10.1142/9781848162105_0003](https://doi.org/10.1142/9781848162105_0003). URL: https://www.worldscientific.com/doi/abs/10.1142/9781848162105_0003 (visited on 11/10/2021).
- [GGPR17] Chris H. Greene, P. Giannakeas, and J. Pérez-Ríos. “Universal few-body physics and cluster formation”. In: *Reviews of Modern Physics* 89.3 (Aug. 28, 2017). Publisher: American Physical Society, p. 035006. DOI: [10.1103/RevModPhys.89.035006](https://doi.org/10.1103/RevModPhys.89.035006). URL: <https://link.aps.org/doi/10.1103/RevModPhys.89.035006> (visited on 11/10/2021).
- [Gla63a] Roy J. Glauber. “Coherent and Incoherent States of the Radiation Field”. In: *Phys. Rev.* 131 (6 1963), pp. 2766–2788. DOI: [10.1103/PhysRev.131.2766](https://doi.org/10.1103/PhysRev.131.2766). URL: <https://link.aps.org/doi/10.1103/PhysRev.131.2766>.
- [Gla63b] Roy J. Glauber. “The Quantum Theory of Optical Coherence”. In: *Phys. Rev.* 130 (6 1963), pp. 2529–2539. DOI: [10.1103/PhysRev.130.2529](https://doi.org/10.1103/PhysRev.130.2529). URL: <https://link.aps.org/doi/10.1103/PhysRev.130.2529>.
- [Goo+10] J. Goold et al. “Ion-induced density bubble in a strongly correlated one-dimensional gas”. In: *Physical Review A* 81.4 (Apr. 5, 2010). Publisher: American Physical Society, p. 041601. DOI: [10.1103/PhysRevA.81.041601](https://doi.org/10.1103/PhysRevA.81.041601). URL: <https://link.aps.org/doi/10.1103/PhysRevA.81.041601> (visited on 08/11/2021).
- [Goo+15] D. S. Goodman et al. “Measurement of the low-energy Na⁺- Na total collision rate in an ion-neutral hybrid trap”. In: *Physical Review A* 91.1 (Jan. 20, 2015). Publisher: American Physical Society, p. 012709. DOI: [10.1103/PhysRevA.91.012709](https://doi.org/10.1103/PhysRevA.91.012709). URL: <https://link.aps.org/doi/10.1103/PhysRevA.91.012709> (visited on 11/10/2021).
- [Gre+15] Maxwell D. Gregoire et al. “Measurements of the ground-state polarizabilities of Cs, Rb, and K using atom interferometry”. In: *Physical Review A* 92.5 (Nov. 20, 2015). Publisher: American Physical Society, p. 052513. DOI: [10.1103/PhysRevA.92.052513](https://doi.org/10.1103/PhysRevA.92.052513). URL: <https://link.aps.org/doi/10.1103/PhysRevA.92.052513> (visited on 11/17/2021).

- [Gri+09] Andrew T. Grier et al. "Observation of Cold Collisions between Trapped Ions and Trapped Atoms". In: *Physical Review Letters* 102.22 (June 4, 2009). Publisher: American Physical Society, p. 223201. DOI: [10.1103/PhysRevLett.102.223201](https://doi.org/10.1103/PhysRevLett.102.223201). URL: <https://link.aps.org/doi/10.1103/PhysRevLett.102.223201> (visited on 08/16/2021).
- [GS58] George Gioumouisis and D. P. Stevenson. "Reactions of Gaseous Molecule Ions with Gaseous Molecules. V. Theory". In: *The Journal of Chemical Physics* 29.2 (Aug. 1, 1958). Publisher: American Institute of Physics, pp. 294–299. ISSN: 0021-9606. DOI: [10.1063/1.1744477](https://doi.org/10.1063/1.1744477). URL: <https://aip.scitation.org/doi/10.1063/1.1744477> (visited on 10/07/2021).
- [Hal+11] Felix H. J. Hall et al. "Light-Assisted Ion-Neutral Reactive Processes in the Cold Regime: Radiative Molecule Formation versus Charge Exchange". In: *Physical Review Letters* 107.24 (Dec. 7, 2011). Publisher: American Physical Society, p. 243202. DOI: [10.1103/PhysRevLett.107.243202](https://doi.org/10.1103/PhysRevLett.107.243202). URL: <https://link.aps.org/doi/10.1103/PhysRevLett.107.243202> (visited on 08/19/2021).
- [Hal+13a] Felix H.J. Hall et al. "Ion-neutral chemistry at ultralow energies: dynamics of reactive collisions between laser-cooled Ca^+ ions and Rb atoms in an ion-atom hybrid trap". In: *Molecular Physics* 111.14 (Aug. 1, 2013), pp. 2020–2032. ISSN: 0026-8976. DOI: [10.1080/00268976.2013.780107](https://doi.org/10.1080/00268976.2013.780107). URL: <https://doi.org/10.1080/00268976.2013.780107> (visited on 08/19/2021).
- [Hal+13b] Felix H.J. Hall et al. "Light-assisted cold chemical reactions of barium ions with rubidium atoms". In: *Molecular Physics* 111.12 (July 1, 2013), pp. 1683–1690. ISSN: 0026-8976. DOI: [10.1080/00268976.2013.770930](https://doi.org/10.1080/00268976.2013.770930). URL: <https://doi.org/10.1080/00268976.2013.770930> (visited on 11/19/2021).
- [Ham+07] K. Hammami et al. "Rotational excitation of HOCO^+ by helium at low temperature". In: *Astronomy & Astrophysics* 462.2 (Feb. 1, 2007). Number: 2 Publisher: EDP Sciences, pp. 789–794. ISSN: 0004-6361, 1432-0746. DOI: [10.1051/0004-6361:20066316](https://doi.org/10.1051/0004-6361:20066316). URL: <https://www.aanda.org/articles/aa/abs/2007/05/aa6316-06/aa6316-06.html> (visited on 09/23/2021).
- [Han+14] A. K. Hansen et al. "Efficient rotational cooling of Coulomb-crystallized molecular ions by a helium buffer gas". In: *Nature* 508.7494 (Apr. 2014), pp. 76–79. ISSN: 1476-4687. DOI: [10.1038/nature12996](https://doi.org/10.1038/nature12996). URL: <https://www.nature.com/articles/nature12996> (visited on 09/23/2021).
- [Här+12] Arne Härter et al. "Single Ion as a Three-Body Reaction Center in an Ultracold Atomic Gas". In: *Physical Review Letters* 109.12 (Sept. 18, 2012), p. 123201. ISSN: 0031-9007, 1079-7114. DOI: [10.1103/PhysRevLett.109.123201](https://doi.org/10.1103/PhysRevLett.109.123201).

123201. URL: <https://link.aps.org/doi/10.1103/PhysRevLett.109.123201> (visited on 01/27/2021).
- [Här13] Arne Härter. “Two-body and three-body dynamics in atom-ion experiments”. Accepted: 2016-03-15T09:05:00Z. Dissertation. Universität Ulm, June 6, 2013. DOI: [10.18725/OPARU-2612](https://doi.org/10.18725/OPARU-2612). URL: <https://oparu.uni-ulm.de/xmlui/handle/123456789/2639> (visited on 10/18/2021).
- [Här+13a] A. Härter et al. “Minimization of ion micromotion using ultracold atomic probes”. In: *Applied Physics Letters* 102.22 (June 3, 2013). Publisher: American Institute of Physics, p. 221115. ISSN: 0003-6951. DOI: [10.1063/1.4809578](https://doi.org/10.1063/1.4809578). URL: <https://aip.scitation.org/doi/10.1063/1.4809578> (visited on 08/18/2021).
- [Här+13b] A. Härter et al. “Population distribution of product states following three-body recombination in an ultracold atomic gas”. In: *Nature Physics* 9.8 (Aug. 2013), pp. 512–517. ISSN: 1745-2473, 1745-2481. DOI: [10.1038/nphys2661](https://doi.org/10.1038/nphys2661). URL: <http://www.nature.com/articles/nphys2661> (visited on 01/27/2021).
- [Hau+15] Daniel Hauser et al. “Rotational state-changing cold collisions of hydroxyl ions with helium”. In: *Nature Physics* 11.6 (June 2015), pp. 467–470. ISSN: 1745-2481. DOI: [10.1038/nphys3326](https://doi.org/10.1038/nphys3326). URL: <https://www.nature.com/articles/nphys3326> (visited on 11/12/2021).
- [Haz+13] Shinsuke Haze et al. “Observation of elastic collisions between lithium atoms and calcium ions”. In: *Physical Review A* 87.5 (May 28, 2013). Publisher: American Physical Society, p. 052715. DOI: [10.1103/PhysRevA.87.052715](https://doi.org/10.1103/PhysRevA.87.052715). URL: <https://link.aps.org/doi/10.1103/PhysRevA.87.052715> (visited on 08/16/2021).
- [Haz+15] Shinsuke Haze et al. “Charge-exchange collisions between ultracold fermionic lithium atoms and calcium ions”. In: *Physical Review A* 91.3 (Mar. 30, 2015). Publisher: American Physical Society, p. 032709. DOI: [10.1103/PhysRevA.91.032709](https://doi.org/10.1103/PhysRevA.91.032709). URL: <https://link.aps.org/doi/10.1103/PhysRevA.91.032709> (visited on 08/17/2021).
- [HH08] Niels E. Henriksen and Flemming Y. Hansen. *Theories of Molecular Reaction Dynamics: The Microscopic Foundation of Chemical Kinetics*. Oxford Graduate Texts. Oxford: Oxford University Press, 2008. 392 pp. ISBN: 978-0-19-920386-4. DOI: [10.1093/acprof:oso/9780199203864.001.0001](https://doi.org/10.1093/acprof:oso/9780199203864.001.0001). (Visited on 08/31/2021).
- [HHD14] A. Härter and J. Hecker Denschlag. “Cold atom-ion experiments in hybrid traps”. In: *Contemporary Physics* 55.1 (Jan. 2, 2014), pp. 33–45. ISSN: 0010-7514. DOI: [10.1080/00107514.2013.854618](https://doi.org/10.1080/00107514.2013.854618). URL: <https://doi.org/10.1080/00107514.2013.854618> (visited on 08/24/2021).

- [HMR73] B. Huron, J. P. Malrieu, and P. Rancurel. "Iterative perturbation calculations of ground and excited state energies from multiconfigurational zeroth-order wavefunctions". In: *The Journal of Chemical Physics* 58.12 (June 15, 1973). Publisher: American Institute of Physics, pp. 5745–5759. ISSN: 0021-9606. DOI: [10.1063/1.1679199](https://doi.org/10.1063/1.1679199). URL: <https://aip.scitation.org/doi/10.1063/1.1679199> (visited on 11/17/2021).
- [Hom+09] Jonathan P. Home et al. "Complete Methods Set for Scalable Ion Trap Quantum Information Processing". In: *Science* 325.5945 (2009), pp. 1227–1230. ISSN: 0036-8075. DOI: [10.1126/science.1177077](https://doi.org/10.1126/science.1177077). URL: <https://science.sciencemag.org/content/325/5945/1227>.
- [HS06] Jeremy M. Hutson and Pavel Soldán. "Molecule formation in ultracold atomic gases". In: *International Reviews in Physical Chemistry* 25.4 (Oct. 1, 2006). Publisher: Taylor & Francis, pp. 497–526. ISSN: 0144-235X. DOI: [10.1080/01442350600921772](https://doi.org/10.1080/01442350600921772). URL: <https://doi.org/10.1080/01442350600921772> (visited on 11/10/2021).
- [HS15] Brianna R. Heazlewood and Timothy P. Softley. "Low-Temperature Kinetics and Dynamics with Coulomb Crystals". In: *Annual Review of Physical Chemistry* 66.1 (2015), pp. 475–495. DOI: [10.1146/annurev-physchem-040214-121527](https://doi.org/10.1146/annurev-physchem-040214-121527). URL: <https://doi.org/10.1146/annurev-physchem-040214-121527>.
- [Hud09] Eric R. Hudson. "Method for producing ultracold molecular ions". In: *Physical Review A* 79.3 (Mar. 31, 2009). Publisher: American Physical Society, p. 032716. DOI: [10.1103/PhysRevA.79.032716](https://doi.org/10.1103/PhysRevA.79.032716). URL: <https://link.aps.org/doi/10.1103/PhysRevA.79.032716> (visited on 08/16/2021).
- [HW05] Annie Hansson and James K. G. Watson. "A comment on Hönl-London factors". In: *Journal of Molecular Spectroscopy* 233.2 (Oct. 1, 2005), pp. 169–173. ISSN: 0022-2852. DOI: [10.1016/j.jms.2005.06.009](https://doi.org/10.1016/j.jms.2005.06.009). URL: <https://www.sciencedirect.com/science/article/pii/S0022285205001384> (visited on 11/17/2021).
- [HW12] Felix H. J. Hall and Stefan Willitsch. "Millikelvin Reactive Collisions between Sympathetically Cooled Molecular Ions and Laser-Cooled Atoms in an Ion-Atom Hybrid Trap". In: *Physical Review Letters* 109.23 (Dec. 5, 2012). Publisher: American Physical Society, p. 233202. DOI: [10.1103/PhysRevLett.109.233202](https://doi.org/10.1103/PhysRevLett.109.233202). URL: <https://link.aps.org/doi/10.1103/PhysRevLett.109.233202> (visited on 08/17/2021).
- [ICZ07] Zbigniew Idziaszek, Tommaso Calarco, and Peter Zoller. "Controlled collisions of a single atom and an ion guided by movable trapping potentials". In: *Physical Review A* 76.3 (Sept. 19, 2007). Publisher: American Physical Society, p. 033409. DOI: [10.1103/PhysRevA.76.033409](https://doi.org/10.1103/PhysRevA.76.033409). URL:

- <https://link.aps.org/doi/10.1103/PhysRevA.76.033409> (visited on 08/11/2021).
- [Idz+09] Zbigniew Idziaszek et al. “Quantum theory of ultracold atom-ion collisions”. In: *Physical Review A* 79.1 (Jan. 15, 2009). Publisher: American Physical Society, p. 010702. DOI: [10.1103/PhysRevA.79.010702](https://doi.org/10.1103/PhysRevA.79.010702). URL: <https://link.aps.org/doi/10.1103/PhysRevA.79.010702> (visited on 08/13/2021).
- [Idz+11] Zbigniew Idziaszek et al. “Multichannel quantum-defect theory for ultracold atom-ion collisions”. In: *New Journal of Physics* 13.8 (Aug. 2011). Publisher: IOP Publishing, p. 083005. ISSN: 1367-2630. DOI: [10.1088/1367-2630/13/8/083005](https://doi.org/10.1088/1367-2630/13/8/083005). URL: <https://doi.org/10.1088/1367-2630/13/8/083005> (visited on 08/13/2021).
- [JA89] D. H. JAKUBAŁA-AMUNDSEN. “Theoretical models for atomic charge transfer in ion-atom collisions”. In: *International Journal of Modern Physics A* 04.4 (Feb. 1, 1989). Publisher: World Scientific Publishing Co., pp. 769–844. ISSN: 0217-751X. DOI: [10.1142/S0217751X89000376](https://doi.org/10.1142/S0217751X89000376). URL: <https://www.worldscientific.com/doi/10.1142/S0217751X89000376> (visited on 10/26/2021).
- [JM20] Krzysztof Jachymski and Florian Meinert. “Vibrational Quenching of Weakly Bound Cold Molecular Ions Immersed in Their Parent Gas”. In: *Applied Sciences* 10.7 (Jan. 2020). Number: 7 Publisher: Multidisciplinary Digital Publishing Institute, p. 2371. DOI: [10.3390/app10072371](https://doi.org/10.3390/app10072371). URL: <https://www.mdpi.com/2076-3417/10/7/2371> (visited on 11/10/2021).
- [Jog+17] J. Joger et al. “Observation of collisions between cold Li atoms and Yb⁺ ions”. In: *Physical Review A* 96.3 (Sept. 25, 2017). Publisher: American Physical Society, p. 030703. DOI: [10.1103/PhysRevA.96.030703](https://doi.org/10.1103/PhysRevA.96.030703). URL: <https://link.aps.org/doi/10.1103/PhysRevA.96.030703> (visited on 11/10/2021).
- [Joh78] B. R. Johnson. “The renormalized Numerov method applied to calculating bound states of the coupled-channel Schroedinger equation”. In: *The Journal of Chemical Physics* 69.10 (Nov. 15, 1978). Publisher: American Institute of Physics, pp. 4678–4688. ISSN: 0021-9606. DOI: [10.1063/1.436421](https://doi.org/10.1063/1.436421). URL: <https://aip.scitation.org/doi/10.1063/1.436421> (visited on 11/17/2021).
- [Jon+06] Kevin M. Jones et al. “Ultracold photoassociation spectroscopy: Long-range molecules and atomic scattering”. In: *Reviews of Modern Physics* 78.2 (May 22, 2006). Publisher: American Physical Society, pp. 483–535. DOI: [10.1103/RevModPhys.78.483](https://doi.org/10.1103/RevModPhys.78.483). URL: <https://link.aps.org/doi/10.1103/RevModPhys.78.483> (visited on 11/10/2021).

- [Jr+15] Humberto da Silva Jr et al. "Formation of molecular ions by radiative association of cold trapped atoms and ions". In: *New Journal of Physics* 17.4 (Apr. 2015). Publisher: IOP Publishing, p. 045015. ISSN: 1367-2630. DOI: [10.1088/1367-2630/17/4/045015](https://doi.org/10.1088/1367-2630/17/4/045015). URL: <https://doi.org/10.1088/1367-2630/17/4/045015> (visited on 09/28/2021).
- [Jyo+16] S. Jyothi et al. "Photodissociation of Trapped Rb_2^+ : Implications for Simultaneous Trapping of Atoms and Molecular Ions". In: *Physical Review Letters* 117.21 (Nov. 18, 2016). Publisher: American Physical Society, p. 213002. DOI: [10.1103/PhysRevLett.117.213002](https://link.aps.org/doi/10.1103/PhysRevLett.117.213002). URL: <https://link.aps.org/doi/10.1103/PhysRevLett.117.213002> (visited on 11/12/2021).
- [KD04] R. V. Krems and A. Dalgarno. "Quantum-mechanical theory of atom-molecule and molecular collisions in a magnetic field: Spin depolarization". In: *The Journal of Chemical Physics* 120.5 (Feb. 1, 2004). Publisher: American Institute of Physics, pp. 2296–2307. ISSN: 0021-9606. DOI: [10.1063/1.1636691](https://aip.scitation.org/doi/10.1063/1.1636691). URL: <https://aip.scitation.org/doi/10.1063/1.1636691> (visited on 11/17/2021).
- [Ket02] Wolfgang Ketterle. "Nobel lecture: When atoms behave as waves: Bose-Einstein condensation and the atom laser". In: *Reviews of Modern Physics* 74.4 (Nov. 20, 2002). Publisher: American Physical Society, pp. 1131–1151. DOI: [10.1103/RevModPhys.74.1131](https://link.aps.org/doi/10.1103/RevModPhys.74.1131). URL: <https://link.aps.org/doi/10.1103/RevModPhys.74.1131> (visited on 10/25/2021).
- [KGJ06] Thorsten Köhler, Krzysztof Góral, and Paul S. Julienne. "Production of cold molecules via magnetically tunable Feshbach resonances". In: *Reviews of Modern Physics* 78.4 (Dec. 1, 2006). Publisher: American Physical Society, pp. 1311–1361. DOI: [10.1103/RevModPhys.78.1311](https://link.aps.org/doi/10.1103/RevModPhys.78.1311). URL: <https://link.aps.org/doi/10.1103/RevModPhys.78.1311> (visited on 11/10/2021).
- [Kim+10] K. Kim et al. "Quantum simulation of frustrated Ising spins with trapped ions". In: *Nature* 465.7298 (June 2010), pp. 590–593. ISSN: 1476-4687. DOI: [10.1038/nature09071](https://www.nature.com/articles/nature09071). URL: <https://www.nature.com/articles/nature09071> (visited on 08/04/2021).
- [Kim+93] M. Kimura et al. "Rate Coefficients for Momentum Transfer, Charge Transfer, and Radiative Association Processes in Collisions of H^+ with He below 10^5 K". In: *The Astrophysical Journal* 405 (Mar. 1, 1993). ADS Bibcode: 1993ApJ...405..801K, p. 801. ISSN: 0004-637X. DOI: [10.1086/172410](https://ui.adsabs.harvard.edu/abs/1993ApJ...405..801K). URL: <https://ui.adsabs.harvard.edu/abs/1993ApJ...405..801K> (visited on 10/06/2021).
- [Kok+99] V. Kokoouline et al. "Mapped Fourier methods for long-range molecules: Application to perturbations in the $\text{Rb}_2(0_u^+)$ photoassociation spectrum".

- In: *The Journal of Chemical Physics* 110.20 (May 22, 1999). Publisher: American Institute of Physics, pp. 9865–9876. ISSN: 0021-9606. DOI: [10.1063/1.478860](https://doi.org/10.1063/1.478860). URL: <https://aip.scitation.org/doi/10.1063/1.478860> (visited on 11/17/2021).
- [Kre08] R. V. Krems. “Cold controlled chemistry”. In: *Physical Chemistry Chemical Physics* 10.28 (July 9, 2008). Publisher: The Royal Society of Chemistry, pp. 4079–4092. ISSN: 1463-9084. DOI: [10.1039/B802322K](https://doi.org/10.1039/B802322K). URL: <https://pubs.rsc.org/en/content/articlelanding/2008/cp/b802322k> (visited on 11/17/2021).
- [Krü+16a] Artjom Krükow et al. “Energy Scaling of Cold Atom-Atom-Ion Three-Body Recombination”. In: *Physical Review Letters* 116.19 (May 12, 2016). Publisher: American Physical Society, p. 193201. DOI: [10.1103/PhysRevLett.116.193201](https://doi.org/10.1103/PhysRevLett.116.193201). URL: <https://link.aps.org/doi/10.1103/PhysRevLett.116.193201> (visited on 11/19/2021).
- [Krü+16b] Artjom Krükow et al. “Reactive two-body and three-body collisions of Ba^+ in an ultracold Rb gas”. In: *Physical Review A* 94.3 (Sept. 6, 2016), p. 030701. ISSN: 2469-9926, 2469-9934. DOI: [10.1103/PhysRevA.94.030701](https://doi.org/10.1103/PhysRevA.94.030701). URL: <https://link.aps.org/doi/10.1103/PhysRevA.94.030701> (visited on 01/27/2021).
- [Krü17] Artjom Krükow. “Three-body reaction dynamics in cold atom-ion experiments”. Accepted: 2017-05-24 ISBN: 9781659141696. Dissertation. Universität Ulm, May 24, 2017. DOI: [10.18725/OPARU-4354](https://doi.org/10.18725/OPARU-4354). URL: <https://oparu.uni-ulm.de/xmlui/handle/123456789/4393> (visited on 10/18/2021).
- [Kry+11] Michał Krych et al. “Sympathetic cooling of the Ba^+ ion by collisions with ultracold Rb atoms: Theoretical prospects”. In: *Physical Review A* 83.3 (Mar. 31, 2011). Publisher: American Physical Society, p. 032723. DOI: [10.1103/PhysRevA.83.032723](https://doi.org/10.1103/PhysRevA.83.032723). URL: <https://link.aps.org/doi/10.1103/PhysRevA.83.032723> (visited on 08/13/2021).
- [KVD89] Kate P. Kirby and Ewine F. Van Dishoeck. “Photodissociation Processes in Diatomic Molecules of Astrophysical Interest”. In: *Advances in Atomic and Molecular Physics*. Ed. by David Bates and Benjamin Bederson. Vol. 25. Academic Press, Jan. 1, 1989, pp. 437–476. DOI: [10.1016/S0065-2199\(08\)60097-4](https://doi.org/10.1016/S0065-2199(08)60097-4). URL: <https://www.sciencedirect.com/science/article/pii/S0065219908600974> (visited on 11/17/2021).
- [L01] Goldstein H; Poole C P; Safko J L. *Classical Mechanics*. 3rd ed. Addison-Wesley, 2001. 638 pp. ISBN: 978-0-201-65702-9.
- [Lan05] P. Langevin. “Une formule fondamentale de théorie cinétique”. In: *Ann. Chim. Phys.* 5 (245 1905).

- [Lev05] Raphael D. Levine. *Molecular Reaction Dynamics*. Cambridge University Press, 2005. ISBN: 978-0-521-14071-3. DOI: [10.1017/CB09780511614125](https://doi.org/10.1017/CB09780511614125). URL: <https://www.cambridge.org/core/books/molecular-reaction-dynamics/8FD43361EC4D5E97467C14D9FF42117E>.
- [LGN12] M. Larsson, W. D. Geppert, and G. Nyman. "Ion chemistry in space". In: *Reports on Progress in Physics* 75.6 (May 2012). Publisher: IOP Publishing, p. 066901. ISSN: 0034-4885. DOI: [10.1088/0034-4885/75/6/066901](https://doi.org/10.1088/0034-4885/75/6/066901). URL: <https://doi.org/10.1088/0034-4885/75/6/066901> (visited on 11/17/2021).
- [LLM91] Landau, L. D. & Lifshitz, and E. M. *Course of Theoretical Physics, Quantum Mechanics non-relativistic theory*. 3rd ed. Vol. 3. Pergamon, 1991. (Visited on 09/20/2021).
- [Mak+03] Oleg P. Makarov et al. "Radiative charge-transfer lifetime of the excited state of (NaCa)⁺". In: *Physical Review A* 67.4 (Apr. 11, 2003). Publisher: American Physical Society, p. 042705. DOI: [10.1103/PhysRevA.67.042705](https://doi.org/10.1103/PhysRevA.67.042705). URL: <https://link.aps.org/doi/10.1103/PhysRevA.67.042705> (visited on 08/13/2021).
- [Mar+16] Esteban A. Martinez et al. "Real-time dynamics of lattice gauge theories with a few-qubit quantum computer". In: *Nature* 534.7608 (June 2016), pp. 516–519. ISSN: 1476-4687. DOI: [10.1038/nature18318](https://doi.org/10.1038/nature18318). URL: <https://www.nature.com/articles/nature18318> (visited on 08/05/2021).
- [MBV96] A. J. Moerdijk, H. M. J. M. Boesten, and B. J. Verhaar. "Decay of trapped ultracold alkali atoms by recombination". In: *Physical Review A* 53.2 (Feb. 1, 1996). Publisher: American Physical Society, pp. 916–920. DOI: [10.1103/PhysRevA.53.916](https://doi.org/10.1103/PhysRevA.53.916). URL: <https://link.aps.org/doi/10.1103/PhysRevA.53.916> (visited on 11/10/2021).
- [Mei+16] Ziv Meir et al. "Dynamics of a Ground-State Cooled Ion Colliding with Ultracold Atoms". In: *Physical Review Letters* 117.24 (Dec. 7, 2016). Publisher: American Physical Society, p. 243401. DOI: [10.1103/PhysRevLett.117.243401](https://doi.org/10.1103/PhysRevLett.117.243401). URL: <https://link.aps.org/doi/10.1103/PhysRevLett.117.243401> (visited on 08/18/2021).
- [Mey01] Pierre Meystre. *Atom Optics*. Springer-Verlag New York, 2001.
- [MFM84] Wolfgang Müller, Joachim Flesch, and Wilfried Meyer. "Treatment of intershell correlation effects in *ab initio* calculations by use of core polarization potentials. Method and application to alkali and alkaline earth atoms". In: *The Journal of Chemical Physics* 80.7 (Apr. 1, 1984). Publisher: American Institute of Physics, pp. 3297–3310. ISSN: 0021-9606. DOI: [10.1063/1.447083](https://doi.org/10.1063/1.447083). URL: <https://aip.scitation.org/doi/10.1063/1.447083> (visited on 11/17/2021).

- [Mic94] Albert Abraham Michelson: "The more important fundamental laws and facts of physical science have all been discovered, and these are now so firmly established that the possibility of their ever being supplanted in consequence of new discoveries is exceedingly remote. ...the future truths of physical science are to be looked for in the sixth place of decimals." In: (1894). 1894, dedication of Ryerson Physical Laboratory, quoted in Annual Register 1896, p. 159.
- [MKD21] Amir Mahdian, Artjom Krüchow, and Johannes Hecker Denschlag. "Direct observation of swap cooling in atom-ion collisions". In: *New Journal of Physics* 23.6 (June 2021). Publisher: IOP Publishing, p. 065008. ISSN: 1367-2630. DOI: [10.1088/1367-2630/ac0575](https://doi.org/10.1088/1367-2630/ac0575). URL: <https://doi.org/10.1088/1367-2630/ac0575> (visited on 08/19/2021).
- [Moh+19] Amir Mohammadi et al. "Minimizing rf-induced excess micromotion of a trapped ion with the help of ultracold atoms". In: *Applied Physics B* 125.7 (June 14, 2019), p. 122. ISSN: 1432-0649. DOI: [10.1007/s00340-019-7223-y](https://doi.org/10.1007/s00340-019-7223-y). URL: <https://doi.org/10.1007/s00340-019-7223-y> (visited on 08/18/2021).
- [Moh+21] Amir Mohammadi et al. "Life and death of a cold BaRb⁺ molecule inside an ultracold cloud of Rb atoms". In: *Physical Review Research* 3.1 (Feb. 26, 2021). Publisher: American Physical Society, p. 013196. DOI: [10.1103/PhysRevResearch.3.013196](https://link.aps.org/doi/10.1103/PhysRevResearch.3.013196). URL: <https://link.aps.org/doi/10.1103/PhysRevResearch.3.013196> (visited on 11/19/2021).
- [MPS05] P. Massignan, C. J. Pethick, and H. Smith. "Static properties of positive ions in atomic Bose-Einstein condensates". In: *Physical Review A* 71.2 (Feb. 14, 2005). Publisher: American Physical Society, p. 023606. DOI: [10.1103/PhysRevA.71.023606](https://link.aps.org/doi/10.1103/PhysRevA.71.023606). URL: <https://link.aps.org/doi/10.1103/PhysRevA.71.023606> (visited on 08/11/2021).
- [MS03] H. J. Metcalf and P. van der Straten. "Laser cooling and trapping of atoms". In: *J. Opt. Soc. Am. B* 20.5 (2003), pp. 887–908. DOI: [10.1364/JOSAB.20.000887](http://josab.osa.org/abstract.cfm?URI=josab-20-5-887). URL: <http://josab.osa.org/abstract.cfm?URI=josab-20-5-887>.
- [MT61] Albert Messiah and G. M Temmer. *Quantum mechanics*. OCLC: 535119. Amsterdam; New York: North-Holland Pub. Co. ; Interscience Publishers, 1961.
- [MW01] Florian Mintert and Christof Wunderlich. "Ion-Trap Quantum Logic Using Long-Wavelength Radiation". In: *Physical Review Letters* 87.25 (Nov. 29, 2001). Publisher: American Physical Society, p. 257904. DOI: [10.1103/PhysRevLett.87.257904](https://link.aps.org/doi/10.1103/PhysRevLett.87.257904). URL: <https://link.aps.org/doi/10.1103/PhysRevLett.87.257904> (visited on 08/04/2021).

- [MW17] Jennifer Meyer and Roland Wester. “Ion-Molecule Reaction Dynamics”. In: *Annual Review of Physical Chemistry* 68.1 (2017). PMID: 28463654, pp. 333–353. DOI: [10.1146/annurev-physchem-052516-044918](https://doi.org/10.1146/annurev-physchem-052516-044918). URL: <https://doi.org/10.1146/annurev-physchem-052516-044918>.
- [MWW10] Jochen Mikosch, Matthias Weidemüller, and Roland Wester. “On the dynamics of chemical reactions of negative ions”. In: *International Reviews in Physical Chemistry* 29.4 (Oct. 1, 2010). Publisher: Taylor & Francis, pp. 589–617. ISSN: 0144-235X. DOI: [10.1080/0144235X.2010.519504](https://doi.org/10.1080/0144235X.2010.519504). URL: <https://doi.org/10.1080/0144235X.2010.519504> (visited on 11/10/2021).
- [Mya+97] C. J. Myatt et al. “Production of Two Overlapping Bose-Einstein Condensates by Sympathetic Cooling”. In: *Physical Review Letters* 78.4 (Jan. 27, 1997). Publisher: American Physical Society, pp. 586–589. DOI: [10.1103/PhysRevLett.78.586](https://link.aps.org/doi/10.1103/PhysRevLett.78.586). URL: <https://link.aps.org/doi/10.1103/PhysRevLett.78.586> (visited on 10/25/2021).
- [Neu+80] W. Neuhauser et al. “Localized visible Ba⁺ mono-ion oscillator”. In: *Phys. Rev. A* 22 (3 1980), pp. 1137–1140. DOI: [10.1103/PhysRevA.22.1137](https://link.aps.org/doi/10.1103/PhysRevA.22.1137). URL: <https://link.aps.org/doi/10.1103/PhysRevA.22.1137>.
- [Ney+17] Brian Neyenhuis et al. “Observation of prethermalization in long-range interacting spin chains”. In: *Science Advances* 3.8 (Aug. 1, 2017). Publisher: American Association for the Advancement of Science Section: Research Article, e1700672. ISSN: 2375-2548. DOI: [10.1126/sciadv.1700672](https://advances.sciencemag.org/content/3/8/e1700672). URL: <https://advances.sciencemag.org/content/3/8/e1700672> (visited on 08/05/2021).
- [OSR61] Thomas F. O’Malley, Larry Spruch, and Leonard Rosenberg. “Modification of Effective-Range Theory in the Presence of a Long-Range (r^{-4}) Potential”. In: *Journal of Mathematical Physics* 2.4 (July 1, 1961). Publisher: American Institute of Physics, pp. 491–498. ISSN: 0022-2488. DOI: [10.1063/1.1703735](https://aip.scitation.org/doi/10.1063/1.1703735). URL: <https://aip.scitation.org/doi/10.1063/1.1703735> (visited on 10/12/2021).
- [PB07] Simon Petrie and Diethard Kurt Bohme. “Ions in space”. In: *Mass Spectrometry Reviews* 26.2 (2007), pp. 258–280. ISSN: 1098-2787. DOI: [10.1002/mas.20114](https://onlinelibrary.wiley.com/doi/abs/10.1002/mas.20114). URL: <https://onlinelibrary.wiley.com/doi/abs/10.1002/mas.20114> (visited on 11/17/2021).
- [PC04] D. Porras and J. I. Cirac. “Effective Quantum Spin Systems with Trapped Ions”. In: *Physical Review Letters* 92.20 (May 20, 2004). Publisher: American Physical Society, p. 207901. DOI: [10.1103/PhysRevLett.92.207901](https://link.aps.org/doi/10.1103/PhysRevLett.92.207901). URL: <https://link.aps.org/doi/10.1103/PhysRevLett.92.207901> (visited on 08/04/2021).

- [Phi98] William D. Phillips. “Nobel Lecture: Laser cooling and trapping of neutral atoms”. In: *Rev. Mod. Phys.* 70 (3 1998), pp. 721–741. DOI: [10.1103/RevModPhys.70.721](https://doi.org/10.1103/RevModPhys.70.721). URL: <https://link.aps.org/doi/10.1103/RevModPhys.70.721>.
- [PR19] Jesús Pérez-Ríos. “Vibrational quenching and reactive processes of weakly bound molecular ions colliding with atoms at cold temperatures”. In: *Physical Review A* 99.2 (Feb. 19, 2019). Publisher: American Physical Society, p. 022707. DOI: [10.1103/PhysRevA.99.022707](https://doi.org/10.1103/PhysRevA.99.022707). URL: <https://link.aps.org/doi/10.1103/PhysRevA.99.022707> (visited on 11/17/2021).
- [PRG15] Jesús Pérez-Ríos and Chris H. Greene. “Communication: Classical threshold law for ion-neutral-neutral three-body recombination”. In: *The Journal of Chemical Physics* 143.4 (July 28, 2015). Publisher: American Institute of Physics, p. 041105. ISSN: 0021-9606. DOI: [10.1063/1.4927702](https://doi.org/10.1063/1.4927702). URL: <https://aip.scitation.org/doi/10.1063/1.4927702> (visited on 01/24/2022).
- [Pur+17] Prateek Puri et al. “Synthesis of mixed hypermetallic oxide BaOCa⁺ from laser-cooled reagents in an atom-ion hybrid trap”. In: *Science* 357.6358 (Sept. 29, 2017). Publisher: American Association for the Advancement of Science, pp. 1370–1375. DOI: [10.1126/science.aan4701](https://doi.org/10.1126/science.aan4701). URL: <https://www.science.org/doi/10.1126/science.aan4701> (visited on 11/12/2021).
- [Pur+19] Prateek Puri et al. “Reaction blockading in a reaction between an excited atom and a charged molecule at low collision energy”. In: *Nature Chemistry* 11.7 (July 2019), pp. 615–621. ISSN: 1755-4349. DOI: [10.1038/s41557-019-0264-3](https://doi.org/10.1038/s41557-019-0264-3). URL: <https://www.nature.com/articles/s41557-019-0264-3> (visited on 11/12/2021).
- [PVD65] Julius Perel, Richard H. Vernon, and Howard L. Daley. “Measurement of Cesium and Rubidium Charge-Transfer Cross Sections”. In: *Physical Review* 138.4 (May 17, 1965). Publisher: American Physical Society, A937–A945. DOI: [10.1103/PhysRev.138.A937](https://doi.org/10.1103/PhysRev.138.A937). URL: <https://link.aps.org/doi/10.1103/PhysRev.138.A937> (visited on 10/26/2021).
- [R20] Jesús Pérez Ríos. *An Introduction to Cold and Ultracold Chemistry: Atoms, Molecules, Ions and Rydbergs*. Springer International Publishing, 2020. ISBN: 978-3-030-55935-9. DOI: [10.1007/978-3-030-55935-9](https://doi.org/10.1007/978-3-030-55935-9). URL: <https://www.springer.com/gp/book/9783030559359> (visited on 09/06/2021).
- [Rat+12] Lothar Ratschbacher et al. “Controlling chemical reactions of a single particle”. In: *Nature Physics* 8.9 (Sept. 2012), pp. 649–652. ISSN: 1745-2481. DOI: [10.1038/nphys2373](https://doi.org/10.1038/nphys2373). URL: <https://www.nature.com/articles/nphys2373> (visited on 08/23/2021).

- [Rat+13] L. Ratschbacher et al. "Decoherence of a Single-Ion Qubit Immersed in a Spin-Polarized Atomic Bath". In: *Physical Review Letters* 110.16 (Apr. 19, 2013). Publisher: American Physical Society, p. 160402. DOI: [10.1103/PhysRevLett.110.160402](https://doi.org/10.1103/PhysRevLett.110.160402). URL: <https://link.aps.org/doi/10.1103/PhysRevLett.110.160402> (visited on 08/17/2021).
- [Rat13] Lothar Ratschbacher. "Investigation of an Atom-Ion quantum hybrid system". Dissertation. St Catherine's college, University of Cambridge, 2013. URL: <https://www.quantum.uni-bonn.de/publications/thesis-ratschbacher>.
- [Rav+12] K. Ravi et al. "Cooling and stabilization by collisions in a mixed ion-atom system". In: *Nature Communications* 3.1 (Oct. 9, 2012), p. 1126. ISSN: 2041-1723. DOI: [10.1038/ncomms2131](https://doi.org/10.1038/ncomms2131). URL: <https://www.nature.com/articles/ncomms2131> (visited on 08/17/2021).
- [Rel+11] Wade G. Rellergert et al. "Measurement of a Large Chemical Reaction Rate between Ultracold Closed-Shell ^{40}Ca Atoms and Open-Shell Yb^+ Ions Held in a Hybrid Atom-Ion Trap". In: *Physical Review Letters* 107.24 (Dec. 7, 2011). Publisher: American Physical Society, p. 243201. DOI: [10.1103/PhysRevLett.107.243201](https://doi.org/10.1103/PhysRevLett.107.243201). URL: <https://link.aps.org/doi/10.1103/PhysRevLett.107.243201> (visited on 08/17/2021).
- [Rel+13] Wade G. Rellergert et al. "Evidence for sympathetic vibrational cooling of translationally cold molecules". In: *Nature* 495.7442 (Mar. 2013), pp. 490–494. ISSN: 1476-4687. DOI: [10.1038/nature11937](https://doi.org/10.1038/nature11937). URL: <https://www.nature.com/articles/nature11937> (visited on 08/17/2021).
- [RW15] I. Rouse and S. Willitsch. "Superstatistical velocity distributions of cold trapped ions in molecular-dynamics simulations". In: *Physical Review A* 92.5 (Nov. 19, 2015). Publisher: American Physical Society, p. 053420. DOI: [10.1103/PhysRevA.92.053420](https://doi.org/10.1103/PhysRevA.92.053420). URL: <https://link.aps.org/doi/10.1103/PhysRevA.92.053420> (visited on 09/22/2021).
- [Sar+16] Dibyendu Sardar et al. "Formation of a molecular ion by photoassociative Raman processes". In: *Journal of Physics B: Atomic, Molecular and Optical Physics* 49.24 (Nov. 2016). Publisher: IOP Publishing, p. 245202. ISSN: 0953-4075. DOI: [10.1088/0953-4075/49/24/245202](https://doi.org/10.1088/0953-4075/49/24/245202). URL: <https://doi.org/10.1088/0953-4075/49/24/245202> (visited on 08/19/2021).
- [SB08] Theodore P. Snow and Veronica M. Bierbaum. "Ion Chemistry in the Interstellar Medium". In: *Annual Review of Analytical Chemistry* 1.1 (July 1, 2008), pp. 229–259. ISSN: 1936-1327, 1936-1335. DOI: [10.1146/annurev.anchem.1.031207.112907](https://doi.org/10.1146/annurev.anchem.1.031207.112907). URL: <https://www.annualreviews.org/doi/10.1146/annurev.anchem.1.031207.112907> (visited on 11/17/2021).

- [Sch+01] F. Schreck et al. "Quasipure Bose-Einstein Condensate Immersed in a Fermi Sea". In: *Phys. Rev. Lett.* 87 (8 2001), p. 080403. DOI: [10.1103/PhysRevLett.87.080403](https://doi.org/10.1103/PhysRevLett.87.080403). URL: <https://link.aps.org/doi/10.1103/PhysRevLett.87.080403>.
- [Sch+07] Sascha Schäfer et al. "Polarizabilities of Ba and Ba₂: Comparison of molecular beam experiments with relativistic quantum chemistry". In: *Physical Review A* 76.5 (Nov. 29, 2007). Publisher: American Physical Society, p. 052515. DOI: [10.1103/PhysRevA.76.052515](https://doi.org/10.1103/PhysRevA.76.052515). URL: <https://link.aps.org/doi/10.1103/PhysRevA.76.052515> (visited on 11/17/2021).
- [Sch12] Stefan Schmid. "Dynamics of a cold trapped ion in a Bose-Einstein condensate". Accepted: 2016-03-15T06:24:11Z. Dissertation. Universität Ulm, Mar. 19, 2012. DOI: [10.18725/OPARU-1950](https://doi.org/10.18725/OPARU-1950). URL: <https://oparu.uni-ulm.de/xmlui/handle/123456789/1977> (visited on 10/18/2021).
- [Sch+12] Stefan Schmid et al. "An apparatus for immersing trapped ions into an ultracold gas of neutral atoms". In: *Review of Scientific Instruments* 83.5 (May 2012), p. 053108. ISSN: 0034-6748, 1089-7623. DOI: [10.1063/1.4718356](https://doi.org/10.1063/1.4718356). URL: <http://aip.scitation.org/doi/10.1063/1.4718356> (visited on 01/27/2021).
- [Sch+16] Steven J. Schowalter et al. "Blue-sky bifurcation of ion energies and the limits of neutral-gas sympathetic cooling of trapped ions". In: *Nature Communications* 7.1 (Aug. 11, 2016), p. 12448. ISSN: 2041-1723. DOI: [10.1038/ncomms12448](https://doi.org/10.1038/ncomms12448). URL: <https://www.nature.com/articles/ncomms12448> (visited on 08/18/2021).
- [Sch93] "Direct photodissociation: The reflection principle". In: *Photodissociation Dynamics: Spectroscopy and Fragmentation of Small Polyatomic Molecules*. Ed. by Reinhard Schinke. Cambridge Monographs on Atomic, Molecular and Chemical Physics. Cambridge: Cambridge University Press, 1993, pp. 109–133. ISBN: 978-0-521-48414-5. DOI: [10.1017/CB09780511586453.007](https://doi.org/10.1017/CB09780511586453.007). URL: <https://www.cambridge.org/core/books/photodissociation-dynamics/direct-photodissociation-the-reflection-principle/71B2AD14278A9E2074C36648AA1E6FF7> (visited on 11/17/2021).
- [SHD10] Stefan Schmid, Arne Härter, and Johannes Hecker Denschlag. "Dynamics of a Cold Trapped Ion in a Bose-Einstein Condensate". In: *Physical Review Letters* 105.13 (Sept. 23, 2010), p. 133202. ISSN: 0031-9007, 1079-7114. DOI: [10.1103/PhysRevLett.105.133202](https://doi.org/10.1103/PhysRevLett.105.133202). URL: <https://link.aps.org/doi/10.1103/PhysRevLett.105.133202> (visited on 01/27/2021).
- [Sik+18a] Tomas Sikorsky et al. "Phase Locking between Different Partial Waves in Atom-Ion Spin-Exchange Collisions". In: *Physical Review Letters* 121.17 (Oct. 25, 2018). Publisher: American Physical Society, p. 173402. DOI:

- 10.1103/PhysRevLett.121.173402. URL: <https://link.aps.org/doi/10.1103/PhysRevLett.121.173402> (visited on 08/17/2021).
- [Sik+18b] Tomas Sikorsky et al. "Spin-controlled atom-ion chemistry". In: *Nature Communications* 9.1 (Mar. 2, 2018), p. 920. ISSN: 2041-1723. DOI: [10.1038/s41467-018-03373-y](https://doi.org/10.1038/s41467-018-03373-y). URL: <https://www.nature.com/articles/s41467-018-03373-y> (visited on 08/19/2021).
- [Siv+12] I. Sivarajah et al. "Evidence of sympathetic cooling of Na⁺ ions by a Na magneto-optical trap in a hybrid trap". In: *Physical Review A* 86.6 (Dec. 26, 2012). Publisher: American Physical Society, p. 063419. DOI: [10.1103/PhysRevA.86.063419](https://doi.org/10.1103/PhysRevA.86.063419). URL: <https://link.aps.org/doi/10.1103/PhysRevA.86.063419> (visited on 08/17/2021).
- [SK+03] Ferdinand Schmidt-Kaler et al. "Realization of the Cirac-Zoller controlled-NOT quantum gate". In: *Nature* 422.6930 (Mar. 2003), pp. 408–411. ISSN: 1476-4687. DOI: [10.1038/nature01494](https://doi.org/10.1038/nature01494). URL: <https://www.nature.com/articles/nature01494> (visited on 07/21/2021).
- [SK14] Carlo Sias and Michael Köhl. "Hybrid Quantum Systems of Atoms and Ions". In: *Quantum Gas Experiments*. Vol. Volume 3. Cold Atoms Volume 3. IMPERIAL COLLEGE PRESS, May 5, 2014, pp. 267–291. ISBN: 978-1-78326-474-2. DOI: [10.1142/9781783264766_0012](https://doi.org/10.1142/9781783264766_0012). URL: https://www.worldscientific.com/doi/abs/10.1142/9781783264766_0012 (visited on 08/24/2021).
- [SK+98] D. M. Stamper-Kurn et al. "Optical Confinement of a Bose-Einstein Condensate". In: *Physical Review Letters* 80.10 (Mar. 9, 1998). Publisher: American Physical Society, pp. 2027–2030. DOI: [10.1103/PhysRevLett.80.2027](https://doi.org/10.1103/PhysRevLett.80.2027). URL: <https://link.aps.org/doi/10.1103/PhysRevLett.80.2027> (visited on 11/10/2021).
- [SLD98] P. C. Stancil, S. Lepp, and A. Dalgarno. "The Deuterium Chemistry of the Early Universe". In: *The Astrophysical Journal* 509.1 (Dec. 10, 1998). Publisher: IOP Publishing, p. 1. ISSN: 0004-637X. DOI: [10.1086/306473](https://doi.org/10.1086/306473). URL: <https://iopscience.iop.org/article/10.1086/306473/meta> (visited on 10/06/2021).
- [Smi01] Boris M Smirnov. "Atomic structure and the resonant charge exchange process". In: *Physics-Uspokhi* 44.3 (Mar. 31, 2001), pp. 221–253. ISSN: 1063-7869, 1468-4780. DOI: [10.1070/PU2001v044n03ABEH000826](https://doi.org/10.1070/PU2001v044n03ABEH000826). URL: <http://stacks.iop.org/1063-7869/44/i=3/a=R01?key=crossref.2cc13148d1779a0aa05b9411e0985749> (visited on 03/29/2021).
- [Smi03] B. M. Smirnov. "Resonant charge exchange in slow collisions involving halogens and oxygen". In: *Journal of Experimental and Theoretical Physics* 97.3 (Sept. 1, 2003), pp. 493–504. ISSN: 1090-6509. DOI: [10.1134/](https://doi.org/10.1134/)

1. 1618336. URL: <https://doi.org/10.1134/1.1618336> (visited on 10/26/2021).
- [Smi+14] W. W. Smith et al. “Experiments with an ion-neutral hybrid trap: cold charge-exchange collisions”. In: *Applied Physics B* 114.1 (Jan. 1, 2014), pp. 75–80. ISSN: 1432-0649. DOI: 10.1007/s00340-013-5672-2. URL: <https://doi.org/10.1007/s00340-013-5672-2> (visited on 08/17/2021).
- [Smi+16] J. Smith et al. “Many-body localization in a quantum simulator with programmable random disorder”. In: *Nature Physics* 12.10 (Oct. 2016), pp. 907–911. ISSN: 1745-2481. DOI: 10.1038/nphys3783. URL: <https://www.nature.com/articles/nphys3783> (visited on 08/05/2021).
- [Smi92] David Smith. “The ion chemistry of interstellar clouds”. In: *Chemical Reviews* 92.7 (Nov. 1, 1992). Publisher: American Chemical Society, pp. 1473–1485. ISSN: 0009-2665. DOI: 10.1021/cr00015a001. URL: <https://doi.org/10.1021/cr00015a001> (visited on 11/17/2021).
- [SML05] Winthrop W. Smith, Oleg P. Makarov, and Jian Lin. “Cold ion-neutral collisions in a hybrid trap”. In: *Journal of Modern Optics* 52.16 (Nov. 10, 2005). Publisher: Taylor & Francis, pp. 2253–2260. ISSN: 0950-0340. DOI: 10.1080/09500340500275850. URL: <https://www.tandfonline.com/doi/citedby/10.1080/09500340500275850> (visited on 08/16/2021).
- [SN19] Peter Schwerdtfeger and Jeffrey K. Nagle. “2018 Table of static dipole polarizabilities of the neutral elements in the periodic table”. In: *Molecular Physics* 117.9 (June 18, 2019), pp. 1200–1225. ISSN: 0026-8976. DOI: 10.1080/00268976.2018.1535143. URL: <https://doi.org/10.1080/00268976.2018.1535143> (visited on 01/27/2021).
- [Str+10] C. Strauss et al. “Hyperfine, rotational, and vibrational structure of the $a^3\Sigma_u^+$ state of $^{87}\text{Rb}_2$ ”. In: *Physical Review A* 82.5 (Nov. 19, 2010). Publisher: American Physical Society, p. 052514. DOI: 10.1103/PhysRevA.82.052514. URL: <https://link.aps.org/doi/10.1103/PhysRevA.82.052514> (visited on 11/15/2021).
- [Sul+12] Scott T. Sullivan et al. “Role of Electronic Excitations in Ground-State-Forbidden Inelastic Collisions Between Ultracold Atoms and Ions”. In: *Physical Review Letters* 109.22 (Nov. 27, 2012). Publisher: American Physical Society, p. 223002. DOI: 10.1103/PhysRevLett.109.223002. URL: <https://link.aps.org/doi/10.1103/PhysRevLett.109.223002> (visited on 08/19/2021).
- [Tom+19] Michał Tomza et al. “Cold hybrid ion-atom systems”. In: *Reviews of Modern Physics* 91.3 (July 15, 2019). Publisher: American Physical Society, p. 035001. DOI: 10.1103/RevModPhys.91.035001. URL: <https://link.aps.org/doi/10.1103/RevModPhys.91.035001> (visited on 08/24/2021).

- [Tru+01] Andrew G. Truscott et al. "Observation of Fermi Pressure in a Gas of Trapped Atoms". In: *Science* 291.5513 (Mar. 30, 2001). Publisher: American Association for the Advancement of Science, pp. 2570–2572. DOI: [10.1126/science.1059318](https://doi.org/10.1126/science.1059318). URL: <https://www.science.org/doi/10.1126/science.1059318> (visited on 10/25/2021).
- [Ulm+12] Juris Ulmanis et al. "Ultracold Molecules Formed by Photoassociation: Heteronuclear Dimers, Inelastic Collisions, and Interactions with Ultrashort Laser Pulses". In: *Chemical Reviews* 112.9 (Sept. 12, 2012). Publisher: American Chemical Society, pp. 4890–4927. ISSN: 0009-2665. DOI: [10.1021/cr300215h](https://doi.org/10.1021/cr300215h). URL: <https://doi.org/10.1021/cr300215h> (visited on 11/10/2021).
- [VW54] Erich Vogt and Gregory H. Wannier. "Scattering of Ions by Polarization Forces". In: *Physical Review* 95.5 (Sept. 1, 1954). Publisher: American Physical Society, pp. 1190–1198. DOI: [10.1103/PhysRev.95.1190](https://link.aps.org/doi/10.1103/PhysRev.95.1190). URL: <https://link.aps.org/doi/10.1103/PhysRev.95.1190> (visited on 01/27/2021).
- [Wec+21] Pascal Weckesser et al. "Observation of Feshbach resonances between a single ion and ultracold atoms". In: *Nature* 600.7889 (Dec. 2021), pp. 429–433. ISSN: 1476-4687. DOI: [10.1038/s41586-021-04112-y](https://www.nature.com/articles/s41586-021-04112-y). URL: <https://www.nature.com/articles/s41586-021-04112-y> (visited on 01/25/2022).
- [Wei+98] Jonathan D. Weinstein et al. "Magnetic trapping of calcium monohydride molecules at millikelvin temperatures". In: *Nature* 395.6698 (Sept. 1998), pp. 148–150. ISSN: 1476-4687. DOI: [10.1038/25949](https://www.nature.com/articles/25949). URL: <https://www.nature.com/articles/25949> (visited on 10/25/2021).
- [Wil+08] Stefan Willitsch et al. "Chemical applications of laser- and sympathetically-cooled ions in ion traps". In: *Physical Chemistry Chemical Physics* 10.48 (Dec. 28, 2008). Publisher: The Royal Society of Chemistry, pp. 7200–7210. ISSN: 1463-9084. DOI: [10.1039/B813408C](https://pubs.rsc.org/en/content/articlelanding/2008/cp/b813408c). URL: <https://pubs.rsc.org/en/content/articlelanding/2008/cp/b813408c> (visited on 10/25/2021).
- [Wil15] S. Willitsch. "Ion-atom hybrid systems". In: *Ion Traps for Tomorrow's Applications* (2015). Publisher: IOS Press, pp. 255–268. DOI: [10.3254/978-1-61499-526-5-255](https://ebooks.iospress.nl/doi/10.3254/978-1-61499-526-5-255). URL: <https://ebooks.iospress.nl/doi/10.3254/978-1-61499-526-5-255> (visited on 08/24/2021).
- [Wit05] Curt Wittig. "The Landau-Zener Formula". In: *The Journal of Physical Chemistry B* 109.17 (May 1, 2005). Publisher: American Chemical Society, pp. 8428–8430. ISSN: 1520-6106. DOI: [10.1021/jp040627u](https://doi.org/10.1021/jp040627u). URL: <https://doi.org/10.1021/jp040627u> (visited on 10/05/2021).

- [WLF19] Martin Will, Tobias Lausch, and Michael Fleischhauer. “Rotational cooling of molecules in a Bose-Einstein condensate”. In: *Physical Review A* 99.6 (June 17, 2019). Publisher: American Physical Society, p. 062707. DOI: [10.1103/PhysRevA.99.062707](https://doi.org/10.1103/PhysRevA.99.062707). URL: <https://link.aps.org/doi/10.1103/PhysRevA.99.062707> (visited on 09/23/2021).
- [Yan+20] Yu Kun Yang et al. “Particle scattering and resonances involving avoided crossing”. In: *New Journal of Physics* 22.12 (Dec. 2020). Publisher: IOP Publishing, p. 123022. ISSN: 1367-2630. DOI: [10.1088/1367-2630/abcfed](https://doi.org/10.1088/1367-2630/abcfed). URL: <https://doi.org/10.1088/1367-2630/abcfed> (visited on 10/05/2021).
- [ZD90] B. Zygelman and A. Dalgarno. “The Radiative Association of He^+ and H^+ ”. In: *The Astrophysical Journal* 365 (Dec. 1, 1990), p. 239. ISSN: 0004-637X. DOI: [10.1086/169475](https://ui.adsabs.harvard.edu/abs/1990ApJ...365..239Z). URL: <https://ui.adsabs.harvard.edu/abs/1990ApJ...365..239Z> (visited on 10/06/2021).
- [ZDC09] Peng Zhang, Alex Dalgarno, and Robin Côté. “Scattering of Yb and Yb^+ ”. In: *Physical Review A* 80.3 (Sept. 28, 2009). Publisher: American Physical Society, p. 030703. DOI: [10.1103/PhysRevA.80.030703](https://doi.org/10.1103/PhysRevA.80.030703). URL: <https://link.aps.org/doi/10.1103/PhysRevA.80.030703> (visited on 10/11/2021).
- [Zha+17a] J. Zhang et al. “Observation of a discrete time crystal”. In: *Nature* 543.7644 (Mar. 2017), pp. 217–220. ISSN: 1476-4687. DOI: [10.1038/nature21413](https://doi.org/10.1038/nature21413). URL: <https://www.nature.com/articles/nature21413> (visited on 08/05/2021).
- [Zha+17b] J. Zhang et al. “Observation of a many-body dynamical phase transition with a 53-qubit quantum simulator”. In: *Nature* 551.7682 (Nov. 2017), pp. 601–604. ISSN: 1476-4687. DOI: [10.1038/nature24654](https://doi.org/10.1038/nature24654). URL: <https://www.nature.com/articles/nature24654> (visited on 08/05/2021).
- [Zip+10a] Christoph Zipkes et al. “A trapped single ion inside a Bose-Einstein condensate”. In: *Nature* 464.7287 (Mar. 2010), pp. 388–391. ISSN: 1476-4687. DOI: [10.1038/nature08865](https://doi.org/10.1038/nature08865). URL: <https://www.nature.com/articles/nature08865> (visited on 08/16/2021).
- [Zip+10b] Christoph Zipkes et al. “Cold Heteronuclear Atom-Ion Collisions”. In: *Physical Review Letters* 105.13 (Sept. 23, 2010). Publisher: American Physical Society, p. 133201. DOI: [10.1103/PhysRevLett.105.133201](https://doi.org/10.1103/PhysRevLett.105.133201). URL: <https://link.aps.org/doi/10.1103/PhysRevLett.105.133201> (visited on 08/18/2021).
- [Zip+11] Christoph Zipkes et al. “Kinetics of a single trapped ion in an ultracold buffer gas”. In: *New Journal of Physics* 13.5 (May 2011). Publisher: IOP Publishing, p. 053020. ISSN: 1367-2630. DOI: [10.1088/1367-2630/13/5/053020](https://doi.org/10.1088/1367-2630/13/5/053020).

5/053020. URL: <https://doi.org/10.1088/1367-2630/13/5/053020> (visited on 08/17/2021).

- [ZW17] Dongdong Zhang and Stefan Willitsch. "CHAPTER 10: Cold Ion Chemistry". In: *Cold Chemistry*. Dec. 5, 2017, pp. 496–536. DOI: [10.1039/9781782626800-00496](https://pubs.rsc.org/en/content/chapter/bk9781782625971-00496/978-1-78262-597-1). URL: <https://pubs.rsc.org/en/content/chapter/bk9781782625971-00496/978-1-78262-597-1> (visited on 11/10/2021).